

Indication of Electron Neutrino Appearance in an
Accelerator-Produced Muon Neutrino Beam

by

Joshua Benjamin Albert

Department of Physics
Duke University

Date: _____

Approved:

Christopher W. Walter, Supervisor

Kate Scholberg

Mark Kruse

Tom Mehen

Henry Greenside

Dissertation submitted in partial fulfillment of the requirements for the degree of
Doctor of Philosophy in the Department of Physics
in the Graduate School of Duke University
2012

ABSTRACT

Indication of Electron Neutrino Appearance in an
Accelerator-Produced Muon Neutrino Beam

by

Joshua Benjamin Albert

Department of Physics
Duke University

Date: _____

Approved:

Christopher W. Walter, Supervisor

Kate Scholberg

Mark Kruse

Tom Mehen

Henry Greenside

An abstract of a dissertation submitted in partial fulfillment of the requirements for
the degree of Doctor of Philosophy in the Department of Physics
in the Graduate School of Duke University
2012

Copyright © 2012 by Joshua Benjamin Albert
All rights reserved except the rights granted by the
Creative Commons Attribution-Noncommercial Licence

Abstract

T2K (Tokai to Kamioka) is a long baseline neutrino experiment with the primary goal of measuring the neutrino mixing angle θ_{13} . It uses a muon neutrino beam, produced at the J-PARC accelerator facility in Tokai, sent through a near detector complex on its way to the far detector, Super-Kamiokande. Appearance of electron neutrinos at the far detector due to oscillation is used to measure the value of θ_{13} .

This dissertation describes the experimental setup, analysis methods, and results from the analysis of T2K data taken from January 2010 through March 2011. Six signal candidate events were observed on an expected background of 1.5 ± 0.3 . The probability to see six or more such events is 0.7% under the $\theta_{13} = 0$ hypothesis. This is the first experiment to exclude $\theta_{13} = 0$ at the 90% confidence level. The 90% confidence level allowed region is $0.03(0.04) < \sin^2 2\theta_{13} < 0.28(0.34)$ with a best fit point of $\sin^2 2\theta_{13} = 0.11(0.14)$ for $\delta_{\text{CP}} = 0$ and $|\Delta m_{32}^2| = 2.4 \times 10^{-3} \text{ eV}^2$ in the normal (inverted) hierarchy.

For my family.

Contents

Abstract	iv
List of Tables	xii
List of Figures	xiii
List of Abbreviations and Symbols	xvii
Acknowledgements	xix
1 Introduction	1
1.1 Dissertation Outline	1
1.2 Author Contributions	2
2 Neutrino Physics	4
2.1 History	4
2.1.1 Assembling the Neutrino Family	4
2.1.2 Symmetry (or lack thereof)	6
2.1.3 Oscillation	8
2.2 The Standard Model Neutrino	12
2.3 Oscillation	16
2.3.1 Two Flavor Model	17
2.3.2 Three Flavor Vacuum Oscillations	22
2.3.3 Matter Effects	25
2.4 CP Violation	28

2.5	Recent Neutrino Oscillation Experiments	30
3	T2K	33
3.1	Introduction	33
3.2	Basic Setup	34
3.3	Off-Axis Beam	35
3.4	J-PARC Accelerator	36
3.5	Neutrino Beamline	37
3.6	ND280	43
3.6.1	INGRID	43
3.6.2	ND280 Off-Axis	45
3.7	Far Detector	50
4	Super-Kamiokande	52
4.1	Overview	52
4.2	Detector Physics	56
4.3	Data Acquisition	59
4.4	Water and Air Purification	61
4.5	Atmospheric Reduction	62
4.6	Reconstruction	64
4.6.1	Vertex Finding	64
4.6.2	Ring Counting	65
4.6.3	Particle ID	65
4.6.4	Decay Electron Tagging	66
4.6.5	Momentum Reconstruction	67
4.6.6	Ring Number Correction	68
4.6.7	POLfit	68

4.7	Calibration	71
4.7.1	Timing	72
4.7.2	PMT Gain	73
4.7.3	Water Parameters	75
4.7.4	Auto-Calibration	76
4.8	Energy Scale	76
4.8.1	Multi-GeV Stopping Muons	77
4.8.2	Sub-GeV Stopping Muons	77
4.8.3	π^0 Mass	78
4.8.4	Decay Electrons	78
4.8.5	Absolute Scale	78
4.8.6	Time Variation	79
4.9	Additional Decay Electron Studies	79
4.10	T2K-Specific Operation	81
5	Analysis Overview and Development	86
5.1	Analysis Strategy	86
5.2	Far Detector Selection Cuts	88
5.2.1	Fiducial Volume Cut	89
5.2.2	Fully Contained Cut	90
5.2.3	Single Ring Cut	90
5.2.4	E-like Ring Cut	91
5.2.5	Visible Energy Cut	92
5.2.6	$\mu \rightarrow e$ Decay Cut	93
5.2.7	POLfit π^0 Mass Cut	94
5.2.8	Reconstructed Neutrino Energy Cut	95

5.3	Sensitivity and Discovery Potential	97
5.3.1	Upper Limit Sensitivity	98
5.3.2	Discovery Potential	99
5.3.3	Sensitivity and Discovery Potential vs. Exposure	100
5.4	Far Detector Cut Optimization	100
5.4.1	Rough Sensitivity Calculation	100
5.4.2	Background Rejection Cut Candidates	102
5.4.3	Optimization Technique	103
5.4.4	Unnecessary Cut Rejection	104
5.4.5	Systematic Considerations	107
5.4.6	Cut Value Optimization	112
5.4.7	Robustness of Cut Optimization	112
6	Analysis Inputs	117
6.1	MC Production	117
6.1.1	Beam Simulation	117
6.1.2	Neutrino Interactions	120
6.1.3	NEUT	121
6.1.4	SKdetsim	124
6.1.5	Additional Corrections	125
6.2	Beam Inputs	125
6.3	Near Detector	125
6.4	Far Detector	126
7	Systematic Errors	127
7.1	Neutrino Interactions	127
7.2	Near Detector	130

7.3	Beam	131
7.4	Far Detector	132
8	ν_e Appearance Analysis	134
8.1	T2K Data Taking	134
8.2	Normalization	136
8.2.1	Far Detector MC Normalization	137
8.2.2	Near/Far Ratio Normalization	138
8.3	Statistical Technique	139
8.3.1	Feldman-Cousins Method	139
8.3.2	Systematic Error Incorporation	143
8.3.3	Method Check and Comparison	144
8.4	Analysis Details	146
8.4.1	Oscillation Computation	146
8.4.2	Oscillation Grids	147
8.4.3	Calculation of N_{exp}	147
8.4.4	Systematic Error Details	150
8.4.5	Toy MC	151
8.4.6	Feldman Cousins Ordering	152
8.5	Results	155
8.6	Analysis Checks	160
9	Conclusions	167
A	Decay Electron Studies	169
A.1	Decay Electron Calibration Details	169
A.2	Muon Polarization	171
A.3	Position and Direction Dependence	175

B ND280 Analysis Details	180
B.1 Event Selections Overview	180
B.2 Track Matching/Vertex Finding	182
B.2.1 Momentum Reconstruction	182
B.3 Particle ID	182
B.4 Additional Considerations	183
C Systematic Error Details	185
C.1 ND280 Systematic Errors	185
C.1.1 ND280 Statistical Uncertainty	185
C.1.2 ND280 Physical Model Uncertainty	186
C.1.3 ND280 Detector Efficiency Uncertainties	187
C.2 Beam Systematic Errors	188
C.3 SK Systematic Errors	192
C.3.1 Reduction/OD Cut Uncertainty	193
C.3.2 Fiducial Volume Cut Uncertainty	193
C.3.3 Energy Scale Uncertainty	194
C.3.4 Ring Counting, Electron PID, and POLfit Mass	194
C.3.5 Atmospheric Neutrino Control Sample	195
C.3.6 Muon PID	199
C.3.7 Decay Electron Efficiency	200
C.3.8 Hybrid π^0	200
Bibliography	203
Biography	215

List of Tables

5.1	Table of “Default” Oscillation Parameters	90
5.2	ν_e Selection Cut Efficiency	96
5.3	Table of Cut Optimizations for Different Systematic Errors	115
5.4	Table of Cut Optimizations for Different Statistical Methods	115
7.1	CC Cross-section Uncertainties	128
7.2	NC Cross-section Uncertainties	128
7.3	Table of SK Detector Systematics	133
8.1	Expected Numbers of Events in the SK FV	138
8.2	Expected and Observed Number of Signal Candidates at SK	157
A.1	Decay Electron Polarization Dependence with Energy	176
C.1	Table of ND280 Detector Systematics	189
C.2	Beam Systematic Errors	192
C.3	Table of SK Systematic Final States	195
C.4	RC Control Sample Breakdown	197
C.5	Table of RC Systematic Atmospheric Samples	197
C.6	Table of Efficiencies and Uncertainties from Atmospheric Control Sam- ples	199
C.7	Hybrid π^0 Efficiencies	202

List of Figures

2.1	Goldhaber Experiment Setup	8
2.2	SK Zenith Distributions	11
2.3	Vector Boson Interaction Feynman Diagrams	14
2.4	Neutrino Masses	18
2.5	Reactor Neutrino Oscillation at Different Scales	21
2.6	Oscillation Probabilities for T2K	24
2.7	Coherent Forward Scattering (for MSW Effect)	25
2.8	T2K $\nu_\mu \rightarrow \nu_e$ Oscillation Probabilities with Various Matter Densities	28
2.9	Allowed Regions for Atmospheric Neutrino Oscillation Parameters from Recent Experiments	32
3.1	Journey of the Neutrino	34
3.2	Neutrino Energy vs. Parent Pion Momentum for Off-Axis Angles . . .	36
3.3	Bunch Timing Structure of SK FC Events	38
3.4	T2K Beamline Overview	39
3.5	Secondary Beamline	40
3.6	Target	41
3.7	Magnetic horn example	41
3.8	T2K Horn System	42
3.9	T2K Off-Axis Flux	42
3.10	ND280 Pit	44

3.11	INGRID Cross	45
3.12	INGRID Module	45
3.13	Off-Axis Detector	46
3.14	P0D Cross-Section	48
3.15	TPC	48
3.16	Example ND280 Event Display	50
4.1	Super-Kamiokande	53
4.2	Cherenkov Ring Projection	54
4.3	Cherenkov Wavefront Diagram	58
4.4	ID PMT	59
4.5	PMT Quantum Efficiency	59
4.6	QTC Operation	60
4.7	Examples of e -like and μ -like SK Events	66
4.8	POLfit Patch Diagram	70
4.9	Example TQ Map	72
4.10	Cherenkov Angle vs. Muon Momentum	77
4.11	Absolute Energy Scale Check with Multi-GeV Stopping Muons	79
4.12	Absolute Energy Scale Check with Sub-GeV Stopping Muons	80
4.13	Absolute Energy Scale Check with π^0 Mass	80
4.14	Absolute Energy Scale Check with Decay Electrons	81
4.15	Absolute Energy Scale Check Summary	82
4.16	Time Variation of Energy Scale	83
5.1	Expected SK Neutrino Spectrum	87
5.2	Asymmetric π^0 Decay Figure	89
5.3	Expected Number of Rings Distribution	91

5.4	Expected PID Distribution	92
5.5	Expected Visible Energy Distribution	93
5.6	Expected Decay Electrons Distribution	94
5.7	Expected POLfit π^0 Mass Distribution	95
5.8	Expected Reconstructed Neutrino Energy Distribution	97
5.9	Sensitivity and Discovery Potential vs. Integrated Beam for Current Analysis	101
5.10	Signal + Background Gaussian for Sensitivity	102
5.11	Cosine Cut Histogram	105
5.12	Cosine Cut Sensitivity Comparison	106
5.13	POLfit π^0 Δ Likelihood histogram	107
5.14	POLfit Cuts 2D Sensitivity Histogram	108
5.15	Energy Scale Uncertainty Effect on POLfit	109
5.16	Energy Scale Uncertainty Effect on Reconstructed Neutrino Energy .	110
5.17	Region of Additional Low Energy Systematic Error	111
5.18	Energy Window Low and High Cut Optimization	113
5.19	POLfit Mass and Reconstructed Energy Optimization	114
6.1	NA61 Diagram	119
6.2	Example Cross-Sections	124
7.1	CCQE Cross-section Shape Uncertainty	129
7.2	FSI Uncertainty at SK	130
7.3	Far/Near Ratio Beam Error	132
8.1	First T2K Event at SK	135
8.2	T2K POT vs. Time	136
8.3	Distribution of μ Momentum in Selected ND280 ν_μ Events	139
8.4	Example Confidence Belts	141

8.5	N_{exp} Distribution with Systematics	152
8.6	N_{obs} Distribution with Systematics	153
8.7	$\Delta\chi_c^2$ Map	154
8.8	Vertex Distribution of T2K FC Events	156
8.9	Selection Cut for Number of Rings	157
8.10	Selection Cuts for PID and Visible Energy	158
8.11	Selection Cuts for Decay Electrons and POLfit	159
8.12	Final Distribution of Reconstructed Neutrino Energy Cut	160
8.13	Final Acceptance Contours vs. δ_{CP}	161
8.14	Final Acceptance Contours vs. Δm_{32}^2	162
8.15	Integrated Region of Background-only PDF for p-value	163
8.16	Timing Distributions for Events at SK Relative to Beam	164
8.17	Distribution of Event Arrival Times vs. POT	165
8.18	Vertex Distribution of ν_e Candidates	166
A.1	Decay Electron Angle, No MC Polarization	174
A.2	Decay Electron Angle, 25% MC Polarization	175
A.3	Water Transparency Position Check with Decay Electrons	177
A.4	Up-Going and Down-Going Decay Electrons	178
A.5	Decay Electron Momentum vs. Time and Position	179
B.1	CC ν_μ Event in ND280 Tracker	181
B.2	PID Cut on ND280 Tracker Data	183

List of Abbreviations and Symbols

Symbols

N_{exp}	Expected number of events.
E_{ν}^{rec}	Reconstructed neutrino energy
\hat{N}_{exp}	Mean expected number of events without any systematic fluctuations

Abbreviations

All abbreviations are defined in the text, but this section is designed to be a helpful reference for some of the more common ones.

SK	Super-Kamiokande
ID	Inner Detector
OD	Outer Detector
POT	Protons on Target
CL	Confidence Level
FC	Fully Contained
F-C	Feldman-Cousins
DAQ	Data Acquisition system
POLfit	Pattern Of Light fitter (π^0 algorithm)
MC	Monte Carlo
PMT	Photo-Multiplier Tube

QBEE	QTC Based Electronics with Ethernet
QTC	Charge to Time Converter
p.e.	Photo-electrons
MPPC	Multi-Pixel Photon Counter
ATMPD	Atmospheric neutrino and Proton Decay
LR	Likelihood Ratio
TOF	Time Of Flight
UL	Upper Limit

Acknowledgements

I have only been able to reach this point thanks to the hard work, love, and dedication of a great many people. This is not a complete list, but there never really can be.

I'd like to thank my family, who somehow put up with me for all these years, and who still inspire me and give me guidance as I push onwards in life. Mom, Dad, there is no way to thank you enough, but I think you know how I feel on that.

Thank you to the people who have taught me through the years have helped shape me to make this possible. There are too many to count, but Al Leopold, Mr. Andrews, Mr. Scott, Mr. McHugh, Dr. Weiss, among many others, thank you. The Pennsylvania Governor's School for the Sciences is what convinced me to go in to physics, I owe so much to that program, and especially to the wonderful people who made it what it was.

Thanks to my friends who have kept me sane through this research, whether near or far. Amy, who got me to question what I have in common with neutrinos (and has been an amazing friend too). Also Rachel, Michelle, Megan, Carrie, Steph, and Cousin Amanda, good friends despite the distance. More locally, Abhijit, Sam, Ivan, Charles, Melanie, Ana, Henok, Kristine, the whole grads09 cookies group, and the Psi U gang. And, of course Mandy, who has been there for me time and again, it has been a joy to go through this with you. Also, you've helped inspire me to put such wonderful letters like β and γ to good use in physics! \llcorner

The T2K collaboration is a nearly 500 member project, including some who

have been tirelessly fighting to make this analysis possible for nearly ten years. My contribution to the analysis in this thesis is only possible because of the work of so many of my T2K colleagues. The same goes for those who dreamed, built, and continue to run Super-Kamiokande. I also thank the US Department of Energy, whose funding made my participation in T2K possible.

Working on T2K and SK has been a life experience to remember. Thanks to Piotr, Joshua, Patrick, JP, Giada, Thomas, Ed, Jen, Okura-san, and of course Roger for giving me reasons to always look forward to visiting Mozumi. The whole gang from the UK who I inevitably end up spending all my time with in Tokai: it's been great. Perhaps some day we can reunite and sing karaoke once more.

Thank you to the T2K Oscillation Analysis group, for making this all come together. Especially Mark, Patrick, Nakayama-san, our fearless leader Nakaya-san, and of course Okumura-san. Thanks also to the ATMPD e-scale group, I think we did a pretty good job with those cosmic ray muons.

Thank you to the Duke HEP Neutrino Group. Kate for providing excellent guidance, and supporting me on perl and Star Trek (and other things). Roger for helping me with stupid coding problems, living in Japan issues, and pretty much everything else, at every hour of the day. And for being an excellent friend in Japan, and beyond. Taritree for being my partner in crime in the group. Tuna-kun, Ashley, Ari, Tutanon, Nick, Mikhail, Joseph, and Jack for being excellent neutrino buddies. Zander for inspiring me with his home-made detectors. And Maxim, Naho, Alex, and Tarek for putting up with my physics questions and being excellent post-docs to look up to (and soon to try to live up to).

And, of course, thank you to my advisor, Chris Walter. Somehow, you got me into a position where I could get a chance to make an impact for the experiment. You guided me when I needed it, stayed back when I didn't (I suppose that is when you got your own work done), and got me to pull the right superfluous material out

of my presentations to make them effective. I expect this will be just the beginning of a string of successful advisees from you.

Introduction

Neutrinos are among the most mysterious particles in physics. They are ubiquitous; there are billions of neutrinos passing through every square centimeter of the earth every second. However, their ubiquity is matched by their elusiveness. They rarely interact with normal matter, as they have no known coupling by the strong or electromagnetic forces. The lack of interactions has meant that we know far less about neutrinos than we do about most other standard model particles. The late 1990s discovery that these “ghost particles” had non-zero mass opened up many new questions about their properties, which we are still trying to answer today. Perhaps most exciting is the possibility that neutrinos could hold clues to explaining the matter-antimatter asymmetry we observe in the universe today.

1.1 Dissertation Outline

The history of neutrino discoveries, including the discovery of neutrino mass through observation of neutrino oscillation is discussed in Chapter 2. This chapter also describes some of the electroweak theory and the oscillation framework we use to describe neutrinos in the standard model.

The experiment that is the subject of this dissertation is the Tokai to Kamioka (T2K) long-baseline neutrino oscillation experiment. T2K is a neutrino beam experiment searching for ν_μ to ν_e oscillation in a nearly pure ν_μ beam, with a baseline of 295 km. The neutrinos are produced at the J-PARC accelerator complex in Tokai, Japan, and are directed through a near detector complex (ND280) on their way to the Super-Kamiokande (SK) detector. Finding significant electron neutrino appearance in this beam would be an indication of non-zero θ_{13} . θ_{13} is the last of the three neutrino mixing angles to be measured.

The first major results of the T2K experiment's ν_e appearance search are the main subject of this dissertation. The experimental setup is described in Chapter 3. A full description of the far detector, SK, is in Chapter 4. An overview of the analysis, and of the development of the analysis, is in Chapter 5. The inputs into the analysis from the various parts of T2K are described in Chapter 6. The systematic error estimation for this analysis is described in Chapter 7. Finally, the analysis procedure and results are detailed in Chapter 8. Chapter 9 summarizes the experimental results, and what they mean for future measurements of the properties of these elusive particles.

1.2 Author Contributions

The work described in this dissertation is made possible by the efforts of the members of the T2K and SK collaborations. My (the author's) specific contributions to the experiment and to the analysis are listed here. Some parts of this dissertation describe (in detail) work done by other T2K collaborators. This is done so that a full description of the analysis can be found in one place. In these cases, credit is assigned to the groups which did the work.

At Super-Kamiokande, I was responsible for all decay electron studies with the energy-scale calibration group (Section 4.8 and Appendix A). I also performed studies of performance and possible improvements to POLfit (Section 4.6.7).

For T2K, I contributed to the SK Monte Carlo (MC) production, and performed studies on the signal rejected by the selection cuts and the backgrounds which were not rejected. I produced studies on the detector sensitivity (Section 5.3) and performed the selection cut optimization used for the official ν_e appearance analysis (Section 5.2 and Section 5.4). I worked on a systematic error estimation technique similar to the hybrid π^0 method (Section C.3.8), but it was not selected for the analysis, and is not discussed in this dissertation, although some of the work was absorbed into the selected technique. I was a central member of the T2K analysis group, co-developed the oscillation analysis used, and performed the analysis on the data when it became available (Chapter 8, among others). The software framework I developed for my analysis is (at time of this writing) being used by others in the collaboration for future oscillation analyses. I also oversaw the assembly and installation of new cables to carry signals from the outer detector (OD) paddle cards to the QBEE boards for the SK-IV electronics upgrade.

2

Neutrino Physics

2.1 History

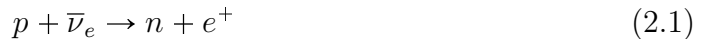
2.1.1 Assembling the Neutrino Family

The first hint to physicists of the existence of neutrinos came from beta-decay of nuclei [1] [2]. Unlike the sharp peaks of alpha or gamma emissions, the spectrum of beta emissions from a decaying atom (such as ^{210}Bi) is continuous and broad. If the only products of a nuclear beta decay were the beta particle (electron) and the daughter nucleus, a discrete spectrum of electron energies would be required to satisfy conservation of energy. This continuous spectrum was quite a puzzle at the time. Eventually, in December 1930, Wolfgang Pauli sent his now famous “Dear Radioactive Ladies and Gentlemen” letter, in which he proposed that a light, spin-1/2 neutral particle (which he called a neutron) emitted in addition to the beta, might both explain the continuous spectrum and also solve some other known issues in nuclear physics.

At the time, it was considered desperate to propose a new particle without it being somehow observed. However, Pauli was on the right track. Enrico Fermi

expanded on this idea, and in 1934 published a paper describing beta decays using these particles as the invisible third participant in the kinematics [3]. By now Fermi was calling this particle a neutrino, to distinguish it from the (much heavier) neutron discovered by Chadwick in 1932 [4].

After this, though, it would be nearly two decades before direct evidence of these neutrinos was seen. Frederick Reines and Clyde Cowan found preliminary evidence for antineutrinos from a reactor interacting in their detector in 1953 [5], and compelling evidence for this in 1956 [6] outside the Savannah River nuclear power plant. Their detector there involved tanks of water with CdCl_2 , a neutron absorber, dissolved in it. Scintillator was used above and below these tanks to detect any emitted photons. The antineutrino reaction detected was inverse beta decay (2.1).



The produced positron would annihilate with an electron in the water, producing a pair of back-to-back gammas (high energy photons), detected in coincidence by each scintillator detector. The neutron would be absorbed by the cadmium, which would then emit a gamma, providing a delayed coincidence with the positron gammas. This work eventually won Reines the Nobel Prize in 1995 (Cowan had already passed away).

After the observation of reactor antineutrinos through inverse beta decay, Ray Davis (working with Don Harmer) attempted [7] to observe the reaction



which had previously been suggested by Pontecorvo [8]. They found that this reaction did not occur. This meant that there was a difference between neutrinos (which would

trigger this reaction) and antineutrinos (from the reactor). This sort of experiment would later prove fruitful for Davis, but not for a very long time.

The story of the neutrino grew more complicated in 1962 with the discovery that there was more than one type of neutrino [9]. A group led by Lederman, Schwartz and Steinberger used the Alternating Gradient Synchrotron (AGS) at Brookhaven to send 15 GeV protons into a fixed beryllium target, producing pions (and other particles, such as kaons, to a lesser extent). The pions would decay to a muon and a neutrino. A thick iron shield stopped the muons and all other charged particles. The neutrinos continued to a spark chamber, where they could interact with the aluminum in the spark chamber. It was observed that the neutrino interactions produced muons, but not electrons. These neutrinos were different than the neutrinos observed from reactors (in experiments such as [6]), so the conclusion was that a new kind of neutrino, which coupled to the muon, would be added to the already-known version that coupled to the electron. Lederman, Schwartz and Steinberger won the Nobel Prize in 1988 for this work.

The final neutrino (that we know of), the tau neutrino, was not discovered until 2000, by the DONUT collaboration [10]. The ν_τ was produced from decays of particles produced in a fixed-target experiment with 800 GeV protons from the Fermilab Tevatron. The identification of ν_τ was achieved with nuclear emulsion targets, by finding a “kink” where the τ produced in a CC ν_τ interaction decays. This discovery was expected, as the ν_τ would be the natural partner to the τ , and there was already indirect evidence for its existence (for example, [11]).

2.1.2 Symmetry (or lack thereof)

In the mid 1950s, the idea that the weak interaction might not observe parity symmetry (as the strong, electromagnetic, and gravitational interactions did) emerged. Tsung Dao Lee and Chen Ning Yang considered this and proposed some ideas to test

it [12], and parity non-conservation was confirmed in 1957 by Chien Shiung Wu [13]. This further led to a proposal from Lee and Yang [14] that neutrinos might only be allowed to have one helicity (and antineutrinos the opposite helicity). It would not be long before this was tested.

The helicity of the neutrino was measured in 1958 by Maurice Goldhaber, Lee Grodzins and Andrew Sunyar [15], using a clever experiment based on the decay of europium-152. The nucleus (with net spin $J = 0$) decays by capturing an electron (inverse beta decay) and yielding excited samarium-152 and a neutrino. As a two-body decay, these would be produced back-to-back. The ^{152}Sm is excited, with total spin $J = 1$, and will decay through a photon emission to its ground state with $J = 0$. If this photon were emitted in the same direction that the ^{152}Sm was traveling, then the photon would have the same spin polarization as ^{152}Sm , by conservation of angular momentum. The mean life of the excited ^{152}Sm was short enough that the spin was unlikely to be influenced by the surrounding atoms. Thus, if the gammas emitted in the same direction as the ^{152}Sm (opposite direction of the neutrino) could be identified, and their spin ($J = 1$) polarization measured, the spin polarization of the neutrino (with $J = 1/2$) could be deduced from conservation of angular momentum.

The identification of forward-directed gammas was possible because the boost for these gammas was such that the photon energy would be in resonance with ^{152}Sm only if it were emitted in the same direction as the excited ^{152}Sm atom was moving. Thus, Sm_2O_3 scattering plates were used to select these photons and direct them to the detector. The helicity of the photons was determined by putting a polarized magnetized iron shield between the ^{152}Eu sample and the rest of the apparatus. The magnetized iron will preferentially absorb photons of opposite spin polarization to its electrons, so this turns the polarization measurement into a comparative rate measurement. Measuring the rate difference with both up and down magnet po-

larizations, this experiment found that the neutrino helicity appeared to be 100% left-handed. See Figure 2.1 for a diagram of the experimental apparatus. This result was consistent with the V-A theory of the weak interaction (Vector-Axial, implies maximal parity violation and left-handed neutrinos), and was a key part of confirming that the weak force behaved in this way.

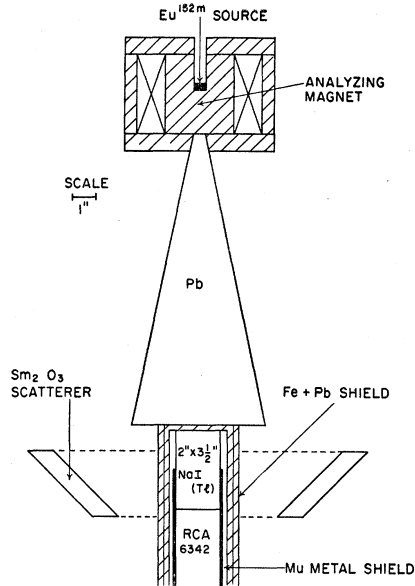


FIGURE 2.1: A sketch of the Goldhaber helicity measurement apparatus (from [15]). This experiment cleverly measures the neutrino helicity by counting photon rates; the neutrinos themselves never need to be detected. The magnet around the ^{152}Eu source preferentially absorbs gammas of a certain polarization, and the Sm_2O_3 scatterers deflect gammas of the appropriate energy to the scintillator. By reversing the magnet polarization and observing the change in rate, the photon helicity, and, by conservation of momentum (and angular momentum), the neutrino helicity, were measured.

2.1.3 Oscillation

One of the longest lasting mysteries in neutrinos began with Ray Davis's most famous experiment, his solar neutrino detector at the Homestake mine in South Dakota. This experiment [16] was based on the same reaction suggested by Pontecorvo (Sec-

tion 2.1.1), except this time neutrinos (not antineutrinos) from the Sun were the source. The reaction employed was



The key to this experiment's success was the ability to count individual atoms which had been converted to argon, made possible by the fact that ${}^{37}\text{Ar}$ is radioactive, with a half-life of 35 days. The detector target was a large tank of, effectively, cleaning fluid. The tank contained 615 tons of tetrachloroethylene, C_2Cl_4 , chosen for the large number of chlorine atoms. The argon atoms created could be removed from the liquid by bubbling helium gas through the tank, and then filtered from the helium. The remaining gas was put into a proportional counter and observed for days, searching for decays. To get an accurate solar neutrino measurement, the efficiencies at every step (extraction, filtering, and measurement in the proportional counter) needed to be known well.

The detector was built in the late 1960s, and ran for many years [17]. Davis used theoretical calculations from Bahcall ([18], for example) to compare the measured neutrino rate with the predicted one, but found that there was a deficit in measured neutrinos. The experiment continued running through 1994, an incredible stretch, always finding a deficit with respect to the prediction. This deficit came to be known as the “solar neutrino problem”. Over the years, other experiments, such as SAGE, GALLEX, and Kamiokande all observed this deficit [19].

Remarkably, the solution to this multi-decade problem was not finding an error in the solar models, nor an experimental mistake or systematic, but rather new physics. In 1968, shortly after Davis first reported the solar neutrino deficit, Pontecorvo suggested [20] that this could be explained if neutrinos could oscillate between the ν_e and ν_μ states, similar to the kaon oscillations observed at the time. This theory, however, could not be properly tested for many years, and alternate explanations

(such as experimental error) did not seem far-fetched, so the solar neutrino problem continued.

Interestingly, the solution to the problem would come from proton decay detectors. These detectors required large volumes of water in which to search for rare (as of yet unobserved) proton decay signals. For these experiments, neutrino interactions were a background, which could mimic a proton decay signal. Two of these proton decay detectors, IMB [21] and Kamiokande [22], became famous for neutrino detection in 1987 after detecting neutrinos from the 1987a supernova in the Large Magellanic Cloud. Aside from the supernova neutrinos, Kamiokande also observed neutrino deficits in both solar neutrinos [23] and neutrinos produced in the upper atmosphere of the earth [24]. These observations did not yet provide sufficient evidence to identify the cause of these neutrino anomalies. That evidence would finally come from the successor to Kamiokande, Super-Kamiokande.

In 1998, the Super-Kamiokande collaboration announced that they had found evidence [11] for neutrino oscillation. In this case, the evidence was in atmospheric neutrinos. Atmospheric neutrinos are produced when cosmic ray particles strike molecules in the upper-atmosphere to produce particles which decay to neutrinos. The most common unstable products of these collisions are pions. A typical decay chain would look like:

$$\pi^+ \rightarrow \mu^+ + \nu_\mu \tag{2.4}$$

$$\hookrightarrow \mu^+ \rightarrow e^+ + \bar{\nu}_\mu + \nu_e \tag{2.5}$$

The measured neutrino flux showed an unexpected dependence on zenith angle for muon neutrinos, but not for electron neutrinos. Figure 2.2 shows these zenith distributions.

This deficit in the observed number of muon neutrinos coming from below, but not from above, was consistent with $\nu_\mu \rightarrow \nu_\tau$ oscillation (some indications of this had

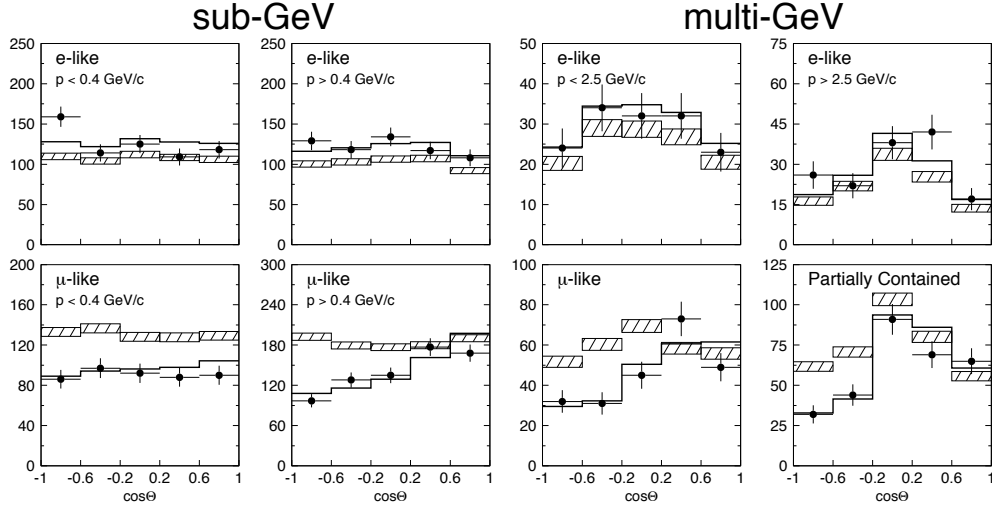


FIGURE 2.2: The zenith angle distributions from Super-Kamiokande [11] indicating $\nu_\mu \rightarrow \nu_\tau$ oscillation. The data are divided into samples based on reconstructed lepton energy. Upward-going particles have $\cos \Theta > 0$ and downward-going ones have $\cos \Theta < 0$. The hatched region is the Monte Carlo expectation for no oscillation (with statistical errors), and the solid line is the expectation with best-fit oscillation. Note the deficit in μ -like events (from muon neutrinos) coming from below. See Chapter 4 for information on atmospheric neutrino reconstruction.

previously been seen in the Kamiokande experiment [25]). This combination of rate, direction, and energy information provided a clear oscillation signal, but the source of neutrinos was from cosmic rays interacting in the Earth's atmosphere (these are higher energy than solar neutrinos), not the Sun, so the solar neutrino problem was not solved yet. More information on Super-Kamiokande can be found in Chapter 4.

Then, in 2002, the Sudbury Neutrino Observatory (SNO) collaboration announced that they had found direct evidence for oscillation in the solar neutrino flux [26][27]. SNO used a D_2O volume with an H_2O region around it, all surrounded by PMTs, to detect both charged current (CC) interactions, electron elastic scattering (ES) interactions, and neutral current (NC) interactions (CC and NC were only possible in D_2O , not H_2O). The CC interaction is only sensitive to ν_e , but ES and NC are sensitive to all neutrino flavors, though ES is more sensitive to ν_e than the others.

The interactions could be statistically distinguished by their direction (ES highly forward peaked, CC slightly backwards peaked, NC roughly uniform, relative to the Sun) and observed energy. By comparing the measured CC, ES, and NC rates, it was determined that there was not a deficit of neutrinos, but a deficit of electron neutrinos. The SNO results were consistent with $\nu_e \rightarrow \nu_{\mu/\tau}$ oscillation. At this point, the solar neutrino problem was solved, and neutrino oscillation was confirmed once again.

The most important consequence of neutrino oscillation is that neutrinos must have mass (this will be discussed in Section 2.2). Ray Davis finally won the Nobel Prize for his solar neutrino experiment (and arguably his patience) in 2002. The years that followed would see rapid progress in neutrino physics, as the parameters of neutrino oscillation were measured with increasing accuracy. Recently, oscillation has been measured in experiments using artificial beams of neutrinos, including the main topic of this dissertation, T2K. Discussion of more recent oscillation experiments is in Section 2.5, after the description of the neutrino oscillation formalism.

2.2 The Standard Model Neutrino

The standard model of particle physics is the theory which encompasses the electroweak theory (itself a unification of the weak interaction and electromagnetism) with quantum chromodynamics, the theory of the strong interaction. It includes all of the particles observed by experiments (so far) and encompasses all known forces, with the exception of gravity. This theory of everything but gravity has done extremely well, and its foundations have withstood all experimental challenges since its inception in the 1970s [28].

The particles of the standard model include quarks, which make up nuclei and other hadronic matter, leptons, which include electrons (and muons and taus) and neutrinos, and the force carrying vector bosons (and the Higgs, which is a scalar

boson, best described in another dissertation). In the standard model, and in all observations to date, neutrinos only interact via the weak nuclear force, thus this is the only part of the standard model that will be discussed here.

The weak nuclear force (also known simply as “weak force”) acts on quarks and leptons, and is based on the symmetry group $SU(2)$. This force has the property that it only interacts with left-handed particles (and right-handed anti-particles), thus making the force maximally violate parity symmetry. In this context, left-handed refers to the chirality of the particle. Chirality is an intrinsic property of a wavefunction, and usually cannot be directly measured, as helicity (defined as the spin of the particle measured along the direction of motion) can. In the limit of a zero mass particle, chirality and helicity become equal. Because the weak force acts in this maximally chiral way, because neutrinos only interact with the weak force, and because neutrinos have very low mass (relative to their energy), all neutrinos detected have negative helicity, corresponding to left-handed chirality (and all antineutrinos have positive helicity).

The carriers of the weak force are three massive vector bosons: the W^+ , W^- , and Z^0 . The charged particles, the W^\pm , are involved in charged current (CC) interactions, and the neutral force carrier, the Z^0 , is involved in neutral-current (NC) interactions. These will be described in more detail later.

All the leptons and quarks which participate in the weak interaction (that is, left-handed ones) can be grouped into irreducible doublet representations of $SU(2)$ [29]. The leptons which don’t interact via the weak force (right-handed ones) are singlets in this group. Thus, the leptons are grouped as follows:

$$\begin{pmatrix} \nu_e \\ e \end{pmatrix}_L, \quad \begin{pmatrix} \nu_\mu \\ \mu \end{pmatrix}_L, \quad \begin{pmatrix} \nu_\tau \\ \tau \end{pmatrix}_L, \quad (e)_R, \quad (\mu)_R, \quad (\tau)_R. \quad (2.6)$$

Of course, the anti-particles also exist, with the chiralities flipped. Note that there are no right-handed neutrinos. The quarks are similarly grouped into electroweak

doublets, though the weak doublets are slightly different from the ordinary strong and electromagnetic groupings, due to the rotation by the CKM matrix [29] (the primed quarks are the rotated states; the CKM matrix [30] [31] is a 3×3 unitary mixing matrix; there is an analogue for neutrinos, which will be discussed later).

$$\begin{pmatrix} u \\ d' \end{pmatrix}_L, \quad \begin{pmatrix} c \\ s' \end{pmatrix}_L, \quad \begin{pmatrix} t \\ b' \end{pmatrix}_L, \quad (u)_R, \quad \text{etc.} \quad (2.7)$$

The weak interaction connects members of these doublets. At first it seems strange that, for example, the left-handed muon and muon neutrino are grouped together, while the right-handed muon is not connected. However, the grouping makes sense in analogy with electromagnetism [29]. Consider the electron spinors, which are doublets where one component is spin-up and the other is spin-down. At an interaction vertex, we have a spin-up electron converted to a spin-down one, and a photon is emitted (or absorbed). The conversion is necessary as the photon is a spin-1 particle. In the analogy, a μ gets converted to a ν_μ and emits a W^- (Figure 2.3).

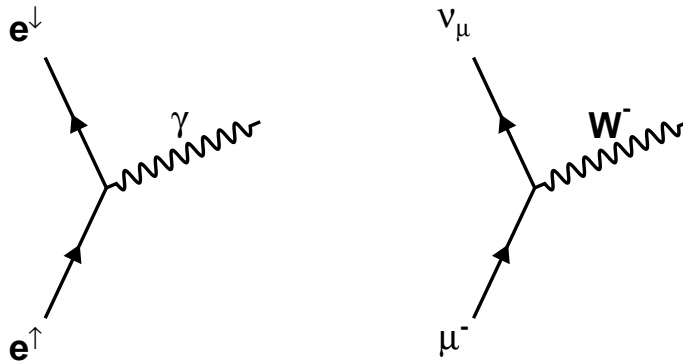


FIGURE 2.3: Feynman diagrams illustrating vector boson interactions. On the left is an electron emitting a photon. The spin-1 photon necessitates a spin flip, so the spin-up and spin-down electrons are a doublet in electromagnetism. Similarly, on the right, a muon decays, emitting a ν_μ and a W^- . The μ_L and ν_μ form a doublet in the weak nuclear interaction.

Thus, CC interactions convert between neutrinos and charged leptons, for example,

$$\nu_l + u \rightarrow l^+ + d \tag{2.8}$$

$$\bar{\nu}_l + d \rightarrow l^- + u \tag{2.9}$$

where l is a lepton (e, μ, τ) and the up and down quarks could be replaced with any quark pair (ignoring CKM mixing for now).

On the other hand, NC interactions, mediated by the Z^0 boson, do not produce leptons, or change quark flavors:

$$\nu_l + q \rightarrow \nu_l + q \tag{2.10}$$

$$\nu_l + l' \rightarrow \nu_l + l' \tag{2.11}$$

Here, q is any quark, and ν_l is any neutrino, and l' is any lepton. The NC interaction does not depend on neutrino flavor.

In the traditional standard model, neutrinos are massless, chargeless, spin-1/2 particles. Observationally, they do have mass, so modifications need to be made to the standard model to incorporate neutrino mass. Some physicists ([29], for example) consider massive neutrinos to be beyond the standard model, while others ([28]) consider them simply to be an extension of it. In the massless neutrino case, chirality is equivalent to helicity, and is (by conservation of angular momentum and momentum) preserved, leaving no need for right-handed neutrinos and the like. With mass, this is not so simple, and it should be possible to boost into a frame where a left-handed neutrino becomes right-handed.

Experimentally, the absolute neutrino masses have never been reliably measured to be anything non-zero. The current best experimental limit is $m_{\bar{\nu}_e} < 2.3$ eV (at 95% CL) [32] based on measurement of tritium decay. The masses of other neutrino flavors are not as tightly restricted, but, assuming the usual three-flavor oscillation

model is true, along with CPT conservation (which implies $m_{\bar{\nu}_e} = m_{\nu_e}$), all the (standard model) neutrino masses are very close to each other. Also, cosmological studies have set even lower limits, for all neutrino flavors. For example, WMAP observations limit neutrino masses to $m_{\nu} < 0.23$ eV (at 95% CL) [33], though this measurement is dependent on cosmological models.

The weak force is, not surprisingly, weak, at least at low energies. It has a very short range (due to massive vector bosons carrying the force) and is usually overshadowed by the strong and electromagnetic forces. The exceptions occur when interactions can only occur through the weak force. Examples of this include charged pion decay, or any neutrino interactions. The weak interaction strength is the reason that neutrinos have such famously low cross-sections. The relative weakness of the force, and its very short range, are due to the high mass of the force carriers (W and Z^0 bosons). In fact, the weak coupling constant before effects of the vector boson masses is larger than the electromagnetic coupling constant. [28].

2.3 Oscillation

Neutrino oscillation is explained by having mass eigenstates made up of linear combinations of weak interaction eigenstates (also known as flavor eigenstates), through a mixing matrix analogous to the CKM matrix used for quarks. This matrix is known as the Pontecorvo–Maki–Nakagawa–Sakata (PMNS) matrix [34]. A diagrammatic representation of this mixing is seen in Figure 2.4. Flavor eigenstates are the states relevant for the weak interaction, while mass eigenstates are important for free particle propagation. The mixing can be parameterized by six quantities (one could substitute others, but one needs at minimum six): Δm_{21}^2 , Δm_{32}^2 , θ_{12} , θ_{23} , θ_{13} , and δ_{CP} . An additional consideration, the ordering of the mass states, is fairly difficult to measure: to first order, without significant matter effects, only the mass differences and mixing angles affect oscillation. Here, we define $\Delta m_{jk}^2 = m_j^2 - m_k^2$, the difference

in the squares of neutrino mass eigenstate masses [35]. For neutrino oscillation, the mass splittings determine the wavelength of oscillation, and the mixing angles determine the amplitude. CP violation (which leads to different oscillation for neutrinos and antineutrinos) is determined by δ_{CP} .

This parameterization is a complete description of neutrino mixing if neutrinos are Dirac particles, that is, if they are distinct particles from their antiparticle partners (like electrons and positrons). If they are Majorana particles (like π^0 s or photons, their own antiparticle partner), additional phases are required, though they do not affect oscillation. The question of whether neutrinos are Dirac or Majorana in nature is unresolved at this time.

The mass splitting between two of the states is much smaller than the splitting to the remaining state. This means that $|\Delta m_{32}^2| \approx |\Delta m_{31}^2|$, and that we can measure the two mass splittings with minimal interference between them. The larger mass splitting ($|\Delta m_{32}^2| \approx |\Delta m_{31}^2|$) is known as the atmospheric mass splitting, as it was measured from atmospheric neutrino experiments, and dominates the oscillation of atmospheric $\nu_\mu \rightarrow \nu_\tau$. The smaller mass splitting, Δm_{21}^2 , is known as the solar mass splitting, and it is measured by solar and reactor neutrino oscillation experiments. We only need to measure two mass splittings, because the third is constrained by $\Delta m_{21}^2 + \Delta m_{32}^2 + \Delta m_{13}^2 = 0$.

2.3.1 Two Flavor Model

A simple case to consider is oscillation between only two neutrino flavors. Note that the following example makes some invalid assumptions (specifically, that different mass eigenstates will have the same energy) [37], but it is easy to understand, and produces the correct equations describing oscillation. Consider a matrix to represent the mass eigenstates (numerical or roman subscripts) in terms of flavor eigenstates

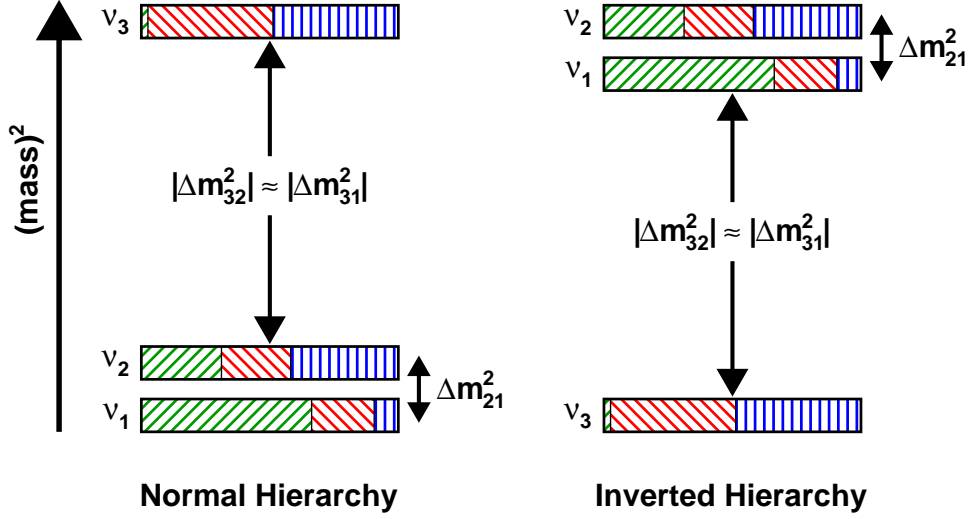


FIGURE 2.4: A visual depiction of the neutrino mass eigenstates. The vertical position of the mass eigenstate indicates the relative m^2 , and the colored region indicates the flavor eigenstate composition. Green upward-right sloping hatching indicates ν_e , red downward-right sloping hatching indicates ν_μ , and blue vertical hatching indicates ν_τ . The tiny sliver of green ν_e in ν_3 is the fraction given by $\sin^2 \theta_{13}$. There are two possible mass hierarchies: left is the normal hierarchy; right is inverted. The mass splittings are not to scale; the solar mass splitting $\Delta m_{\odot}^2 = \Delta m_{21}^2 = 7.5 \times 10^{-5}$ eV is approximately 30 times smaller than $\Delta m_{\text{atm}}^2 \approx |\Delta m_{31}^2| \approx |\Delta m_{32}^2| = 2.4 \times 10^{-3}$ eV. The mixing angles represented here are listed in Table 5.1, with $\sin^2 2\theta_{13} = 0.1$. Figure inspired by [36].

(Greek subscripts):

$$\begin{pmatrix} \nu_\alpha \\ \nu_\beta \end{pmatrix} = \begin{pmatrix} \cos \theta & \sin \theta \\ -\sin \theta & \cos \theta \end{pmatrix} \begin{pmatrix} \nu_1 \\ \nu_2 \end{pmatrix}. \quad (2.12)$$

The mass states are eigenstates for plane wave solutions to Schrödinger's equation, and different mass eigenstates travel at different speeds. We can write down the evolution of such a mass eigenstate plane wave solution,

$$|\psi_j(\vec{x}, t)\rangle = e^{-i(E_j t - \vec{p}_j \cdot \vec{x})/\hbar} |\psi_j(0)\rangle. \quad (2.13)$$

And so we can use this to calculate, to first order, the oscillation probability of a neutrino in one flavor state to another flavor state:

$$P(\nu_\alpha \rightarrow \nu_\beta) = |\langle \psi_\beta(0) | \psi_\alpha(t) \rangle|^2. \quad (2.14)$$

The probability is just the square of the matrix element between a pure flavor eigenstate ($\psi_\beta(0)$) with the propagated state of the initial flavor state. We assume the neutrino is traveling near the speed of light, and that $p/c \gg m$.

$$\begin{aligned} E_j &= \sqrt{m_j^2 + p_j^2} \\ &= p_j \sqrt{1 + m_j^2/p_j^2} \approx p_j + \frac{m_j^2}{2p_j}. \end{aligned} \quad (2.15)$$

Considering just the direction of motion,

$$|\psi_j(\vec{x}, t)\rangle = e^{-i((p_j + \frac{m_j^2}{2p_j})t - p_j x)/\hbar} |\psi_j(0)\rangle. \quad (2.16)$$

And, finally, with $t = L/v$, $v \approx c$, $p \approx E$ (all acceptable to this order),

$$|\psi_j(\vec{x}, t)\rangle = e^{-i\frac{m_j^2}{2\hbar} \frac{L}{E}} |\psi_j(0)\rangle. \quad (2.17)$$

We plug this into Equation 2.14 and let $\hbar = 1$,

$$\begin{aligned} \langle \psi_\beta(0) | \psi_\alpha(L(t)) \rangle &= \left(\cos \theta e^{-im_1^2 \frac{L}{2E}} \langle \psi_1(0) | + \sin \theta e^{-im_2^2 \frac{L}{2E}} \langle \psi_2(0) | \right) \\ &\quad \times \left(-\sin \theta | \psi_1(0) \rangle + \cos \theta | \psi_2(0) \rangle \right). \end{aligned} \quad (2.18)$$

Now, because the neutrino mass eigenstates are normalized orthogonal states,

$\langle \psi_j | \psi_k \rangle = \delta_{jk}$, and we have:

$$\begin{aligned} \langle \psi_\beta(0) | \psi_\alpha(L(t)) \rangle &= \cos \theta \sin \theta \left(e^{-im_2^2 \frac{L}{2E}} - e^{-im_1^2 \frac{L}{2E}} \right) \\ &= e^{i\phi} \sin 2\theta \sin \left(\frac{\Delta m^2}{4} \frac{L}{E} \right), \end{aligned} \quad (2.19)$$

where the $e^{i\phi}$ term is an unobservable phase factor. This yields (with consideration of units and magnitude squaring) a final result of:

$$\Rightarrow P(\nu_\alpha \rightarrow \nu_\beta) = \sin^2 2\theta \sin^2 \left(\frac{1.27 \Delta m^2 (\text{eV}^2) L (\text{km})}{E (\text{GeV})} \right). \quad (2.20)$$

Equation 2.20 describes oscillation where only two flavors are considered. The oscillation frequency is determined by the mass splitting, and the amplitude is determined by the mixing angle. It turns out that the mass differences measured (between all three neutrinos) are such that oscillation can be divided into two main regimes where the two flavor case is a good approximation. Over small L/E , oscillation is dominated by the atmospheric mass splitting. Over large L/E , the atmospheric oscillations tend to average out, and the solar mass splitting dominates observable oscillation. This means that the two-flavor oscillation picture is quite useful, even though there are, as we currently understand, three flavors. Figure 2.5 shows an example of how the mass scales separate, using reactor neutrino oscillation as an example.

As mentioned before, the above derivation makes a key invalid assumption: that the neutrino energy will be the same for any mass eigenstate. If one considers a neutrino being produced by a simple process, such as pion decay ($\pi^+ \rightarrow \mu^+ + \nu_\mu$) at rest, it is clear that kinematics require both the neutrino energy and momentum to be a function of the neutrino mass. This is a tricky issue, and there are many papers which attempt to resolve this, for example, [37]. If one carefully computes a two-body decay and considers the entanglement between the product particles (to satisfy conservation of energy and momentum), the oscillations will still emerge, under certain conditions:

- The neutrino must travel a distance short enough that the wavepackets for individual mass states do not separate.

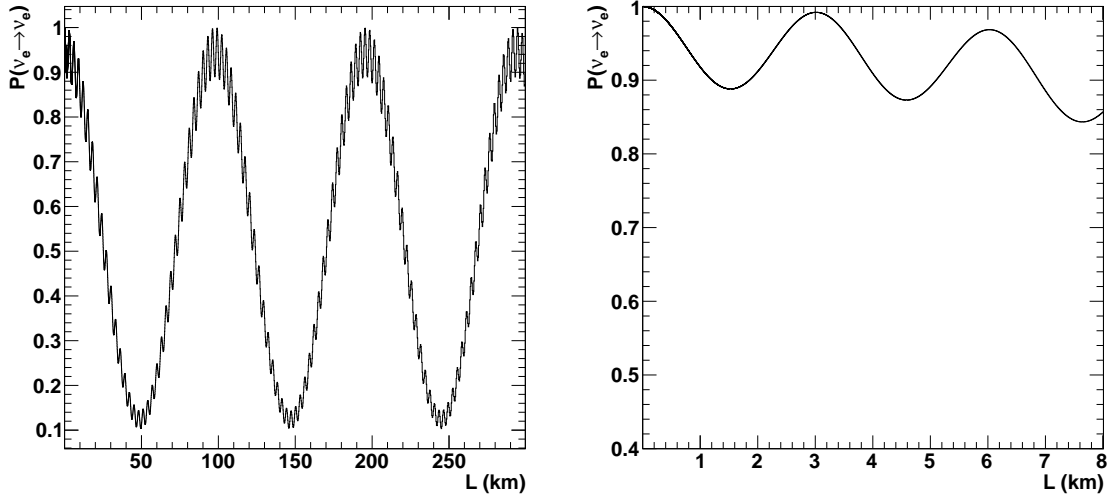


FIGURE 2.5: The $\nu_e \rightarrow \nu_e$ (or $\bar{\nu}_e \rightarrow \bar{\nu}_e$) oscillation probability, as a function of distance, assuming 3 MeV neutrinos. The left plot shows the oscillation over long distances, and the right plot shows oscillations over short distances. Note the y -axis is zoomed in for the right plot. The high-frequency wiggles on the left plot are the primary feature of the plot on the right. Thus, for an oscillation experiment over small L/E , two-flavor oscillation using the Δm_{32}^2 equation is appropriate, while large L/E would work well with the Δm_{21}^2 equation, as the higher frequency oscillations would be washed out by measurement uncertainties. The following oscillation parameters are assumed: $\sin^2 2\theta_{12} = 0.8704$, $\sin^2 2\theta_{23} = 1.0$, $\Delta m_{21}^2 = 7.6 \times 10^{-5} \text{eV}^2$, $\Delta m_{32}^2 = 2.4 \times 10^{-3} \text{eV}^2$, $\sin^2 2\theta_{13} = 0.11$, $\delta_{\text{CP}} = 0$, normal hierarchy, no matter effects.

- The momentum spread of the parent particle must be large enough to cover the momentum difference in the non-neutrino daughter due to different neutrino masses.
- The neutrino is observed.

All these conditions are easily met for any neutrino detected in a neutrino oscillation experiment. The phase difference between wavefunctions for each mass eigenstate can still be computed, even without assuming a constant energy between eigenstates, and the familiar equation is recovered.

2.3.2 Three Flavor Vacuum Oscillations

We can extend the two-flavor oscillation case to three flavors fairly simply. The mixing matrix (Equation 2.12) is extended to three flavors by combining three 2×2 rotation matrices, and adding in a complex phase. The addition of a phase can be understood as follows [38]: a unitary matrix, in general, can be described by N^2 real parameters. Of these, $2N - 1$ can be absorbed into the neutrino eigenstate wavefunctions as arbitrary phases (with an overall phase unobservable). This leaves $(N - 1)^2$ parameters left. The 2×2 matrix has only a single free parameter. The 3×3 matrix has four free parameters, one of which is a complex phase.

An additional two complex phases are added, however, if neutrinos are Majorana particles. In that case, where neutrinos and antineutrinos are the same particle, it is no longer possible to absorb the excess phases into the mass eigenstates [39][40]. In this case, we add on an extra Majorana phase matrix. However, these remaining Majorana phases are on the matrix diagonal. It can be shown that such on-diagonal phases will not affect neutrino oscillation, so it is impossible to determine whether neutrinos are Dirac or Majorana by observing oscillation alone.

$$\begin{aligned} \begin{pmatrix} \nu_e \\ \nu_\mu \\ \nu_\tau \end{pmatrix} &= \begin{pmatrix} 1 & 0 & 0 \\ 0 & c_{23} & s_{23} \\ 0 & -s_{23} & c_{23} \end{pmatrix} \begin{pmatrix} c_{13} & 0 & s_{13}e^{-i\delta} \\ 0 & 1 & 0 \\ -s_{13}e^{i\delta} & 0 & c_{13} \end{pmatrix} \\ &\times \begin{pmatrix} c_{12} & s_{12} & 0 \\ -s_{12} & c_{12} & 0 \\ 0 & 0 & 1 \end{pmatrix} \begin{pmatrix} e^{i\alpha_1/2} & 0 & 0 \\ 0 & e^{i\alpha_2/2} & 0 \\ 0 & 0 & 1 \end{pmatrix} \begin{pmatrix} \nu_1 \\ \nu_2 \\ \nu_3 \end{pmatrix} \end{aligned} \quad (2.21)$$

In Equation 2.21 (and 2.22), $c_{jk} = \cos \theta_{jk}$, and $s_{jk} = \sin \theta_{jk}$. When the four mixing matrices (three rotation plus the Majorana phase matrix) are multiplied together, we have the PMNS matrix, which we will designate U (Equation 2.22).

$$\begin{aligned}
U = & \begin{pmatrix} c_{12}c_{13} & s_{12}c_{13} & s_{13}e^{-i\delta} \\ -s_{12}c_{23} - c_{12}s_{23}s_{13}e^{i\delta} & c_{12}c_{23} - s_{12}s_{23}s_{13}e^{i\delta} & s_{23}c_{13} \\ s_{12}s_{23} - c_{12}c_{23}s_{13}e^{i\delta} & -c_{12}s_{23} - s_{12}c_{23}s_{13}e^{i\delta} & c_{23}c_{13} \end{pmatrix} \\
& \times \begin{pmatrix} e^{i\alpha_1/2} & 0 & 0 \\ 0 & e^{i\alpha_2/2} & 0 \\ 0 & 0 & 1 \end{pmatrix} \quad (2.22)
\end{aligned}$$

Now, with the simple extension of Equation 2.17 to three flavors and Equation 2.22, we can write the evolution of a neutrino flavor eigenstate as

$$|\psi_\alpha(\vec{x}, t)\rangle \approx \sum_j U_{\alpha j}^* e^{-i\frac{m_j^2}{2\hbar} \frac{L}{E}} |\psi_j(0)\rangle. \quad (2.23)$$

Then, we can use this to produce the equivalent of Equation 2.19:

$$\langle \psi_\beta(0) | \psi_\alpha(L(t)) \rangle = \sum_j U_{\alpha j}^* e^{-im_j^2 L/2E} U_{\beta j}. \quad (2.24)$$

Through the same method as with the two flavor case, we can produce the full oscillation probability. Note that this makes the same faulty assumption as we did in Section 2.3.1, but the result we get is still correct, for the same reasons. After some algebra, we find [35]

$$\begin{aligned}
P(\nu_\alpha \rightarrow \nu_\beta) = & \delta_{\alpha\beta} \\
& -4 \sum_{j>k} \Re(U_{\alpha j}^* U_{\beta j} U_{\alpha k} U_{\beta k}^* \sin^2(1.27\Delta m_{jk}^2 L/E)) \\
& +2 \sum_{j>k} \Im(U_{\alpha j}^* U_{\beta j} U_{\alpha k} U_{\beta k}^* \sin(2.54\Delta m_{jk}^2 L/E)), \quad (2.25)
\end{aligned}$$

where \Re and \Im are the real and imaginary parts of the enclosed quantities, and $\Delta m_{jk}^2 = m_j^2 - m_k^2$.

For T2K, the goal is to observe neutrino mixing governed by θ_{13} . Figure 2.6 shows the T2K ν_μ oscillation probabilities as a function of neutrino energy. The T2K beam

energy is peaked near 600 MeV, on the first $\nu_\mu \rightarrow \nu_e$ oscillation maximum. In this range, the Δm_{32}^2 (atmospheric) oscillations dominate. Though the primary effect is $\nu_\mu \rightarrow \nu_\tau$ oscillation (the same ν_μ disappearance that led to oscillation discovery at SK in 1998), $\nu_\mu \rightarrow \nu_e$ oscillation may be observed if θ_{13} is non-zero, over the same range of energies. At very low energies (large L/E), the Δm_{21}^2 (solar) oscillations are visible.

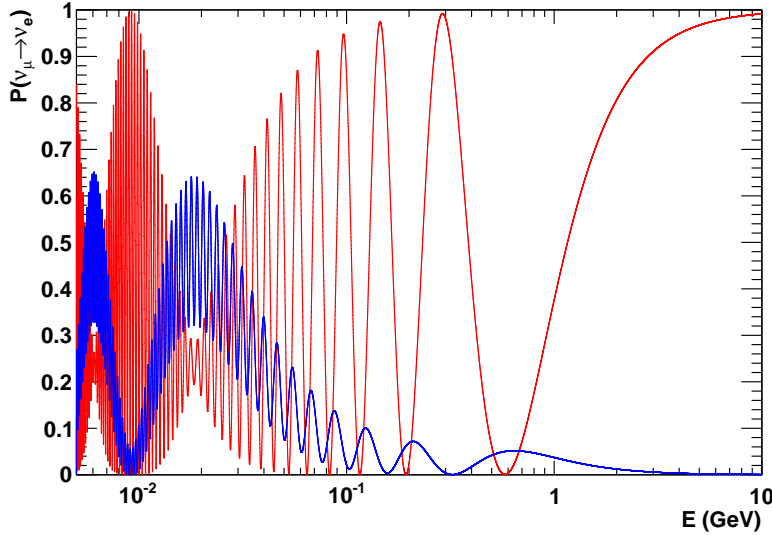


FIGURE 2.6: The $\nu_\mu \rightarrow \nu_e$ (blue) and $\nu_\mu \rightarrow \nu_\mu$ (red) oscillation probabilities, as a function of energy, assuming a 295 km baseline. Note the logarithmic x -axis. At the energies T2K is designed for (~ 600 MeV), the oscillations are well described by Δm_{32}^2 (atmospheric) oscillations alone. At very small energies, the solar oscillation can be observed, but this is outside of the useful range for T2K. The following oscillation parameters are assumed: $\sin^2 2\theta_{12} = 0.8704$, $\sin^2 2\theta_{23} = 1.0$, $\Delta m_{21}^2 = 7.6 \times 10^{-5} \text{eV}^2$, $\Delta m_{32}^2 = 2.4 \times 10^{-3} \text{eV}^2$, $\sin^2 2\theta_{13} = 0.11$, $\delta_{\text{CP}} = 0$, normal hierarchy, 3.2 g/cm^3 constant matter density.

Thus, for the main energies of interest to T2K, we can get a good idea of how oscillations will work by neglecting the solar oscillation term, and describing oscillation as

$$P(\nu_\mu \rightarrow \nu_e) \approx \sin^2 \theta_{23} \sin^2 2\theta_{13} \sin^2 \left(\frac{\Delta m_{32}^2 L}{4E} \right). \quad (2.26)$$

2.3.3 Matter Effects

All these calculations so far have been assuming the neutrinos propagate through a vacuum. This is not always the case. In 1978, Lincoln Wolfenstein [41] pointed out that electron neutrinos passing through matter would be affected by coherent elastic forward scattering (see Figure 2.7). This modifies the potential experienced by the neutrinos. Neutral current scattering off of matter is flavor independent, and so will not affect oscillation. However, the charged current (W^\pm) will only act between particles of like lepton flavor. Because normal matter is filled with electrons, but not muons or taus, this changes how the electron neutrinos propagate, but not the other flavors, thus affecting oscillation [42][40]. The matter effects were further studied by Smirnov and Mikheyev [43], and are frequently known as the MSW effect.

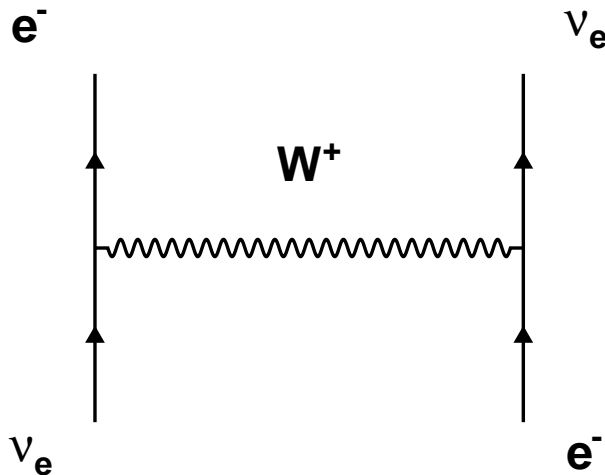


FIGURE 2.7: Neutrinos passing through matter undergo forward elastic scattering. In the case of CC forward scattering, only electron neutrinos can undergo this interaction (as muons and taus are not part of normal matter). This reaction adds a potential term to the neutrino propagation Hamiltonian.

We can treat this interaction as an extra potential experienced by electron neutrinos, given by

$$V = \pm\sqrt{2}G_F N_e, \quad (2.27)$$

where G_F is the Fermi coupling constant and N_e is the electron density per unit volume in the matter [40]. The sign will be positive for ν_e , and negative for $\bar{\nu}_e$. In the two flavor case, it is fairly easy to compute the behavior. We use the Schrödinger equation, considering the evolution of a state where the neutrino can be in the e flavor eigenstate, or the μ flavor eigenstate (ignoring τ for now). We will begin in the mass eigenstate basis, then transform to flavor:

$$i\frac{d}{dt}\begin{pmatrix} \nu_1 \\ \nu_2 \end{pmatrix} = \begin{pmatrix} E_1 & 0 \\ 0 & E_2 \end{pmatrix} \begin{pmatrix} \nu_1 \\ \nu_2 \end{pmatrix}. \quad (2.28)$$

The energy states can be simplified using Equation 2.15 and $E \approx p$, separating into a momentum term proportional to the identity matrix (\mathbb{I}), and a mass term. We can further pull out a diagonal mass term to make the formula in terms of mass differences:

$$i\frac{d}{dt}\begin{pmatrix} \nu_1 \\ \nu_2 \end{pmatrix} = \left(p\mathbb{I} + \frac{1}{2E}m_1^2\mathbb{I} + \frac{1}{2E}\begin{pmatrix} 0 & 0 \\ 0 & \Delta m^2 \end{pmatrix} \right) \begin{pmatrix} \nu_1 \\ \nu_2 \end{pmatrix}. \quad (2.29)$$

The terms proportional to the identity matrix have no effect on oscillation, so we can remove them. Now we convert into the flavor basis using the matrix from Equation 2.12:

$$\begin{aligned} i\frac{d}{dt}\begin{pmatrix} \nu_e \\ \nu_\mu \end{pmatrix} &= \frac{1}{2E}U\begin{pmatrix} 0 & 0 \\ 0 & \Delta m^2 \end{pmatrix}U^\dagger\begin{pmatrix} \nu_e \\ \nu_\mu \end{pmatrix} \\ &= \frac{\Delta m^2}{2E}\begin{pmatrix} \sin^2\theta & \cos\theta\sin\theta \\ \cos\theta\sin\theta & \cos^2\theta \end{pmatrix}\begin{pmatrix} \nu_e \\ \nu_\mu \end{pmatrix}. \end{aligned} \quad (2.30)$$

Now, we can add on a component proportional to the identity matrix (which will not affect oscillation) and perform some trigonometric substitutions to reach a nice simple matrix, which is the Hamiltonian for vacuum oscillations, in the flavor basis:

$$i \frac{d}{dt} \begin{pmatrix} \nu_e \\ \nu_\mu \end{pmatrix} = \frac{\Delta m^2}{4E} \begin{pmatrix} -\cos 2\theta & \sin 2\theta \\ \sin 2\theta & \cos 2\theta \end{pmatrix} \begin{pmatrix} \nu_e \\ \nu_\mu \end{pmatrix}. \quad (2.31)$$

This coupled equation, when solved, will yield the ordinary two-flavor oscillation formulae. We modify it by adding in the ν_e interaction potential, from Equation 2.27:

$$i \frac{d}{dt} \begin{pmatrix} \nu_e \\ \nu_\mu \end{pmatrix} = \frac{\Delta m^2}{4E} \begin{pmatrix} -\cos 2\theta + \frac{4\sqrt{2}G_F N_e E}{\Delta m^2} & \sin 2\theta \\ \sin 2\theta & \cos 2\theta \end{pmatrix} \begin{pmatrix} \nu_e \\ \nu_\mu \end{pmatrix}. \quad (2.32)$$

Now, if the density is a function of position, this equation becomes more difficult to solve. For constant density, we find that we can make a substitution to bring the equation back to the original dynamics. First, we subtract off $G_F N_e \mathbb{I} / \sqrt{2}$, not affecting oscillation. Then, we substitute

$$\Delta m_M^2 = \Delta m^2 \sqrt{\sin^2 2\theta + (\cos 2\theta - x_\nu)^2} \quad (2.33)$$

and

$$\sin^2 2\theta_M = \frac{\sin^2 2\theta}{\sin^2 2\theta + (\cos 2\theta - x_\nu)^2} \quad (2.34)$$

with

$$x_\nu = \frac{2\sqrt{2}G_F N_e E}{\Delta m^2} \quad (2.35)$$

and the oscillation dynamics of Equation 2.31 are restored, but with a modified mass splitting and a modified mixing angle [40].

Obviously, as matter density becomes small, vacuum oscillations are restored. Also, certain densities and energies (such that $x_\nu = \cos 2\theta$) will result in a resonance condition, maximizing oscillation. These sorts of features also show up in the three-flavor oscillation with matter effects, though the math is considerably more complicated. A tractable solution was found by Barger, *et. al.* [44], performing the calculation in the mass eigenstate basis. This solution was implemented in the T2K oscillation code as [45]; see [46] for more details on the implementation.

For T2K, the matter effects are not very large, as the earth is not very dense near the crust, and the neutrinos do not travel very far. Thus, Equation 2.26 is still useful for understanding T2K performance. However, the matter effects are included in the full analysis, to be as accurate as possible. The effect of different matter densities on oscillation for T2K is shown in Figure 2.8.

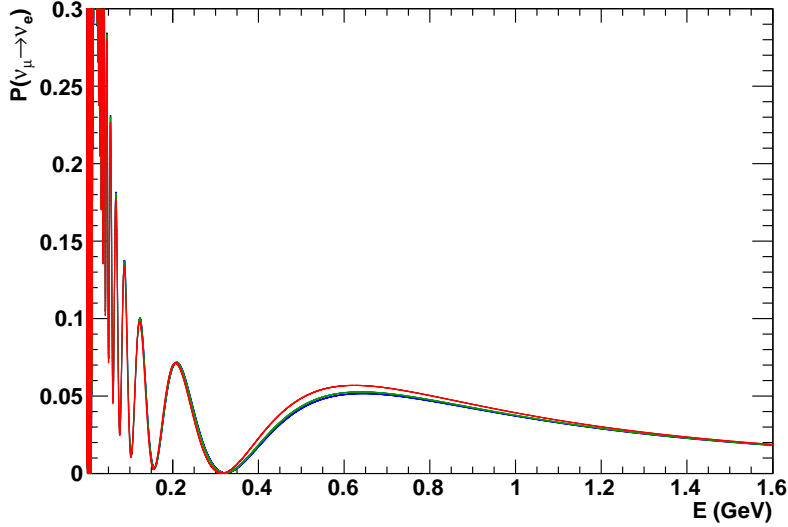


FIGURE 2.8: The $\nu_\mu \rightarrow \nu_e$ oscillation probabilities, as a function of energy, assuming a 295 km baseline. The effect of matter on oscillation is shown. The blue, red, and green curves assume 3.2, 2.5, and 0.0 g/cm³ constant density along the beam path. Note that the matter effects do not affect the oscillation very much, and that the exact value for density is not very important (2.5 and 3.2 g/cm³ are almost indistinguishable). The following oscillation parameters are assumed: $\sin^2 2\theta_{12} = 0.8704$, $\sin^2 2\theta_{23} = 1.0$, $\Delta m_{21}^2 = 7.6 \times 10^{-5} \text{eV}^2$, $\Delta m_{32}^2 = 2.4 \times 10^{-3} \text{eV}^2$, $\sin^2 2\theta_{13} = 0.11$, $\delta_{\text{CP}} = 0$, normal hierarchy.

2.4 CP Violation

To date, the only examples of CP violation (change in physics if you invert positional coordinates ($\vec{x} \rightarrow -\vec{x}$) and swap all particles and anti-particles) observed in particle physics come from the quarks. This can be attributed to the CP-violating phase of

the CKM matrix. The CKM matrix, however, is close to diagonal, and does not lead to very much quark mixing, and consequently, not very much CP violation. These rare CP-violating effects have been observed, first in 1964 in neutral kaon decays [47], and more recently in B decays [48].

CP violation has not been observed in neutrinos to date, though it could be observed through neutrino oscillation. One interesting feature to note is that CP violation cannot be observed in a neutrino disappearance experiment. In Equation 2.24, if $\alpha = \beta$, the mixing matrix contribution is reduced to $U_{\alpha j}^* U_{\alpha j}$, which is real. Thus, the only way to observe neutrino oscillation CP violation is to measure the oscillation rate from one flavor to another. Because the neutrino mixing angles (with the possible exception of θ_{13}) are larger than the CKM angles, it is possible that neutrino CP violation could be relatively large.

Another necessary condition for observation of CP violation is that all three mixing angles be non-zero. The difference in oscillation between neutrinos and antineutrinos will be proportional to the following [48]:

$$J_{\text{CP}} = \Im (U_{\mu 3} U_{e 3}^* U_{e 2} U_{\mu 2}^*) = \frac{1}{8} \cos \theta_{13} \sin 2\theta_{12} \sin 2\theta_{23} \sin 2\theta_{13} \sin \delta_{\text{CP}}. \quad (2.36)$$

Given that the other mixing angles are known to be relatively large, if θ_{13} can be shown to be relatively large as well, it should be possible to perform oscillation experiments to observe the difference in $P(\nu_{\mu} \rightarrow \nu_e)$ and $P(\bar{\nu}_{\mu} \rightarrow \bar{\nu}_e)$. The first step, before we can search for CP violation, is to measure θ_{13} , and show that it is sufficiently large that a CP violation measurement is possible. That is the long-term goal of the T2K program.

Why is CP violation in neutrinos interesting? For one, it is a very fundamental property of the universe, and should be measured. For another, measuring the mixing angles and CP phases of neutrino oscillation may provide clues as to their origin (the

standard model sets the angles, phases, and masses arbitrarily to match data). It is also possible that careful measurement of neutrino oscillation parameters will show that the current three-neutrino model is insufficient. The LSND experiment showed evidence for such a case [49], though it has not been confirmed by later experiments, such as MiniBooNE [50].

The greatest CP violation mystery, however, is the fact that the universe is dominated by matter, and not anti-matter. There does not appear to be any “primary” anti-matter in the universe, simply short-lived antiparticles produced from collisions of normal matter [48]. However, the asymmetry is quite slight, as the measured number of baryons divided by the number of photons is on the order of 10^{-10} [51]. Unless we assume that the universe began with this slight asymmetry, we need a physical mechanism. This could be generated with baryon number violating interactions, C and CP violation, and a departure from thermal equilibrium [52][48]. A popular mechanism (called leptogenesis) involves heavy right-handed Majorana neutrinos violating CP in their decay and producing a lepton asymmetry, which is then converted into the baryon asymmetry we see today [53]. Unfortunately, the CP-violating phases of heavy right-handed neutrinos need not be related to the ones measurable in left-handed ones. However, it would be surprising (theoretically) for CP violation to exist for heavy right-handed neutrinos but not for the light ordinary neutrinos [54]. Thus, finding CP violation in neutrino oscillation would be considered “archeological” evidence for the leptogenesis model of baryon asymmetry production [51].

2.5 Recent Neutrino Oscillation Experiments

A brief description of some recent neutrino oscillation experiments is included here, to better set the context for T2K.

K2K (KEK to Kamioka) [55] was the first long-baseline neutrino experiment to

operate with a distance scale of hundreds of kilometers. A beam of muon neutrinos was sent from KEK (a high energy accelerator research laboratory, in Tsukuba, Japan) across 250 km to Super-Kamiokande, with near detectors to measure the beam before oscillation. The experiment ran from 1999-2004. By comparing the spectrum of muon neutrinos observed at the far detector to that at the near detector, the atmospheric oscillation parameters (Δm_{32}^2 and θ_{23}) were measured. Searches for electron neutrino appearance in the beam (the primary goal of T2K) were also conducted [56].

Another recent neutrino beam experiment is MINOS (Main Injector Neutrino Oscillation Search) [57]. This experiment used the Main Injector at Fermilab in Batavia, Illinois to produce a muon neutrino beam. This beam is sent through a near detector at Fermilab, and a far detector at the Soudan Mine in northern Minnesota, 735 km away. This experiment produced the current best measurement for Δm_{32}^2 [57], which is critical for T2K's measurement of θ_{13} . MINOS has also conducted searches for electron neutrino appearance [58], as well as $\bar{\nu}_\mu$ oscillation studies [59] with the beam in antineutrino production mode.

Measurements of the atmospheric neutrino oscillation parameters (Δm_{32}^2 and θ_{23}) from these beam experiments, as well as Super-Kamiokande's atmospheric neutrino analyses, are shown in Figure 2.9.

The last mixing angle to be measured is θ_{13} . While it can be measured by electron neutrino appearance in a muon neutrino beam (as done in MINOS and T2K), it can also be measured by searching for electron antineutrino disappearance in reactor experiments. Reactors produce large fluxes of electron antineutrinos at energies around 3 MeV. At a baseline of around 1 km, this can be useful for measuring θ_{13} .

The signal for θ_{13} for a reactor experiment comes from the oscillation probability

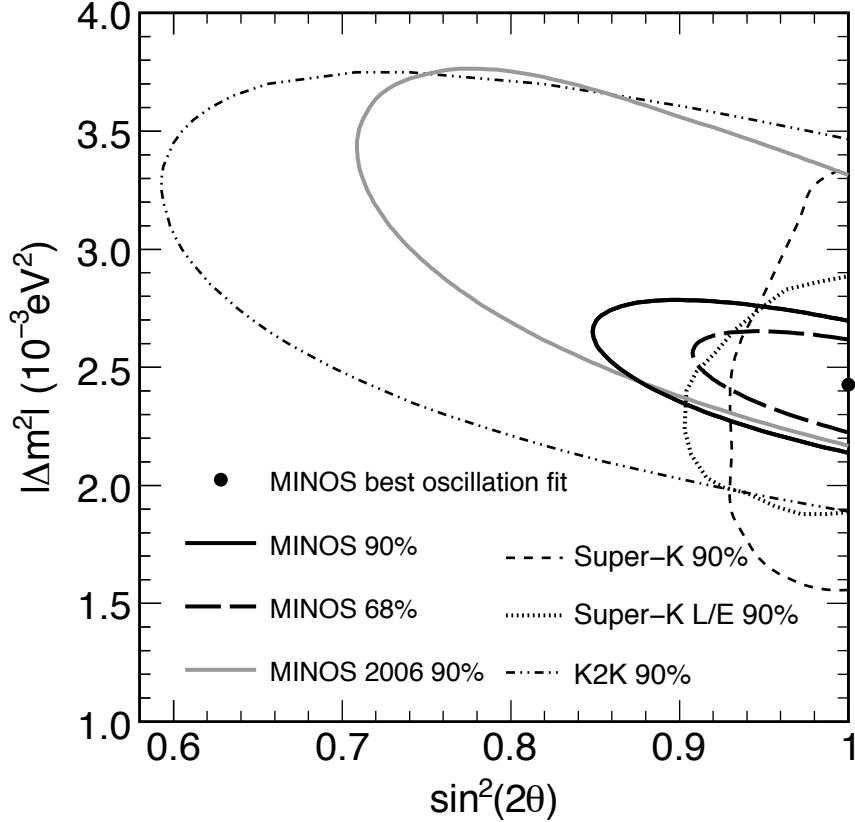


FIGURE 2.9: Plot of the allowed regions for atmospheric neutrino oscillation parameters from recent oscillation experiments. Contours from MINOS, K2K, and Super-Kamiokande are shown. From [60]. See [60] for full references. The SK 90% allowed region has been updated since this plot was made [61].

[48] (to first order):

$$P(\bar{\nu}_e \rightarrow \bar{\nu}_e) = 1 - \sin^2 2\theta_{13} \sin^2 \left(\frac{\Delta m_{31}^2 L}{4E} \right). \quad (2.37)$$

The CHOOZ experiment [62] featured a Gd-loaded liquid scintillator detector located ~ 1 km from the Chooz nuclear power plant in Chooz, France. This detector measured the electron antineutrino spectrum after oscillation, and this spectrum was fit to set the best limit on $\sin^2 2\theta_{13}$ at the time, as a function of $|\Delta m_{32}^2|$ [62].

3.1 Introduction

The T2K long-baseline neutrino beam experiment was proposed in 2001 with the primary goal to observe $\nu_\mu \rightarrow \nu_e$ oscillation, thereby making a measurement of, or setting an improved limit on, θ_{13} .

The beam source and near detector complex are located in Tokai, Japan, and the far detector is Super-Kamiokande (SK), a highly successful neutrino detector in its own right. The initial proposal [63] called for a five-year experiment. After the five-year run (or $5 \times 750 \text{ kW} \times 10^7 \text{ s}$ integrated beam power), a new stage of the experiment may be considered, featuring a switch to antineutrino mode to measure δ_{CP} and an upgrade to a more powerful beam and larger far detector (Hyper-Kamiokande [64] [65]).

Aside from the primary goal of measuring θ_{13} , T2K should provide an improved measurement of the atmospheric neutrino mass splitting Δm_{32}^2 and the mixing angle θ_{23} , as well as a very sensitive sterile neutrino search.

3.2 Basic Setup

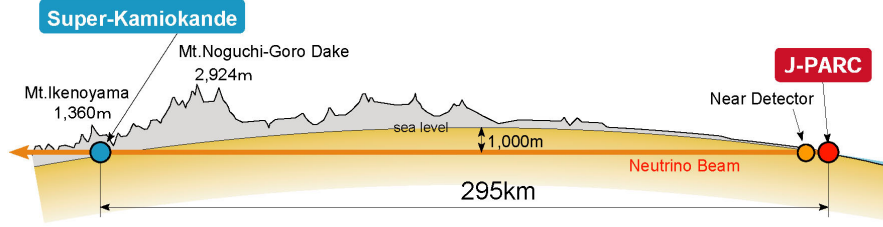


FIGURE 3.1: Side view of the T2K experiment, not to scale. The brown line shows the journey of the neutrino from J-PARC, through the near detector complex, 295 km beneath Honshu, the main island of Japan, and finally to Super-Kamiokande.

The T2K experiment consists of a neutrino beam source (Section 3.3), a near detector complex (Section 3.6), and a far detector (Chapter 4). The T2K beam is based on producing charged pions from proton collisions on a fixed target, directing the pions forward, and having them decay to neutrinos and muons. The accelerator for T2K is the proton synchrotron at J-PARC (Japan Proton Accelerator Research Complex). The beam is produced in an off-axis configuration [66] to make a ν_μ beam with a narrow energy maximum tuned for oscillation purposes. The near detector complex is approximately 280 m downstream from the production target. It consists of a multi-component off-axis detector inside of a magnet, and the INGRID on-axis detector. The far detector, Super-Kamiokande, is 295 km away. An overview of this setup is in Figure 3.1.

The measurement of θ_{13} is possible because the probability for muon neutrinos to oscillate into electron neutrinos is given (to first order) by

$$P(\nu_\mu \rightarrow \nu_e) = \sin^2 \theta_{23} \sin^2 2\theta_{13} \sin^2 \left(\frac{\Delta m_{32}^2 L}{4E} \right). \quad (3.1)$$

All the parameters in Equation 3.1 are fairly well known, except θ_{13} . See Section 2.3 for more information on oscillation. The experiment was designed with distance and

beam energy such that, around the peak neutrino energy (0.6 GeV), the $\nu_\mu \rightarrow \nu_e$ oscillation appearance probability is maximal, and the $\nu_\mu \rightarrow \nu_\mu$ survival probability is minimal (See Figure 2.6). Thus, the ν_e signal is maximized, and backgrounds from ν_μ are minimized, at the far detector. The main T2K analysis, ν_e appearance, involves identifying these electron neutrino events from amongst remaining backgrounds at the far detector, and using the number observed to compute $\sin^2 2\theta_{13}$. The ν_μ flux is measured at the near detector, to help predict the far detector flux, and reduce systematic uncertainties.

3.3 Off-Axis Beam

The pions are produced by directing a proton beam at a graphite target. The resulting pions are directed forwards using magnetic focusing horns (described in Section 3.5), and allowed to decay in a tunnel, terminated by the beam dump. The primary beam component is ν_μ , largely produced by pion decay,

$$\pi^+ \rightarrow \mu^+ + \nu_\mu. \quad (3.2)$$

This is the dominant decay mode for π^+ , with a branching ratio greater than 99.9%. The $\pi^+ \rightarrow e^+ + \nu_e$ decay is heavily suppressed by chirality constraints in this two-body weak decay. The muons mostly hit the beam dump before decaying, while most pions will decay before this. This allows for a very pure ν_μ beam. The main beam contamination comes from the decay-muons themselves decaying (3.3) and from kaons (3.4) which are also produced (though in much smaller multiplicity) at the target.

$$\mu^+ \rightarrow e^+ + \nu_e + \bar{\nu}_\mu \quad (3.3)$$

$$K^+ \rightarrow \pi^0 + e^+ + \nu_e \quad (3.4)$$

Additional contributions come from K_L^0 production at the target, some K^- and π^- decays, and some other assorted decays from particles produced at the target or in

nearby materials, such as the magnetic horns.

The neutrino beam is actually pointed 2.5° away from the far detector, Super-Kamiokande, roughly below it. This is advantageous, because there is less variation in neutrino energy as a function of pion energy when sampling off-axis. By selecting a different off-axis angle, the peak neutrino energy can actually be tuned, a consequence of the $\pi^+ \rightarrow \mu^+ + \nu_\mu$ decay kinematics (see Figure 3.2). At the T2K off-axis angle, the peak energy is ~ 0.6 GeV. The result is a highly pure ν_μ beam, especially at the peak energy, which is tuned for optimal ν_e appearance.

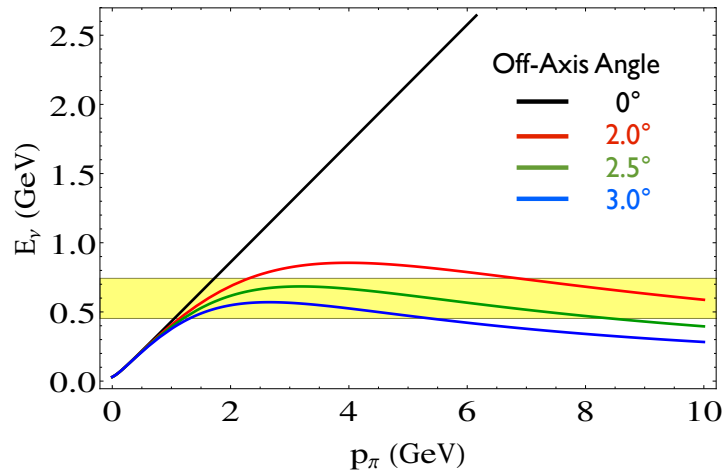


FIGURE 3.2: Plot of neutrino energy from a pion decay, assuming several different off-axis angles. This is calculated analytically from the decay kinematics. The yellow region, from 450 MeV to 750 MeV, is the T2K oscillation maximum (see Figure 2.6).

3.4 J-PARC Accelerator

The J-PARC accelerator complex in Tokai, Ibaraki Prefecture, consists of three accelerators [67]: a linear accelerator (LINAC), a rapid-cycling synchrotron (RCS), and the main ring (MR). This accelerator complex supplies particles to many experiments in materials and life sciences, hadron physics, and neutrino physics, including T2K [68].

The beam begins with a H^- (negatively ionized hydrogen) beam accelerated to 181 MeV in the LINAC (all the beam energy values given here for the accelerator are kinetic energies). Charge-stripping foils convert this into a H^+ beam as it is injected into the RCS. The RCS holds two bunches at a time, and accelerates the beam up to 3 GeV, with a 25 Hz cycle. About 5% of these bunches are passed on to the main ring, while the rest go to be used for other experiments. The main ring has a harmonic number of nine (meaning it could hold nine equally spaced bunches of protons), though it held six bunches/spill for T2K Run I (January - June 2010), and eight bunches/spill for T2K Run II (November 2010 - March 2011). It accelerates the protons to 30 GeV. For T2K beam production, these protons are fast-extracted, meaning all proton bunches leave the main ring in a single turn. Because of this, the individual bunches can be seen in the timing structure of the neutrino beam, even at the far detector (see Figure 3.3). The extraction is performed by a set of five kicker magnets, pushing the beam from the MR into the T2K neutrino beamline. This acceleration/extraction cycle occurs at a rate of approximately 0.3 Hz during normal T2K operation.

3.5 Neutrino Beamline

The protons extracted from the main ring are directed into the primary beamline. This focuses the beam and points it into the proper direction towards Kamioka. The primary beamline protons then pass into the secondary beamline, which contains the target station, decay volume, and beam dump (Figure 3.4). While the primary beamline is in vacuum, the secondary beamline is in a helium gas-filled volume, at one atmosphere of pressure.

The protons collide with the target, producing mainly pions (with some kaons and other particles) which traverse the secondary beamline (Figure 3.5). The secondary beamline contains the target (Figure 3.6) and magnetic horns, as well as the decay

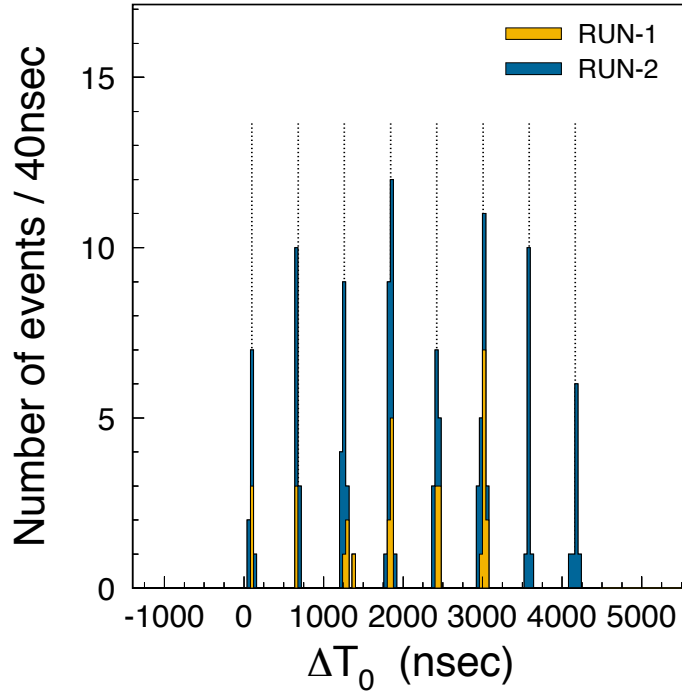


FIGURE 3.3: Timing distribution of on-timing fully contained (see Chapter 4) events detected at the far detector, SK. ΔT_0 is the timing difference from the spill time, corrected for neutrino flight time and photon travel length differences in the SK tank by reconstructed position. The yellow and blue stacked histograms represent events from run I and run II, respectively (see Section 8.1). The bunch structure is clearly visible in the timing, and it can be seen that run I had 6 bunches, while run II had 8. The dotted vertical lines show the 581 ns-interval bunch center positions.

volume and beam dump. Also included is a baffle to collimate the beam before it reaches the target and first horn, and an optical transition radiation monitor (OTR), between the baffle and first horn, to measure the proton beam profile. The OTR uses a thin titanium-alloy foil, placed at 45° to the beam. Transition radiation is produced in the visible range when charged particles pass through the foil, and this light is collected after a series of mirrors for beam measurements.

The target itself has, at its core, a graphite rod, 91.4 cm long, 2.6 cm in diameter. Surrounding that is a 2 mm thick graphite tube, inside a 0.3 mm thick titanium case.

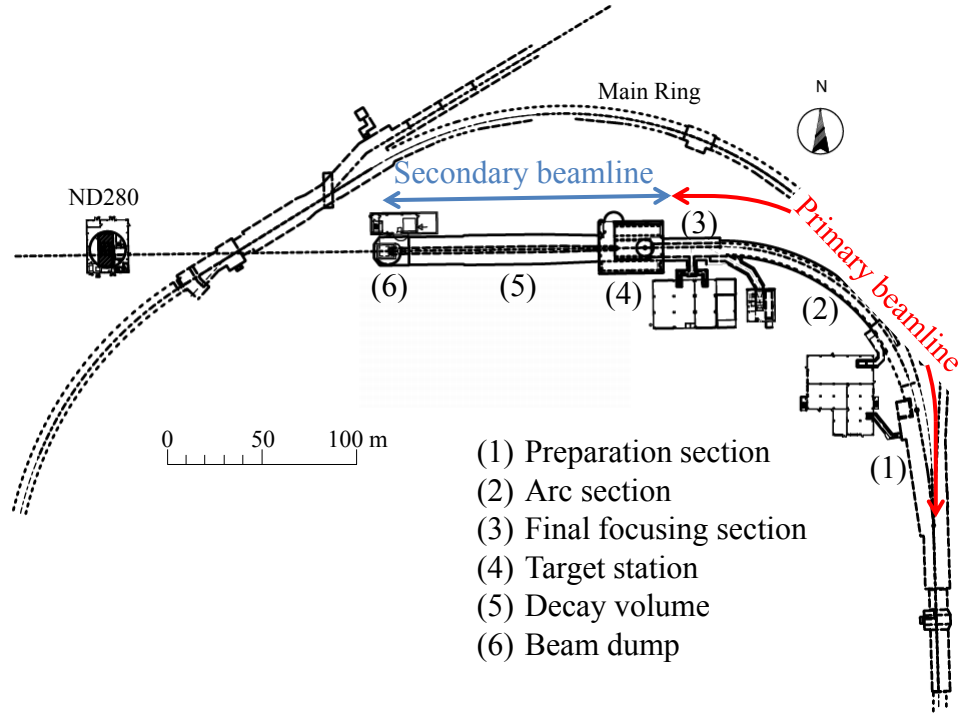


FIGURE 3.4: Diagram of the T2K beamline, viewed from above, with labels. Both the primary and secondary beamline components are shown. From [69].

Between these three layers, helium gas is circulated for cooling purposes. The target is placed inside of the first magnetic horn. Thus, the first magnetic horn collects the pions produced and directs them forward to the other horns. The second magnetic horn is located just beyond the first, while the third horn is a few meters downstream. These horns focus the positively charged pions, and the target and horn shapes and positions are optimized to maximize the neutrino flux.

The principle of the magnetic horns is to use a toroidal magnetic field to bend positively charged particles moving radially to the forward direction (Figure 3.7). Negatively charged particles will be directed away from the forward direction. If the horn current is reversed, it will instead select negatively charged particles, which could be used for an antineutrino beam experiment. A cross-section of the T2K three-horn system, along with example pions, is shown in Figure 3.8. The magnetic field

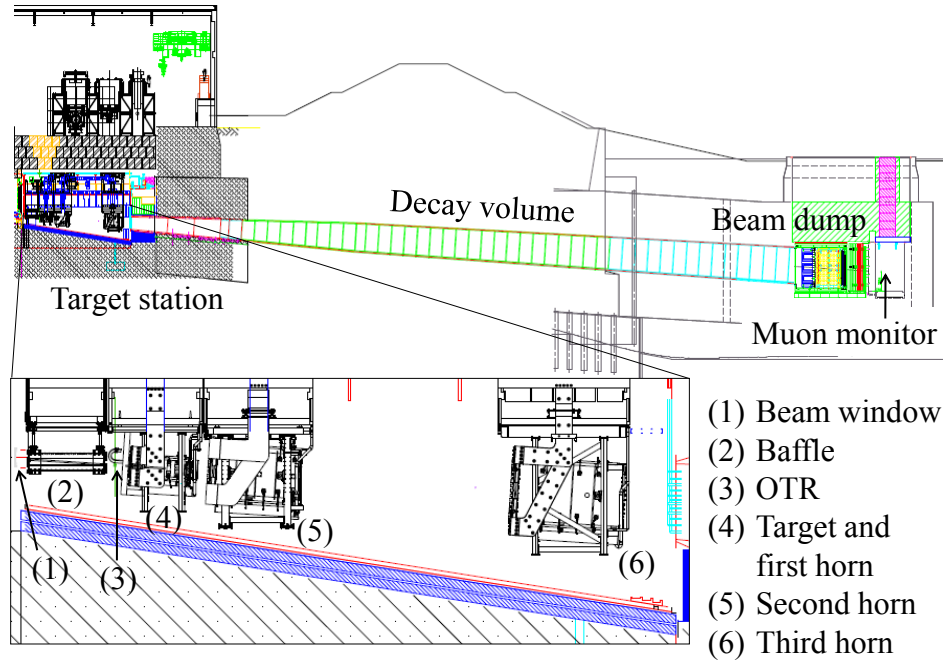


FIGURE 3.5: Diagram of the T2K secondary beamline, as viewed from the side. A magnified view of the target station is shown, with labels. From [69].

inside the horns varies as $1/r$, where r is the distance from the horn axis. The second and third horns (used for focusing) feature the traditional double-parabola shape, where the horn length is longer further off-axis. This compensates for the lower magnetic field at larger radii. See [70] for more details on focusing horn physics. The inner conductors of the magnetic horns are as thin as possible, to reduce pion absorption. The inner conductor for each horn is made of 3 mm thick aluminum.

Beyond the three magnetic horns is the decay volume. It is a 96 m long steel tunnel. In this region, the now-focused pions can decay to produce the muon neutrino beam. At the end of this tunnel is the beam dump. The core of the beam dump is 75 tons of graphite, with many iron plates around it. There are also water-cooled aluminum cooling modules. The beam dump will stop all pions, and all muons below ~ 5.0 GeV/c. Just beyond the beam dump is the muon monitor, used to monitor

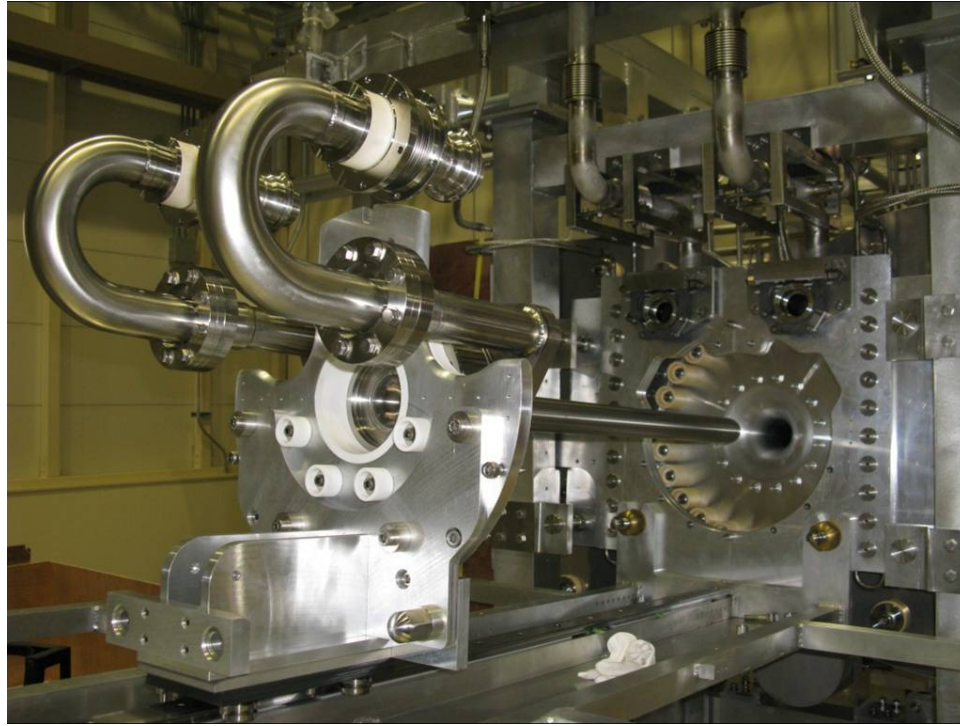


FIGURE 3.6: Photograph of the T2K target. It is lined up with the first horn, in the background, but not yet moved into position. The pipes for cooling helium can be seen.

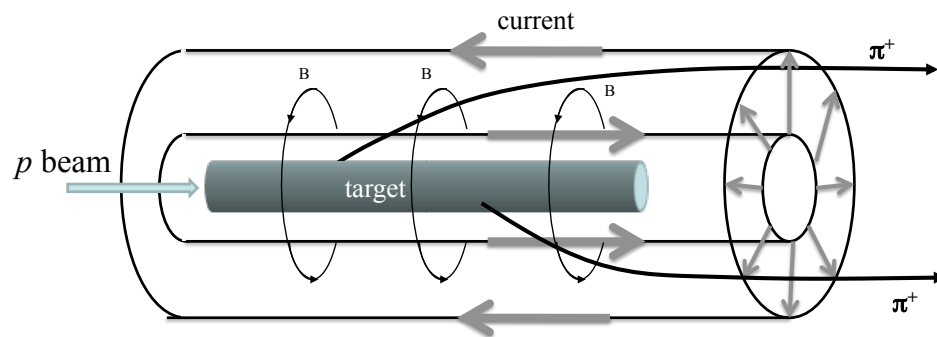


FIGURE 3.7: Cartoon showing how charged particles are deflected inside of a magnetic horn. From [71].

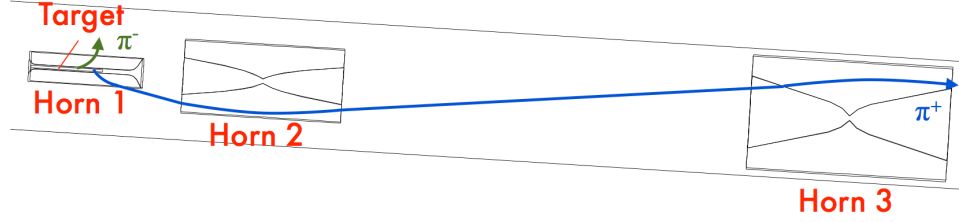


FIGURE 3.8: Cross-sectional illustration of the T2K horn system. Note the traditional double-parabola-like shape on the second and third horn. The target is placed inside the first horn to maximize efficiency for this relatively low energy neutrino beam. Hypothetical trajectories are drawn to illustrate how positive pions can be focused, while negative pions are defocused (trajectories are somewhat exaggerated). From [71].

the neutrino beam direction and intensity on a bunch-by-bunch basis. The expected beam flux at 2.5° off-axis is shown in Figure 3.9.

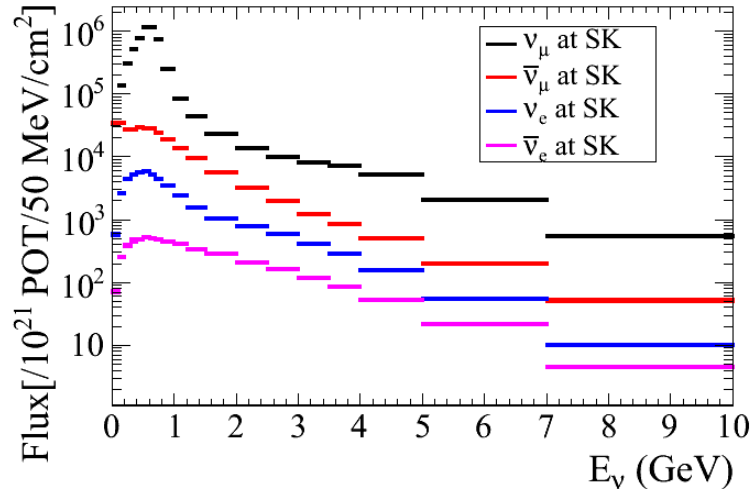


FIGURE 3.9: Expected flux to be observed at the far detector from the T2K beam. The different components of flux are shown separately. Note the y -axis has a log scale. Note the sharp peak in ν_μ flux, made possible by the off-axis technique. Plot produced by the T2K beam group.

3.6 ND280

The near detector complex (ND280) is used to characterize the neutrino beam before it has oscillated. The INGRID detector measures the on-axis beam profile, while the off-axis detectors (collectively called ND280, also the term for the whole complex, so “ND280 Off-Axis” will be used in this dissertation) measure the properties of the beam at the angle which the far detector will observe it. An illustration of the ND280 complex is in Figure 3.10.

3.6.1 INGRID

The INGRID on-axis detector consists of 16 identical modules with alternating layers of scintillating tracking material and iron plates [69]. The majority of the modules are in a cross shape, centered on axis, with seven modules in a vertical column, and seven modules in a horizontal row. Additionally, two more modules are located outside of the main cross, to help check the axial symmetry of the neutrino beam (Figure 3.11).

Each module has nine iron plate layers and 11 tracking plane layers. These tracking planes in turn consist of 48 scintillating bars, 24 oriented horizontally and 24 vertically. These alternating planes face the oncoming beam so that a muon produced in a neutrino interaction, moving in the beam direction, would pass through multiple layers. Finally, additional tracking planes are installed perpendicular to the other planes on the sides of the modules, as veto planes, to reject events originating from outside the module (the first and last of the 11 main layers can serve this purpose on the remaining sides, see Figure 3.12).

The iron plates serve as target mass, and provide additional segmentation to the modules to help in detecting tracks. Also, the plates will stop electrons and pions, so the muon events can be more certainly identified. The scintillator planes feature

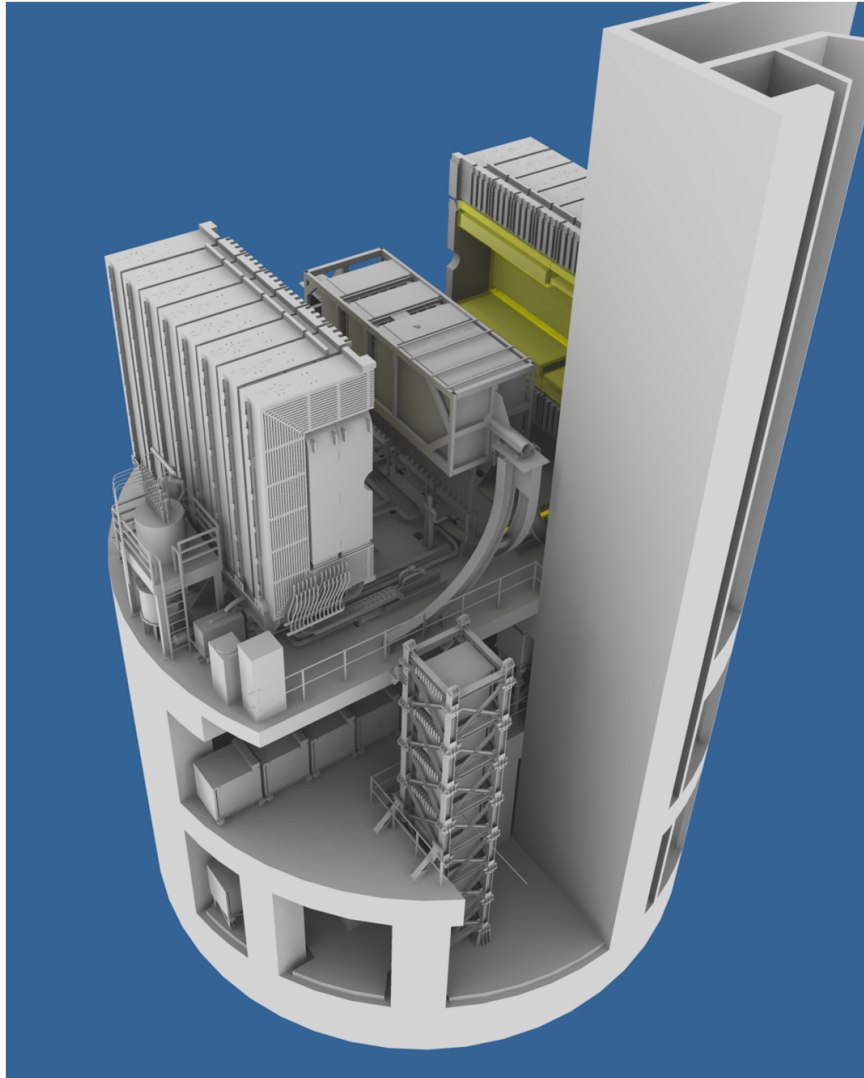


FIGURE 3.10: Illustration of the ND280 pit and detectors. Near the bottom is INGRID, with the vertical modules in the foreground and horizontal modules behind them. The off-axis detector is above, with the magnet in the open state to show the normally enclosed detectors. The neutrino beam direction is into the page, perpendicular to the INGRID cross. From [69].

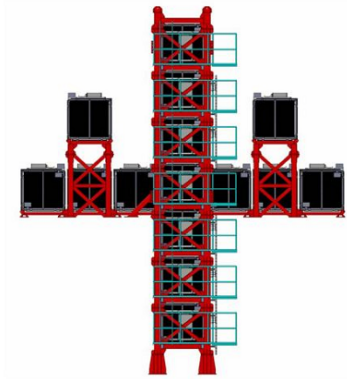


FIGURE 3.11: The arrangement of the 16 INGRID modules in the cross shape with two off-axis modules. From [69].

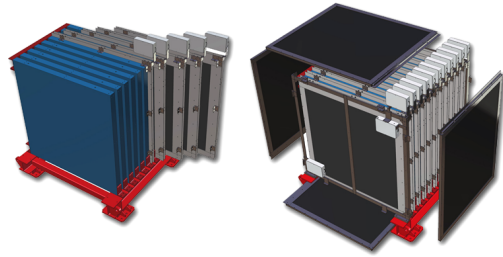


FIGURE 3.12: Exploded diagrams of a single INGRID module. The left figure shows the tracking planes in blue, with the iron plates inserted. The figure on the right shows the veto planes being added. From [69].

wavelength-shifting (WLS) fiber to collect the light and bring it to the photosensor. The photosensor used in INGRID (and for most of the ND280 detectors) is the Multi-Pixel Photon Counter (MPPC) [72][73]. This technology was chosen for several reasons, including size, cost, stability, and the high magnetic field encountered in the off-axis detector [72].

INGRID's primary purpose is to verify the beam direction and event rate stability. By counting the number of beam muon events in each module, a beam profile can be generated, and the center computed. An additional proton module is also included, different from the 16 INGRID modules. It has finer tracking capabilities and is placed in the center of the INGRID cross between the horizontal and vertical segments. It is designed to detect both the muon and proton track, to better check the MC simulation of CCQE events. More information on INGRID can be found in [69].

3.6.2 ND280 Off-Axis

The off-axis detector is an ensemble of the π^0 -detector (P0D), three time projection chambers (TPCs), two fine grain detectors (FGDs), a set of electromagnetic

calorimeters (ECals), and a side muon range detector (SMRD), all wrapped inside the refurbished UA1 magnet (Figure 3.13), providing a dipole magnetic field of 0.2 T. These detectors are positioned 2.5° off-axis, in line with the far detector. Information on all these components can be found in [69].

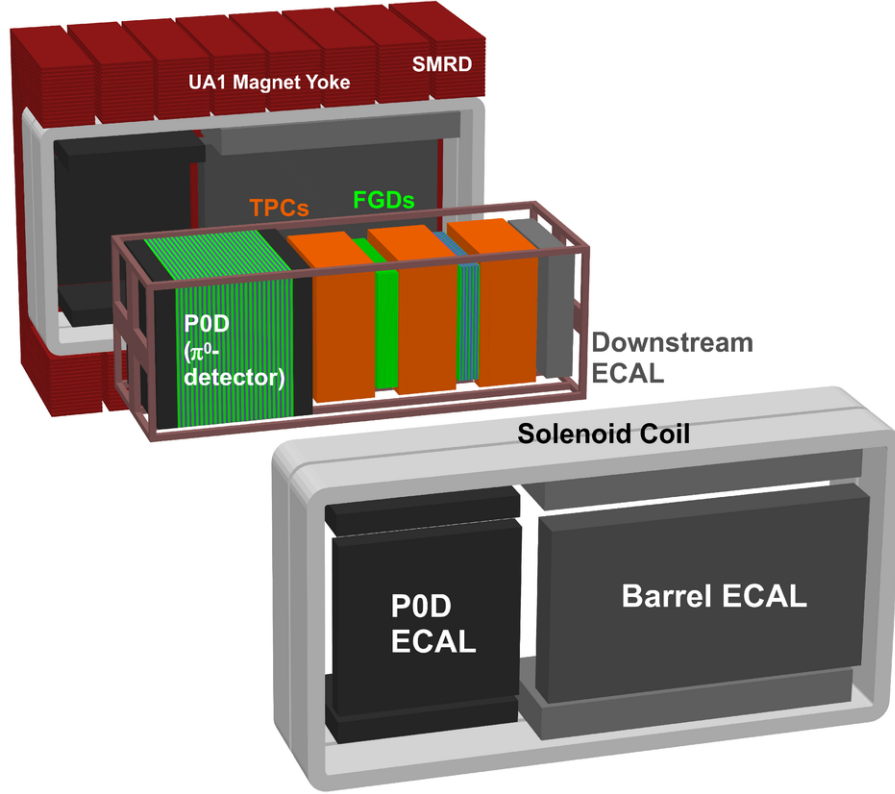


FIGURE 3.13: The off-axis detector ensemble. From [69].

The first component of the off-axis detector (moving in the beam direction) is the P0D. The P0D is primarily used to measure NC π^0 production ($\nu_\mu + N \rightarrow \nu_\mu + N + \pi^0 + X$) on a water target. This interaction is the primary reducible background at SK. The P0D consists of scintillator bars, arranged in the x and y directions, alternating with fillable water target bags and lead and brass sheets (see Figure 3.14). The detector can be run with the water bags either filled or empty, providing a differential measurement of the NC π^0 cross section on water.

The scintillator bars have a triangular cross section, and use a WLS fiber to bring the light to the MPPCs. The upstream and downstream ends of the P0D have several layers with lead sheets and no water, forming the upstream and central ECals. These help provide a veto for the P0D and help contain electromagnetic showers. The resolution of the scintillator bars is sufficient to reconstruct both charged particle tracks and electromagnetic showers, the latter produced by the $\pi^0 \rightarrow \gamma + \gamma$ decay.

The next component is the tracker, which is made up of three TPCs and two FGDs, alternating. The TPCs operate on the principle of charged particles passing through the TPC gas and ionizing it. These ionization electrons are drifted to the detector planes by an electric field. The combination of the Y-Z position on the plane where the electrons drift to, along with timing information, allows 3-D tracks to be reconstructed with high precision.

The TPCs feature a 95% argon gas mixture as the drift gas. Each of the three TPCs has 3000 L of the argon mixture. Around this is a gap volume filled with carbon dioxide as an insulating gas. The TPCs are designed such that there is a cathode plane at the center of the TPC, and electric fields pulling electrons away from it on either side (Figure 3.15). Each side of the TPC is instrumented with bulk MicroMegas detectors [74] which serve both as an anode and a sensor. More detailed information on the TPC design and construction can be found in [75].

The TPCs have three major purposes in reconstruction. The excellent 3-D track resolution allows for good measurement of the number and directions of the tracks, to help identify different neutrino interactions. The magnetic field will cause charged particle tracks to curve, and from this curvature the momentum of charged particles can be reconstructed. Lastly, particle-ID can be performed based on the amount of ionization left by the particle of a known momentum. This last feature is critical for measuring the intrinsic beam electron neutrino fraction.

The FGDs provide most of the target mass inside the tracker system, each one

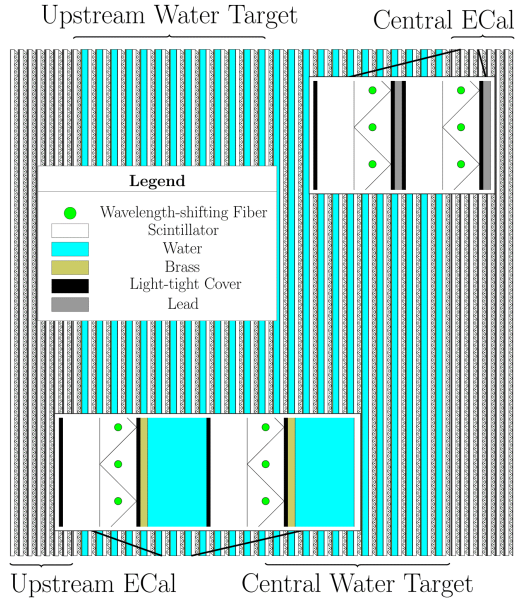


FIGURE 3.14: Cross-section of the POD. The neutrino beam is moving left to right. The insets show how the triangular prism scintillator bars are arranged in horizontal and vertical planes, and how the water target regions and ECal regions have different layering. From [69].

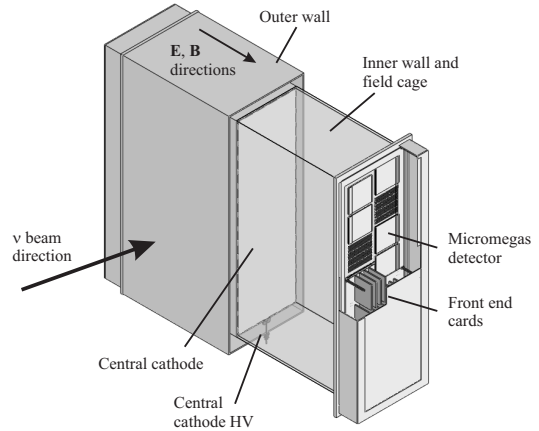


FIGURE 3.15: Diagram of a TPC module, with cutaways to show interior components. From [69].

with 1.1 tons of target material. The first FGD has 5760 scintillator bars, in 30 layers, alternating x and y orientations. Each pair of layers with an x layer and a y layer is called an XY module. WLS fiber carries the light to the MPPCs. The second FGD is arranged with an alternating series of seven XY modules and six 2.5 cm thick layers of water (totaling 2688 scintillator bars and 15 cm total thickness of water). These different target materials will help determine the different cross-sections on carbon and water. The FGDs help track charged particles very near the interaction vertex.

Surrounding these components is the ECal, a sampling calorimeter. ECal modules

use lead sheets as absorbers, with layers of plastic scintillator as the active detector. The light from the scintillators is brought, via WLS fiber, to the MPPCs. The ECal has modules in three major regions. Six modules surround the P0D on the four sides parallel to the beam, and are attached to the magnet (the top and bottom ECals need two separate modules each so the magnet can be opened). Six modules also surround the tracker in a similar fashion. Finally, there is the downstream ECal, located in the same basket as the P0D and tracker, but at the far downstream end. The modules in each ECal region have a different number and thickness of layers to satisfy physics requirements and space constraints within the magnet.

The ECals collect information about particles leaving the P0D and tracker. This can help for momentum and direction reconstruction, and particle-ID. They can also serve as a veto, and detect photons which do not convert in the P0D or tracker. A key function of the ECals is to identify showering events around the tracker, useful for π^0 reconstruction. The tracker and downstream ECals have around 10 radiation lengths of lead plate, while the P0D ECal has 3.6 radiation lengths (the P0D itself is already designed to detect π^0 s, so the ECal does not need to).

Finally, there is the SMRD [76]. The UA1 magnet features a large steel yoke made up of parallel segmented steel plates, enclosing the magnet. There are a total of 16 layers of 4.8 cm thick steel, with 1.7 cm air gaps between them. The yoke provides a region of high permeability for the magnetic flux to return through, boosting the strength of the electromagnet. In these gaps, a total of 440 scintillator modules are inserted. These modules (which make up the SMRD) surround the detector, though not all of the gaps are filled with scintillator modules. The innermost gap is always filled, and other gaps are filled differently for different regions, with all parts of the yoke instrumented with between three and six layers of modules. Light from these scintillator modules is carried via WLS fiber to MPPCs. The layers of steel between the SMRD modules may allow some range measurements to be made, which can help

reconstruct muon momentum.

The SMRD has three main functions. First, it records muons traveling at large angles from the beam and can help measure their momenta. Next, it can trigger on cosmic ray muons entering the ND280 detector, and this can be useful for calibration and veto purposes. Lastly, it helps identify beam-related event interactions from the magnet and outside the detectors.

All of these detector components work together to reconstruct neutrino events (and some backgrounds). An example event display is shown in Figure 3.16. For the analysis described in this dissertation (Section 6.3), the number of CC ν_μ interactions detected in the ND280 tracker is used as an input.

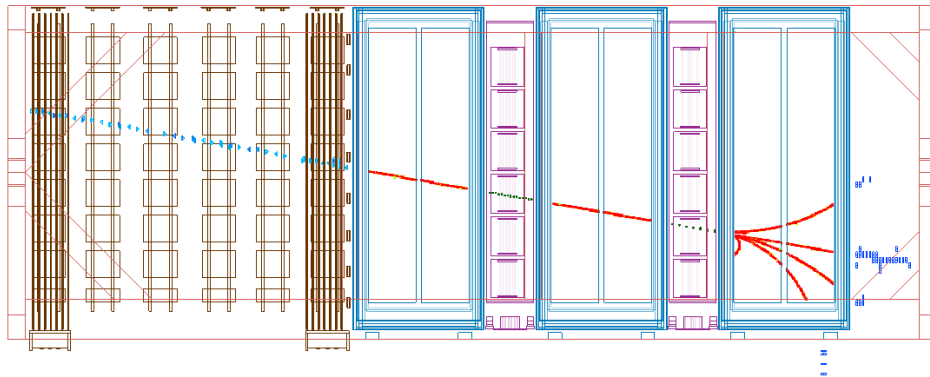


FIGURE 3.16: An example of a ND280 off-axis event display. This shows a muon originating from upstream of the detector, and passing through most of it. From left to right, the muon tracks can be observed in the upstream (P0D) ECal, the P0D, the central (P0D) ECal, all three TPCs and the two FGDs, and the downstream ECal, and a bit on the tracker ECal (on the bottom). Note that the muon produces secondary particles in the third tracker, and these secondaries are collected in the ECals.

3.7 Far Detector

The far detector for T2K is Super-Kamiokande (SK). The design and operation of SK, along with details on reconstruction algorithms, are found in Chapter 4. Details

on T2K-specific features of SK are found in Section 4.10.

Super-Kamiokande

4.1 Overview

Super-Kamiokande (SK) is a neutrino and proton decay experiment located near Kamioka, Japan, inside Mt. Ikenoyama. This is the same mountain where its predecessor experiment (Kamioka Nucleon Decay Experiment, or KamiokaNDE) was located. SK is a large ring-imaging water Cherenkov detector [77], and serves as the far detector for T2K. A diagram of the detector complex is shown in Figure 4.1. The location deep within a mountain provides shielding against the vast majority of cosmic ray muons. Only muons with an energy of at least 1.3 TeV have the ability to penetrate the kilometer of rock (2700 meters water equivalent) necessary to reach SK. This keeps the cosmic muon rate down to around 3 Hz.

Approximately 50,000 tons of water are contained within the welded stainless steel cylindrical tank, 42 m tall and 39 m in diameter. The tank itself is divided into two main regions, the inner detector (ID) and outer detector (OD). These regions are separated by the wall containing the photomultiplier tubes (PMTs). The PMT wall consists of a steel framework, 55 cm thick, housing both the 11,129 inward facing

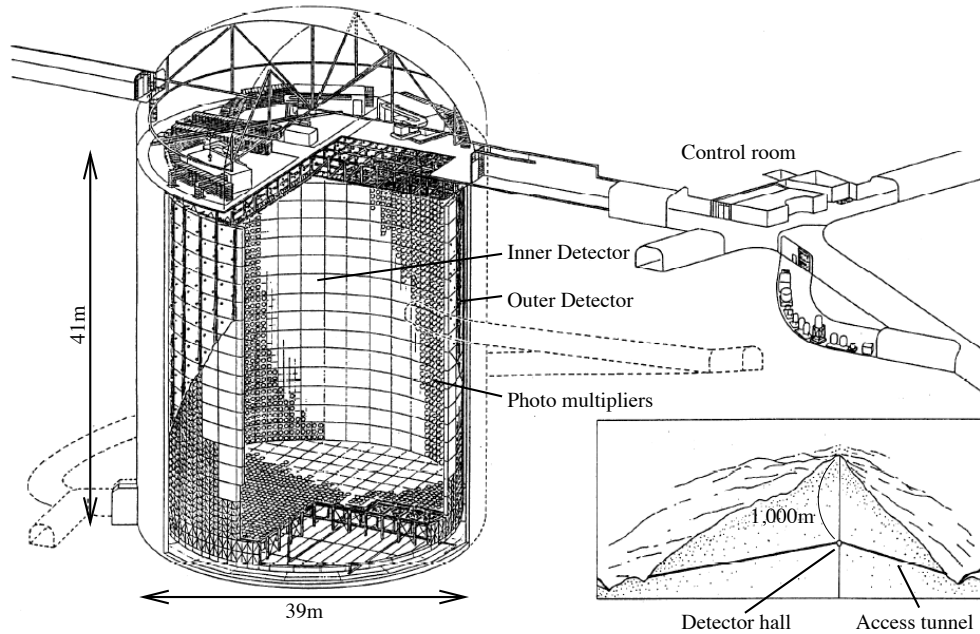


FIGURE 4.1: A sketch of the Super-Kamiokande facility. The detector complex is located inside Mt. Ikenoyama, beneath approximately 1 km of rock. The easiest access to the detector is by car, via a horizontal access tunnel. The cylindrical detector contains 50 kton of water, and is 39 m in diameter and 42 m tall. Also visible in this sketch are the control room area (middle-right) and the water purification system area (curved tunnel to the right). The cutaway view of the detector shows how the tank is divided into an inner and outer region by the PMT wall. The main detector electronics are located in the “huts” visible on top of the tank, inside the detector dome. Figure from [63].

PMTs (ID PMTs) and the 1,885 outward facing ones (OD PMTs). This optically separates the ID and OD, leaving approximately 2.6 m between the OD PMTs and the tank outer wall. This OD acts as a veto region to identify particles entering the tank from outside.

The ID wall has effectively 40% of its surface covered by the PMTs (except for SK-II, described later). The rest of the wall surface is covered in a black sheet, to minimize reflections which can make event reconstruction difficult. The ID uses 50 cm diameter hemispherical PMTs produced by Hamamatsu. These act as pixels

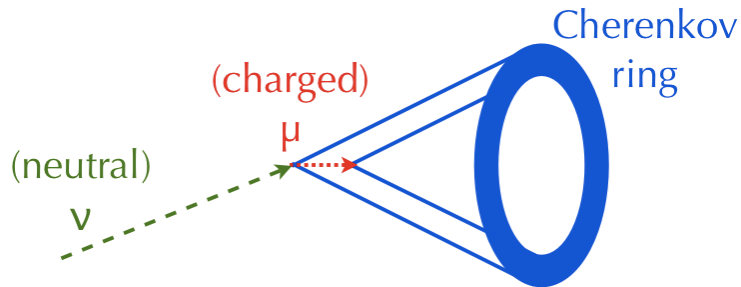


FIGURE 4.2: A cartoon of how a typical SK neutrino event is detected by a Cherenkov ring. A neutrino enters the tank, and interacts with a water molecule, producing a muon. This muon travels for some distance at faster than c/n ($0.75 c$), losing energy and emitting Cherenkov radiation in a cone. This cone of light projects forward to the detector wall, where it is detected by the PMTs as a ring. The muon drops below Cherenkov threshold before it reaches the tank wall, so the ring is not filled in.

which are used to reconstruct Cherenkov light images. When charged particles travel through the water at faster than c/n (n , the index of refraction, is approximately 1.33 in water) they emit a cone of Cherenkov radiation (Figure 4.2). This light, when projected on to the (approximately) flat walls of the detector, appears as a ring. If the charged particle travels all the way to the detector wall, the ring will appear filled in, and if it does not travel very far in the water before dropping below Cherenkov threshold, it will appear very thin. The timing, width, shape, sharpness, and intensity of these rings are the key to reconstructing the trajectories of particles within SK.

The OD uses 20 cm PMTs, each fitted with a wavelength-shifting plate to increase the efficiency of light detection. The walls of the OD are lined with Tyvek (manufactured by DuPont), a highly reflective white sheet, also improving the efficiency. The OD serves as an active veto against incoming particles, but is also a passive shield against neutrons or gammas produced by radioactive decay in the surrounding rock. Thus, a clean neutrino signal at SK is one or more rings detected in the ID, with no significant light detected in the OD.

Super-Kamiokande has been operating since April 1996, though not continuously. Its operation can be divided into four main periods. The first operational period is known as SK-I, lasting from 1996-2001. This was the original detector configuration, with 11,146 ID PMTs. This period produced the discovery of atmospheric neutrino oscillation [11].

At the end of SK-I in July 2001, the detector was shut down for scheduled maintenance. The tank was drained so the PMTs could be accessed, work was completed, and the tank began filling in September. On November 12, however, with the water filled to 32 m, one of the PMTs at the bottom of the tank imploded under the pressure. This created a shock wave in the water which caused further PMT implosions, destroying over half of the total ID and OD PMTs. The exact cause of the accident will likely never be known, but it has been narrowed down to a few PMTs, one of which must have somehow been weakened during maintenance.

In the aftermath of this catastrophe, a decision was made not to end SK, though it would take considerable time to acquire the PMTs necessary to replace the destroyed ones. From 2003 to Fall 2005, SK was run with around half the usual number of ID PMTs, arranged in a checkerboard pattern. The OD had been fully reconstructed. To guard against a similar disaster in the future, acrylic covers were added over the PMTs, and a fiber-reinforced plastic shell was added to the base of the PMT. This casing should protect tubes in the event of another implosion, and has been included on all SK PMTs since 2003. The period from 2003-2005 where the ID was at half-coverage is known as SK-II [46].

In Fall 2005, the SK tank was drained once again (the final time to date) for reconstruction. The vast majority of the missing PMTs were replaced, though the new covers necessitated that a few PMTs be left out. Thus, the ID was replenished to 11,129 tubes, all protected by the plastic shells with acrylic covers. The detector ran in this state from the end of 2005 to summer 2008, with this period known as

SK-III.

During summer 2008, an electronics upgrade was performed [78]. A major motivation for this upgrade was to prepare for T2K. This was done without the need to open and drain the tank. The upgraded system replaced the hardware trigger with a system where every hit is recorded, and a software system applies triggering. This hardware [79] allows for much higher data throughput, allowing for lower energy thresholds, or more complex triggering. Such special triggers can include neutron tagging for solar ν_e events, and the T2K beam trigger. Other benefits include reduced dead-time, which improves decay electron finding efficiency, and higher data rates for supernova bursts. The period after the upgrade was completed is known as SK-IV, which continues through the time of this writing.

SK was used as the far detector for K2K [55] from 1999 through 2004, during SK-I and SK-II. T2K has used SK as the far detector entirely during the SK-IV period. As this dissertation is based on T2K, the detailed discussion of SK operation will be based on the SK-IV configuration.

4.2 Detector Physics

As described in Section 4.1, SK is a ring-imaging Water Cherenkov detector. Cherenkov radiation, however, is not the primary form of energy loss for particles passing through the detector.

The equation for energy loss per distance traveled due to Cherenkov radiation is given by [80]

$$-\left(\frac{dE}{dx}\right) = \frac{4\pi e^2}{c^2} \int_{\beta n(\omega) > 1} \omega d\omega \left(1 - \frac{1}{\beta^2 n^2(\omega)}\right). \quad (4.1)$$

This energy loss turns out to be far smaller than the energy loss due to other effects. For muons in the SK water, the primary energy loss mechanism is ionization, for the energies relevant for T2K (100 MeV to 10 GeV) [35]. While the muons are above

Cherenkov threshold, the ionization loss per unit distance is relatively constant, around 2.2 MeV/cm. Based on this relation, if the total length over which a muon emits Cherenkov light is known, the momentum of that muon can be calculated. Of course, the momentum can also be calculated from the total amount of Cherenkov light emitted. All this would also apply to protons and pions, although they have additional complications due to their propensity to interact with nuclei in the water.

The energy loss for electrons (and positrons) is somewhat more complicated. Electrons, having a far lower mass than muons or pions, are far more susceptible to having their trajectory altered through collisions with electrons or nuclei in the atoms. The change in trajectory will result in the emission of bremsstrahlung radiation. Above several tens of MeV, bremsstrahlung radiation becomes the dominant form of energy loss for electrons. Not only does this produce extra photons (which can themselves pair-produce to e^+e^- pairs), but it alters the electron trajectory. These effects cause the Cherenkov rings for electrons to be more diffuse. The phenomenon where bremsstrahlung and pair production combine to produce many particles from the initial single one is called showering.

High energy photons (γ s) in SK will pair-produce to e^+e^- pairs, after which point they behave much like a shower from an electron. Both γ s and electrons are showering particles. This can make it difficult to distinguish between an electron shower and a γ shower. For T2K, this is especially critical in the case of $\pi^0 \rightarrow \gamma\gamma$ decays, which may, in certain cases, mimic a single-electron event (See Section 4.6.7). The average pair production length in water is ~ 46 cm (computed from the radiation length in water, 36 cm) [80]. The effects of showering cause the range (distance traveled) of electrons and photons to be much smaller than that of muons of comparable energy. The SK particle ID (PID) operates by distinguishing showering rings (from electrons and γ s) from non-showering rings (from muons, pions, and protons).

Cherenkov light is only emitted when $\beta > 1/n$. This radiation can be interpreted

as being like the sonic boom of an aircraft traveling at faster than the speed of sound. In this analogy, the angle at which this light is emitted can be computed (see Figure 4.3). The Cherenkov cone angle is thus given by $\beta n = 1/\cos\theta$. As the index of refraction of water is ~ 1.33 (at the relevant wavelengths), the critical Cherenkov angle is $\theta_c \approx 42^\circ$.

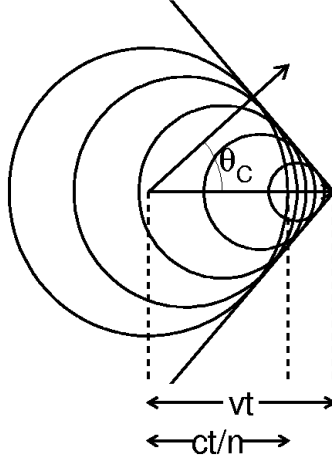


FIGURE 4.3: Diagram of Cherenkov radiation wavefronts. Diagram from [46], see [81] for more details.

The number of Cherenkov photons emitted per unit distance per unit wavelength is given by [35]

$$\frac{d^2N}{dx d\lambda} = \frac{2\pi\alpha}{\lambda^2} \left(1 - \frac{1}{\beta^2 n^2(\lambda)} \right). \quad (4.2)$$

Integrating this over the range where the SK PMTs are most sensitive (350-500 nm [77]), we find approximately 300 Cherenkov photons per cm, or ~ 150 photons/MeV. Thus, the number of detected photons (after several corrections) can be used to measure the energy of particles in SK.

The ID PMTs (Figure 4.4), covering $\sim 40\%$ of the ID wall surface, detect these Cherenkov photons. The PMT quantum efficiency (the fraction of photons incident on the PMT photocathode surface to produce a photo-electron) is given in Figure 4.5.

The peak efficiency is about 21%, at 360-400 nm. The photocathode is a bialkali coating on the PMT bulb inner surface, and photoelectrons produced are drawn to the dynode chain where they are multiplied. To ensure the photoelectrons are not diverted away from the dynodes, the magnetic field must be maintained as low as possible. This is done with a set of Helmholtz coils around SK, which cancel out the Earth's magnetic field.

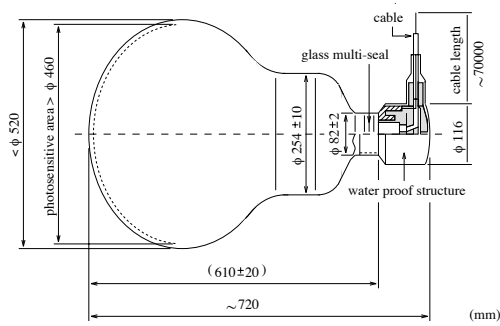


FIGURE 4.4: Diagram of an ID PMT, from [77].

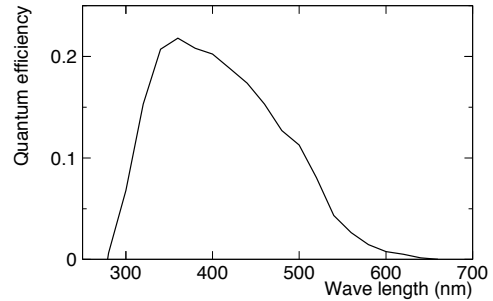


FIGURE 4.5: PMT photocathode quantum efficiency as a function of wavelength. From [77].

4.3 Data Acquisition

The main feature of the SK-IV data acquisition (DAQ) system is the introduction of new front-end boards, called QBEE. This stands for QTC Based Electronics with Ethernet, and QTC stands for Charge to Time Converter. In this system, each recorded PMT hit is self-triggered, a significant upgrade from the old system used for SK-I through SK-III. A total of 550 QBEE boards are used, with up to 24 PMTs connected to each board. Each board is equipped with 8 QTCs, each of which has three PMT input channels. More information on the QBEEs, especially the QTC application-specific integrated circuit (ASIC), can be found in [79].

For the ID, PMT signals are sent to the QBEE boards via a coaxial cable, separate

from the high voltage (HV) power supply. For the OD, there is only a single coaxial cable for both signal and power, so one extra step is required before the QBEEs. The OD cables are fed into boards called paddle cards. These boards feature a high-pass filter to extract the signal from the HV base. The signal is then sent to the QBEEs.

PMT signals, once they cross the triggering threshold, are integrated over a 400 ns period. This integrated charge is converted to a pulse time by the QTC. The QTC outputs a square pulse, where the leading edge timing indicates the hit time (trigger time), and the pulse length is proportional to the integrated charge. A diagram of the QTC operation is shown in Figure 4.6. After the 400 ns charge time, 350 ns is required for discharge, and that is followed by 150 ns veto period. Any PMT signals in the discharge or veto periods are ignored. The total processing time is 900 ns, after which the circuit is ready to trigger once more.

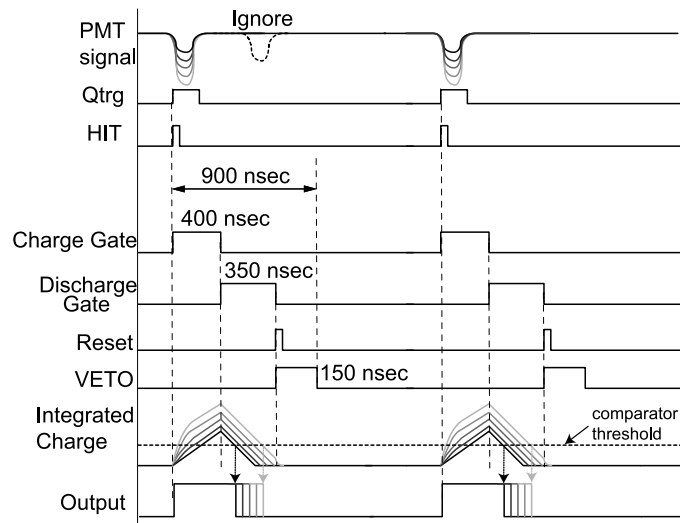


FIGURE 4.6: Diagram of the QTC operation. The PMT signal triggers charge integration, and this integrated charge is converted into a pulse length output. The operation has a 400 ns charge integration, and a 350 ns discharge time. Finally, there is a 150 ns veto time, totaling 900 ns for a PMT hit to be registered. In this time, between the initial integration and the end of the veto, any other hits on that PMT will be ignored. From [79].

The QTC output pulses are fed into a time to digital converter (TDC), which

digitizes the pulses' times and lengths. This information is then sent, via Ethernet, to the online data processing computers (online PCs). Each QBEE can transfer up to 11.8 MB/s of data. The online PCs collect the data from the QBEEs, and sort the PMT hit information by time. This information from all the PMTs is merged, and software triggering can be applied. The result of software triggering is a series of candidate events. The PMT hit information for each event is organized and written to disk. During normal detector operation, about 470 MB/s of data are produced by the PMTs, of which 9 MB/s is put into candidate events and written to disk [69].

4.4 Water and Air Purification

The SK tank water must be kept very pure for two main reasons. First, most contamination will reduce the transparency of the SK water. Better transparency means more light can be collected, and better event reconstruction is possible. Also, if the water transparency varies over time, this can lead to improperly calibrated energy reconstruction. Secondly, if radioactive contaminants get into the water, they can produce signals that look similar to neutrino events. There are two main systems to reduce these problems: the water purification system, and the radon-free air system.

The SK water is constantly being circulated and cleaned, and the purification system processes ~ 30 tons/hour. It uses filters and a reverse osmosis system to remove particulate contaminants, membrane and vacuum degasifiers to remove dissolved gasses (especially radon), and a cartridge polisher to remove heavy ions. The water is cooled to 13° to limit growth of bacteria, and a UV sterilizer kills any bacteria present. The source for SK water is the mine itself. More information on the water purification system can be found in [77].

Significant concentrations of radon are found in the mine, a product of uranium decay. Not only is it a health risk for SK workers, but it is a background for low

energy neutrino analyses. To counteract this, radon-free air is produced at a “radon hut” outside the mine entrance. Here, air from outside is collected, filtered, and then sent into the mine. It is circulated through the control room area, to the dome above the SK tank, and to parts of the water purification system. The system can flow $50 \text{ m}^3/\text{minute}$ [82], and the radon concentration in the air at SK is kept around $40 \text{ Bq}/\text{m}^3$, well below the level in the rest of the mine (which exceeds $1000 \text{ Bq}/\text{m}^3$ during the summer [83]). The World Health Organization recommends a limit of $100 \text{ Bq}/\text{m}^3$ to minimize health hazards [84]. The result is a low radioactive background rate in the SK water, safe air in the SK tank area, and water transparency of $\sim 100 \text{ m}$.

4.5 Atmospheric Reduction

This section describes SK atmospheric neutrino analysis; the reduction is somewhat different for T2K (see Section 4.10).

Further classification is required after event candidates are selected by the software triggers. This dissertation is focused on the high energy events, such as those from atmospheric neutrinos. These are studied by the atmospheric neutrino and proton decay (ATMPD) group at SK. The ATMPD software and algorithms were the basis for T2K analysis at SK. The high energy events are categorized into groups. These classifications include:

- **Fully Contained (FC):** The tracks of all charged particles in the event are contained within the inner detector (ID).
- **Partially Contained (PC):** The event begins in the ID, but at least one of the particles escapes and deposits energy in the outer detector (OD).
- **Upward Going Muon (UPMU):** A muon enters the detector from below,

passing through the OD. This is caused by an atmospheric neutrino interacting in the rock below the detector.

Events not classified into any of these categories (including cosmic-ray muon events) can be saved for use for calibration or other studies.

The process of selecting these categories of events from the full data set is called reduction. Only fully contained events have been used (so far) in T2K analysis, so PC and UPMU events will be ignored for now. For more information on all reduction processes, see [85], [61], [46], and [86].

FC reduction is a five-step process. The first two steps generally select good events in the ID, with few hit PMTs in the OD, and no over-active PMTs in the ID. The third step is specifically designed to reject cosmic-ray muons, with checks of muon fits and more sophisticated and tighter cuts on the OD. Also, muons which travel through the regions of the OD where the PMT cable bundles leave the detector are less likely to be detected. Thus, there are plastic scintillator counters on the cable bundles, and these counters are used in the third FC reduction step to further reject cosmic muons.

The fourth reduction step is the flasher cut. PMTs which malfunction may produce light due to internal electrical discharges. These PMTs are called flashers. The flasher light may be incorrectly reconstructed as a neutrino event. SK shift members are careful to look for signs that PMTs have become flashers, and disable them, but it is still possible for some flasher events to enter the dataset. These are removed by the flasher cut, which is largely based on a pattern matching cut. Flashers tend to produce the same pattern of light, over and over. Thus, the charge pattern correlation is computed between data events, and events which are highly correlated with each other are rejected as flashers.

The fifth FC reduction step uses tighter cuts and more sophisticated fitting to

remove more muon events. Finally, a fully contained fiducial volume (FCFV) sample can be made. Here, a vertex cut is made to require that the reconstructed vertex is inside of 200 cm from the ID walls, and a 30 MeV cut is made on visible energy (the reconstructed event energy, assuming electron tracks). After this, a rate of ~ 10 FC FV events per day remain. This system selects good events without the need for human judgement of event quality, though experts will look at the FC events, as well as the events rejected in the final FC reduction steps, to ensure that the process is working properly.

4.6 Reconstruction

ATMPD reconstruction of events is performed using software known as “APfit”. This program runs through several steps, refining the reconstruction, and adding more information about the event. The basic principle is that the event vertex is found using PMT timing information, the number of rings (each from a charged particle) is counted using a Hough transformation-based algorithm coupled with a likelihood, the PID is determined with the ring topology (fuzziness), and momentum is found via look-up table based on the total corrected charge measured. The full procedure is detailed in the following subsections. More information on reconstruction can be found in papers ([85]), theses ([46] and [86]), and proceedings ([87]).

4.6.1 *Vertex Finding*

The first piece of APfit is called “autofit”. First, it is assumed that all ID light is produced at a single point. After subtracting the time-of-flight (TOF) to each PMT, a distribution of residual PMT hit times is constructed. The hypothetical vertex is varied, and the point where the residual time distribution best fits a Gaussian is treated as the event vertex. Then, a preliminary direction is computed by taking the vector sum of the vectors to each PMT, weighted by the PMT charge.

Now, the direction and Cherenkov angle are varied to find an optimal fit to a Cherenkov ring edge. This is done by analyzing the charge distribution as a function of opening angle, for different directions. After this, the vertex can be re-fit, this time assuming photons are emitted along the path of the particle.

4.6.2 Ring Counting

Now that the vertex is well defined, a method based on the Hough transform [88] is used to count the number of rings. By assuming a fixed vertex and 42° rings, the PMT space can be converted into a (θ, ϕ) space, where peaks in the distribution correspond to ring candidates. These candidates are evaluated, one at a time, in order of the size of their Hough transform peaks.

The evaluation involves constructing two likelihoods based on expected ring parameters and the PMT charge information. One likelihood is for a single ring, the other is for the two-ring case. If the likelihood is better in the two-ring case, that ring is considered found, and the process is repeated for a third ring. This will continue until up to five rings are identified. Ring information for previously identified rings is not modified by subsequent rings.

4.6.3 Particle ID

Each ring will be identified as e -like (showering) or μ -like (non-showering) based on their charge pattern. A likelihood method is used for each ring, comparing the charge profile to a template for an e -like or μ -like ring. Examples of e - and μ -like events are shown in Figure 4.7. In addition to the charge pattern likelihood, the measured Cherenkov angle can be used to add additional PID discrimination for low energy muons, provided they are single-ring events.

The event displays such as those in Figure 4.7 are common for displaying SK data. The SK cylinder wall is “unrolled” and is represented by the large rectangle.

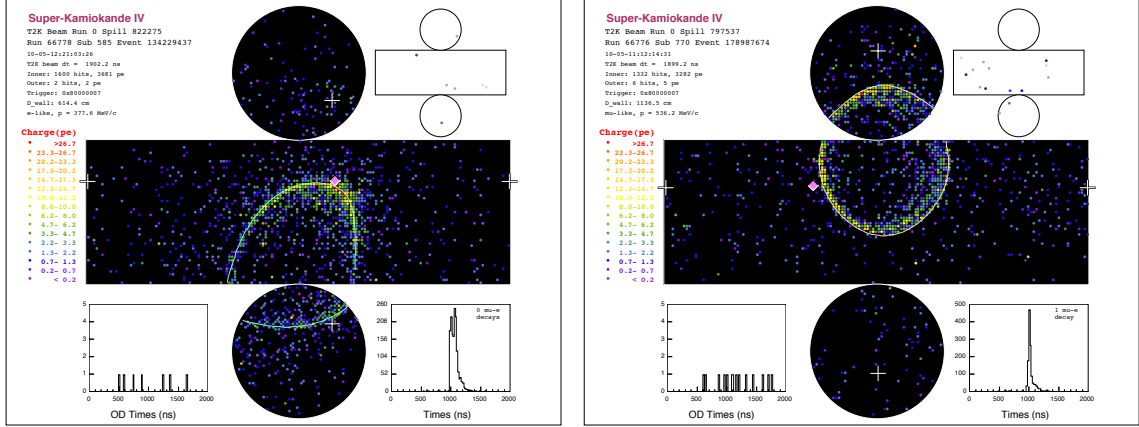


FIGURE 4.7: Event displays showing examples of e -like (left) and μ -like (right) rings. The color scale indicates charge. Thin lines showing the reconstructed rings are drawn.

The circle above and below this rectangle are the top and bottom of the detector, respectively. The large cylinder projection is the ID, and the smaller one on the top right is the OD. The dots are PMT hits. The color and size of the dots may vary to indicate timing or charge, and will be defined on the specific event display. These are data events taken during SK-IV, and specifically from T2K.

Now that the PID is established, for single-ring events only, an additional correction to the vertex can be performed. For single-ring events, as the Cherenkov light traveled mainly in the particle direction, the vertex resolution along that direction may be poor. To improve the vertex resolution, a fitter called MS-fit is run. In this fit, the PID is taken into account for computing the charge expectation, along with effects such as water scattering of light. The fitter iteratively modifies the vertex and direction of the single ring until a new optimal vertex is found.

4.6.4 Decay Electron Tagging

Up to this point, only PMT hits from a narrow time window around the event would be considered. The typical time window is from -50 ns to 250 ns around the peak of the TOF-subtracted hit time distribution. This time window will be used for

momentum reconstruction as well.

The decay electron tagging searches outside of this window. The 40 μs period after an event is checked for peaks in the number of hit PMTs over time. The peaks are required to be larger than might be expected by statistical fluctuation of background noise (if near the parent event, the background includes the parent event and its scattered light). This peak indicates a decay-e candidate.

If such a peak is found, a sliding 50 ns time window is utilized. The TOF-subtracted time window which maximizes the number of hit PMTs is used, and this number of PMTs is referred to as N_{50} . If $N_{50} > 30$, the total number of photoelectrons is less than 2000 p.e., and the time to the parent event is greater than 600 ns, a fit can be made on that electron. These good decay-e candidates have their vertex and direction reconstructed using a low energy fitting algorithm called “Kai-fit”. The decay-e candidates which do not satisfy these criteria cannot be properly fit, but are still counted as decay-e candidates, and can help identify neutrino events as having a muon.

This tagging procedure is quite effective, tagging 95% of μ^+ events, and 81% of μ^- events. The inefficiency mostly stems from decays very close to the parent event. The reason that μ^- has lower efficiency is because μ^- is captured into an oxygen nucleus around 18% of the time [89]. If the muon is captured, the oxygen will emit a low energy gamma which has a lower reconstruction efficiency than most decay electrons.

4.6.5 Momentum Reconstruction

Returning to the primary event (time window of -50 ns to +250 ns), the next step is momentum reconstruction. For multi-ring events, the first step is to separate the rings. The charge from each PMT is divided into a fraction assigned to each ring, according to the expected charge distributions for each ring. This is important when

the rings overlap. To do this, it is assumed that the distribution of light should be uniform azimuthally around the particle direction, and is only a function of the opening angle.

Now that each ring has its own charge pattern, this charge is corrected for several effects. Light attenuation in water, PMT acceptance as a function of angle, reflection off PMTs, PMT gain, and water scattering are all considered. The PMT gain and water quality parameters are measured frequently (as they vary over time), and so the corrections will be dependent on when the event occurred. The result is a corrected charge called RTOT. RTOT is converted into a momentum using a lookup table generated from MC.

4.6.6 Ring Number Correction

A final step is applied to reject low energy rings which overlap considerably with higher energy ones. These are usually mis-reconstructed “fake” rings, or sub-structure from particle showers. After these rings are removed, the ring separation and momentum reconstruction must be repeated. At this point, the main reconstruction is complete, the final vertex is known, as well as the PID, direction, and momentum for each found ring.

4.6.7 POLfit

After the main reconstruction, a special algorithm is applied to deal with hidden rings, particularly from π^0 s. The typical case is a NC π^0 interaction ($\nu + N \rightarrow \nu + N + \pi^0$). A π^0 is very short-lived, and will decay to a pair of high energy photons ($\pi^0 \rightarrow \gamma\gamma$). Depending on the momentum of the π^0 at decay time, the energy of those decay γ s may be very asymmetric, or very overlapping. In either of these cases, it is possible that one of the γ rings will not be found by reconstruction. This can cause a NC π^0 event to be reconstructed as a CC single-electron event. For T2K,

where CC single-electron events are the signal, this is a serious problem.

The solution is a special algorithm called POLfit (Pattern Of Light fitter) [90]. This algorithm is designed to be applied to single-ring e -like events, on the assumption that a second ring exists, but was not picked up by ring-counting (or was rejected by ring number correction). The principle is to find the most likely second ring candidate, reconstruct the invariant mass of the two rings, and see if the invariant mass is similar to that of a π^0 ($m_{\pi^0} = 135$ MeV). This invariant mass can be used in event selection (and is for T2K).

The inputs to POLfit are the direction of the single found ring, the vertex, and the charge observed for each PMT (within the standard time window). The vertex and direction of the first ring are assumed to be fixed. A θ - ϕ spherical coordinate system is used to define the direction of the second ring, and the PMT hit information is used to orient this coordinate system so that it is most likely that both rings will be on the “equator”. The 2-ring system is now defined by three parameters: θ and ϕ direction of the second ring, and fraction of total energy in the second ring (γ , which can range from 0 to 0.5). This grid is the start of the second ring search.

POLfit uses a library called expq (expected charge) to quickly produce charge patterns for a given (θ, ϕ, γ) . For the first step, the direct light from a hypothetical particle with some momentum and direction is computed assuming an axially symmetric Cherenkov cone coming only from the vertex. The direct light to each PMT is computed from a lookup table generated from MC, as a function of particle (e or γ), momentum, distance to PMT, and angle to particle direction. This is a fast computation.

A more difficult problem is calculating scattered light. To simplify this, the detector is split into patches for a scattering matrix (see Figure 4.8). The matrix elements $\langle i, j \rangle$ indicate how much direct light on a patch i would be scattered to patch j . The direct and scattered patches need not be the same (the matrix does not

need to be square). The patches are considered in polar coordinates from the vertex, and only need to be calculated once for the vertex, rather than for each (θ, ϕ, γ) triple. This is a computationally efficient approximation. The matrix elements are computed by integrating scattered light along the path from the vertex to the center of patch i . This integration incorporates the water parameters.

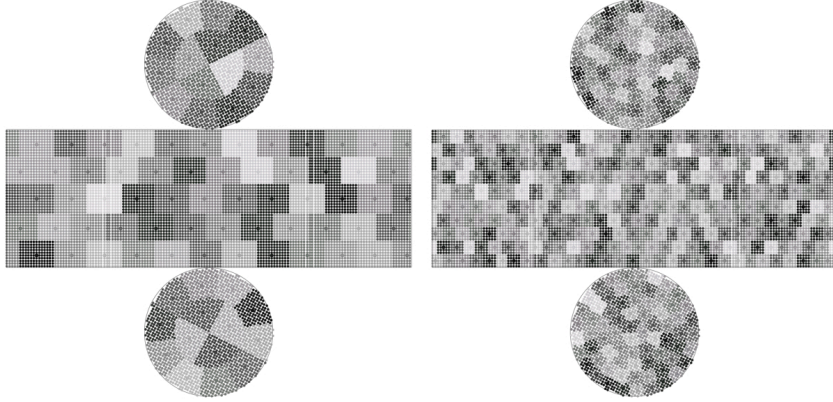


FIGURE 4.8: Example of “patches” for POLfit scattered light calculation. The left SK diagram shows different direct light patches i , and the right SK diagram shows different scattered light patches j . The different number of patches for direct and scattered light will cause the light scattering matrix to be non-square.

The scattering matrix is used to compute scattered light for each PMT patch, based on the direct light already calculated. Then, some corrections are made for effects such as the solid angle taken up by each PMT, and the scattered light is added to the direct light for each PMT. Finally, the full light pattern is normalized so that the total charge on this pattern produced is the same as the total observed charge.

Using the expq library to produce these charge patterns, the search for the second ring is done entirely using a pattern matching likelihood. The observed pattern is compared to the computed hypothetical one, and a likelihood is constructed based on the observed and computed charge for each PMT. This process is done for each point in the (θ, ϕ, γ) grid, and for both a single electron ($1e$) assumption and a two-

photon (π^0) assumption. The log likelihood difference between these is what POLfit will optimize over.

$$\Delta L(\theta, \phi, \gamma) = \log(L_{\pi^0}(\theta, \phi, \gamma)) - \log(L_{1e}(\theta, \phi, \gamma)) \quad (4.3)$$

The likelihood difference can be calculated for any value of (θ, ϕ, γ) , and this likelihood difference function is put into MIGRAD, a minimizer from the MINUIT package of fitters [91]. This algorithm works by following derivatives to the minimum. The initial (θ, ϕ, γ) grid helps keep MIGRAD from getting caught on a local minimum. MIGRAD will iteratively compute likelihoods for different (θ, ϕ, γ) until the optimum ΔL is found.

With the optimal (θ, ϕ, γ) , an invariant mass can be computed, but there is one more step, which was added in 2010. Using the direction of the new ring in the 2-ring event, the standard APfit momentum reconstruction is performed. This momentum reconstruction takes into account more details (such as PMT reflection) than POLfit does with expq. The new momenta for the two rings are then used to compute an invariant mass, which is the primary output of POLfit.

Note that this invariant mass will be produced for the optimal ΔL , regardless of whether ΔL is positive (more π^0 -like than e -like). For most cases where there truly is no second ring, POLfit will return a very small invariant mass, either because it finds the second ring on top of the first, or because the second ring has a very low energy.

4.7 Calibration

Information on SK calibration can be found in [77], though this is primarily for the SK-I period. Updated descriptions of the calibration procedures come from talks given by the SK calibration group at collaboration meetings.

4.7.1 Timing

The PMT relative timing is critical for vertex-finding. The relative timing of the PMTs is found by producing a TQ (Time-Charge) map for each PMT. A diffuser ball is lowered to the center of the tank, connected to a fiber optic cable. A laser pulse is split, with one part going to a trigger PMT, the other to the diffuser ball. The diffuser ball spreads the light isotropically. For each PMT, the measured time and charge are recorded. This process is repeated many times for different intensities. The time and charge information is plotted together for each PMT, making what is called a TQ map (Figure 4.9). The measured time will depend on the measured charge, because higher charge will reach the discriminator threshold faster. The TQ map for each PMT is fitted, and this fitted function is used to correct timing offsets, and in the detector simulation.

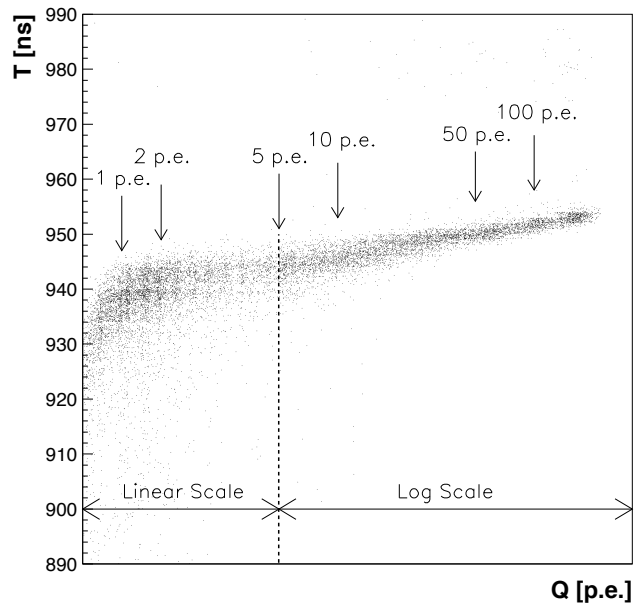


FIGURE 4.9: Example TQ map for SK-I (from [77]). The TQ map for SK-IV is similar to this.

4.7.2 PMT Gain

PMTs are like snowflakes – no two are exactly alike. Consequently, the HV on each PMT must be set separately so that the gains of all PMTs are uniform. The first step of this process was done before PMT installation (prior to SK-II and SK-III). Some 420 PMTs were specially tested to find HV values so that they would produce the same charge for a test light intensity. These special PMTs were placed in columns and positions on the tank top and bottom so that they would sample all parts of the detector, and all distances from the center. At the beginning of SK-II and SK-III, a diffuser ball was used to flash xenon lamp light isotropically through the tank. The charge measured by each PMT was recorded, and an expected charge could be computed based on water attenuation and distance, with the calibration PMTs used to help set the expected charge. After this, the HV on each PMT was adjusted to bring the measured charge in line with that of the other PMTs.

This first step roughly calibrated the PMTs to have equal sensitivity, but they would not have equal gains. The xenon calibration is relatively high energy, with multiple photoelectrons per PMT per trigger. The charge measured in this case is proportional to (4.4),

$$Q_{\text{obs}} \propto N_{\text{photon}} \times QE \times \text{gain}. \quad (4.4)$$

Thus, the gain and quantum efficiency (QE) should be disentangled. This is done by performing two calibration measurements. First, a calibration is done with intense light (many photons per trigger per PMT), measuring the total charge for each PMT. Then, a calibration is done with very dim light (zero or one photon per trigger per PMT), measuring the hit rate for each PMT. Thus, we have:

$$N_{\text{hit}} \propto N_{\text{photon}} \times QE \quad (4.5)$$

and so we find

$$\text{gain} \propto \frac{Q_{\text{obs}}}{N_{\text{hit}}}. \quad (4.6)$$

In this way (and averaging over many measurements), the relative gain for each PMT can be measured. These relative gains are applied to data to correct the gain measurements on a PMT by PMT basis.

Finally, the overall PMT gain must be calculated. This is done by finding the peak in the charge distribution for measurement of a single photo-electron (SPE). This is done using a weak, but high-rate light source (the same one that was used for the hit rate measurement above). This is the Ni+Cf ball, which uses the spontaneous fission of ^{252}Cf as a neutron source to drive the neutron capture/gamma emission reaction $^{58}\text{Ni}(n,\gamma)^{59}\text{Ni}$. The emitted gammas will have an energy of ~ 9 MeV, a low enough energy to have few multiply-hit PMTs. From this, the SPE distribution can be plotted and fitted, and a value for converting picoCoulombs of charge from PMTs to photoelectrons (pC2pe) can be found. The value measured for SK-IV in 2008 was 2.658 pC/p.e. [92]. The global pC2pe value can be combined with the relative PMT gain measurement to find a final pC2pe table, converting measured charge for each PMT to photoelectrons (which are then converted to momentum). A further correction is made for the non-linearity of PMT response with many p.e. at once.

The effect of PMT quantum efficiency is dealt with by measuring it and adding it to the detector simulation (it is not specifically corrected in reconstruction). The measurement is made using the Ni+Cf ball data, with a calculation for the number of hits expected at each PMT based on water attenuation, wall reflection, and PMT acceptance (due to angle).

The time variation of PMT gain is measured using the peak of the dark noise data charge distribution. Dark noise refers to PMT hits which occur spontaneously. Generally, dark noise is not large enough to cause problems with reconstruction, but

the single-hit charge is a good indicator of PMT gain, and it can be measured without the need for any calibration light sources or dependence on water transparency. Thus, fitting the peak of the dark noise charge spectrum over time provides the time dependence of gain. These data agree well with periodic Ni+Cf calibration. One interesting feature of the PMT gain is that it is generally increasing, at $\sim 2.5\%$ /year. The cause of this increase is not clear, though it is easy to correct for.

4.7.3 Water Parameters

There are two main measurements of SK water parameters. First is the scattering measurement. This is done using eight light injectors positioned around the SK tank (2 on top, 5 on the side, one on the bottom). These light injectors direct laser light of various wavelengths into the tank. Most of the light will be detected by the PMTs opposite the injector, but some of it will be scattered, and detected by other PMTs. By analyzing the distributions of this scattered light, fits can be done for symmetric scattering, (like Rayleigh scattering, light is equally scattered forward and back), asymmetric scattering (like Mie scattering), and absorption. These measured parameters are inputs to the detector simulation. Of the three parameters, only absorption changes over time in a way that significantly affects reconstruction.

The next is the attenuation measurement. Of course, attenuation is a function of scattering and absorption, but it is measured separately. This is measured using the vertical through-going muon data.

The cosmic ray muon rate at SK is ~ 3 Hz. Muons starting at the top of the tank and going out the bottom, always staying at least 2 m from the wall, and traveling almost straight down are selected. Such events can have their entrance and exit points easily reconstructed. Such muons will emit light uniformly along the track, and so the expected light detected by each PMT can be easily computed based on distance, gain, angular acceptance, and attenuation length. By comparing expected

light to measured, it is possible to measure the attenuation length.

As muons are always passing through the detector, this attenuation length is computed approximately daily. The attenuation measurement is included as a correction in the reconstructed momentum calculation (as part of the corrected charge, RTOT). It is not used for MC, as the MC attenuation is not varied.

4.7.4 *Auto-Calibration*

An auto-calibration trigger fires at SK every 1 s. This trigger will be accompanied by a flash of the diffuser ball at the center of the tank, or the firing of one of the water calibration lasers. The laser information is used to compute water parameters, as described in Section 4.7.3. The diffuser ball information is used to check the time dependence of gain and the TQ-map, although this is only a cross-check, and is not used in reconstruction. The diffuser ball flashes are also useful for finding bad PMTs, as the tank should be lit up uniformly.

The auto-calibration trigger is normally fired at 1 Hz. However, if there is a T2K trigger signal present (1 ms wide), the auto-calibration trigger will not fire. This does not adversely affect the calibration, and it prevents any calibration events from entering the T2K data.

4.8 Energy Scale

The calibration data described so far is used to compute the corrected charge for each PMT, measured in photo-electrons. There is a look-up table which converts this to reconstructed momentum (Section 4.6.5), based on MC. Thus, an extra calibration step is necessary to ensure that the MC p.e. to momentum conversion is accurate. This is done with the energy scale calibration. Four different samples are used for this work.

4.8.1 Multi-GeV Stopping Muons

Much like the vertical through-going muons, vertical stopping muons can also be used for calibration. The reconstructed muon momentum divided by the distance the muon travels in the detector (range) should be constant. The muon start point can be reconstructed fairly normally, and the end point can be found by the location of the decay electron. The ratio of momentum over range is checked between data and MC for several bins in range.

4.8.2 Sub-GeV Stopping Muons

For highly relativistic particles ($\beta \approx 1$), the Cherenkov ring angle is constant, with $1/\cos\theta_c = \beta n$. However, for low energy muons, the angle dependence on momentum is measurable (See Figure 4.10). Thus, the Cherenkov angle provides a means of measuring the muon momentum which does not depend on the water transparency or PMT gain. Thus, the energy scale is set by comparing the muon momentum, as measured by Cherenkov angle, with the muon momentum measured by corrected charge.

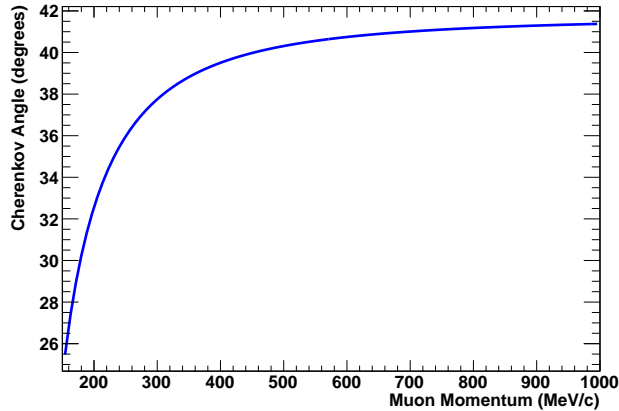


FIGURE 4.10: Plot of the Cherenkov angle in water as a function of muon momentum.

4.8.3 π^0 Mass

Atmospheric neutrinos with NC π^0 interactions provide a useful calibration point. The invariant mass of the π^0 is 135 MeV, and this provides a stable point to check against. Because atmospheric neutrino interactions are much less frequent than cosmic ray muons, this is a low-statistics calibration.

4.8.4 Decay Electrons

Cosmic ray muons stopping in the detector will decay into electrons with a decay time of 2.2 μ s (unless a μ^- is captured by a nucleus). The decay spectrum, the Michel spectrum [93], is well known. Checking the mean of this spectrum provides another calibration point for energy, this time at lower energies, \sim 20-50 MeV.

4.8.5 Absolute Scale

The goal of absolute energy scale calibration is to keep data and MC matching, and to keep them both corresponding to known physical quantities, such as the π^0 mass and Michel spectrum. The four calibration samples are checked, and the MC/Data ratios are checked. If the MC and data do not agree, several steps can be taken to bring them back into agreement. A general scaling factor for all energies can be applied, the global PMT gain can be adjusted, or the MC photon production rate can be changed. Also, past corrections to the RTOT calculation have been motivated by differences in the energy scale for different calibration samples.

The absolute scale checks are best done when the MC water parameters are tuned to the time period of the data. This was done for the stopping muon and decay electron samples, which have high statistics. For the sub-GeV muons and π^0 s, the full SK-IV dataset is used, to obtain sufficient statistics. Examples of absolute energy scale calibration plots are shown in Figures 4.11, 4.12, 4.13, and 4.14. A summary plot of the absolute energy scale calibration is in Figure 4.15.

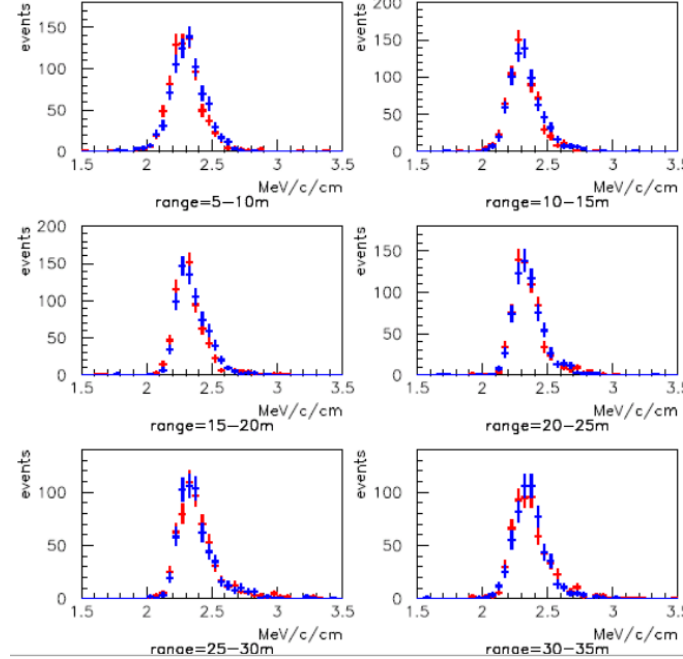


FIGURE 4.11: Plots from the SK-IV absolute energy scale check with high energy stopping muons. The six histograms are of momentum (reconstructed from p.e.)/range for stopping muons, in six bins of range. Red is data, blue is MC. Data are from April 2009, and MC is tuned to the measured water parameters from that month.

4.8.6 Time Variation

The multi-GeV stopping muons and decay electrons have high enough statistics to be used to check time variation, as well as absolute scale. Figure 4.16 shows the time variation of stopping muon momentum/range and decay electron momentum as a function of time, through SK-IV. The generation of these plots has been automated. Each bin is approximately 10 days. These plots show that the conditions of the SK detector are such that the energy scale is stable over time.

4.9 Additional Decay Electron Studies

In addition to the absolute scale and time variation measurements, the decay electrons have been also used for other calibration checks, including PID time variation,

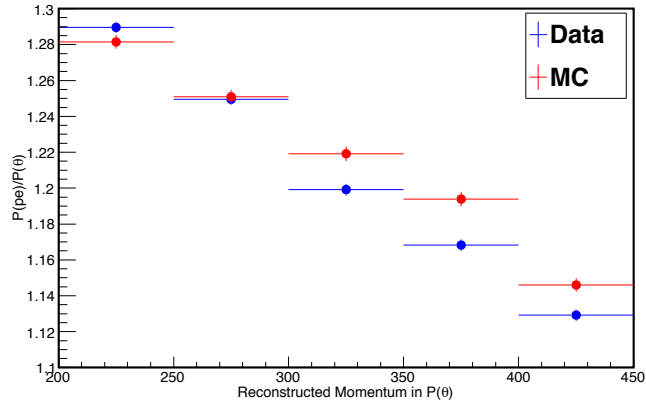


FIGURE 4.12: The sub-GeV stopping muon check is done by taking the ratio of momentum reconstructed from p.e. and the momentum reconstructed from the Cherenkov angle. This ratio is plotted for data (blue) and MC (red). The plot is binned by reconstructed momentum from the Cherenkov angle. Error bars are statistical. The ratio of MC/data for this ratio is used for the absolute energy scale check.

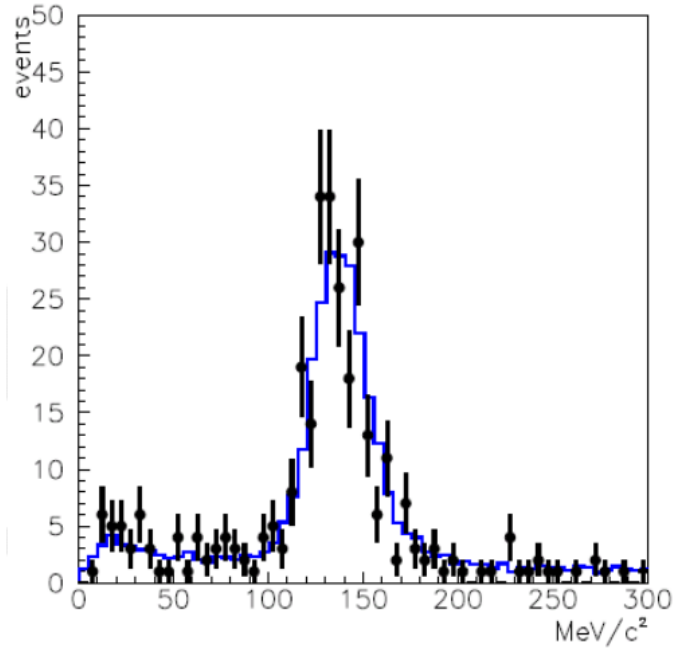


FIGURE 4.13: Plot of the π^0 invariant mass peak from SK-IV atmospheric data and MC. The black points are data, and the blue histogram is MC. Error bars are statistical.

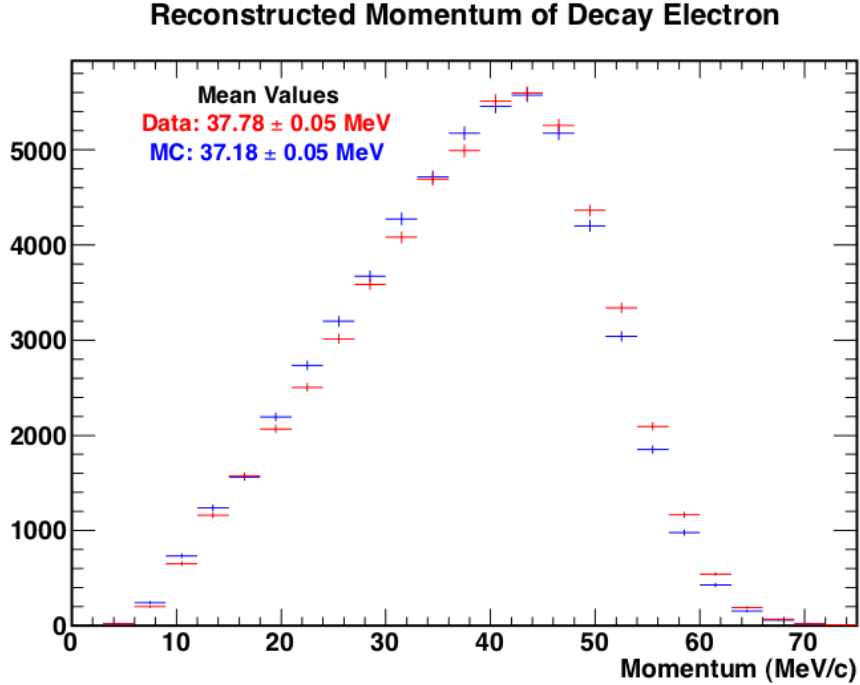


FIGURE 4.14: Reconstructed decay electron momentum spectrum. Red points are data, blue are MC. Error bars are statistical. The difference in the mean of the data and MC spectra is used in the absolute energy scale check. Data are from April 2009, and MC is tuned to the water parameters from that month.

position variation and direction variation of energy scale. These are discussed in more detail in Appendix A.

4.10 T2K-Specific Operation

During the entire T2K run period, SK has been in the SK-IV stage, following the 2008 electronics upgrade. This hardware upgrade (along with the switch to software triggers) allows for continuous data taking, with software-only triggers. In order to avoid any possible triggering bias, a 1 ms wide window of data is recorded for every T2K beam spill. The trigger signal is sent from J-PARC to SK via a private network connection, with the GPS time of the spill. The beam arrival time is computed by adding the neutrino time-of-flight ($\sim 984 \mu\text{s}$) and correcting for any hardware delays.

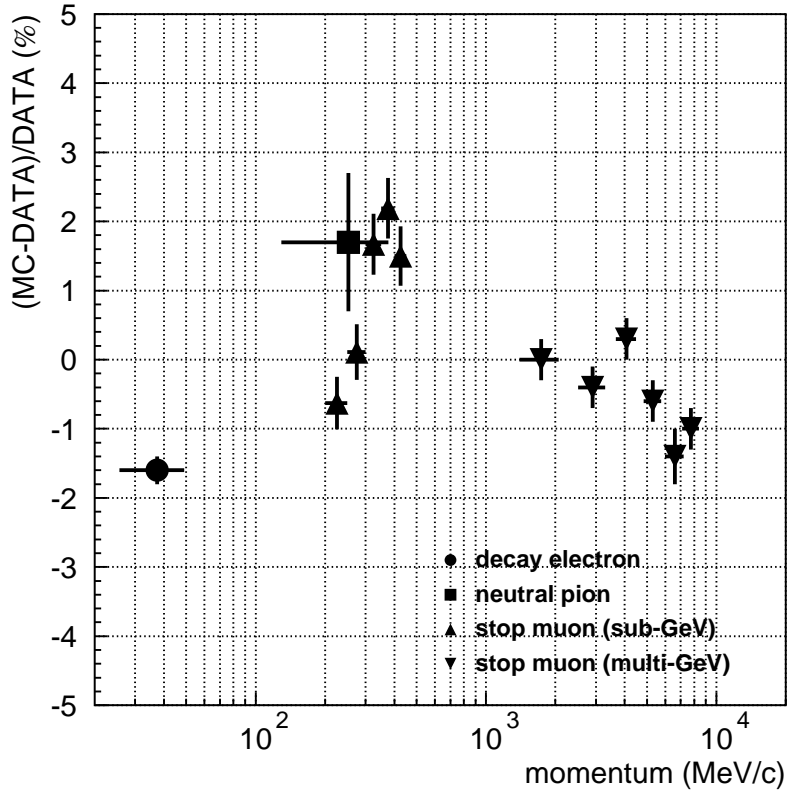


FIGURE 4.15: The $(MC/Data - 1)$ values for each of the absolute energy scale checks (Figures 4.11, 4.12, 4.13 and 4.14). Error bars are statistical. The maximum deviation from unity is $+2.19\%/ -1.6\%$. Overall, there is good agreement between data and MC.

All data within $\pm 500 \mu s$ of this arrival time are saved. The timing of SK PMT hits is checked with a redundant clock system at SK, using two independent GPS modules as well as a rubidium atomic clock. This redundancy ensured that a stable clock was always available to tag events. Events in the $-2 \sim +10 \mu s$ timing window around the expected beam arrival time are considered on-timing events, and are used in data analysis. The rest of the recorded data is used for background studies and as a backup in case the beam and SK clocks become de-synchronized.

After the 1 ms time window of data was recorded, offline software triggers and

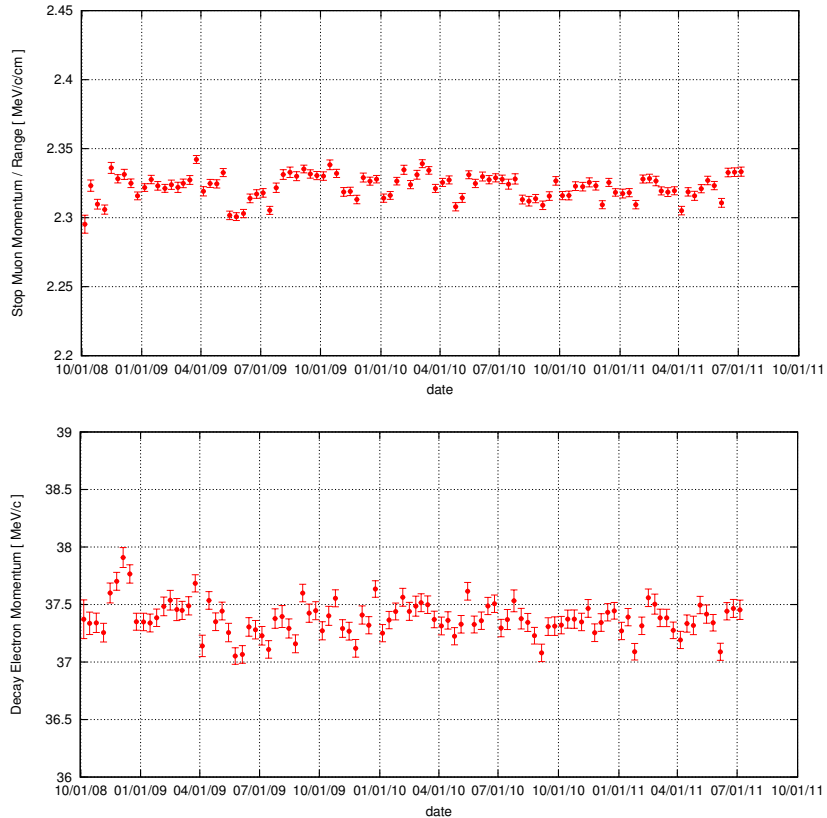


FIGURE 4.16: Plot of the time variation of energy scale through SK-IV. The upper profile histogram shows stopping muon momentum/range, and the lower one shows decay electron momentum. These plots were automatically generated by the automatic energy scale time variation process.

selection cuts are applied [94]. There are five cuts to select good spills at SK from the beam good spills. All together, less than 1% of good beam spills were rejected by these cuts [95].

1. **SK DAQ alive:** Obviously, the SK DAQ must be operational.
2. **Bad subrun cut:** As with ATMPD studies, entire subruns of data may be rejected if there is a problem. The most common problem is a persistent flasher. This cut rejected $\sim 0.5\%$ of spills in the T2K data period described in this dissertation.

3. **DAQ/GPS error cut:** It is required that a minimum number of hits is seen in both the ID and OD in the 1 ms time window. This threshold (48000 and 6000 hits for the ID and OD, respectively) is low enough that it will be achieved from the dark hit rate, unless there is a DAQ problem. Also, at least one of the GPS units must be free of an error flag. No spills were rejected for this reason in the data sample used for this dissertation.

4. **Special data block cut:** The SK data are recorded in units of 17 μs blocks. There are two kinds of special data blocks, however. One is the “pedestal block”, for taking pedestal data from the ADCs. The other is the “TDC reset block”, which resets some counters on the TDC chips. The TDC reset blocks and pedestal blocks are produced once every 4096 and 65536 blocks, respectively. If a spill contains an event in the on-timing range $-2 \sim +10 \mu\text{s}$ from the leading edge of the arrival time), then no TDC reset block or pedestal block is allowed to overlap in a range of $-5 \sim +35 \mu\text{s}$ from the first (or likely only) on-timing event of that spill. If there is such an overlap, the spill is considered bad. If there are no on-timing events, then this same overlap cut is applied for $-5 \sim +35 \mu\text{s}$ from the arrival time leading edge (which is at the center of the $-500 \sim +500 \mu\text{s}$ T2K window). This cut rejects only 0.08% of spills.

5. **Pre-activity cut:** To prevent decay electrons from earlier stopped muons and pions from affecting events, it is required that there be no detector activity in the 100 μs before an event in the beam spill on-timing range ($-2 \sim +10 \mu\text{s}$ from the leading edge of the arrival time). If there is no event in that spill, it is required that there is no detector activity in the 100 μs before the on-timing range begins. This cut rejects 0.3% of spills.

The next step is event classification. Here, events from good spills are classified

as calibration (rejected), outer detector (OD), low energy (LE), flasher, or fully contained (FC). For this analysis, only FC events are used for the ν_e appearance analysis.

First, calibration events are rejected. Then, events with a hit cluster in the OD with 16 or more hits are classified as OD events. Remaining events are tested with two cuts for low energy classification. If the event has less than 200 p.e. of charge in the ID in a 300 ns time window ($PE_{300} < 200$), it is classified as LE. Also, if more than half of the total charge in this 300 ns time window comes from a single PMT, the event will be classified as LE ($PE_{MAX}/PE_{300} > 0.5$). This cut effectively rejects backgrounds due to radioactivity near the PMTs without harming signal efficiency. Finally, the usual SK flasher cut (See Section 4.5) using pattern matching is applied to reject flasher event candidates. Events passing all these cuts are classified as FC event candidates, and are studied in the ν_e appearance analysis (Section 5.2).

Analysis Overview and Development

This chapter includes an overview of the ν_e appearance analysis strategy, and some details on the work done by the author on analysis development. The analysis optimization and sensitivity studies were significant contributions from the author to the overall analysis.

5.1 Analysis Strategy

As described previously, T2K works by sending a ν_μ beam from J-PARC 295 km to SK. The goal is to find evidence for electron neutrino appearance in the beam. The off-axis angle is chosen to maximize ν_e appearance and ν_μ disappearance, so backgrounds are minimized. The near detector measures the beam before oscillation, and this measurement is used to normalize the expectation at the SK. By comparing the expected number of ν_e events for various oscillation parameters to the observed number, it is possible to measure θ_{13} .

The key, then, is to identify ν_e events at SK with high efficiency and low background. The basic idea is to select charged current quasi-elastic (CCQE) ν_e events

at SK. This interaction mode,

$$\nu_e + n \rightarrow e^- + p, \quad (5.1)$$

is the dominant interaction at the peak T2K beam energies. These events will appear at SK as a single electron-like ring. The selection cuts are designed to isolate this sample. The spectrum of neutrinos at SK (with oscillation, before any cuts, computed from MC) is plotted in Figure 5.1.

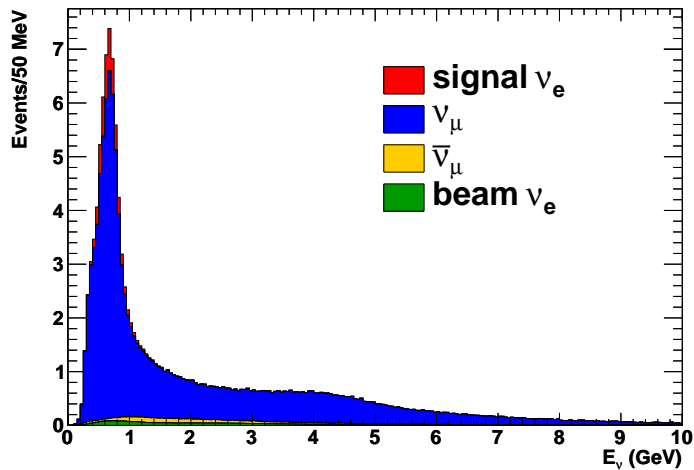


FIGURE 5.1: Expected spectrum of neutrino events at SK, colored by neutrino type. This is computed from MC, with oscillation (Table 5.1) applied. The signal events are calculated assuming $\sin^2 2\theta_{13} = 0.1$. No selection cuts are applied, and the plot is normalized to the expectation of events in the SK true FV with beam time corresponding to the T2K analysis described in this dissertation.

The primary backgrounds at SK are beam (intrinsic) ν_e events, and neutral current (NC) π^0 events.

Intrinsic ν_e events come from the ν_e contamination in the beam. This contamination is due to ν_e production at the beam source, from muon decay or kaon production (as described in Section 3.3). This contamination is difficult to reject, because it is true ν_e in the beam, though some level of rejection is possible by rejecting high energy

ν_e events. The kaon-produced ν_e tend to have energies above that of the oscillation maximum where most the signal is expected.

NC π^0 backgrounds are a problem only when the event is mis-reconstructed. The interaction goes as

$$\begin{aligned} \nu_\mu + p &\rightarrow \pi^0 + \nu_\mu + p \\ &\hookrightarrow \gamma + (\gamma), \end{aligned} \tag{5.2}$$

where one of the two γ s is not properly reconstructed, either due to overlap with the first, or because it has much lower energy than the first (asymmetric π^0 decay, see Figure 5.2). This case leaves a single reconstructed e -like ring, mimicking signal.

The cuts used to select signal and reject these backgrounds are described in Section 5.2, and the optimization procedure used to select these cuts is described in Section 5.4.

5.2 Far Detector Selection Cuts

Signal candidate events are selected using the tools developed for SK ATMPD analysis. The goal is to distinguish between the $\nu_\mu \rightarrow \nu_e$ signal events and all backgrounds. The primary signal is CCQE events, for which the neutrino energy can be reconstructed using only the outgoing lepton and the beam direction (this reconstruction only works for CCQE events, which appear as a single e -like ring at SK).

For all the plots in this section (and much of this dissertation), the oscillation parameters in Table 5.1 will be used. Some of these parameters were chosen for convenience (normal hierarchy and δ_{CP} are chosen arbitrarily), and others come from measurements. The choice of $\sin^2 2\theta_{13} = 0.1$ is loosely based on a 90% limit [62]. The multi-experiment fit measurements of $\sin^2 2\theta_{12}$, $\sin^2 2\theta_{23}$, Δm_{21}^2 , and Δm_{32}^2 can be found in [96]. The earth density is based loosely on a simplified version [61] of the PREM model of earth density [97]. The true value of earth density very near the

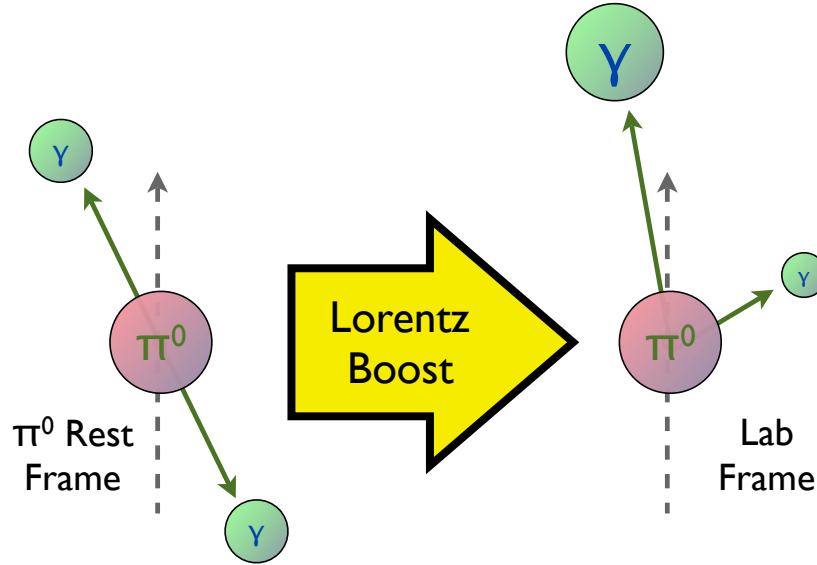


FIGURE 5.2: Illustration of asymmetric π^0 decay. In the center of mass frame (rest frame) of the π^0 , the decay to a pair of gammas must be symmetric and back-to-back, based on conservation of momentum. When the decay is considered in the lab frame (via Lorentz boost), the decay may not be symmetric. The figure shows a π^0 decay in the rest frame on the left, with the π^0 direction of motion (in the lab frame) indicated by the dashed arrow. Both gammas will have equal energy. On the right, the same decay is considered in the lab frame. Here, the π^0 has significant momentum, and thus the decay gammas are boosted. The more forward-going gamma has a much higher energy than the less forward-going one. This is an example of an asymmetric π^0 decay, which is a significant background for T2K.

surface is slightly lower than this, but T2K is insensitive to small changes in matter density with the MSW effect (See Figure 2.8).

These cuts were optimized for the T2K analysis. The optimization procedure is described in Section 5.4. The cuts are as follows:

5.2.1 Fiducial Volume Cut

This cut requires that the reconstructed vertex be within the fiducial volume (FV), the region of the ID at least 200 cm from the PMT wall boundary. This cut removes events which occur close to the detector wall, which are difficult to reconstruct prop-

Table 5.1: Table of oscillation parameter values used in this analysis except where otherwise specified.

Parameter	Value
Δm_{21}^2	$7.6 \times 10^{-5} \text{eV}^2$
Δm_{32}^2	$2.4 \times 10^{-3} \text{eV}^2$
$\sin^2 2\theta_{12}$	0.8704
$\sin^2 2\theta_{23}$	1.0
$\sin^2 2\theta_{13}$	0.1 (or 0.0)
δ_{CP}	0.0
Mass Hierarchy	normal
ν travel distance	295 km
Earth Density	3.2g/cm^3

erly. It also helps reduce backgrounds from radioactive materials in the PMTs and their casings [98], as well as events originating outside the inner detector. This cut is applied as part of the normal FC reduction, and is not unique to the T2K ν_e analysis.

5.2.2 Fully Contained Cut

This cut requires that the number of hit PMTs in the OD PMT cluster with the highest charge is less than 16. This is the standard cut for SK-III and SK-IV to define an event as “Fully Contained”. This both removes events which start outside the detector (like cosmic rays) and events where the lepton leaves the detector, making it impossible to measure its energy. This cut is applied as part of the normal FC reduction, and is not unique to the T2K ν_e analysis. The FC reduction also requires an event to have a visible energy of at least 30 MeV to qualify as fully contained. This cut is applied in the reduction, though this $E_{\text{vis}} > 30 \text{ MeV}$ selection is redundant with the later visible energy cut.

5.2.3 Single Ring Cut

This cut requires that only one ring be found in the ID using the regular ring-finding algorithms. CCQE events usually have only one ring, as the proton produced will

rarely exceed Cherenkov threshold (the proton Cherenkov threshold is 1.06 GeV/c), and the only other product particle is the lepton corresponding to the neutrino. This cut, and the expected number of rings distribution, are shown in Figure 5.3.

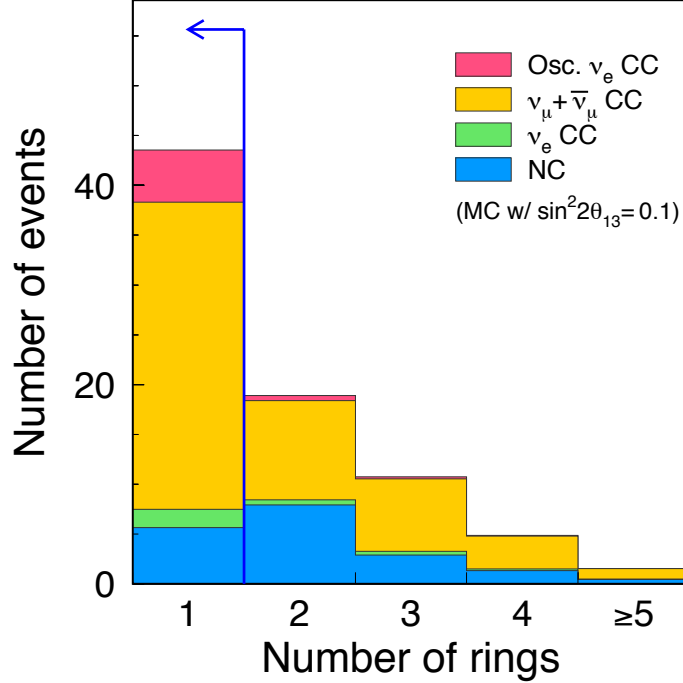


FIGURE 5.3: Expected number of rings distribution for T2K FCFV events. The blue arrow shows the selection cut for ν_e appearance, $N_{\text{ring}} = 1$. The MC is normalized to the Run I + Run II POT., and three flavor oscillation is applied with the parameters from Table 5.1. The MC was generated as described in Section 6.1, and scaled up by 1.036, according to the ND280 measurement result. The different event types are indicated by the colors shown in the legend.

5.2.4 *E-like Ring Cut*

This cut requires that the single ring found be e -like. A CCQE ν_e interaction will produce a single electron, which should leave an e -like ring. Most CC ν_μ interactions will leave a μ -like ring. The standard SK PID parameter is used to make this cut. This cut, and the expected PID distribution, are shown in Figure 5.4.

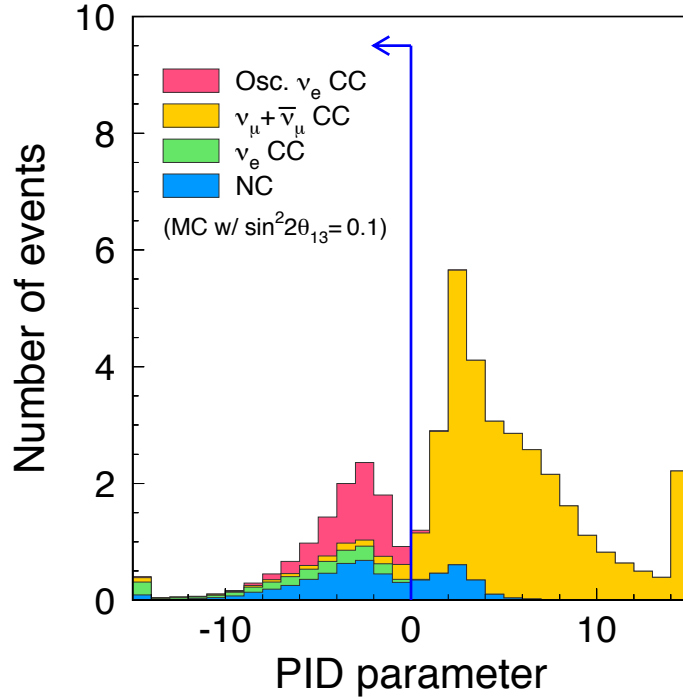


FIGURE 5.4: Expected PID distribution for T2K FCFV single-ring (1R) events. The blue arrow shows the selection cut for ν_e appearance. Higher PID parameter indicates μ -like, lower PID parameter indicates e -like. For MC and normalization details, see the caption for Figure 5.3.

5.2.5 Visible Energy Cut

This cut requires that the total visible energy in the inner detector (ID) be greater than 100 MeV. The visible energy is defined as the sum of the reconstructed energies of all the rings identified in the ID, assuming the rings were produced by electrons. This cut removes low energy and noise events, such as Michel electrons from cosmic rays muons or low energy muon neutrinos, radioactive decay, or solar neutrino events. This cut, and the expected visible energy distribution, are shown in Figure 5.5.

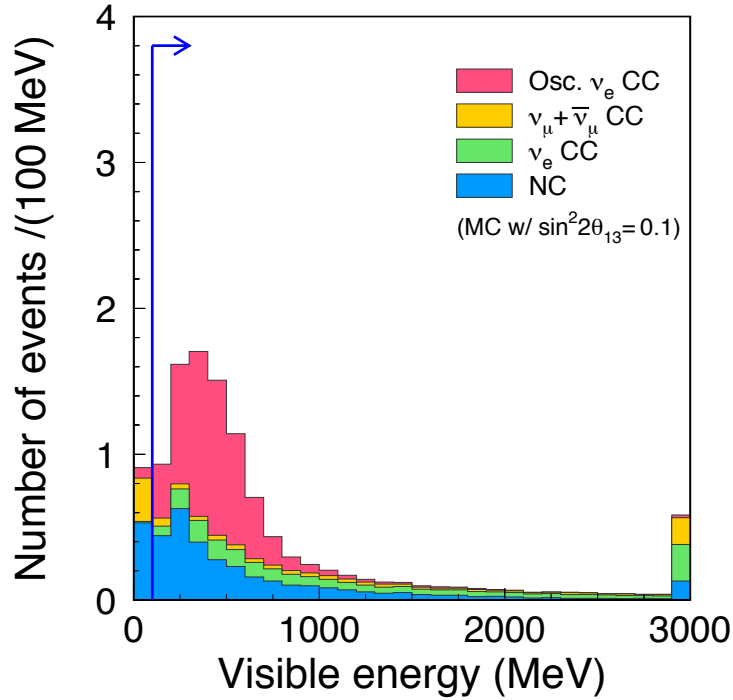


FIGURE 5.5: Expected visible energy distribution for T2K FCFV 1R e -like events. The blue arrow shows the selection cut for ν_e appearance, $E_{\text{vis}} > 100$ MeV. For MC and normalization details, see the caption for Figure 5.3.

5.2.6 $\mu \rightarrow e$ Decay Cut

This cut uses the standard SK decay electron finding algorithms to search for $\mu \rightarrow e$ decays. If any decay electrons are found, the event is rejected. The decay electrons are measured as a delayed electron signal. This cut, and the expected number of decay electrons distribution, are shown in Figure 5.6. Decay electrons are a reliable indicator that a muon or pion was present in the event, even if the decaying particle was below Cherenkov threshold. This cut rejects non-CCQE events and CC ν_μ events.

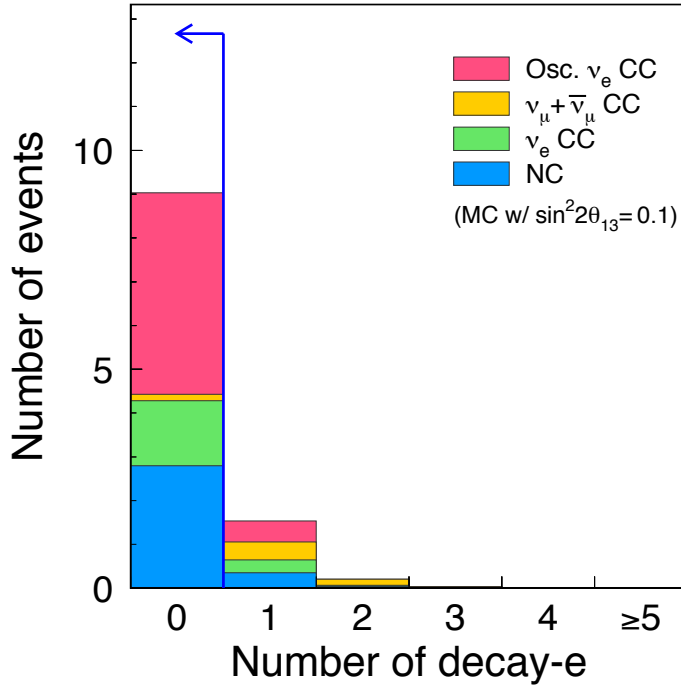


FIGURE 5.6: Expected number of decay electrons distribution for T2K FCFV 1R e -like events with $E_{\text{vis}} > 100$ MeV. The blue arrow shows the selection cut for ν_e appearance, $N_{\mu \rightarrow e} = 0$. For MC and normalization details, see the caption for Figure 5.3.

5.2.7 POLfit π^0 Mass Cut

The POLfit algorithm (Section 4.6.7) is used to search for a possible second gamma ring, which could indicate a π^0 event, the primary reducible background for T2K. The best-matching second-ring candidate is found, and the invariant mass is computed. The invariant mass is required to be below 105 MeV. Events without a real second ring tend to have low invariant masses. This cut, and the expected POLfit π^0 invariant mass distribution, are shown in Figure 5.7.

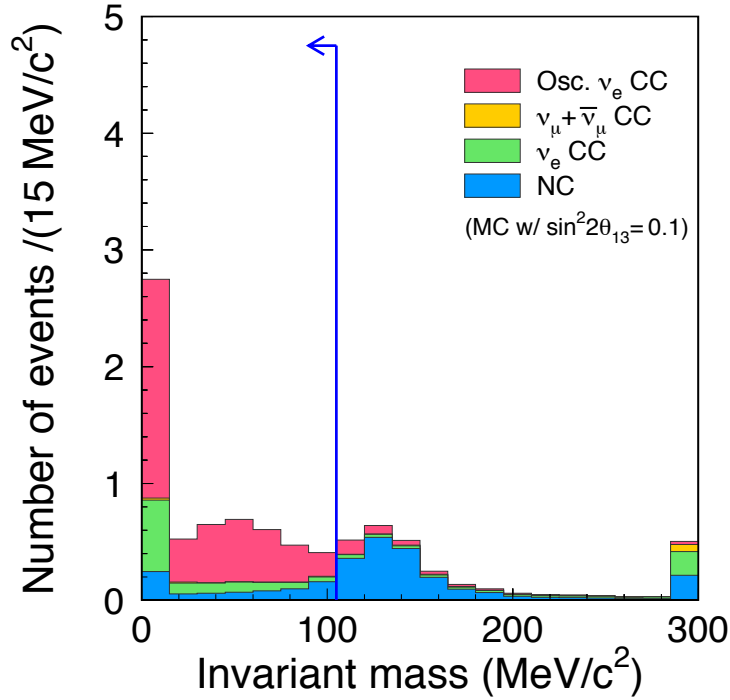


FIGURE 5.7: Expected POLfit π^0 invariant mass distribution for T2K FCFV 1R e -like events with $E_{\text{vis}} > 100$ MeV and no decay electrons. The blue arrow shows the selection cut for ν_e appearance, $m_{\pi^0} < 105$ MeV/ c^2 . For MC and normalization details, see the caption for Figure 5.3.

5.2.8 Reconstructed Neutrino Energy Cut

The neutrino energy can be calculated for a CCQE interaction ($\nu_l + n \rightarrow l^- + p$) using the reconstructed lepton momentum and the known neutrino beam direction. Accurate reconstruction is difficult or impossible for other interaction modes. The proton will usually stay below Cherenkov threshold for T2K, but the known beam direction makes its reconstruction unnecessary. A simplified version of the reconstructed momentum is given in Equation 5.3, where m_N and m_l are the masses of the nucleon and lepton, respectively, E_l is the lepton energy, p_l is the lepton momentum, and $\theta_{\nu-l}$ is the angle between the lepton momentum and the known neutrino beam direction. A more detailed formula is given in Equation 5.4, where the proton

and neutron mass are given separately (we assume a neutrino interaction; reverse m_p and m_n for an antineutrino interaction), and we assume a nuclear potential V of 27 MeV. The formula considering the nuclear potential (Equation 5.4) was used for analysis. These formulas are:

$$E_\nu = \frac{m_N E_l - m_l^2/2}{m_N - E_l + p_l \cos \theta_{\nu-l}} \quad (5.3)$$

and

$$E_\nu = \frac{2(m_n - V) E_l - m_l^2 + 2m_n V - V^2 + m_p^2 - m_n^2}{2(m_n - V - E_l + p_l \cos \theta_{\nu-l})}. \quad (5.4)$$

In order to better identify signal events, we require $0 \text{ MeV} < E_\nu^{\text{rec}} < 1250 \text{ MeV}$. The intrinsic background ν_e produced from kaon decay tend to have higher energies. This cut, and the expected E_ν^{rec} distribution, are shown in Figure 5.8.

The efficiency for event selection (estimated from MC) for each step is shown in Table 5.2.

Table 5.2: Efficiency for ν_e selection after each cut. All efficiencies are measured against the number of interactions inside the SK true FV, before reduction or any cuts. Efficiencies are given separately for ν_μ CC, intrinsic ν_e CC, NC, and the $\nu_\mu \rightarrow \nu_e$ CC signal. The low FC FV efficiency for NC events is due to the FC requirement that $E_{\text{vis}} > 30 \text{ MeV}$, which rejects nearly all NC elastic interactions. All MC CC samples include three-flavor oscillations for $\sin^2 2\theta_{13}=0.1$ and $\delta_{\text{CP}} = 0$, in the normal hierarchy.

	$\nu_\mu + \bar{\nu}_\mu$ CC	ν_e CC	NC	$\nu_\mu \rightarrow \nu_e$ CC
(1) FC FV	77.9%	95.7%	25.8%	96.3%
(2) single ring	45.8%	60.1%	8.0%	83.8%
(3) e -like	1.5%	59.7%	5.2%	82.8%
(4) $E_{\text{vis}} > 100 \text{ MeV}$	1.1%	59.3%	4.5%	81.6%
(5) no delayed electron	0.21%	48.8%	3.9%	73.9%
(6) non- π^0 -like	0.06%	34.8%	1.1%	68.3%
(7) $E_\nu^{\text{rec}} < 1250 \text{ MeV}$	0.04%	23.1%	0.86%	66.1%

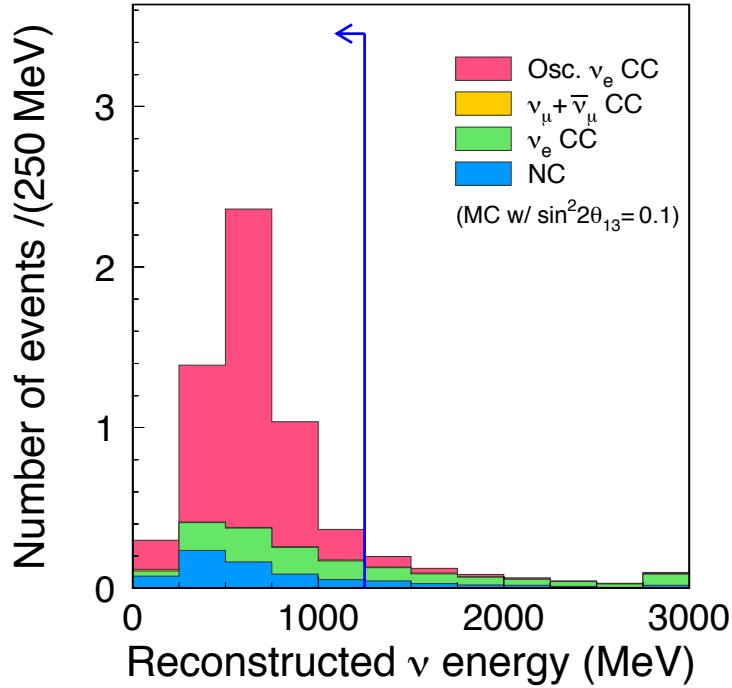


FIGURE 5.8: Expected reconstructed neutrino energy distribution for T2K FCFV 1R e -like events with $E_{\text{vis}} > 100$ MeV, no decay electrons, and $m_{\pi^0} < 105$ MeV/ c^2 . The blue arrow shows the selection cut for ν_e appearance, $0 \text{ MeV} < E_{\nu}^{\text{rec}} < 1250$ MeV. For MC and normalization details, see the caption for Figure 5.3.

The application of these selection cuts described here to data is found in Chapter 8. Sections 5.3 and 5.4 describe the analysis sensitivity and optimization, and Chapters 6 and 7 describe the specific inputs to the analysis and systematic errors, respectively.

5.3 Sensitivity and Discovery Potential

For purposes of cut optimization, planning future beam time allocation, and comparing different experiments, it is useful to have a measure of the experimental sensitivity to oscillation parameters. This was done in three ways for this analysis.

First is the upper limit sensitivity (Section 5.3.1). This is a measure of the average

upper limit on $\sin^2 2\theta_{13}$ which will be set, assuming that $\sin^2 2\theta_{13} = 0$. In effect, this answers the question “if there really is only background, how tight a limit will be set?” Next is discovery potential (Section 5.3.2). This is a measure of what the true value of $\sin^2 2\theta_{13}$ must be so that the experiment is likely to exclude $\sin^2 2\theta_{13} = 0$ at the 90% CL.

Both sensitivity and discovery potential are computed using the full analysis technique (Section 8.4). For cases where a quick estimate of sensitivity is all that is needed (for example, in cut optimization), a simplified sensitivity calculation (Section 5.4.1) is used.

5.3.1 Upper Limit Sensitivity

The sensitivity calculation is made by taking the average upper limit using the full computation method, assuming $\sin^2 2\theta_{13} = 0$. The exact background point we choose is $\sin^2 2\theta_{13} = 0.0$, $\delta_{CP} = 0$, $|\Delta m_{32}^2| = 2.4 \times 10^{-3} \text{ eV}^2$. We do it separately for normal and inverted hierarchy. The UL (Upper Limit) is parameterized by an expected number of events. That is, the value of \hat{N}_{exp} at the point where the limit contour lies (for a particular Δm^2 or δ_{CP}).

The averaging procedure is performed separately for every horizontal band on the plot (that is, for each grid value of δ_{CP} or Δm_{32}^2). If there is no upper limit contour for a fixed value of Δm^2 or δ_{CP} , we will assume the upper limit \hat{N}_{exp} to occur at $\sin^2 2\theta_{13} = 1.0$, the physical boundary. For every horizontal band on the plot, we do the following averaging procedure:

$$N_{\text{exp-sens}} = \sum_{N_{\text{obs}}=0}^{\infty} \text{Poisson}(N_{\text{obs}}, N_{\text{bkg}}) \times N_{\text{exp-UL}}(N_{\text{obs}}). \quad (5.5)$$

The locus of these average upper limit values makes the sensitivity curve. The condition that we bound the upper limit at $\sin^2 2\theta_{13} = 1.0$ can cause some points

where the sensitivity line is not smooth, but this is still an appropriate representation of the true sensitivity.

This definition of sensitivity is consistent with the one prescribed in [99], the average upper limit. There is an ambiguity about what kind of average to use, and the median is sometimes preferred over the mean. However, the traditional median is not useful here, as T2K has low statistics, especially at low exposures. The median upper limit for $\sin^2 2\theta_{13} = 0.0$ is then the upper limit for the median number of observed events for $\sin^2 2\theta_{13} = 0.0$. With 1.5 events expected, the median is not a useful statistic, as we cannot calculate limits for non-integer numbers of observed events. That is why the mean upper limit is taken.

5.3.2 Discovery Potential

The upper limit sensitivity is a measure of what the upper limit contour is when only background is measured. It is also important, however, to understand the behavior of the lower limit if some signal is measured. The key feature of the lower limit is when it stops being equal to $\sin^2 2\theta_{13} = 0.0$. Thus, we define the discovery potential as the true value of $\sin^2 2\theta_{13}$ such that, if the measurement were repeated many times, at least 50% of those measurements would have a lower limit of $\sin^2 2\theta_{13} > 0$. This procedure can be done for any CL.

The actual implementation of this procedure requires a background oscillation point to be chosen. As with sensitivity, we choose $\sin^2 2\theta_{13} = 0.0$, $\delta_{\text{CP}} = 0$, $\Delta m_{32}^2 = 2.4 \times 10^{-3} \text{ eV}^2$. The PDF for this point is shown in Figure 8.6. The Feldman-Cousins method (see Section 8.3.1) is used to select the values of N_{obs} for which this point is in the acceptance region for some CL. Then, all that is left is to find which oscillation points will produce a value of N_{obs} outside the acceptance region more than 50% of the time. This can be accomplished with a simple Poisson toy MC. Systematic effects can be neglected in this toy MC because they are already considered in the analysis

for $\sin^2 2\theta_{13} = 0$, and they are unlikely to alter the median value of N_{obs} at the tested oscillation point.

5.3.3 Sensitivity and Discovery Potential vs. Exposure

The upper limit sensitivity and discovery potential can be plotted as a function of integrated beam power. These plots give an idea of the expected sensitivity of the experiment. They are not an exact indicator of future sensitivity, because improvements to the analysis (both with more sophisticated techniques and reduction of systematic errors) will likely be implemented in the future. The plots here assume the analysis (Chapter 8) and systematic errors (Chapter 7) are as described in this dissertation. The 90% upper limit sensitivity, 3σ discovery potential, and 5σ discovery potential are plotted in Figure 5.9.

5.4 Far Detector Cut Optimization

The basics of event selection are fixed by our requirements to select candidate events which appear to be CCQE ν_e interactions, and which satisfy the conditions for good reconstruction at Super-K. There is some flexibility in the cuts used mainly to reduce backgrounds, however. Several possible methods for background (primarily π^0) rejection were considered, before the optimal cuts (Section 5.2) were found.

5.4.1 Rough Sensitivity Calculation

For a basic estimate of sensitivity which is quick to calculate, we use a simple analytic sensitivity calculation which depends only on the expected number of signal and background events, and a systematic error fraction. This is not a valid sensitivity at these statistics [100], but it behaves well enough for purposes of cut optimization.

At some point in oscillation space, we consider the expected signal (S) and background (B). We treat the distribution of expected events observed as a Gaussian,

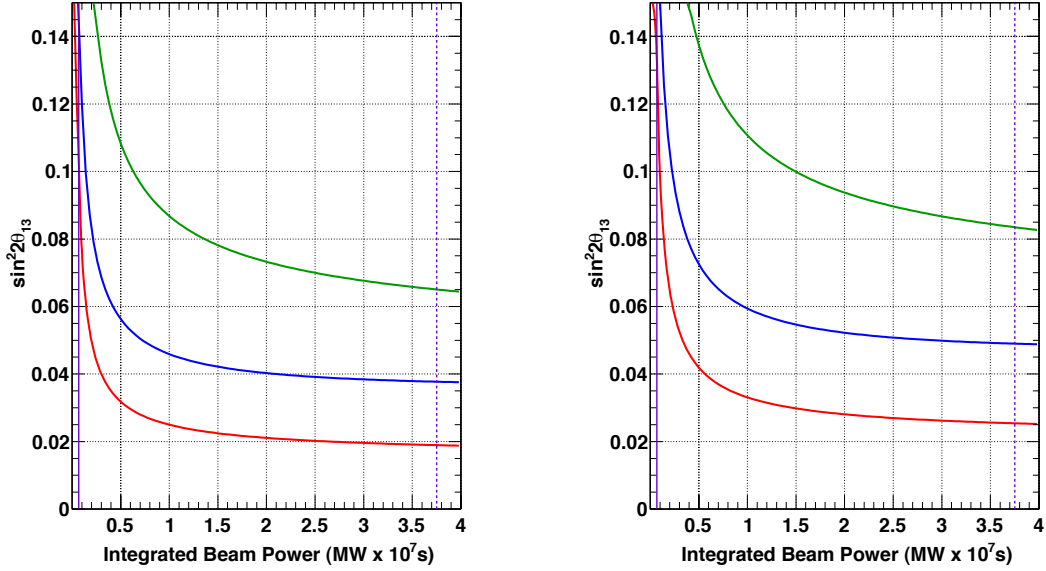


FIGURE 5.9: T2K sensitivity and discovery potential as a function of integrated beam power. The red curve is upper limit sensitivity at the 90% CL. The blue curve is discovery potential at 3σ , and the green curve is discovery potential at 5σ . The solid purple vertical line represents the delivered beam for Run I+II (the period analyzed for this dissertation), and the dashed purple line represents the final goal. The plot on the left (right) is for normal (inverted) hierarchy. The analysis method, systematic errors, and selection cuts from the Run I+II analysis are used. The following oscillation parameters are assumed: $\sin^2 2\theta_{12} = 0.8704$, $\sin^2 2\theta_{23} = 1.0$, $\Delta m_{21}^2 = 7.6 \times 10^{-5} \text{eV}^2$, $|\Delta m_{32}^2| = 2.4 \times 10^{-3} \text{eV}^2$, $\delta_{\text{CP}} = 0$.

with mean $S + B$ and a width given by the quadratic sum of the statistical and systematic errors. We consider an analysis to be sensitive at a point if 90% of the area of this Gaussian distribution is located above B . Otherwise, the analysis is not sensitive at that point. A term α is the fractional systematic uncertainty on background. This is illustrated in Figure 5.10. This condition, to be sensitive at an oscillation point, can be computed entirely analytically. The condition for an oscillation point to be in the sensitivity region is:

$$1.28 \geq \frac{S}{\sqrt{S + B + \alpha^2 B^2}}. \quad (5.6)$$

The locus of oscillation points where Equation 5.6 is satisfied exactly (with $=$ instead

of \geq) is where the rough sensitivity curve could be drawn. We term the value of $\sin^2 2\theta_{13}$ where this contour is drawn to be the rough sensitivity. This rough sensitivity was used extensively during cut optimization.

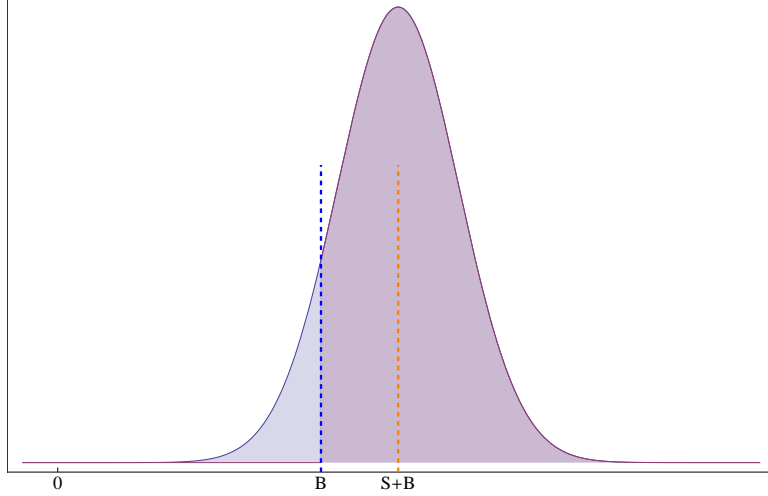


FIGURE 5.10: An example of the Gaussian approximation used in the rough sensitivity calculation. As some oscillation point, we have an expected mean signal (S) and background (B). We assume a probability distribution function about this mean $S+B$, with a width equal to the statistical error ($\sqrt{S+B}$) and systematic error (αB) added in quadrature. A region containing 90% of the total PDF area is computed from positive infinity integrating downward. The sensitivity contour will be drawn through the locus of points for which the left side of this 90% region lines up exactly with the background-only value (as it is in this figure).

5.4.2 Background Rejection Cut Candidates

The analysis cuts can be separated into two major categories: signal selection, and background rejection. The signal selection cuts are all included in the final analysis, and are described in detail in Section 5.2. These cuts include fully contained, fiducial volume, visible energy, single-ring, e -like, and no decay electron. These cuts isolate the signal (primarily $\nu_\mu \rightarrow \nu_e$ CCQE events) with minimal loss of efficiency. Modifications to these cuts were not considered by the author during the cut optimization process, due to their high efficiency and/or their ubiquitousness in SK analysis. See

[101] for an example of an investigation into modifying one of these cuts. Beyond these are cuts which may reject significant amounts of signal in the endeavor to reduce background. These cuts are the POLfit π^0 mass cut (Section 5.2.7), the reconstructed neutrino energy cut (Section 5.2.8), the POLfit π^0 Δ likelihood cut, and the lepton direction cut. The first two background rejection cuts were (after tuning) used in the final analysis, while the final two are described below and were not used. These were the four cuts to be optimized.

The POLfit Δ -likelihood cut is used to reject π^0 -like events. While POLfit calculates an invariant mass, it also computes a likelihood value which indicates whether an event is more π^0 -like or e -like. A cut can be made on the difference between these likelihoods. In earlier studies (for example, [102]), a cut value of $\log(L(\pi^0)) - \log(L(e)) < 80$ was used.

The lepton direction cut, also called the cosine cut, is used to reject neutral current coherent pion events. These events, where the neutrino interacts with the nucleus as a whole (coherent interaction), rather than individual nucleons, tend to be very forward directed. The very forward directed neutral pions will decay to gammas, which may also be forward directed, and the overlapping rings may make their individual identification difficult or impossible. This cosine cut may be used to remove the most forward directed rings, as they are often caused by NC coherent π^0 production. The cut, in its previous implementation (again, [102] is an example), was set to $\cos\theta_{\nu-e} < 0.9$, where $\theta_{\nu-e}$ is the angle between the beam direction and the reconstructed outgoing lepton direction.

5.4.3 Optimization Technique

The optimal set of selection cuts is actually a function of many factors, including systematic uncertainties from various sources, beam exposure, the actual value of θ_{13} , whether we would rather optimize for setting an upper limit or discovery potential,

and so on. In order to maintain an analysis unbiased by the data, this optimization was completed in April 2010, before the vast majority of the data were collected. At that time, the upcoming run's beam exposure and the systematic errors were unknown, along with many other analysis features. Thus, a major goal of this optimization was to show that the selection cuts would be robust against a wide range of exposures and other unknowns. Note that the optimization analysis presented here was done using MC available at the time, and not the version of MC used in the published analysis.

The choice of analysis method can have an effect on what the optimal cuts will be, but this effect is small. Thus, a simple figure of merit was chosen for optimization, the rough sensitivity calculation (Section 5.4.1).

The target exposure being optimized for was $50 \text{ kW} - 10^7 \text{ s}$ (1.04×10^{20} POT), while a range of $10 \sim 100 \text{ kW} - 10^7 \text{ s}$ was looked at. The first step is to reject unnecessary cuts. After that, we must test the effect of certain systematic errors on the optimization. The next step is to optimize the cuts with these systematic error constraints. The final step is to test for robustness against several factors.

5.4.4 Unnecessary Cut Rejection

The first cut rejected was the cosine cut. Earlier informal studies had shown that it had very limited utility. The first step was to simply test the sensitivity with and without this cut. Figure 5.11 shows the distribution of $\cos \theta_{\nu-e}$, assuming $\sin^2 2\theta_{13} = 0.1$. It is clear that the ν_μ background peaks at higher $\cos \theta_{\nu-e}$ than signal, but the difference is not so large as to be a truly effective discriminator. Any cut on this variable will reduce signal efficiency. The rough sensitivity as a function of exposure with and without this cut is shown in Figure 5.12. For the entire exposure range being considered, the cosine cut actually *reduces* sensitivity. Clearly, this cut is not useful here, at this level. Further studies showed no improvement to sensitivity at

these exposures, even if the cut value was moved to $\cos \theta_{\nu-e} < 0.99$. Under certain circumstances, at much higher exposures, this cut may be useful, but it is detrimental at low exposures, so we removed it.

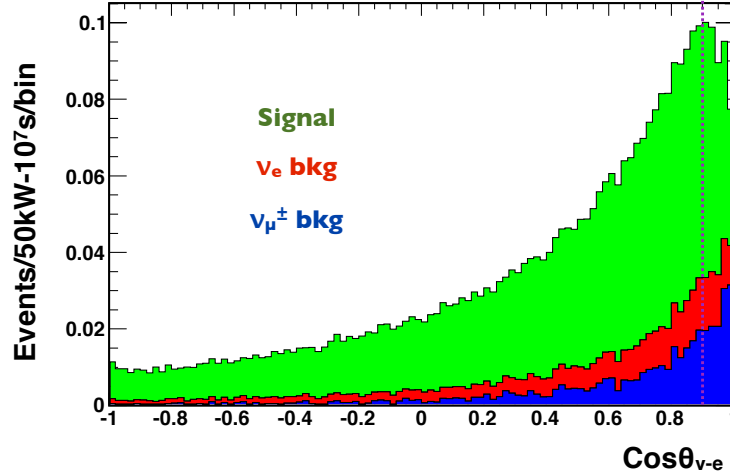


FIGURE 5.11: Distribution of MC events as a function of the cosine of the angle between the neutrino beam and the reconstructed lepton direction ($\cos \theta_{\nu-e}$). The standard signal selection cuts are all applied, and loose cut values for the background rejection cuts are also applied. The standard cosine cut value is indicated by the dashed line. Note that the signal component peaks at a lower $\cos \theta_{\nu-e}$ than background, but that the difference is small. The different MC components are indicated by colors in the stacked histogram, labelled on the plot. Green is signal, red is intrinsic ν_e background, blue is ν_μ and $\bar{\nu}_\mu$ background. We assume $\sin^2 2\theta_{13} = 0.1$.

The next cut checked was the POLfit Δ -likelihood (ΔL) cut. An earlier, less optimized version of POLfit was in use when the POLfit ΔL cut was proposed. With the improvements to POLfit, this cut became less necessary. Figure 5.13 shows the POLfit ΔL distribution, and the old cut value. There is clearly some merit to this cut, as the π^0 -like tail is dominated by background, though it is small. The effectiveness of this cut is best considered in conjunction with the POLfit mass cut, because both of them serve to reject π^0 events. Figure 5.14 shows the rough sensitivity (color axis) as a function of the POLfit mass cut value and POLfit ΔL cut value. The absolute best $\sin^2 2\theta_{13}$ sensitivity occurs around $\Delta L < 90$ and $m_{\pi^0} < 110$ MeV,

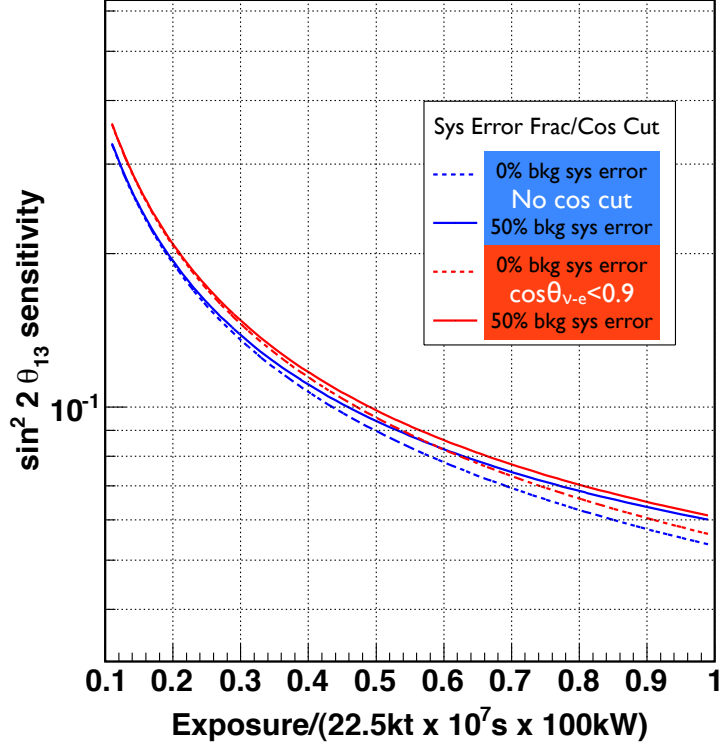


FIGURE 5.12: Comparison of rough sensitivity with and without the cosine cut, and with and without large systematic errors, as a function of beam exposure. Blue is without the cosine cut, red is with $\cos \theta_{\nu-e} < 0.90$. Solid lines have a 50% systematic error on background, dashed lines have no systematic errors. Note that, at no point, does adding the cosine cut improve the sensitivity. This plot only shows the first 2.7% of the full planned T2K integrated beam power.

though the decrease in sensitivity that comes from reducing the ΔL cut is negligible. The $\sin^2 2\theta_{13}$ sensitivity goes from ~ 0.094 at the optimal cut point to ~ 0.096 if we move to the top of the histogram, where the ΔL cut is so loose that it is meaningless. On the other hand, the right side of the histogram, where the m_{π^0} cut is negligible, has a dramatic loss in sensitivity no matter what the ΔL cut is. The conclusion is that the POLfit π^0 mass cut is essential, while the POLfit ΔL cut adds very little.

The drawbacks of using the POLfit ΔL cut include a new systematic error term associated with the cut, and a more complicated analysis. All of the other cuts are explainable in terms of physics quantities (kinematics), but ΔL corresponds only

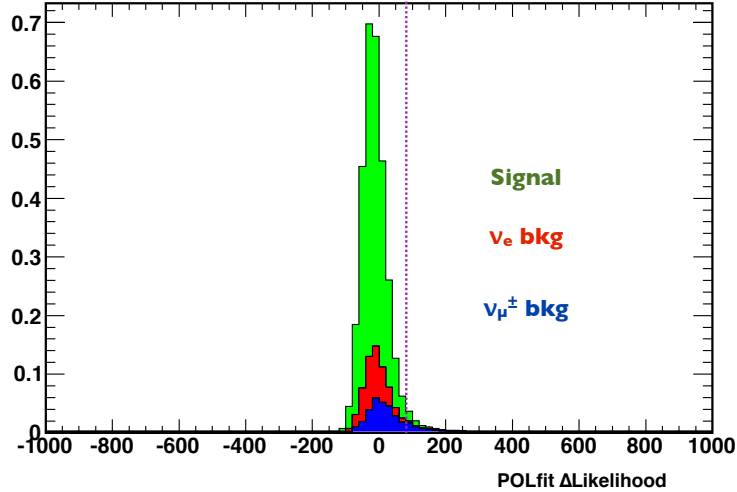


FIGURE 5.13: Distribution of MC events as a function of the POLfit Δ -Likelihood. The different MC components are indicated by colors in the stacked histogram, labelled on the plot. Green is signal, red is intrinsic ν_e background, blue is ν_μ and $\bar{\nu}_\mu$ background. We assume $\sin^2 2\theta_{13} = 0.1$. The dashed purple line indicates the old standard cut value. Lower values are events which are more e -like, higher values are more π^0 -like. Note that the standard cut ($\Delta L < 80$) removes background with very little signal efficiency loss, but that only a small fraction of the background is removed.

to a fitting likelihood. Without a kinematic basis for the cut, with the increased systematics due to its use, and with the minimal benefits from adding this cut, we chose to remove it from the set of cuts.

5.4.5 Systematic Considerations

The remaining background reduction cuts are the POLfit π^0 mass cut and the reconstructed neutrino energy cut. Without systematic uncertainties, it is simple to find an optimal cut value. However, systematic uncertainties are cause for concern, and we wanted to consider what kinds of problems could be introduced by introducing these cuts, and how systematics might affect the cut optimization.

The first check was for how the energy scale uncertainty might affect cut optimization. The SK energy scale error is of particular concern as it was dominant in

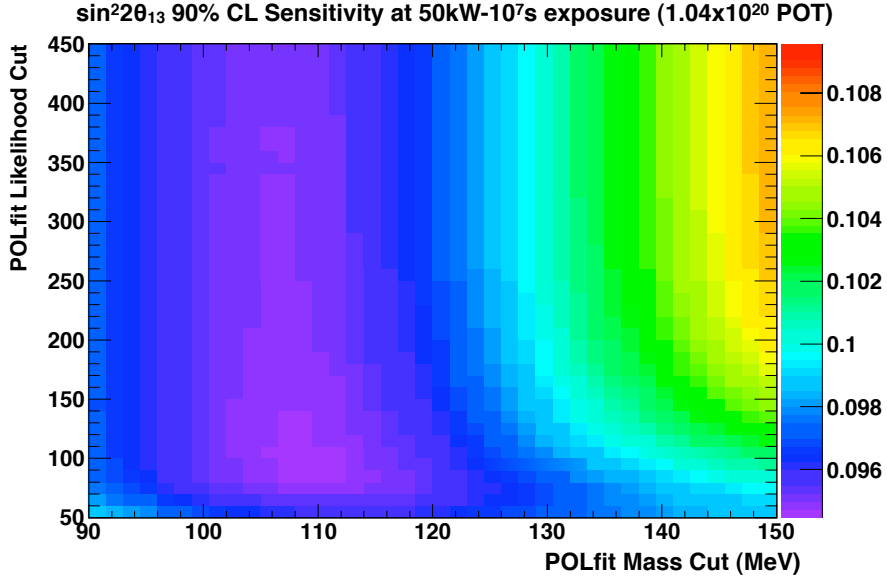


FIGURE 5.14: Rough sensitivity (in $\sin^2 2\theta_{13}$, color axis) as a function of the cut value for POLfit π^0 mass cut (x -axis) and POLFit Δ -Likelihood cut (y -axis). Purple is the best sensitivity (lowest value of $\sin^2 2\theta_{13}$). Note that the absolute minimum is not far from the local minimum at a very loose cut in ΔL , but it is quite a bit better than the local minimum at very loose cut in m_{π^0} . From this, we decided to use the mass cut, but reject the ΔL cut.

the K2K ν_μ disappearance analysis [55], and it can vary greatly with the selected cut values. The estimated energy scale error at the time was 1%, so the cut values were varied by $\pm 1\%$ in energy to see how the number of events remaining would change. This is illustrated in Figures 5.15 and 5.16.

The energy scale uncertainty will shift a POLfit mass cut of 110 MeV/ c^2 (at 50 kW – 10⁷s) by ± 1.1 MeV, changing the number of events passing all cuts by ~ 0.03 events, assuming $\sin^2 2\theta_{13} = 0.1$. This is a $\sim 1\%$ shift in the expected number of passing events. For background only, the uncertainty changes the number of events by $\sim 3\%$. A lower value of the POLfit mass cut would only decrease this energy scale shift. Thus, the effect of the energy scale uncertainty on the POLfit mass cut uncertainty is small enough to ignore for the optimization.

Both low and high cuts for a reconstructed energy window were considered, with

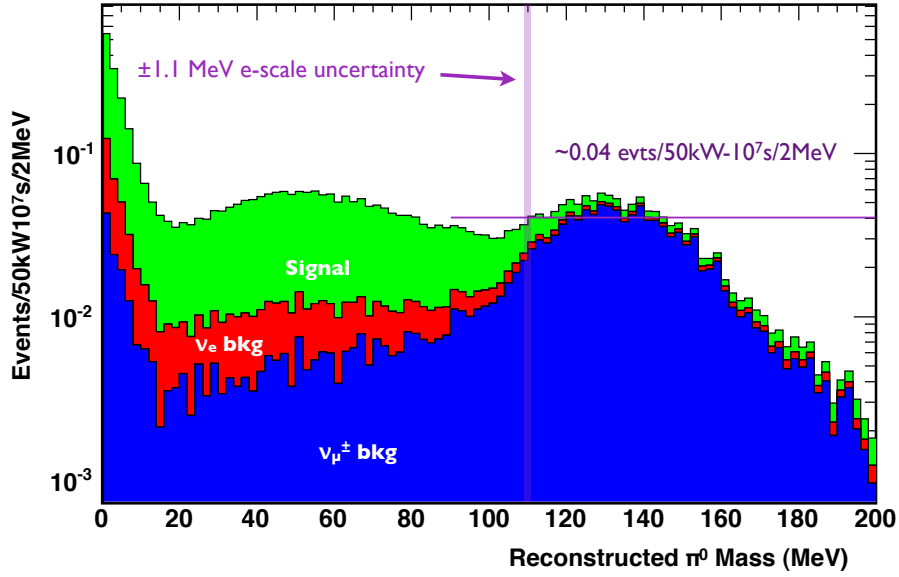


FIGURE 5.15: Distribution of MC events as a function of POLfit invariant mass. The MC has been oscillated with $\sin^2 2\theta_{13} = 0.1$, $\delta_{\text{CP}} = 0$ and $\Delta m^2 = 2.4 \times 10^{-3} \text{eV}^2$, and all cuts except the POLfit mass cut are applied. The events are divided into ν_μ and $\bar{\nu}_\mu$ background (nearly entirely NC, blue), beam ν_e background (red), and signal (green). This plot was generated using an older version of the MC than was used in the final analysis. The y-axis is log scale. A POLfit mass cut of 110 MeV/ c^2 is considered with a 1% energy scale uncertainty. The shift in number of events cut from a 1% energy scale shift is ~ 0.03 , approximately a 1% shift in the total number of events. If $\sin^2 2\theta_{13} = 0$, the shift would be closer to 3% of the total number of events. Either way, this shift is much smaller than other uncertainties, so we decided that the energy scale uncertainty should not affect the POLfit mass cut optimization.

an example window of (330 MeV, 1200 MeV) for this test. With this example window, the final reconstructed neutrino energy cut ($E_\nu^{\text{rec}} < 1250 \text{MeV}$) is even less affected by the energy scale uncertainty. With the 1% energy scale uncertainty, this results in a shift of ~ 0.008 events for the low cut, and a shift of ~ 0.011 events for the high cut. This is an even smaller effect than for the POLfit mass cut, so the energy scale uncertainty's effect on the reconstructed neutrino energy window cuts can also be ignored in this optimization.

Special consideration was made for the POLfit efficiency uncertainty, as this might

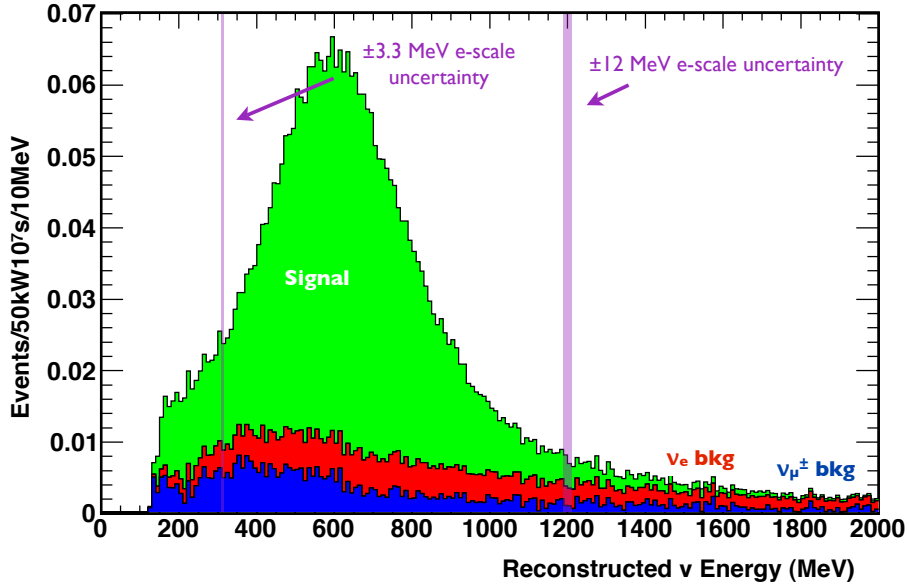


FIGURE 5.16: Distribution of MC events as a function of reconstructed neutrino energy. The MC has been oscillated with $\sin^2 2\theta_{13} = 0.1$, $\delta_{\text{CP}} = 0$ and $\Delta m^2 = 2.4 \times 10^{-3} \text{ eV}^2$, and all cuts except the reconstructed neutrino energy cut are applied. The events are divided into ν_μ and $\bar{\nu}_\mu$ background (nearly entirely NC, blue), beam ν_e background (red), and signal (green). This plot was generated using an older version of the MC than was used in the final analysis. A reconstructed neutrino energy window of (330 MeV, 1200 MeV) is considered with a 1% energy scale uncertainty. The shift in number of events cut from a 1% energy scale shift is ~ 0.01 for both the low and high cuts. This shift is small enough that it can be safely neglected during optimization.

motivate us to adjust the cut value. To test this, we modified the rough sensitivity figure of merit to include an additional 20% systematic uncertainty on the POLfit rejection rate. Re-running the optimization with this, very little difference in the optimal cut point is found. Thus, the POLfit efficiency uncertainty is negligible for this optimization.

At low energies, the signal events ($\nu_\mu \rightarrow \nu_e$ oscillated) are predominantly CC-nonQE. Additionally, the backgrounds below ~ 500 MeV are of some concern, especially in light of the MiniBooNE low energy excess [103]. Because of the background uncertainty, along with signal which is less reliable, we decided to add an extra con-

servative systematic error to the backgrounds. Specifically, for optimization, we are considering a 60% uncertainty on background events with $E_\nu^{\text{rec}} < 500$ MeV, *in addition* to the original 30% uncertainty on all background events. Both these numbers are just rough, conservative estimates, not necessarily indicative of realistic uncertainties. This region of additional systematic error is illustrated in Figure 5.17. This extra systematic error should influence the cut optimization to reject these problematic events.

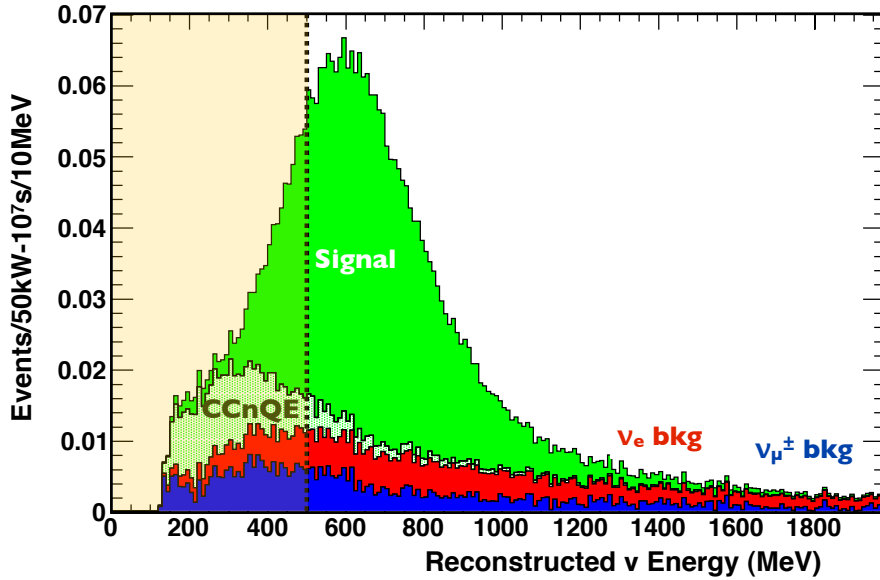


FIGURE 5.17: Distribution of MC events as a function of reconstructed neutrino energy. The MC has been oscillated with $\sin^2 2\theta_{13} = 0.1$, $\delta_{\text{CP}} = 0$ and $\Delta m^2 = 2.4 \times 10^{-3} \text{ eV}^2$, and all cuts except the POLfit mass cut are applied. The events are divided into ν_μ and $\bar{\nu}_\mu$ background (nearly entirely NC, blue), beam ν_e background (red), and signal (green). The signal region is additionally subdivided into a CCQE (solid) and CC non-QE (dotted) region. This plot was generated using an older version of the MC than was used in the final analysis. Note that, at low energies, the signal is dominated by CCnonQE events. In the region below 500 MeV (shaded), an additional 60% systematic error is added to the existing background uncertainty to account for the problematic nature of these low energy events.

5.4.6 Cut Value Optimization

This is now a three-dimensional optimization problem: the energy window low cut, the energy window high cut, and the POLfit mass cut. Through a 3D grid search, the optimal values were found, using the modified rough sensitivity method. The equation to identify the sensitivity for each set of cuts is similar to Equation 5.6, but with the additional background uncertainty added:

$$1.28 = \frac{S}{\sqrt{S + B + \alpha^2 B + \beta^2 B_{\text{low}}}}. \quad (5.7)$$

Here, $\alpha = 30\%$, and $\beta = 60\%$. By varying $\sin^2 2\theta_{13}$ until Equation 5.7 is satisfied, a map of sensitivities can be produced. The results are most clearly represented in two 2D plots, described below.

First, we fix the POLfit mass cut at $m_{\pi^0} < 105$ MeV, which will eventually be the final value. We vary the low and high cuts of the energy window, in a 2D grid, and find where the optimal point is. This is illustrated in Figure 5.18. While there is clearly an optimal value for the high cut, there is no obvious optimal value for the low cut, as a cut value of zero is just as good or better than any other cut value. This indicates that we can remove the energy window low cut entirely, leaving only a maximum reconstructed neutrino energy cut. Note that, despite introducing a large systematic error on these low energy events, the optimal cut value is still zero.

With that cut removed, it is a simple 2D optimization to find the remaining cuts. A 2D grid of cut values shows the optimal sensitivity at $m_{\pi^0} < 105$ MeV/ c^2 , and $E_{\nu}^{\text{rec}} < 1250$ MeV. See Figure 5.19 for the grid and details.

5.4.7 Robustness of Cut Optimization

In the end, only the maximum reconstructed neutrino energy and the POLfit mass cuts were free to be optimized over. This two-dimensional space is simple enough

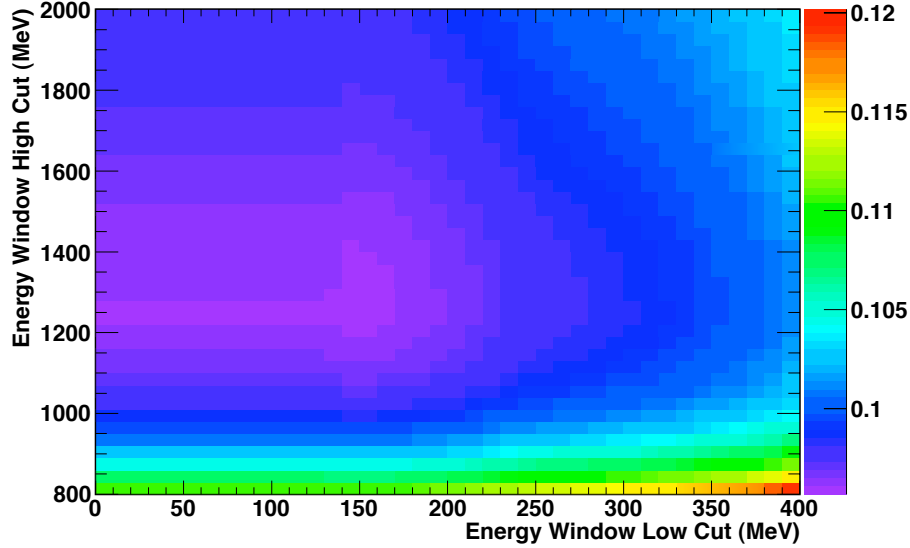


FIGURE 5.18: Modified (see Equation 5.7) rough sensitivity (in $\sin^2 2\theta_{13}$, color axis) as a function of the reconstructed neutrino energy low cut value (x -axis) and high cut value (y -axis). Purple is the best sensitivity (lowest value of $\sin^2 2\theta_{13}$). We assume a POLfit mass cut of $m_{\pi^0} < 105 \text{ MeV}/c^2$. Note that, while there is a clear minimum in the y -direction, the x -direction minimum is reached as the cut value approaches zero. Thus, we chose to remove the energy window low cut, leaving only a maximum reconstructed neutrino energy. Note also that, due to the visible energy cut, there is no change in sensitivity in $E_{\text{low}} \in (0, 100) \text{ MeV}$.

to check using alternate figures of merit, and different conditions, to determine how robust the cut optimization is.

The first thing to check was robustness against different systematic error levels. At the time of this optimization, signal systematic errors were not considered. The 2D optimization grid was re-run, and approximate optimal cuts were found with the following systematic error schemes:

- Rough sensitivity, no systematic error.
- Rough sensitivity, 30% background systematic error.
- Rough sensitivity, 30% background systematic error with an additional 60% systematic error on events with $E_{\nu}^{\text{rec}} < 500 \text{ MeV}$.

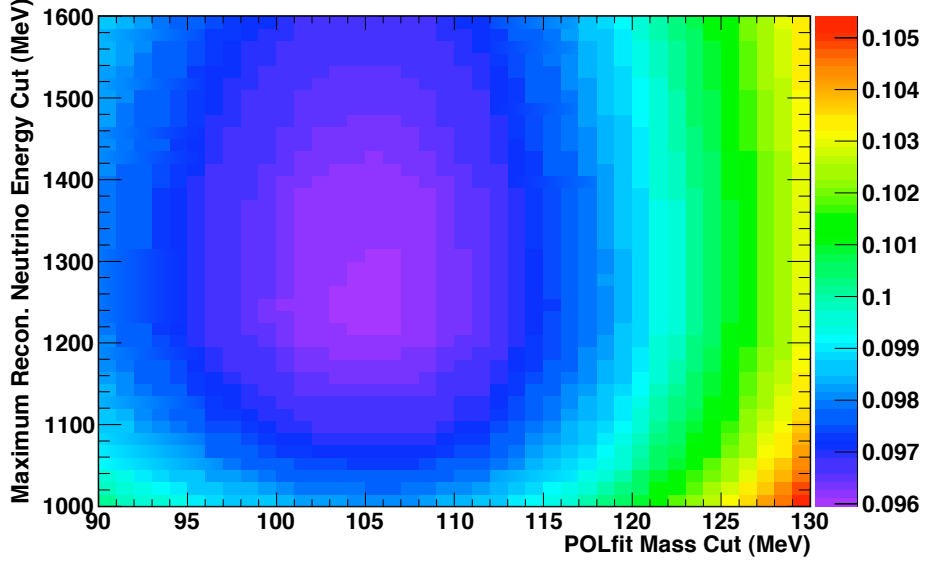


FIGURE 5.19: Modified (see Equation 5.7) rough sensitivity (in $\sin^2 2\theta_{13}$, color axis) as a function of POLfit π^0 mass cut value (x -axis) and the maximum reconstructed neutrino energy cut value (y -axis). Purple is the best sensitivity (lowest value of $\sin^2 2\theta_{13}$). There is no lower bound on the reconstructed neutrino energy (although there is a cut on total visible energy). The optimal value for the POLfit mass cut is $m_{\pi^0} < 105$ MeV/ c^2 , and the optimal value for the reconstructed energy cut is $E_{\nu}^{\text{rec}} < 1250$ MeV.

- Rough sensitivity, 60% background systematic error with an additional 60% systematic error on events with $E_{\nu}^{\text{rec}} < 500$ MeV.

The optimal cut values for each of these schemes are listed in Table 5.3. The listed optimal values are approximate, as there is typically a region where the cut is close enough to optimal that improvement cannot be observed by eye on a 2D color plot (where the optimal sensitivity varies by less than 1% or so).

The next set of checks was for different statistical analysis methods (the optimization was conducted before the statistical method was determined). More details on statistical methods can be found in Section 8.3.3. We re-ran the 2D optimization using each of the following methods to compute the sensitivity:

- Feldman Cousins (F-C), with no systematic error (see Section 8.3.1 and [99]).

Table 5.3: Table of cut optimizations for different systematic error cases.

Systematic Error Scheme	E_ν^{rec} Cut	POLfit Mass Cut
Rough sensitivity, no systematic error	1300 MeV	107 MeV
Rough sensitivity, 30% background systematic error	1250 MeV	106 MeV
Rough sensitivity, 30% bkg sys error + 60% low energy bkg sys error	1260 MeV	105 MeV
Rough sensitivity, 60% bkg sys error + 60% low energy bkg sys error	1220 MeV	102 MeV

- F-C with profile likelihood to add systematic error. The error is computed to be equivalent to 30% on all background added in quadrature with 60% on low energy backgrounds, and then this error is applied to all backgrounds. This background error computation is applied to all the following methods.
- F-C with the number of background events scaled up by the 1σ systematic uncertainty, so we use $B' = B(1 + \delta)$, where δ is the 30% + 60% low energy uncertainty.
- Method of Rolke [104] with 30% + 60% low energy uncertainty.

The approximate optimal cut values for these methods are listed in Table 5.4.

Table 5.4: Table of cut optimizations for different statistical methods.

Statistical Method	E_ν^{rec} Cut	POLfit Mass Cut
F-C, no systematic error	1220 MeV	104 MeV
F-C with profile likelihood and 30% bkg sys error + 60% low energy bkg sys error	1220 MeV	105 MeV
F-C with background scaled up by 30% bkg sys error + 60% low energy bkg sys error	1250 MeV	105 MeV
Method of Rolke with 30% bkg sys error + 60% low energy bkg sys error	1200 MeV	103 MeV

Using these various systematic errors and statistical methods does not change the optimal cut points by very much. The rough sensitivity varies by ~ 0.001 over this

range of optimal cut points, between $\sin^2 2\theta_{13} = 0.096$ and 0.097 . The sensitivity change is similar for the other statistical methods and systematic cases. Thus, we conclude that a single set of cuts should be sufficient for whatever systematics and statistical method we would use.

Finally, we checked whether the cuts would be optimal for different beam exposures. We re-ran the rough sensitivity analysis with $30\% + 60\%$ low energy background systematics assuming beam exposures of $20 \text{ kW} - 10^7 \text{ s}$ and $100 \text{ kW} - 10^7 \text{ s}$. In each of these cases, the sensitivity with the chosen cuts was close to optimal, varying by at most 2% in $\sin^2 2\theta_{13}$ from the best point. Thus, we decided we would not need to make the cuts dependent on the beam exposure. With this, the optimization was complete, and the cuts were finalized.

It is notable that the optimal cuts for low exposure are much looser than the optimal cuts for high exposure. This can be attributed to the fact that we are not sensitive to low $\sin^2 2\theta_{13}$ at low exposures, regardless of the cuts. Thus, with the best possible sensitivity near $\sin^2 2\theta_{13} = 0.1$, we only have sensitivity when the expected signal is much larger than the expected background. Thus, background rejection is relatively unimportant compared to maximizing signal acceptance. Also, systematic errors (which are larger for backgrounds than signal) are small, relative to statistical errors. For future analyses on more data, tighter cuts and/or more sophisticated analysis methods will be necessary.

Analysis Inputs

6.1 MC Production

Despite normalization from the near detector, the analysis is largely dependent on MC (Monte Carlo) simulation. The near and far detectors are very different, and have different acceptances, so accurate simulation is necessary for all parts of the experiment.

6.1.1 Beam Simulation

The T2K beam simulation was developed by the T2K Beam Working Group, with input from the NA61/SHINE collaboration. Information in this section largely comes from T2K internal technical notes [105][106][107], though published references are provided where possible.

The T2K beam simulation, called JNUBEAM, uses a multi-step process to predict the fluxes at the near and far detectors. The results of the NA61/SHINE experiment [108] were used to tune the MC simulation. A diagram of NA61 is shown in Figure 6.1. The JNUBEAM simulation is based on GEANT3 [109], although it was found that the hadronic interaction models included in GEANT3 (such as

GCALOR or GFLUKA) were not as good as FLUKA [110] [111] at reproducing the NA61/SHINE results for the angles relevant to T2K beam production [105]. Thus, FLUKA version 2008.3c was implemented to compute primary interactions off the main target and baffle. This target simulation in FLUKA was done separately from the rest of the beam simulation. The information on the particles leaving the target was then passed on to the GEANT3 simulation, where hadronic interactions were implemented with GCALOR [112]. The full geometry of the target, magnetic horns, etc., is implemented in this simulation, along with their magnetic fields. The simulation tracks the various particles through the horns, to the point when the pion (or muon, or kaon, etc.) decays [48]. At this point, the probability for the decay-neutrino to be going in the direction of SK or ND is computed, along with the energy of such a neutrino. In the case of muons, this decay takes into account the muon polarization. This information is used to compile the expected neutrino flux.

An extra step of tuning was included. The NA61/SHINE experiment measured the angular and energy spectra of charged pion production from a 31 GeV momentum proton beam on a carbon target. The 31 GeV momentum proton has a kinetic energy of very nearly 30 GeV (a 31.00 GeV/c momentum proton has a kinetic energy of 30.08 GeV), which is the kinetic energy of protons from the J-PARC beam. NA61/SHINE (SPS Heavy Ion and Neutrino Experiment) is an experiment utilizing protons from the CERN SPS with a large acceptance spectrometer to measure the spectra and angular distributions of products from proton-carbon collisions on a thin (2 cm thick) target. Only the data from the first NA61 run, taken in 2007, is used. Later NA61 data has been taken using other targets, including a replica of the T2K target, but that data was not analyzed and ready at the time of this analysis.

The NA61 data are used to tune the simulation. There are three tuning steps applied, two for interactions in the target (simulated by FLUKA), and one for interactions further downstream (simulated with GEANT3 with GCALOR).

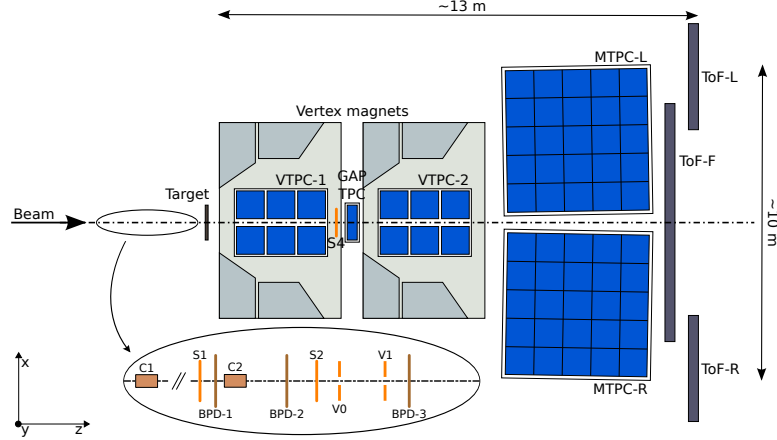


FIGURE 6.1: Diagram of the NA61/SHINE experiment (from [108]). A beam of 31 GeV/c momentum protons from the CERN SPS pass through a series of Cherenkov and scintillation counters, as well as beam position detectors, before hitting the target. The secondary particles produced are detected first in TPCs located inside superconducting dipole magnets. Further downstream, the particles are detected by a pair of larger volume main TPCs. Finally, there are scintillator time-of-flight detectors. The full setup acts as a large acceptance hadron spectrometer. The $p - \theta$ distributions of produced hadrons are measured and used as inputs for the T2K beam simulation.

The first step is tuning of secondary pions (pions produced from the interactions of beam protons on the graphite). The multiplicity of pions in momentum-direction ($p - \theta$) space is adjusted to match the 2007 NA61 data. Note that the multiplicity reweighting is normalized so as not to affect the total cross-section. The total cross-section from FLUKA is good enough that no normalization change is necessary here. The reweighting is only applied for $p - \theta$ bins covered by NA61; the other bins simply use the FLUKA prediction. This tuning is applied to all pions produced in the FLUKA region, the baffle and target.

The next step is the tuning of tertiary pions (pions produced from secondary proton interactions) in the target and baffle. This reweighting is more difficult because the secondary proton energies are lower than the primary protons (and the NA61 protons), so a correction is required to transform the $p - \theta$ distributions from

NA61 to match the secondary proton energies. This transformation is done through Feynman scaling [113], with some modifications to make the technique more suitable for the particular range of proton energies [114]. Thus, the tertiary pions are given reweighting to match the NA61 results.

Finally, tuning of the total cross-section is applied to events outside of the FLUKA region. The GCALOR cross-sections do not agree very well with experiments, so the cross-sections are tuned to match the FLUKA cross-sections, which agree with experiment much better. This tuning mostly affects the interactions with the aluminum in the horns. This is different than the tuning of FLUKA to NA61. In that case, the total cross-section does not change, but the $p - \theta$ distribution does. In this case, the $p - \theta$ distribution is unchanged, but the total cross-section is altered.

6.1.2 Neutrino Interactions

The computed neutrino flux is passed on to be used in event simulation at the near and far detectors. There are two neutrino interaction generators used for T2K: GENIE (Generates Events for Neutrino Interaction Experiments) [115] and NEUT [116][117]. NEUT is a generator used for Super-Kamiokande atmospheric neutrino analyses [85], and was used for computing cross-sections and generating events from the beam flux in the T2K MC. GENIE was used as a cross-check for the T2K MC, and for estimating cross-section systematic errors. The versions used were NEUT version 5.0.6, and GENIE version 2.6.0.

The two interaction generators differed to a small extent. NEUT predicted a 10% higher event rate at SK than GENIE, and a 12% higher rate in the ND280 FGD than GENIE. This difference was one of the inputs to the cross section systematic error estimations. The differences are largely due to input parameter choices for each generator, such as the axial mass.

The interaction generators (in particular NEUT, which was used to generate the

final MC for the analysis) are used to generate a list of vectors: the positions, momenta, and directions of primary interaction products which are passed on to the detector simulators. The calculation of interactions not only considers the incident neutrino acting off a nucleon (free or bound), but also the chance for particles produced in the primary interaction to re-interact before leaving the nucleus. These re-interactions are called final state interactions (FSI). The effects of FSI are most commonly observed with pions.

NEUT is also used to generate cross-section tables which are integrated with the flux for normalization purposes (Section 8.2).

The vector lists from NEUT or GENIE are passed on to the near and far detector simulations. The detector simulation for ND280 uses GEANT4 [118] as the basic simulation library. More details on the ND280 detector simulation can be found in [69].

6.1.3 NEUT

As NEUT is the primary neutrino interaction generator for this analysis, it will be described here briefly. For more details, see [117]. NEUT was first developed for the Kamiokande experiment in the 1980s [119], initially focused on atmospheric neutrino interactions in water. Since then, it has been continually expanded, and now calculates neutrino interactions on a variety of materials at a variety of energies. Interactions are only considered between neutrinos and nuclei; neutrino-electron interactions have a much smaller cross-section and can be neglected in this analysis [46].

There are two main steps to how the interactions are modeled. First, the interaction of the neutrino and target nucleon (or nucleus) is considered. After this, if the interaction was with a bound nucleon (such as in ^{16}O), and a hadron was produced, this hadron must travel through the nucleus before it can escape and be observed

in the detector. Because the hadron can interact via the strong interaction, there is a significant probability for re-interaction (FSI). The following neutrino interactions are considered in NEUT:

- CC/NC (quasi-)elastic scattering $(\nu N \rightarrow lN')$
- CC/NC single π production $(\nu N \rightarrow lN'\pi)$
- CC/NC single γ production $(\nu N \rightarrow lN'\gamma)$
- CC/NC single K production $(\nu N \rightarrow l\Lambda K)$
- CC/NC single η production $(\nu N \rightarrow lN'\eta)$
- CC/NC deep inelastic scattering (DIS) $(\nu N \rightarrow lN'h)$
- CC/NC coherent π production $(\nu^{16}\text{O} \rightarrow l\pi X)$

where N and N' are nucleons (proton or neutron), l is the lepton (charged or neutrino, depending on CC/NC), h is hadrons, and X is the remaining nucleus [117]. Some of the more significant of these interactions will be described here.

There are two major models for used for computing CCQE scattering cross-sections. The neutrino-nucleon cross-section is computed based on the Llewellyn-Smith model [120]. However, if the nucleon is inside a nucleus, the nuclear medium must be considered. This is done using the relativistic Fermi gas (RFG) model by Smith and Moniz [121]. The RFG model draws nucleon momenta from a flat distribution up to the Fermi momentum of $p_f = 225$ MeV/c. The effect of Pauli blocking is taken into account in a simple way by requiring recoil nucleons produced in ^{16}O to have a momentum greater than p_f . Neutral current cross-sections are computed based on the charged current ones [122][123][117]. The primary parameter for computing CCQE cross-sections is the axial mass (M_A), which, for this analysis, is taken to be $M_A^{QE} = 1.21 \pm 0.20(\text{GeV}/c)^2$.

Single meson production (π , K , η) is simulated with the Rein and Sehgal model [124][125], with an intermediate baryon resonance, such as $\Delta(1232)$. This baryon usually decays to a pion, and so this mode is critical, as it produces the π^0 background at T2K.

Another interaction possibility is that a neutrino can interact with the ^{16}O nucleus as a whole, rather than an individual nucleon. Based on the kinematics in this case, the product pion angular distribution is highly peaked in the forward direction [126]. This coherent pion scattering is another background concern for T2K.

Deep inelastic scattering (DIS) is a process whereby the neutrino interacts with a constituent quark of a nucleon, breaking up the nucleon in the process. DIS is mostly an important effect for higher energy interactions (above 2 GeV). This process is simulated using the GRV98 parton distribution function [127] with corrections from Bodek and Yang [128].

The second part of the NEUT calculation is to handle the propagation of hadronic particles through the nucleus. In NEUT, FSI is implemented through a microscopic cascade model [129]. In this, the π is propagated through the nucleus in finite steps. At each step, depending on the position and momentum of the π , there is some probability for re-interaction. This same process can be done for other mesons as well. See [130] and [117] for more details.

The parameters for the models used by NEUT have been tuned to fit experimental data, both for primary interactions and FSI. The input data are also used for calculating the cross-section uncertainties. Some example CC neutrino and antineutrino cross-sections are shown in Figure 6.2. For the T2K analysis, the NEUT cross-section tuning was updated using data from SciBooNE [131][132], MiniBooNE [133], K2K [134], and other experiments.

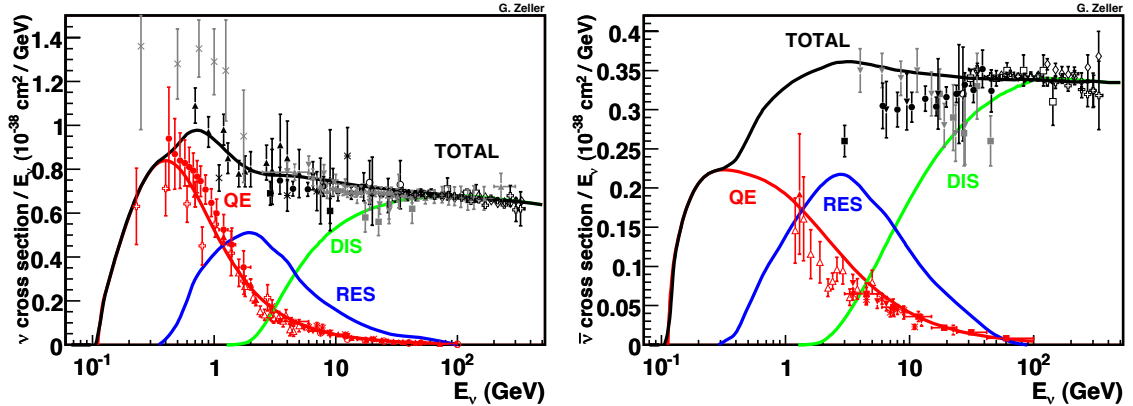


FIGURE 6.2: Neutrino (left) and antineutrino (right) charged current cross-sections. The contributions from CCQE, resonant pion production ($CC1\pi$), and deep inelastic scattering are shown. Data used to make these fits [135] are overlaid. From [135].

6.1.4 *SKdetsim*

The far detector simulation is called *SKdetsim*. It is based on a modified version of GEANT3 [109], with the SK detector geometry. GEANT handles most particle interactions and Cherenkov light production, though many simulation aspects have been custom coded. Many parameters of the simulation are tuned to calibration data, including the PMT and electronics response, water parameters, and reflectivity of the various materials in the tank.

The Cherenkov photon propagation accounts for absorption, Mie scattering, and Rayleigh scattering. For T2K (and ATMPD as well), the tuning parameters are fixed for the entire MC production (this is in contrast to SK low energy analysis, which produces MC for many different time periods with different tuning parameters).

Hadronic interactions in the water are handled with CALOR physics package [136] by default, as it reproduces pion interactions well around 1 GeV. For pions with momentum below 500 MeV, however, a custom routine is used [119]. Good agreement is found between *SKdetsim*-produced MC and data; see Section 4.8 for an example of this.

6.1.5 Additional Corrections

It should be noted that the actual beam flux MC used to produce the Super-K MC was a more primitive version than the one described in Section 6.1.1. The version described above (and used for analysis) was version 10dv3. The version used for MC production at SK and ND280 was version “10a nominal”. There were numerous small updates between these versions, though the major updates were the addition of the three reweighting factors described in Section 6.1.1, and also the switch from GCALOR to FLUKA for the target and baffle simulation.

It is a time consuming and CPU intensive task to regenerate detector MC, and the beam flux is updated more frequently than the SK detector simulation. Therefore, the flux version update is provided as binned flux ratio histograms, 10dv3/10a, for each MC neutrino type (ν_μ , beam ν_e , $\bar{\nu}_\mu$, signal ν_e). This reweighting is applied during analysis (Section 8.4.3) to correct the MC with the latest tuning.

6.2 Beam Inputs

The number of protons delivered for T2K was monitored at the beam source by beam current monitors in the J-PARC beam, and the OTR in the neutrino beamline. This was used to initially normalize MC predictions for the near and far detector in this analysis. The final normalization, however, came from the near detector.

6.3 Near Detector

Measuring the neutrino beam at both the near and far detectors allows for the cancellation of some systematic uncertainties. Because the two detectors operate on very different principles, this was done by comparing data and MC at ND280, and then using the data/MC ratio to normalize the SK measurement.

The near detector study used only data from T2K Run I (January - June 2010).

This is acceptable because the statistical uncertainties using just this data were already lower than systematic uncertainties. After including cuts based on ND280 detector downtime, a total of 2.88×10^{19} POT is used for the ND280 inputs to the analysis.

Simplicity was a goal of the first analysis at ND280. Thus, only the ND280 tracker was used for the measurement. ND280 used a CC inclusive analysis, that is, the analysis is designed to select CC ν_μ events, not just specifically CCQE events, as the SK analysis is. Future analyses will likely incorporate inputs from the other detector components, such as the POD, ECals, and SMRD.

The basic idea was to select CC ν_μ events originating in the fiducial volume of the FGDs. The reconstructed momentum by track curvature and ionization charge in the TPCs are used to perform particle ID, and to confirm that the most energetic track is from a muon. The total number of events observed is compared to MC to make a normalization factor for the SK analysis. For more detailed information on the ND280 CC inclusive analysis, see [137].

This ND280 analysis was developed by members of the ND280 working group. Details of the ND280 analysis are summarized in Appendix B.

6.4 Far Detector

The input from the far detector, Super-Kamiokande, is the number of ν_e candidate events observed. The events are selected through a series of cuts, described in Section 5.2.

Systematic Errors

The remaining inputs for the analysis are systematic errors. They are applied to the analysis by fluctuating the number of expected events in a toy MC (see Section 8.4.3). Thus, all systematic errors are presented as the effect of some uncertainty on the number of neutrino events that will be detected (either at ND280 or SK) and pass the selection cuts. Unless otherwise specified, these uncertainties are treated as symmetric Gaussian uncertainties.

7.1 Neutrino Interactions

The neutrino interaction systematic uncertainties were computed by the T2K Neutrino Interactions Working Group (NIWG). The NIWG also improved NEUT for the T2K run. Information on the computation of these systematic uncertainties comes from T2K internal technical notes [138][139][140].

The cross-section uncertainties for NEUT come from comparisons to external data. Interaction tuning parameters are shifted by their uncertainties based on the external data, in both GENIE and NEUT. The variations in the neutrino interactions and FSI from these systematic shifts are propagated to the predictions for the number

of events expected at SK or ND280 through MC regeneration or reweighting. The resulting uncertainties in interaction rates for different neutrino interaction modes are given in a simple form for use in the analysis, as ratios of a given cross-section (such as $CC1\pi^0$) to the CCQE cross-section. This is a useful choice, as the event rates are normalized by the near detector, which is primarily measuring CCQE events. The non-CCQE interactions are divided into six cross-section categories. Table 7.1 and Table 7.2 give the CC and NC cross section uncertainties, respectively. The uncertainties are 100% correlated between energy bins, and there is no correlation between interaction modes.

An additional 6% uncertainty is applied to CC ν_e interactions. This error accounts for the ν_e/ν_μ cross-section ratio uncertainty. This error is not listed in Table 7.1, but is applied on top of the interaction mode cross-section errors.

Table 7.1: Fractional systematic uncertainty on charged current neutrino interaction cross-sections.

Mode	< 2 GeV	> 2 GeV
CC $1\pi^0$	30%	20%
CC Coherent	100%	100%
CC Other	30%	25%

Table 7.2: Fractional systematic uncertainty on neutral current neutrino interaction cross-sections.

Mode	< 2 GeV	> 2 GeV
NC $1\pi^0$	30%	20%
NC Coherent	30%	30%
NC Other	30%	30%

For CCQE itself, a “shape error” is provided, based on the expected variations that would arise from the different target materials and acceptances at SK and

ND280. This shape error is given as a function of neutrino energy, and, unlike the other cross-section errors, is only applied at SK. The main uncertainties for CCQE come at low energies, where variations between models become more pronounced. The final CCQE shape error was largely based on comparisons between NEUT and another interaction library, NuWro [141]. The CCQE shape error is shown in Figure 7.1.

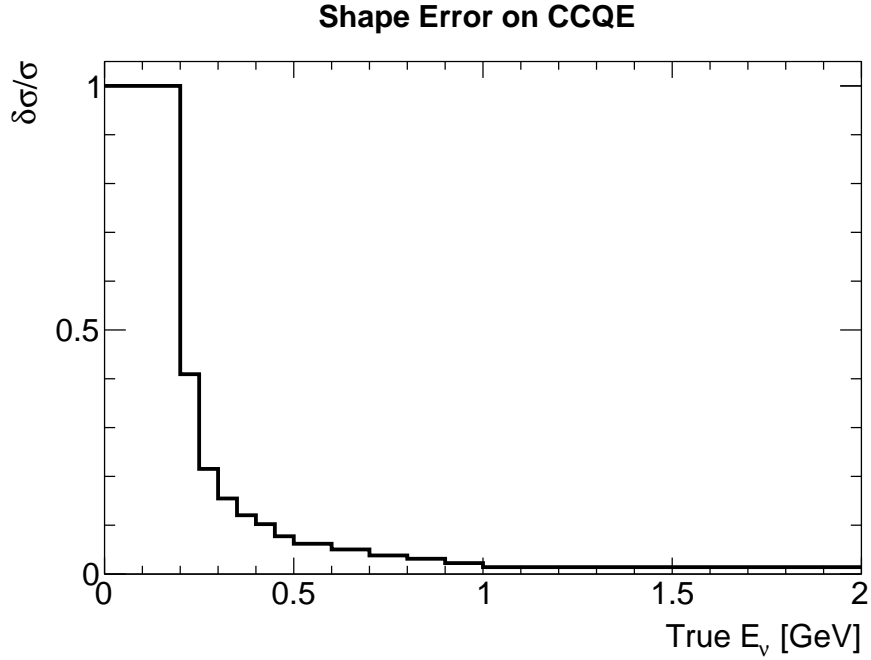


FIGURE 7.1: Fractional systematic uncertainty on charged current quasi-elastic events, as a function of true neutrino energy. This is a “shape error”, applied only on the SK events. It is designed to parameterize the uncertainties on interaction rates due to different targets and acceptances at SK and ND280.

Finally, an FSI error is estimated for both SK and ND280, in different ways. At SK, the uncertainty due to FSI effects is parameterized as a function of reconstructed neutrino energy, as effects such as pion absorption affect the final visible energy in the event. Additionally, for simplicity, the FSI error at SK was computed for signal and background separately. For ND280, the FSI uncertainties were applied by producing

specially adjusted ND280 MC and observing the differences in event totals. The FSI effects were small for ND280, as expected (see Section C.1.2). The FSI errors for SK are shown in Figure 7.2.

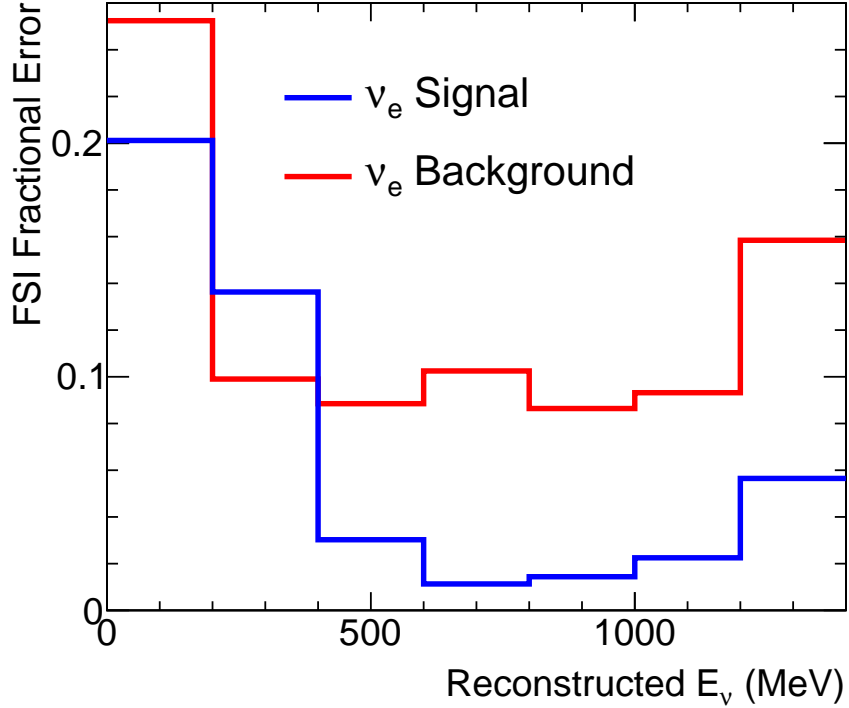


FIGURE 7.2: Fractional systematic uncertainty on final state interactions (FSI) for SK. The signal and background samples are computed assuming $\sin^2 2\theta_{13} = 0.1$. This uncertainty is a function of reconstructed neutrino energy.

7.2 Near Detector

The systematic uncertainty for the ND280 detector is grouped into three parts: statistical, physical model systematics (due to neutrino interaction uncertainties), and detector systematics (due to the detector and analysis efficiency uncertainty). The T2K ND280 group computed these uncertainties for the analysis.

- Statistical Uncertainty: $\pm 2.7\%$, implemented as a Poisson error in the analysis

on the number of ND280 events.

- Physical Model: $\pm 3.7\%$, implemented as a Gaussian error on the number of ND280 events, with no correlation to SK uncertainties.
- Detector Systematics: ${}_{-3.6}^{+4.2}$, implemented as a $\pm 4.2\%$ Gaussian error on the number of ND280 events, with no correlation to SK uncertainties.

Details on how these error estimates were produced can be found in a T2K internal technical note [142]. This is summarized in Appendix C.1.

7.3 Beam

For the beam systematic errors, it is critical to consider the cancellation between the near and far detectors. Thus, the beam systematic error is delivered as an uncertainty on the ratio of the number of selected events expected at the far detector to the number expected at the near detector $\delta(N_{\text{SK}}/N_{\text{ND}})$. The spectrum shape at the near and far detectors will affect the flux uncertainty cancelation. As the far detector spectrum shape varies depending on the oscillation parameters, this systematic error is computed from beam inputs and expected spectra at different oscillation points. Details on how the beam systematic uncertainty is calculated can be found in internal T2K technical notes [143][106][107], and it is summarized in Appendix C.2.

For the analysis, this error computation was done by software provided by the beam group, which took the expected spectra at SK and ND280 as inputs. To avoid complications caused by combining different software pieces, and to save CPU time, the beam error was pre-calculated on a grid of 50×50 points in oscillation space. Computing the beam error on this coarse grid had a negligible effect on the results, as the beam error did not change very rapidly between grid points. Using a pre-computed grid means the beam error computation does not need to be re-done during analysis processing.

An example of these oscillation grids are shown in Figure 7.3. Note that the beam

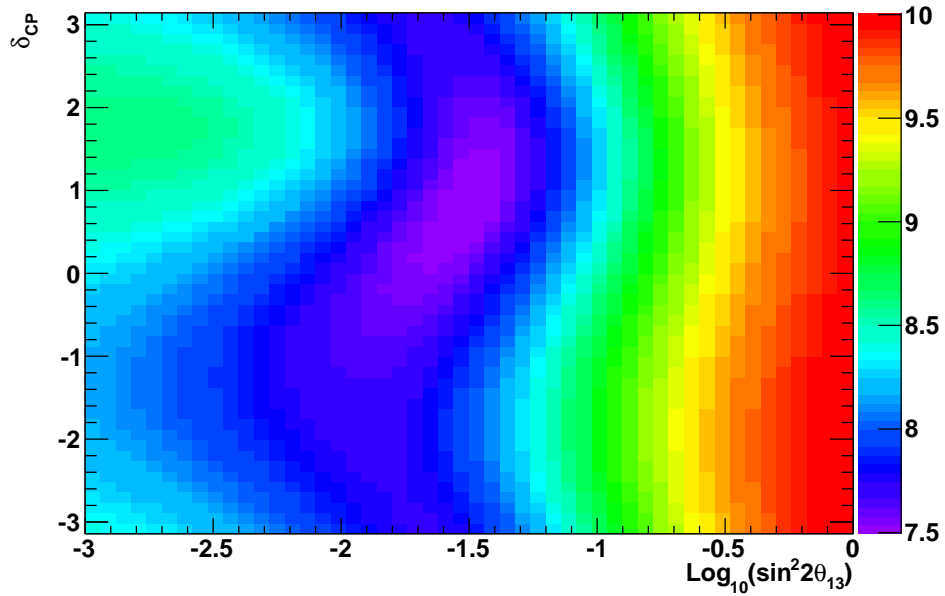


FIGURE 7.3: Beam error, given as the uncertainty on the far/near ratio at each oscillation point. The beam error has been computed on a 50×50 grid in $\log_{10}(\sin^2 2\theta_{13}) - \delta_{\text{CP}}$ oscillation space. The color scale indicates the uncertainty in %. This is for the normal hierarchy, with $\Delta m^2 = 2.4 \times 10^{-3} \text{ eV}^2$.

error gets larger for high values of $\sin^2 2\theta_{13}$, and has an absolute minimum for a small (but non-zero) value of $\sin^2 2\theta_{13}$. This is because the beam error is minimized when the spectrum of CC inclusive ν_μ events at ND280 looks as much like the spectrum of ν_e candidate events at SK as possible. Grids such as this one are computed for each range of oscillation parameters to be plotted (Δm^2 and δ_{CP} , always vs. $\sin^2 2\theta_{13}$ on a log scale). Typical beam errors are between 7.5% and 10%.

7.4 Far Detector

Each of the SK ν_e selection cuts (Section 5.2) has a systematic error associated with it, although both the visible energy cut and the reconstructed neutrino energy cut share the same error source, the energy scale uncertainty. Additionally, there is a

special error just for π^0 events, because they are a significant background, and there are significant uncertainties on their rejection efficiency, related to multiple cuts.

Each of the SK systematic errors is computed separately for signal events ($\nu_\mu \rightarrow \nu_e$) and background events (ν_μ , beam ν_e , $\bar{\nu}_\mu$). Then, during analysis, the uncertainties on signal and background are applied in a correlated way. This is reasonable, as the leading background (beam ν_e) will have similar systematic behavior to the signal.

Table 7.3 summarizes all the systematic errors for the event rate at the far detector. These errors were estimated by members of the T2K-SK group. More information on how these errors were estimated (largely from internal T2K notes) is summarized in Section C.3.

Table 7.3: Table of SK detector systematics. Here, signal is defined as $\nu_\mu \rightarrow \nu_e$ events, and background is defined as events from ν_μ , ν_e , and $\bar{\nu}_\mu$.

Source	Signal Sys. Error	Background Sys. Error
Reduction/OD Cut	1.0%	1.0%
Fiducial Volume	1.0%	1.0%
Energy Scale	0.4%	1.1%
Ring Counting	3.9%	8.3%
Muon PID	0.0%	1.0%
Electron PID	3.8%	8.0%
POLfit Mass	5.1%	8.7%
Decay Electron Efficiency	0.1%	0.3%
Hybrid π^0 Error	–	3.6%

ν_e Appearance Analysis

The analysis was conducted as a counting experiment, using near detector information to supplement MC predictions, and comparing the predicted number of $\nu_\mu \rightarrow \nu_e$ candidate events at SK with the observed number. The Feldman-Cousins method [99] is used to compute contours from this observation, and systematic errors are incorporated through a semi-Bayesian technique.

Some of the main contributions by the author to the experiment are described in this chapter. These include the investigation and use of the Feldman-Cousins with systematic errors technique, and the development of the oscillation analysis technique including the analysis software and framework.

8.1 T2K Data Taking

The T2K beam commissioning began in 2009, with the first beam neutrino events detected in the INGRID near detector in November 2009. Super-Kamiokande detected its first T2K event February 24, 2010, featuring a clearly reconstructed π^0 (Figure 8.1).

The first physics run for T2K (Run I) was from January to June 2010. During

Super-Kamiokande IV

T2K Beam Run 300017 Spill 1143942
Run 66498 Sub 160 Event 37004534
10-02-24:06:00:06
T2K beam dt = 1386.3 ns
Inner: 1267 hits, 2347 pe
Outer: 2 hits, 1 pe
Trigger: 0x80000007
D_wall: 650.8 cm

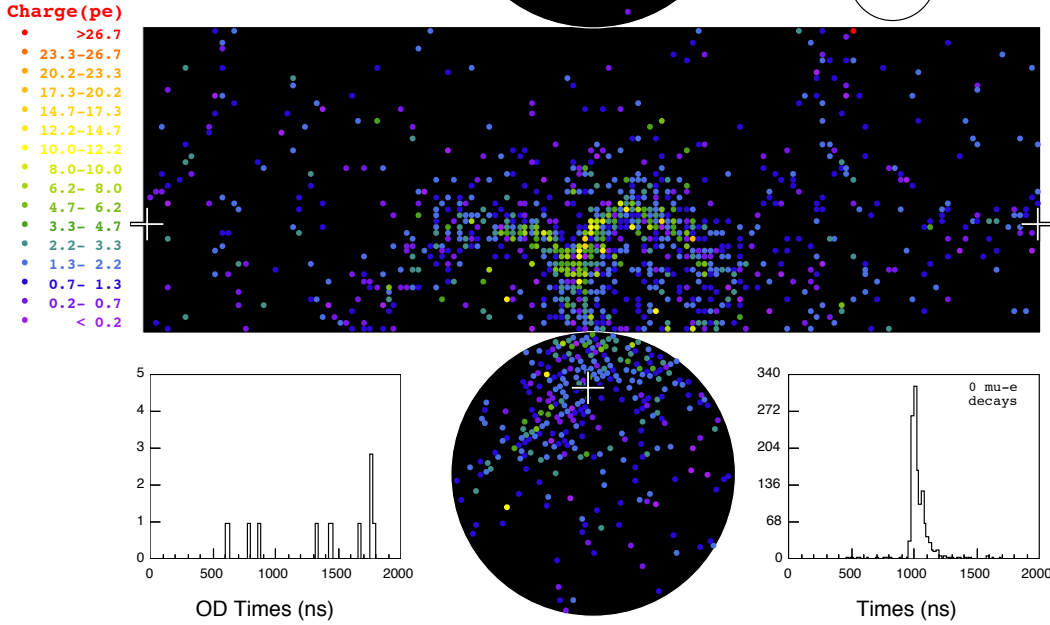


FIGURE 8.1: Event display of the first T2K event observed at Super-Kamiokande. Each dot represents a PMT hit. Color indicates the measured charge on each PMT. A pair of e -like rings can be clearly seen, and they have a reconstructed invariant mass of $133.8 \text{ MeV}/c^2$, very close to the π^0 mass. There is also a thin non-showering ring visible, on the sides and top of the display.

this time, 3.23×10^{19} POT were delivered for physics study. The second physics run (Run II) was from November 2010 until the Great East Japan Earthquake on March 11, 2011. The earthquake shut down the neutrino beam and near detectors, although Super-Kamiokande continued operating nearly entirely normally. The combined Run I+II beam delivered 1.431×10^{20} POT for physics analysis, and was used for the published results, and this dissertation. See Figure 8.2 for a plot of POT as a function of time, and information on the T2K runs.

The analysis described in this dissertation was applied to the data twice: first, on the Run I data alone, later on the Run I+II data. The optimization was sufficiently robust that the analysis method did not need modification to apply to these different beam exposures.

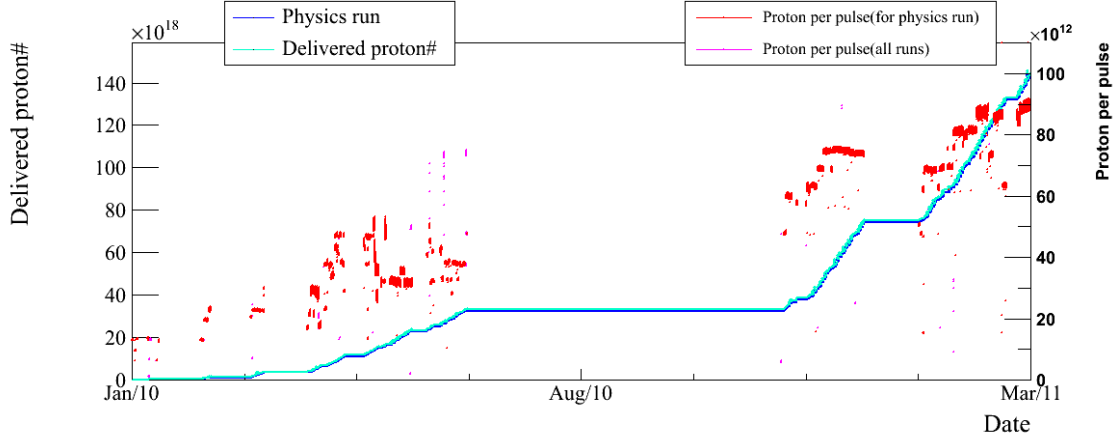


FIGURE 8.2: Plot of T2K POT vs. time. Note that Run I was from January 2010 through June. This period delivered 3.23×10^{19} POT for physics study, at 6 bunches per pulse. Run II was from November 2010 until the earthquake in March 2011. It delivered 1.108×10^{20} POT for physics study, at 8 bunches per pulse. Near the very end of Run II, the beam cycle time was decreased from 3.2 s to 3.04 s, to increase the number of protons delivered. The maximum beam power was achieved during this final period, 145 kW.

8.2 Normalization

As a counting experiment, the observation/expectation measurement is critically dependent on normalization. There are two stages of normalization in this analysis. First, the MC needs to be normalized to the expected number of events at both the near detector and the far detector. Then, in the analysis, the far detector expectation is adjusted by the ratio of the near detector observation and expectation. This can help cancel systematic errors related to the beam flux and cross-sections.

8.2.1 Far Detector MC Normalization

The SK MC is generated with interactions uniformly distributed throughout a volume extending to 50 cm beyond the inner detector wall. A MC-only cut is made to remove interactions occurring inside of PMT volumes (which are evacuated), and the rest is, nearly entirely, just water, so this uniform distribution is as we would expect. The relative distributions of neutrino energies and interaction modes are correct, but the absolute normalization needs to be applied separately.

We compute the total number of interactions expected in the fiducial volume by integrating the flux (used in the simulation) with the total neutrino cross-section per nucleon (used in the simulation), and scaling it to the number of nucleons in the FV, with a mass of 22.5 kton. The cross-sections provided by NEUT are already adjusted to account for the relative ratio of oxygen protons and neutrons, and free protons (hydrogen) in water. This integration is performed numerically, on a range from 0 to 10 GeV with 50 MeV bins. This cut-off at 10 GeV is deemed acceptable as it is expected to be a small effect, changing the total normalization by less than 1% compared to integrating up to, say, 15 GeV. Because we normalize based on the 10 GeV range, and our MC is produced only in this range, we are normalizing the produced MC correctly. Additionally, it is highly unlikely for a neutrino with energy above 10 GeV to produce a signal candidate, as the signal selection cuts are designed to select lower energy neutrinos.

This integration process is done for each MC species (ν_μ , ν_e , $\bar{\nu}_\mu$, $\nu_\mu \rightarrow \nu_e$). For the background samples, it is assumed that there will be no oscillation; for the signal sample, 100% oscillation is assumed.

The expected number of events in the FV for 10^{21} POT is shown in Table 8.1. These numbers are for the 10a version of the MC, so flux reweighting (Section 6.1.5) will need to be applied after normalization.

Table 8.1: Unoscillated expected numbers of events in the SK FV for 10^{21} POT. This is computed by integrating the 10a flux with the NEUT cross sections from 0 to 10 GeV, and scaling to the SK FV mass.

ν_μ	$\bar{\nu}_\mu$	beam ν_e	signal ν_e
1446	70.46	29.16	1518

Now, to get a MC scaling factor, we divide the number we get from this integration by the number of events in the true fiducial volume in the MC. We can then adjust the scaling factor to the experimental POT.

8.2.2 Near/Far Ratio Normalization

The ND280 measurement for this analysis is based on T2K Run I data. The details of this analysis are described in Section 6.3 and Appendix B, and the systematic uncertainties are discussed in Section 7.2. Figure 8.3 shows the expected and observed distribution of muon momentum from events passing the CC inclusive selection cuts. In all, 1529 events are observed, while 1459 are expected in the NEUT MC (before the MC reweighting, see Section 6.1.5). After correcting these numbers for pile-up, the low-gain MicroMegas module, the out of FGD background, and the MC flux reweighting, these numbers become:

- $N_{\text{data}}^{\text{FGD}} = 1456$
- $N_{\text{MC}}^{\text{FGD}} = 1405$.

This leaves a data/MC correction of 1.036 ± 0.028 (stat.) $^{+0.044}_{-0.037}$ (det. sys.) ± 0.038 (phys. model).

This Data/MC ratio is consistent with unity within systematic errors. The errors on detector efficiency (det. syst.) and on cross sections and fluxes (phys. syst.) are larger than the statistical error on this measurement, and thus more statistics (such as data from Run II) would not reduce errors by much. Due to time constraints, and because the near detector configuration changed between Run I and Run II, it was

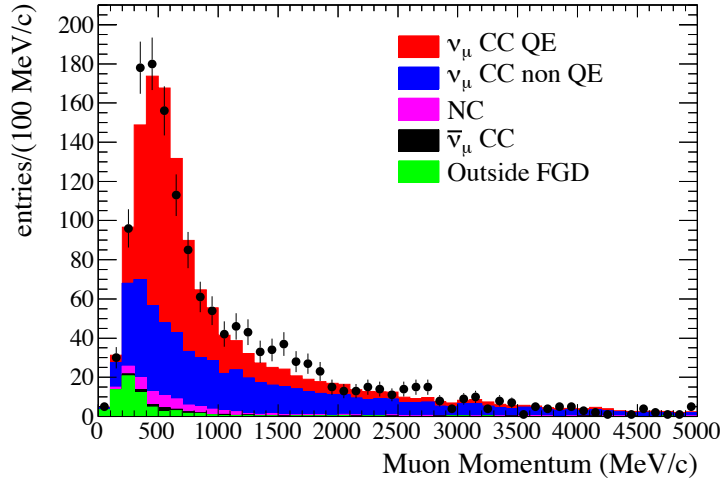


FIGURE 8.3: Distribution of measured μ momenta in events passing the CC inclusive analysis cuts in the ND280 tracker. The black points are data, and the colored histogram is MC.

decided to only use the Run I data for this normalization.

The far detector expectation is scaled by this ratio. This procedure significantly reduces beam and cross-section systematic uncertainties (Sections 7.3 and 7.1).

8.3 Statistical Technique

8.3.1 Feldman-Cousins Method

The Feldman-Cousins method (F-C, not to be confused with Fully Contained) is a frequentist statistical technique for constructing confidence intervals, as proposed in [99], though the technique was already known in statistics much earlier [144]. It allows for construction of confidence bands with good coverage without needing to choose between a upper-limit or a two-sided measurement before analysis. This merging of the limit and measurement analysis is the reason this is sometimes called the “Unified Method”.

The confidence limits set are designed to satisfy the Neyman construction [145]. This is a frequentist construction for an interval on a measured parameter at a

confidence level α (such as 90%). It states that, if we repeat the experiment many times, the interval should contain the true value of the measured parameter a fraction α of those times. In terms relevant to T2K, if we conducted the T2K experiment many times, each time making a new (and independent) measurement of $\sin^2 2\theta_{13}$, the true value of $\sin^2 2\theta_{13}$ should be inside our 90% confidence level (CL) region in 90% of the experimental results. In contrast to a Bayesian interpretation, this is not a statement about the PDF for $\sin^2 2\theta_{13}$, as its true value is fixed and unknown.

The way to produce an interval satisfying this is to consider the distribution of the measurable quantity x (such as ν_e event candidates, N_{obs}) for a given value of the fundamental parameter μ (such as $\sin^2 2\theta_{13}$). Following the notation in [99], we assume larger μ tends to yield larger x (this holds true for $\sin^2 2\theta_{13}$ and N_{obs}). For each possible value of μ , we can predict the PDF of x . One can select a region of the x PDF to be in the acceptance region for each μ . This region is called the confidence belt. An example confidence belt map is shown in Figure 8.4. For continuous x , we want a region between x_1 and x_2 which satisfies:

$$P(x \in [x_1, x_2] | \mu) = \alpha \quad (8.1)$$

Here, $P(x|\mu)$ is the PDF for x , the probability distribution to get some x assuming some value of μ . However, for discrete measurable parameters, like N_{obs} , we want our condition to avoid undercoverage, and exact coverage will not ordinarily be possible. Thus, we aim for *at least* 90% coverage, satisfying:

$$P(N_{\text{obs}} \in [N_1, N_2] | \sin^2 2\theta_{13}) \geq \alpha \quad (8.2)$$

If we choose the acceptance region in x for each μ before running the experiment, we will be fine. Thus, we could decide to always select a region which is only bounded on one side ($P(x < x_1 | \mu) = 1 - \alpha$), and this would produce an upper limit on μ . Alternatively, we could select a region bounded on each side ($P(x < x_1 | \mu) =$

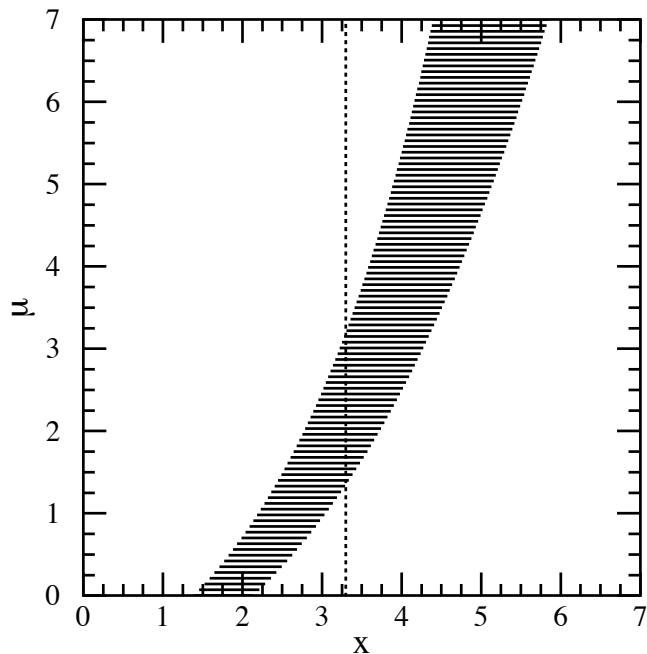


FIGURE 8.4: Example confidence belts, from [99]. The x -axis is the measurable parameter, and the μ -axis is the physics parameter. For each value of μ , a confidence belt is set up, selecting regions of x such that $P(x \in [x_1, x_2] | \mu) = \alpha$. After this set of belts (the horizontal lines) is created, the experiment is run, and a value of x is measured. This measurement is shown by the vertical dashed line. All values of μ for which the dashed line intersects the confidence belt are included in the final confidence interval. This clearly illustrates the difference between a confidence belt (in the measured parameter, horizontal lines) and a confidence interval (in the physical parameter, vertical line).

$P(x > x_2 | \mu) = (1 - \alpha)/2$) which would produce a 2-sided measurement on μ . Then, once we make a measurement, we take the set of all μ whose confidence belts contain the measured x . This set is our final confidence interval. Because we already showed that the confidence belt for any μ will contain the measured x in 90% of trials, then this must be true for the unknown true value of μ . Thus, whatever the true value of μ is, it will be included in the final confidence interval 90% of the time, and the coverage for this method is good. Figure 8.4 illustrates this.

The problem occurs when the choice of confidence belt is made based on the data. If x is small, one would be tempted to make an upper limit. If x is large, one would try to make a measurement. However, making this choice based on the data will result in *actual* coverage belts which undercover (contain the true μ less than 90% of the time). Details on how this happens can be found in [99], which refers to this phenomenon as “flip-flopping”. The F-C method solves this problem with an ordering principle which selects confidence bands, potentially making either a limit or a measurement, without changing the algorithm based on data.

The ordering principle in F-C is the likelihood ratio (LR)

$$LR = P(x|\mu) / P(x|\mu_{\text{best}}), \quad (8.3)$$

where x and μ are as described before, and μ_{best} is the physically allowed value of μ with maximal $P(x|\mu)$. The confidence band for each μ will be chosen to accept only values of x with a LR greater than some critical value. This critical value is chosen for each μ to correctly fill a 90% region (or whatever CL α we are using). This technique not only avoids the “flip-flopping” problem, but also properly treats physical boundaries in the true parameter space.

For this analysis, the exact form of the likelihood ratio uses the Poisson PDF (8.4). Here, θ is taken to represent all oscillation parameters.

$$LR = \frac{\text{Pois}(N_{\text{obs}}|\theta)}{\text{Pois}(N_{\text{obs}}|\theta_{\text{best}})} \quad (8.4)$$

In the actual analysis implementation, we perform the ordering according to $-2 \ln(LR)$. This can be used analogously to a χ^2 difference between a point being checked and the best-fit point. The $\Delta\chi^2$ analogy is sometimes helpful for relating the F-C method to other techniques.

One remaining issue is for the case where a measurement of fewer events than background is made. In this case, the limits on μ will be tighter than they would

have been if background alone were measured. Thus, an experiment with poorer background reduction may have a stronger limit than an experiment where backgrounds are removed, while neither experiment actually sees a signal. One solution to this is to report the expected experimental sensitivity (defined as the average upper limit obtained if there is no signal) along with the upper limit, so that a downward fluctuation in background is understood as only that.

8.3.2 *Systematic Error Incorporation*

One significant deficiency of F-C as described above and in the paper [99] is the lack of systematic error incorporation. This problem actually runs deeper than F-C, and is an issue with most frequentist methods. The trouble is the concept of systematic errors in an experiment to be repeated many times. The systematic error is (by definition) meant to identify the uncertainty in measurements which will remain despite repeated measurements. So, as an example, if we were wrong about the mass in the SK fiducial volume by 10% (an extreme example), this would not change from experiment to experiment, and so our measurement would be off in all the experiments. Because of this, the easy thing, which is to construct a PDF for our systematic errors, is not compatible with the strictly frequentist view.

While there are possible ways to incorporate systematic uncertainties without leaving the frequentist framework (see, for example, [104]), there are some potential drawbacks with these solutions. After comparing the characteristics of a few options (see Section 8.3.3), we decided to use a semi-Bayesian technique to incorporate systematic errors. This technique is described in some detail in [146], and is often associated with Cousins and Highland [147].

The fundamental strategy is to integrate over the systematic error PDFs. This is accomplished with a toy Monte Carlo method. At every point in oscillation space, we make a distribution of expected events. Without systematic errors, this distribution

would be exactly the Poisson distribution with the expected signal plus background (N_{exp}) as the mean. With systematic errors, we randomly draw systematic shifts on the number of events from each of our systematic error PDFs. We model most of the systematic errors as Gaussian distributions, with a few exceptions. For each set of randomly drawn shifts, we make a Poisson distribution for the shifted N_{exp} , and we sum all these distributions, and normalize. The resultant distribution is like a Poisson distribution, but it has been smeared out by the systematic errors. A 90% (or other CL) region is selected in this new smeared PDF, using the ordering principle from Equation 8.4. From this point on, the method is the same as ordinary F-C. This smeared Poisson distribution will be referred to as the N_{obs} PDF.

Philosophically, we are proceeding as if the systematic effects would change randomly over many experiments. This semi-Bayesian outlook has been used in other neutrino beam analyses (MINOS [148] [149] and K2K [56], for example). Full details on the procedure are in Section 8.4.

8.3.3 Method Check and Comparison

Prior to settling on the semi-Bayesian method described in Section 8.3.2, multiple methods were studied and considered. These considered methods include:

- **TRolke**: This is a method detailed by Rolke, Lopez and Conrad [104], and implemented into the ROOT analysis framework [150]. The fundamental method is based on the large-sample approximation to the likelihood ratio test statistic. That is, for high statistics, $-2\log(\text{LR})$ will converge to a χ^2 distribution which can be used to set limits. A disadvantage of this method is that this approximation is not always valid at low statistics, but it is significantly faster, computationally, than the full F-C treatment. The systematic error implementation is done through the “profile likelihood” method. This method replaces the ordinary F-C likelihood ratio with one where both the numerator and

denominator are optimized over systematic error parameters (nuisance parameters). By finding the maximum likelihood by shifting systematic parameters in both terms of the LR, the LR is no longer a function of the systematic shifts. See [104] for a full description of the profile likelihood method.

- **Feldman Cousins with Profile Likelihood:** It is possible to apply the profile likelihood method to Feldman Cousins without needing to approximate the LR distribution, as TRolke does. Without an existing implementation of this method, a ROOT class, capable of computing F-C limits with systematic error incorporation, was created for these studies. The ordinary likelihood ratio can be replaced with a simple profile likelihood ratio, similar to TRolke. This is a fully frequentist implementation of systematic errors within Feldman Cousins, at the expense of non-guaranteed coverage.
- **Feldman Cousins with Systematics in N_{exp} distribution:** This is the semi-Bayesian method used in the final analysis.
- **Feldman Cousins with Systematics in N_{exp} distribution and LR:** This is a variation on the semi-Bayesian technique, where, in addition to the “smeared” N_{obs} PDF, we also use a smeared probability in the likelihood ratio. This extra step was (upon further study) not necessary to achieve proper coverage, and had no noticeable benefit as far as the power of the technique is concerned.

All of these methods have advantages and disadvantages. In the end, we selected the method most used by past experiments measuring $\sin^2 2\theta_{13}$, as this would make it easiest to present the results. Additionally, the low expected beam exposure made it especially important that our method have proper coverage and good behavior at low statistics.

8.4 Analysis Details

8.4.1 Oscillation Computation

The first consideration for the oscillation analysis is the calculation of oscillation probabilities. A software package developed for the SK collaboration called Prob3++ [45] was used. This software calculates oscillation probabilities including full three flavor oscillation and matter effects. More information on the calculation is found in (Section 2.3.3). This software has been used for published atmospheric neutrino analyses from SK in the past [61]. The oscillation parameters in Table 5.1 are assumed.

To speed computations, a pre-calculated table for oscillations is used. For each of the oscillation points sampled, oscillation probabilities are computed for $\nu_\mu \rightarrow \nu_\mu$, $\nu_\mu \rightarrow \nu_e$, $\nu_e \rightarrow \nu_e$, and $\bar{\nu}_\mu \rightarrow \bar{\nu}_\mu$. The probability is computed for neutrino energies binned every 5 MeV from 0 to 2 GeV, and every 25 MeV from 2 to 10 GeV. Contributions from beam $\bar{\nu}_e$, and any other oscillation case (such as ν_τ appearance, or $\bar{\nu}_\mu \rightarrow \bar{\nu}_e$) are considered small and are ignored.

While it is not explicitly plotted in the final contours, our measurement of θ_{13} does depend on the value of θ_{23} . The plots produced for this analysis assume $\sin^2 2\theta_{23} = 1.0$. Because the oscillation probability for ν_e appearance goes (to first order) as $2 \sin^2 2\theta_{13} \sin^2 \theta_{23}$, one could replace the $\sin^2 2\theta_{13}$ -axis of the contour plots by

$$\sin^2 2\theta_{13} \rightarrow 2 \sin^2 2\theta_{13} \sin^2 \theta_{23} \quad (8.5)$$

to get the approximate measurement and sensitivity for other values of θ_{23} .

This approximation breaks down for large θ_{13} if $\sin^2 2\theta_{23}$ gets too small, though it holds well for values of $\sin^2 2\theta_{23}$ which are reasonably close to one. For $\delta_{\text{CP}} = 0$ and $\sin^2 2\theta_{23} = 0.89$, this approximation is accurate to within 1% for $2 \sin^2 2\theta_{13} \sin^2 \theta_{23} < 0.35$. This value of $\sin^2 2\theta_{23}$ is below the global 90% CL minimum [48], showing this approximation holds very well for $\delta_{\text{CP}} = 0$. The approximation is not as good

for other values of δ_{CP} , but T2K contours would not shift by more than $\sim 5\%$ in $2\sin^2 2\theta_{13}\sin^2 \theta_{23}$ for any value of δ_{CP} , for any $\sin^2 2\theta_{23} \geq 0.89$. The value of $\sin^2 2\theta_{23} \geq 0.89$ was chosen based on the 68% CL limit from the T2K ν_μ disappearance analysis [151].

8.4.2 Oscillation Grids

In order to calculate confidence levels with the Feldman-Cousins method, the N_{obs} PDF must be computed for many oscillation points. In our implementation, there is no simple reliable way to smooth contours between oscillation points, so a fine grid is necessary to prevent the final contour plots from looking very “pixelated”. We used a grid with 325 points evenly distributed linearly on the $\sin^2 2\theta_{13}$ axis, between 0 and 1, and 325 points evenly distributed on the other axis, either linearly in δ_{CP} or logarithmically in Δm^2 . An additional column is computed at $\sin^2 2\theta_{13} = 0$, to properly treat the background only case. This produces reasonably smooth contours, but an additional step, involving fitting or smoothing the contour lines, was required. For the δ_{CP} contours, the function used for fitting (both the best fit line and the upper and lower contours) is given by

$$y = \alpha_0 + \alpha_1 \sin((x + \beta)\pi) + \alpha_2 e^{\sin((x+\beta)\pi)} + \alpha_3 e^{\sin(-(x+\beta)\pi)} \quad (8.6)$$

where $y = \sin^2 2\theta_{13}$, $x = \delta_{\text{CP}}$, and α_i and β are fitted terms. This equation was able to fit the contours extremely well, and so the δ_{CP} plots required no additional smoothing. The Δm^2 contours are not easily described analytically, so the “Smooth” function in ROOT [152] was selectively applied to regions of the contours to reach publication quality without damaging the contour features.

8.4.3 Calculation of N_{exp}

The mean expected number of events at SK (\hat{N}_{exp}) is calculated for every oscillation point in the grid. In addition to this central value for the expected number of events, a

PDF for N_{exp} is produced incorporating systematic errors, from which a PDF for N_{obs} is produced by adding Poisson fluctuations. This N_{obs} PDF is our parameterization of how likely it is that we will observe N events at SK. The equations for \hat{N}_{exp} and $N_{\text{exp}}(\vec{\delta})$ are motivated below, where $\vec{\delta}$ represents a set of systematic shifts. Non-final equations are indicated with a superscript “*”. I will contract what each term is a function of as necessary to keep the equations readable.

We begin with a simple sum over SK MC events:

$$\hat{N}_{\text{exp}}^* = \sum_{\text{all MC evts}} \left(\Theta_{\text{cuts}} \times \gamma_{\text{norm}}(x) \times P_{\text{osc}}(\theta_{13}, \Delta m^2, \delta_{CP}, E_\nu^{\text{true}}, x) \right), \quad (8.7)$$

where Θ_{cuts} gives 1 if the event passes all selection cuts, and 0 if it fails,

γ_{norm} is the MC normalization factor (see Section 8.2 for details),

$x = \nu_\mu, \nu_e, \bar{\nu}_\mu, \nu_\mu \rightarrow \nu_e$, the neutrino species,

and P_{osc} is the oscillation probability computed from Prob3++ (see Section 8.4.1).

Next, we add in reweighting of the MC to the 10dv3 beam tuning (see Section 6.1.5 for the beam tuning description):

$$\hat{N}_{\text{exp}}^* = \sum_{\text{all MC evts}} \left(\Theta_{\text{cuts}} \times \gamma_{\text{norm}} \times P_{\text{osc}} \times w_{10a \rightarrow 10d}(E_\nu^{\text{true}}, x) \right). \quad (8.8)$$

We reweight this MC-only number using the ND280 off-axis tracker data (see Section 6.3). The ratio of single-muon CC candidate events in tracker data over the number of single-muon CC candidate events in the ND280 MC is our scaling factor. The spectrum is not considered, as we are just scaling the total number. This result is our central value for N_{exp} :

$$\hat{N}_{\text{exp}} = \left(\frac{N_{\text{NDOA1}\mu}^{\text{data}}}{N_{\text{NDOA1}\mu}^{\text{MC}}} \right) \sum_{\text{all MC evts}} \left(\Theta_{\text{cuts}} \times \gamma_{\text{norm}} \times P_{\text{osc}} \times w_{10a \rightarrow 10d}(E_\nu^{\text{true}}, x) \right). \quad (8.9)$$

Now, we can calculate the N_{exp} distribution with systematic shifts. For simplicity, all the constant (not changing with systematics) reweighting factors will be grouped together as $W_{\text{SKMC}} = \gamma_{\text{norm}} \times P_{\text{osc}} \times w_{10a \rightarrow 10d}$. The first step is to add the systematic errors for SK events. See Chapter 7 for details on these errors. Each δ_i is a systematic shift from a particular systematic error source. The sources included here include errors on cross section, nuclear effects and SK detector efficiency. The systematic errors may depend on an event's true neutrino energy (E_ν^{true}), reconstructed neutrino energy (E_ν^{rec}), interaction mode (m), and/or neutrino species (x), depending on the particular error source:

$$N_{\text{exp}}^* = \left(\frac{N_{\text{NDOA1}\mu}^{\text{data}}}{N_{\text{NDOA1}\mu}^{\text{MC}}} \right) \sum_{\text{all MC evts}} \left(\Theta_{\text{cuts}} \times W_{\text{SKMC}} \times \prod_{i=\text{sys error}} (1 + \delta_i(E_\nu^{\text{true}}, E_\nu^{\text{rec}}, m, x)) \right). \quad (8.10)$$

Next, we expand the ND280 MC into bins (which, in itself, does not actually change this equation from the last) and add in the ND280 event count errors. These errors δ_j include the cross section and nuclear effect errors at ND280, as well as the ND280 efficiency and statistical errors. The cross section errors are 100% correlated between ND280 and SK (except for the CCQE shape error), so that δ_i (for i a cross-section error) will be the same in both places. All other errors are not correlated between near and far detector:

$$N_{\text{exp}}^* = \left(N_{\text{NDOA1}\mu}^{\text{data}} / \sum_{m,x,E_\nu^{\text{true}}} \left(N_{\text{NDOA1}\mu}^{\text{MC}}(m, x, E_\nu^{\text{true}}) \times \prod_{j=\text{sys error}} (1 + \delta_j) \right) \right) \times \sum_{\text{all MC evts}} \left(\Theta_{\text{cuts}} \times W_{\text{SKMC}} \times \prod_{i=\text{sys error}} (1 + \delta_i) \right). \quad (8.11)$$

Finally, we add in the beam systematic error (Section 7.3). This error is not

correlated with the other systematic errors, and depends only on the oscillation parameters. The beam error is the error on the extrapolation between near detector and far detector:

$$\begin{aligned}
N_{\text{exp}}(\vec{\delta}) &= (1 + \delta_{\text{far/near}}(\theta_{13}, \Delta m^2, \delta_{CP})) \\
&\times \left(N_{\text{NDOA}1\mu}^{\text{data}} / \sum_{m,x,E_\nu^{\text{true}}} \left(N_{\text{NDOA}1\mu}^{\text{MC}} \times \prod_{j=\text{sys error}} (1 + \delta_j) \right) \right) \\
&\times \sum_{\text{all MC evts}} \left(\Theta_{\text{cuts}} \times W_{\text{SKMC}} \times \prod_{i=\text{sys error}} (1 + \delta_i) \right). \quad (8.12)
\end{aligned}$$

This is our final equation for N_{exp} . Drawing many values of the systematic shifts from their PDFs lets us build the N_{exp} PDF and the N_{obs} PDF.

8.4.4 Systematic Error Details

All the systematic error shifts, unless otherwise specified, are drawn from symmetric Gaussian distributions, with widths equal to the uncertainties given in Chapter 7. We do not allow the drawn shift to be such that we will get a negative number of events. If a randomly drawn δ value is less than -100%, we will set it to exactly -100%, to avoid the negative case. This procedure was shown to have no significant impact on the analysis.

For the SK errors, the signal and total background uncertainties are taken from Table 7.3. Signal and background are considered 100% correlated, and each source of error (vertex, energy scale, etc.) is independent. The total background error was calculated assuming uncorrelated background components.

The cross section errors (applied to both ND and SK) are found in Tables 7.1 and 7.2, plus the 6% ν_e/ν_μ ratio error. The CCQE shape error (only applied for SK) is in Figure 7.1. These depend on the neutrino species, true neutrino energy, and

interaction mode. The nuclear effect (FSI) errors at SK are found in Figure 7.2, and are a function of reconstructed energy and whether the event is signal or background. The FSI/other physical effect error for ND280 is a single 3.7% uncertainty on the total. The ND280 efficiency error is a simple Gaussian error (while an asymmetric error was provided, it was expanded conservatively to a symmetric error for simplicity with nearly no effect on the N_{exp} distribution), and a ND280 statistical error is applied as a Poisson distributed error (not Gaussian) with the other systematic errors. Note that errors are applied to ND280 on a bin-by-bin basis (as this is how the ND280 group provided their data and MC to the analysis group), while errors are applied to SK on an event-by-event basis.

The beam errors (which are a function of oscillation point) were pre-computed in a 50×50 grid for each plot's set of oscillation parameters, to save CPU time. The resulting beam error maps are described in Section 7.3.

8.4.5 Toy MC

At each oscillation point tested, 5000 random draws of the systematic parameters (δ_i) are performed. Applying these draws to $N_{\text{exp}}(\vec{\delta})$ (Equation 8.12) produces the N_{exp} PDF. An example of this distribution is shown in Figure 8.5.

For each draw of $N_{\text{exp}}(\vec{\delta})$, we produce a Poisson distribution with mean N_{exp} , and we sum these distributions and normalize to produce the N_{obs} PDF. In the analytic limit, this is:

$$\mathcal{L}_{N_{\text{obs}}}(N) = \int_0^\infty \text{Poisson}(N, \mu) \mathcal{L}_{N_{\text{exp}}}(\mu) d\mu \quad (8.13)$$

where $\text{Poisson}(N, \mu)$ is the Poisson probability of observing N events given an expected mean of μ , and \mathcal{L} represents a PDF.

The N_{obs} PDF at each oscillation point is used as an input to the Feldman-Cousins

N_{exp} PDF

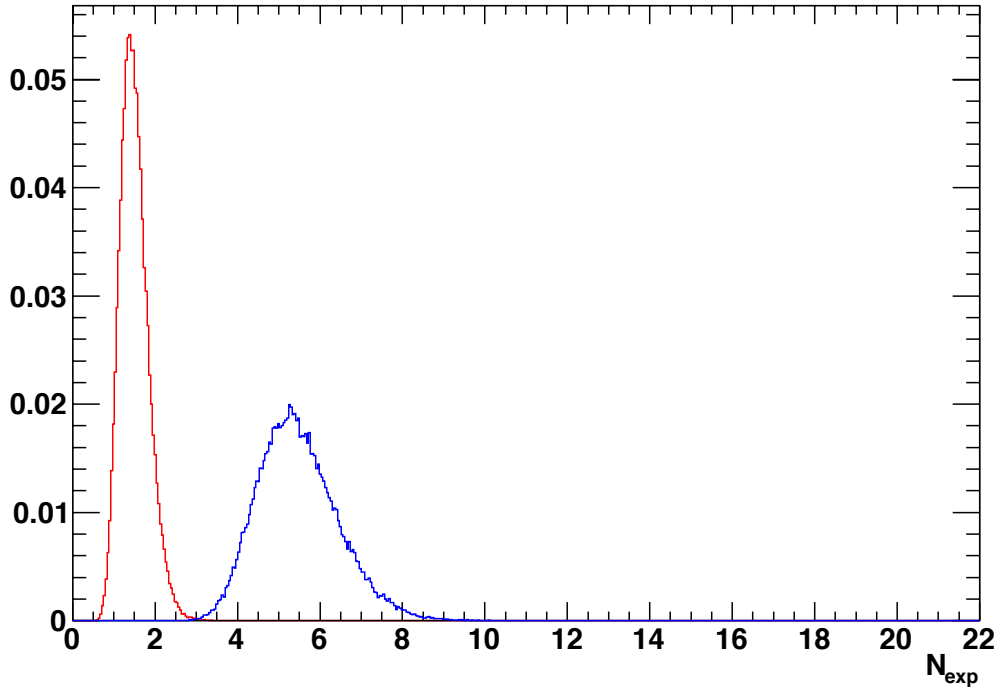


FIGURE 8.5: N_{exp} distribution from all systematic errors at normal hierarchy, $\delta_{CP} = 0$, $\Delta m_{32}^2 = 2.4 \times 10^{-3} \text{ eV}^2$, with $\sin^2 2\theta_{13} = 0.0$ in red, and, $\sin^2 2\theta_{13} = 0.1$ in blue. Normalization is arbitrary.

calculation. An example of this distribution is shown in Figure 8.6.

8.4.6 Feldman Cousins Ordering

The likelihood ratio (Equation 8.4) described in Section 8.3.1 is used to define the confidence band for each oscillation point. Values of N_{obs} are added, in decreasing order of LR, until at least 90% of the N_{obs} PDF is included. The $\Delta\chi^2 = -2\log(LR)$ for the final bin added in this way is stored, and the set of all these makes the $\Delta\chi_c^2$ map. This critical value map, along with the mean expected number of events at each point, is all that is needed to convert the final measured number of events into a 90% CL acceptance contour. One need simply compare the LR using the true N_{obs} to the critical value at each oscillation point. This critical map can be produced for

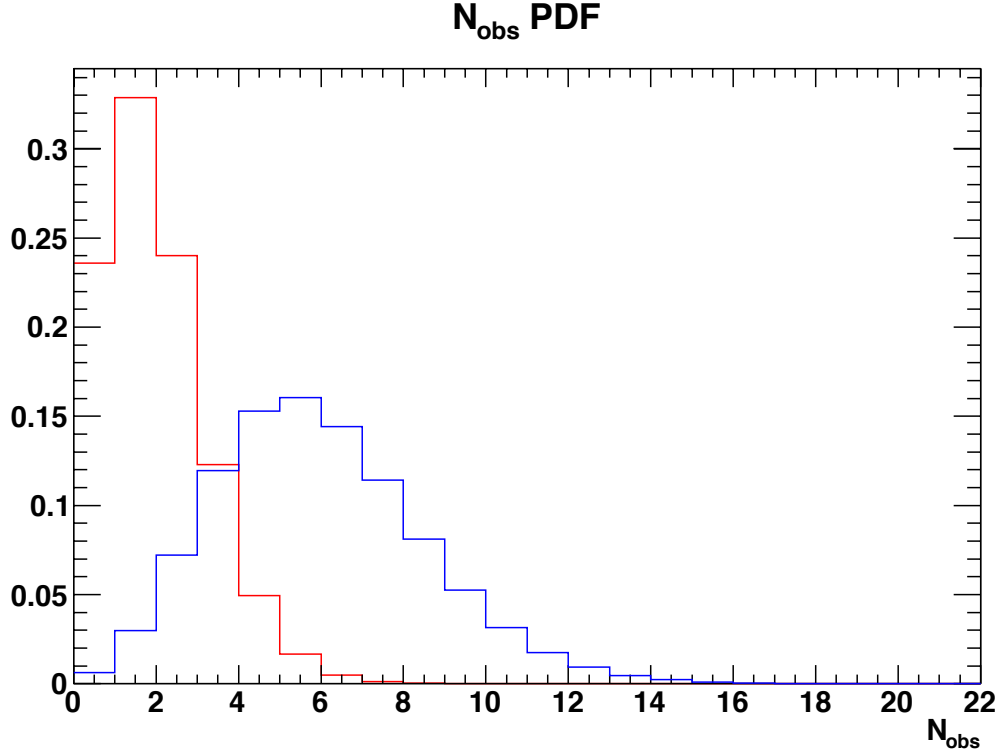


FIGURE 8.6: N_{obs} distribution from all systematic errors at normal hierarchy, $\delta_{CP} = 0$, $\Delta m_{32}^2 = 2.4 \times 10^{-3} \text{ eV}^2$, with $\sin^2 2\theta_{13} = 0.0$ in red, and, $\sin^2 2\theta_{13} = 0.1$ in blue. Normalization is arbitrary.

each CL (68%, 90%, 3σ , etc.).

An example $\Delta\chi_c^2$ map is shown in Figure 8.7. The variation in critical values is caused by discreteness effects (we are at low statistics) and proximity to boundaries in the oscillation parameter space.

We repeat the LR equation here, for reference.

$$LR = \frac{\text{Pois}(N_{\text{obs}}|\theta)}{\text{Pois}(N_{\text{obs}}|\theta_{\text{best}})} \quad (8.14)$$

One subtlety of the method is how to define θ_{best} . It is, of course, a set of oscillation parameters (not necessarily unique) which gives N_{best} , the value of N_{exp}

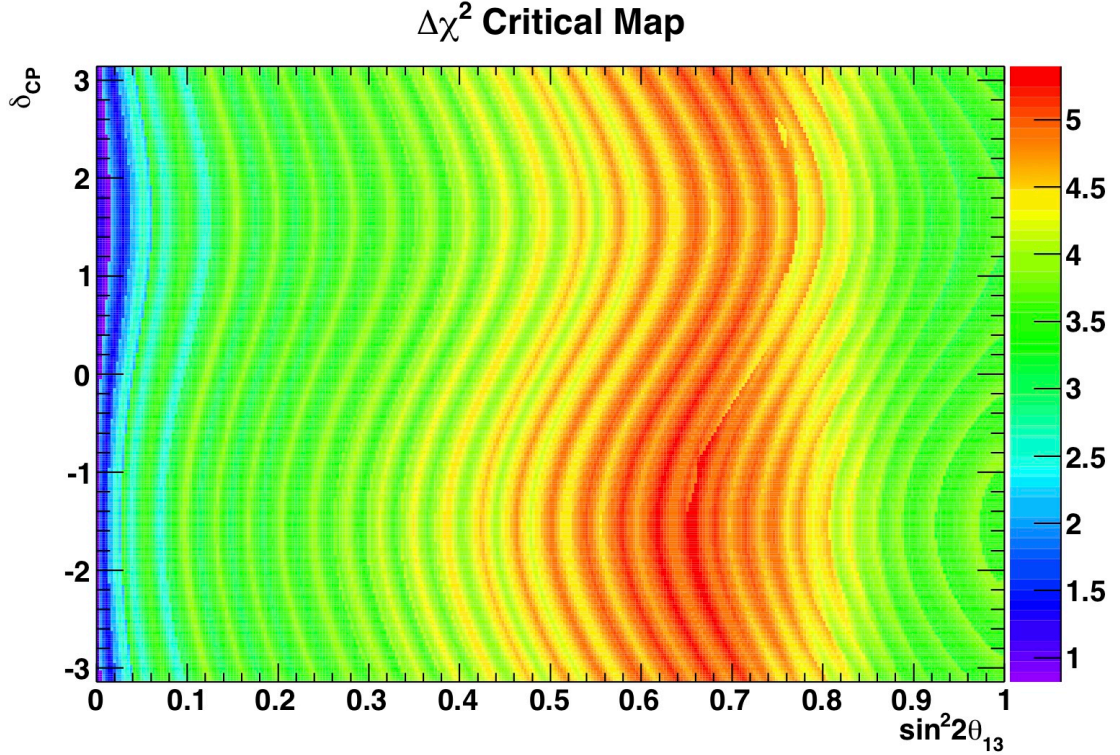


FIGURE 8.7: $\Delta\chi_c^2$ map for normal hierarchy at the 90% CL. This is produced in the “raster scan” style, so best-fit points are restricted to fixed values of δ_{CP} .

closest to N_{obs} , while still in the physical parameter space. We can define N_{best} as:

$$N_{\text{best}} = \begin{cases} N_{\text{min}}, & \text{for } N_{\text{obs}} < N_{\text{min}} \\ N_{\text{max}}, & \text{for } N_{\text{obs}} > N_{\text{max}} \\ N_{\text{obs}}, & \text{otherwise} \end{cases} \quad (8.15)$$

The definition of N_{min} and N_{max} is a choice we can make. We can do it as a “global scan”, where we find the minimum and maximum values of \hat{N}_{exp} across the whole set of parameters over which we plot. We can also do it as a “raster scan”, where we find the minimum and maximum values of \hat{N}_{exp} for fixed Δm^2 and δ_{CP} . In this raster scan case, each horizontal line in the final plots has its own N_{min} and N_{max} . It is for the determination of N_{min} that we computed a special column of oscillation points at $\sin^2 2\theta_{13} = 0$.

For the plots vs. δ_{CP} , we do a raster scan. We do not actually have any real sensitivity to δ_{CP} , and this method is also used by the NO ν A experiment (which presented their sensitivity vs. δ_{CP}). For the plots vs. Δm^2 , we do a global scan. We do have real sensitivity to Δm^2 , and this method was used by the CHOOZ experiment (which presented their results vs. Δm^2).

8.5 Results

As part of the unbiased analysis, the analyzers (and the rest of the collaboration) did not apply the event selection cuts to far detector data beyond the single-ring e -like cut until the analysis was ready to be performed (data were taken and systematic errors were determined, at least in preliminary form). At the May 2011 T2K collaboration meeting, this “blinding” was lifted, and the full Run I+II data set was analyzed. The selection cuts (described in Section 5.2) were applied as follows:

There were 88 events passing fully contained fiducial volume (FC FV) cuts. These are events with vertices at least 200 cm inside the ID wall, and no charge cluster in the OD. The vertex distributions are shown in Figure 8.8.

Of these, 41 events had only a single reconstructed ring. See Figure 8.9 for the cut distributions. Of these, eight were reconstructed as e -like. See Figure 8.10 (left) for the PID distribution. This is now a largely ν_e CCQE sample, but the background rejection cuts are not yet applied.

The visible energy cut was applied next. See Figure 8.10 (right) for the visible energy distribution. One low energy event was cut. Next, the decay electron cut was applied. See Figure 8.11 (left) for the decay electron distribution. The single event cut likely had a muon or pion present but below Cherenkov threshold. Six event candidates remained.

Next, the POLfit m_{π^0} cut was applied. The invariant mass distribution is in Figure 8.11 (right), though no events had a π^0 -like invariant mass, so none were

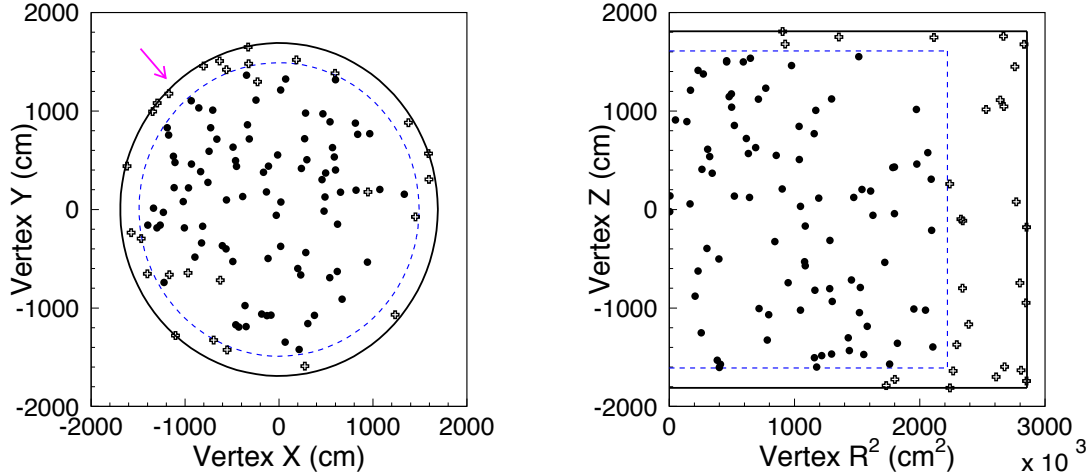


FIGURE 8.8: Reconstructed vertex distributions for fully contained (FC) T2K events with at least 30 MeV of visible energy. Events in the fiducial volume (FV) are shown as dots, events outside the FV are crosses. The left plot shows the x - y plane, as viewed from above. The right plot shows the r^2 - z plane. We use r^2 so that equal area on these plots represents equal volume. The solid line indicates the inner detector wall, the outer detector is not illustrated here. The dashed blue line is the fiducial volume boundary, 200 cm away from the wall. The arrow on the left plot indicates the neutrino beam direction. There is a slight deficit of FC events near the wall on the downstream side of the detector, but this is expected. Events tend to produce particles moving forward, and events near the downstream wall are more likely to have a product particle penetrate the PMT wall and deposit light in the OD, removing the event from the FC sample.

rejected. Finally, the reconstructed neutrino energy cut was applied, to reject high energy beam ν_e . No events were rejected by this cut, leaving the final count of six events passing all cuts. This is a significant observation with an expected background of 1.5 ± 0.3 events. The event selections are summarized in Table 8.2.

This observation of six events is put into the Feldman-Cousins analysis framework described in Section 8.4. This results in acceptance contours, as seen in Figure 8.13 and Figure 8.14. For $|\Delta m_{32}^2| = 2.4 \times 10^{-3} \text{ eV}^2$ and $\delta_{\text{CP}} = 0$, this results in a 90% CL allowed region of $0.03(0.04) < \sin^2 2\theta_{13} < 0.28(0.34)$ for the normal (inverted) hierarchy. The best fit value is $\sin^2 2\theta_{13} = 0.11(0.14)$ for the normal (inverted)

Table 8.2: Event reduction for the ν_e appearance search at the far detector. After each selection criterion is applied, the numbers of observed (Data) and MC expected events of ν_μ CC, intrinsic ν_e CC, NC, and the ν_e CC signal, are given. All MC CC samples include three-flavor oscillations for $\sin^2 2\theta_{13}=0.1$ and $\delta_{\text{CP}} = 0$, in the normal hierarchy.

	Data	$\nu_\mu + \bar{\nu}_\mu$ CC	ν_e CC	NC	$\nu_\mu \rightarrow \nu_e$ CC
(0) interaction in FV	n/a	67.2	3.1	71.0	6.2
(1) fully contained FV	88	52.4	2.9	18.3	6.0
(2) single ring	41	30.8	1.8	5.7	5.2
(3) e -like	8	1.0	1.8	3.7	5.2
(4) $E_{\text{vis}} > 100$ MeV	7	0.7	1.8	3.2	5.1
(5) no delayed electron	6	0.1	1.5	2.8	4.6
(6) non- π^0 -like	6	0.04	1.1	0.8	4.2
(7) $E_\nu^{\text{rec}} < 1250$ MeV	6	0.03	0.7	0.6	4.1

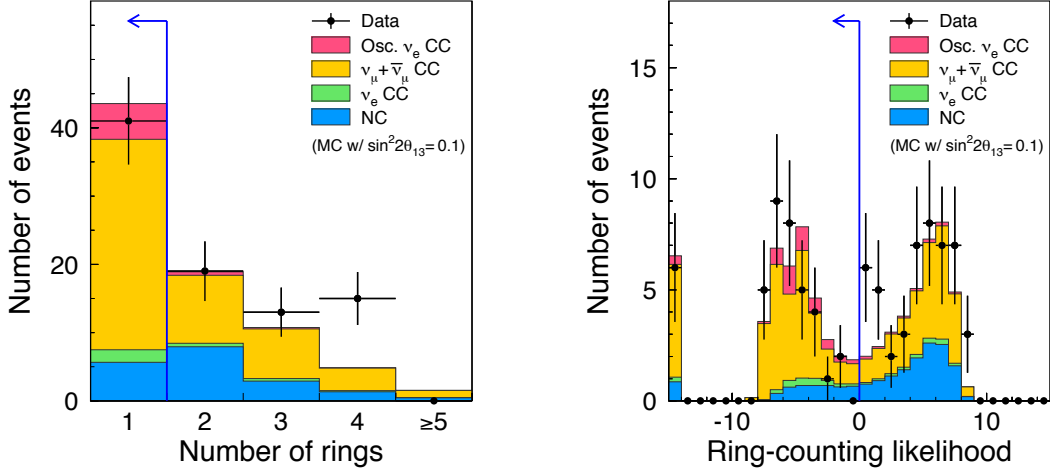


FIGURE 8.9: MC expectation and observed data for the ring-counting cut. Colored areas are MC expectation, and black dots and lines are data. The left plot shows the distribution of the number of events, and the right plot shows the ring-counting likelihood. For the likelihood, negative values indicate single-ring events. The MC expectations are produced assuming three-flavor oscillations for $\sin^2 2\theta_{13}=0.1$ and $\delta_{\text{CP}} = 0$, in the normal hierarchy. This corresponds to cut (2) in Table 8.2. Note that the data error bars here, and in Figures 8.9 through 8.12, are symmetric Poisson errors (\sqrt{N}), and do not account for the asymmetric nature of statistical error.

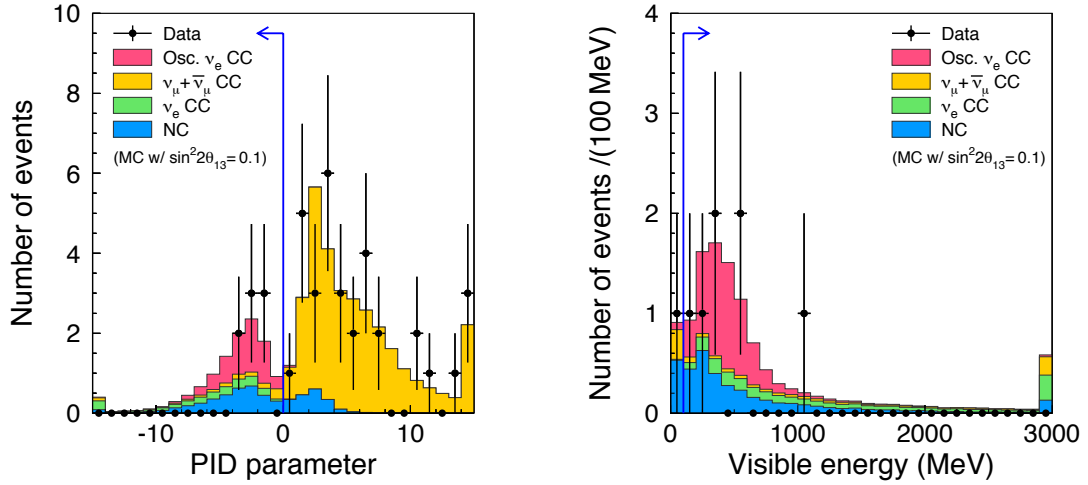


FIGURE 8.10: MC expectation and observed data for the particle ID and visible energy cuts. Colored areas are MC expectation, and black dots and lines are data. The left plot shows the distribution of particle ID likelihoods, with left being e -like, and right being μ -like. The right plot shows the visible energy distribution. The MC expectations are produced assuming three-flavor oscillations for $\sin^2 2\theta_{13}=0.1$ and $\delta_{\text{CP}} = 0$, in the normal hierarchy. These correspond to cuts (3) and (4) in Table 8.2. Note that the data error bars here, and in Figures 8.9 through 8.12, are symmetric Poisson errors (\sqrt{N}), and do not account for the asymmetric nature of statistical error.

hierarchy. Notably, this is the first experiment to exclude $\sin^2 2\theta_{13} = 0$ at the 90% CL.

The previous best limit on $\sin^2 2\theta_{13}$ came from the CHOOZ experiment [62], with a 90% limit of approximately $\sin^2 2\theta_{13} < 0.15$. The T2K result is consistent with this. The T2K best-fit is slightly below this for normal hierarchy, and approximately equal to this limit for inverted hierarchy, though it depends on δ_{CP} , which CHOOZ is insensitive to. The upper limit on $\sin^2 2\theta_{13}$ from T2K ($\sin^2 2\theta_{13} < 0.28$ for normal hierarchy) is not competitive with CHOOZ. However, CHOOZ did not set a lower limit on $\sin^2 2\theta_{13}$, as T2K did.

While our result is a measurement of $\sin^2 2\theta_{13}$ which is inconsistent with zero, the contours alone do not reveal exactly how inconsistent our measurement is. We made the decision to draw 90% contours before completing the analysis. However, we can

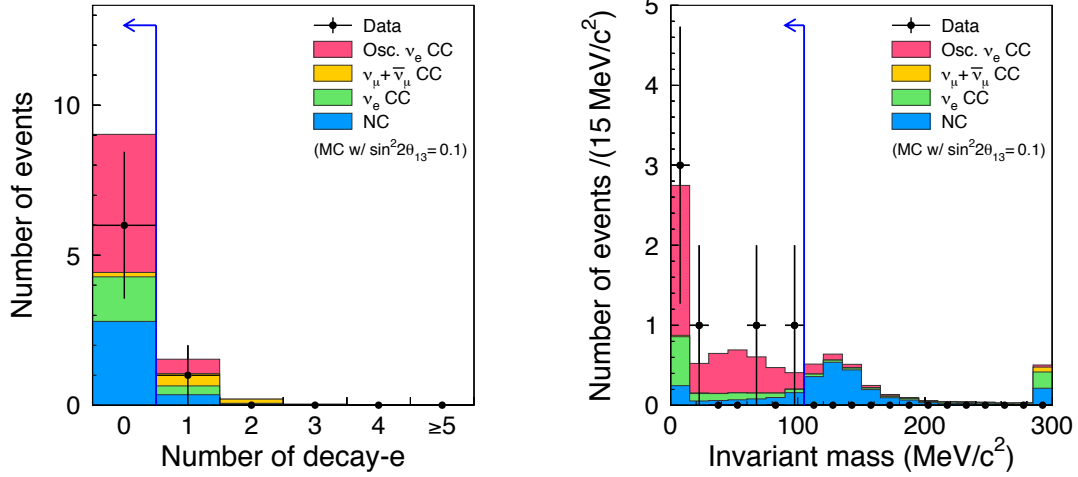


FIGURE 8.11: MC expectation and observed data for the decay electron and POLfit π^0 mass cuts. Colored areas are MC expectation, and black dots and lines are data. The left plot shows the distribution of number of decay electrons. The right plot shows the POLfit π^0 mass distribution. The MC expectations are produced assuming three-flavor oscillations for $\sin^2 2\theta_{13}=0.1$ and $\delta_{\text{CP}} = 0$, in the normal hierarchy. These correspond to cuts (5) and (6) in Table 8.2. Note that the data error bars here, and in Figures 8.9 through 8.12, are symmetric Poisson errors (\sqrt{N}), and do not account for the asymmetric nature of statistical error.

supplement this with the p-value to observe six or more events if $\sin^2 2\theta_{13} = 0$. We can find this p-value by integrating the N_{obs} PDF for $\sin^2 2\theta_{13} = 0$ (red curve in Figure 8.6) from zero to five events. Figure 8.15 shows this PDF, normalized, and on a logarithmic scale. The integrated area is 99.3%, which can be interpreted as a p-value of 0.7%.

It is common in high energy physics to represent the significance of a finding in terms of standard deviations (σ) in a Gaussian distribution [48]. While the PDF we integrate to get the p-value (Figure 8.15) is decidedly non-Gaussian, finding the appropriate σ value is still useful for comparison between experiments. As the integration region in Figure 8.15 is one-sided, we will use the one-sided Gaussian standard deviation area, rather than a two-sided one. Thus, we find the significance corresponding to this p-value to be 2.48σ (rather than 2.72σ , as one would get if

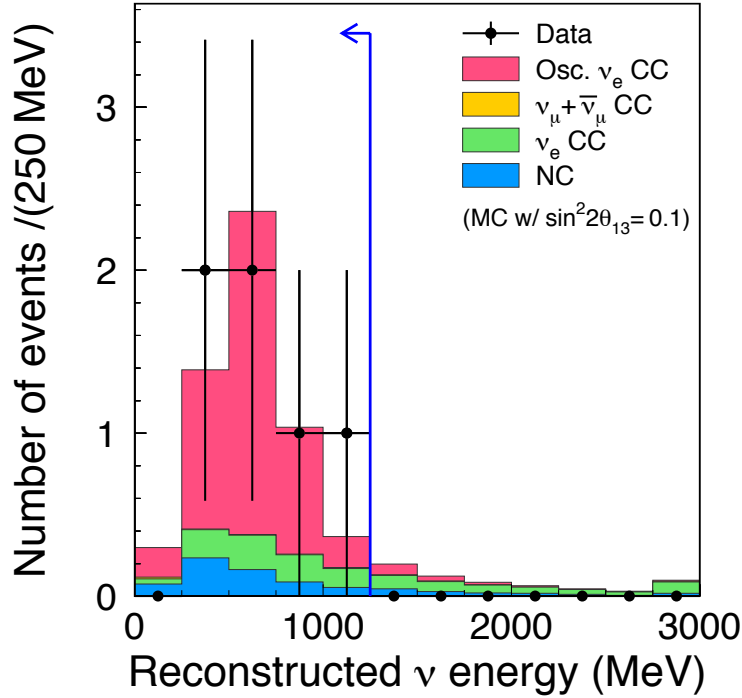


FIGURE 8.12: MC expectation and observed data for the reconstructed neutrino energy cut. Colored areas are MC expectation, and black dots and lines are data. This is the final signal selection cut, and shows the six remaining events after all cuts. The MC expectations are produced assuming three-flavor oscillations for $\sin^2 2\theta_{13}=0.1$ and $\delta_{\text{CP}} = 0$, in the normal hierarchy. This corresponds to cut (7) in Table 8.2. Note that the data error bars here, and in Figures 8.9 through 8.12, are symmetric Poisson errors (\sqrt{N}), and do not account for the asymmetric nature of statistical error.

this were a two-sided measurement). Note that this is not a statement that we have excluded $\sin^2 2\theta_{13} = 0$ to 2.48σ , or the 99.3% CL. That would require that particular confidence level to have been selected prior to the analysis. This is just a statement of how consistent our measurement is with the $\sin^2 2\theta_{13} = 0$ hypothesis.

8.6 Analysis Checks

Several data distributions were checked for unusual features, and the code used to produce these results was compared with an independent parallel analysis. Some of

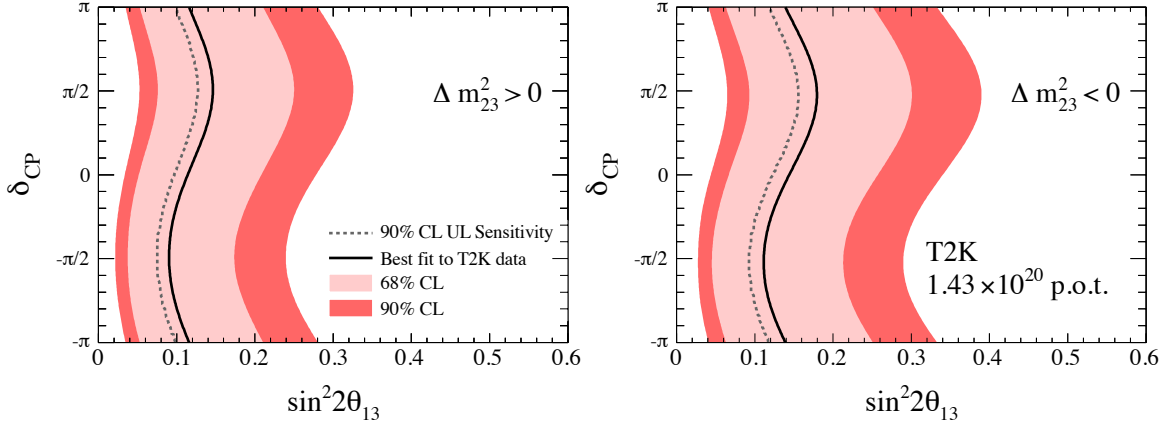


FIGURE 8.13: Final acceptance contours in the parameter space of $\sin^2 2\theta_{13}$ vs. δ_{CP} , for normal (left) and inverted (right) hierarchy. It is assumed that $|\Delta m_{32}^2| = 2.4 \times 10^{-3} \text{ eV}^2$. The contours are made in the “raster scan” style, so best-fit points are restricted to fixed values of δ_{CP} . The shaded regions indicate the 68% (lighter) and 90% (darker) confidence level contours. Note that $\sin^2 2\theta_{13} = 0$ is not in the 90% contour. T2K is the first experiment to make a measurement of $\sin^2 2\theta_{13}$ inconsistent with 0 at the 90% level. The solid line indicates the best fit point (where 6 events are expected), and the dashed line indicates the 90% CL upper limit sensitivity. Because a positive signal was observed, this sensitivity is not very relevant, but we show it for completeness. An old convention for Δm_{23}^2 is used here; this convention matches that in [153]. The convention used in this dissertation would show $\Delta m_{32}^2 > 0$ for the left plot (normal hierarchy) and $\Delta m_{32}^2 < 0$ for the right plot (inverted hierarchy).

the key distributions from these checks are included here.

Distributions of event arrival times indicated good matching with the T2K beam. Figure 8.16 (left) shows the arrival times for all events in the 1 ms T2K beam trigger, relative to the trigger center. Two off-timing FC events were recorded, only one in the FV. This was within the background expectation (from atmospheric neutrinos and other backgrounds). These background events were easily rejected by the beam timing cut. Figure 8.16 (right) shows the arrival times for all on-timing FC events, with an absolute timing offset applied. This figure is similar to Figure 3.3, though the six ν_e appearance candidates are highlighted.

The cumulative number of events relative to accumulated POT can be checked for indications that the beam or detector operation was abnormal for some time period.

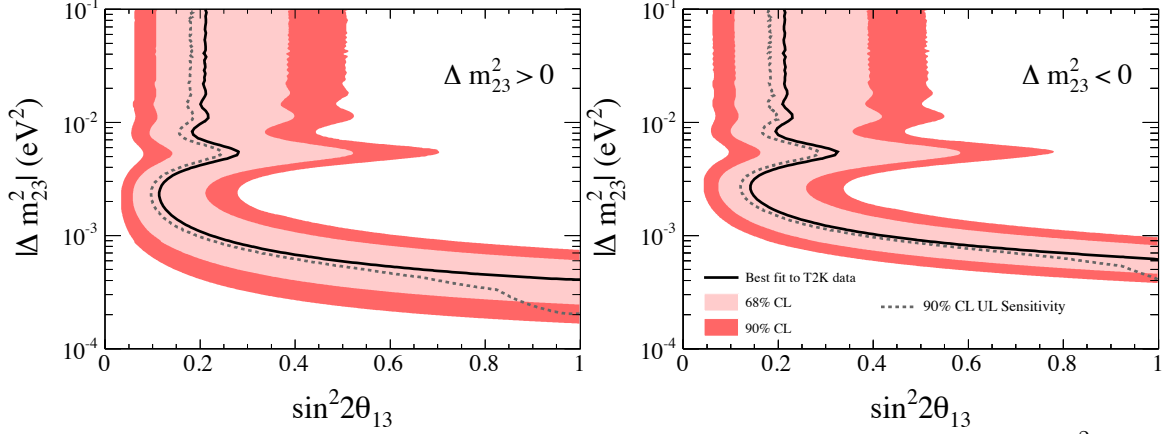


FIGURE 8.14: Final acceptance contours in the parameter space of $\sin^2 2\theta_{13}$ vs. Δm_{32}^2 , for normal (left) and inverted (right) hierarchy. It is assumed that $\delta_{\text{CP}} = 0$. The contours are made in the “global scan” style, so best-fit points are found anywhere in the plotted range. The shaded regions indicate the 68% (lighter) and 90% (darker) confidence level contours. Note that $\sin^2 2\theta_{13} = 0$ is not in the 90% contour. T2K is the first experiment to make a measurement of $\sin^2 2\theta_{13}$ inconsistent with 0 at the 90% level. The solid line indicates the best fit point (where 6 events are expected), and the dashed line indicates the 90% CL upper limit sensitivity. The dip in the sensitivity at low $|\Delta m_{32}^2|$ is an artifact caused by low statistics and a change in the expected number of events as a function of Δm_{32}^2 where $\sin^2 2\theta_{13} = 0$. An old convention for Δm_{23}^2 is used here; this convention matches that in [153]. The convention used in this dissertation would show $\Delta m_{32}^2 > 0$ for the left plot (normal hierarchy) and $\Delta m_{32}^2 < 0$ for the right plot (inverted hierarchy).

The cumulative distributions for all FC events (left) and all signal candidate events (right) are shown in Figure 8.17. Kolmogorov-Smirnov (KS) tests were performed to see how well the cumulative event distributions fit to the cumulative POT. The KS test is based on the maximum distance between the expected (exactly linear with POT) and observed distributions. In both cases, the KS test result indicated no significant anomaly.

The vertex distribution of events passing all selection cuts (Figure 8.18) looks less uniform. Several events are located near the FV boundary on the side of the SK tank where the T2K beam enters. This might suggest that some background mimicking ν_e signal events was entering from outside the detector. Several extensive studies

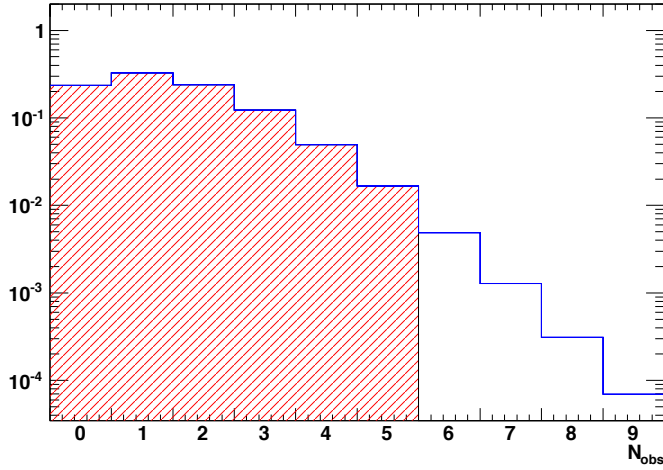


FIGURE 8.15: The normal hierarchy N_{obs} PDF as $\sin^2 2\theta_{13} = 0$ with $\Delta m_{32}^2 = 2.4 \times 10^{-3} \text{ eV}^2$ and $\delta_{\text{CP}} = 0$. The region from zero to five events is integrated (hatched region in red) to get 0.9934. Thus, the p-value for our measurement, assuming $\sin^2 2\theta_{13} = 0$, is 0.66%. This is equivalent to a one-sided 2.48σ significance.

were performed by T2K-SK group members to determine if this was the case [154]. Studies using MC of events with vertices outside of the ID showed it was extremely unlikely for such events to pass selection cuts. Also, there was no indication that this sort of event pile-up near the FV boundary was present in SK-IV atmospheric data. Finally, statistical tests showed that this distribution is unlikely, but that it would not be unreasonable for it to appear as a statistical fluctuation. Further information on the vertex distributions can be found in an internal T2K note [154].

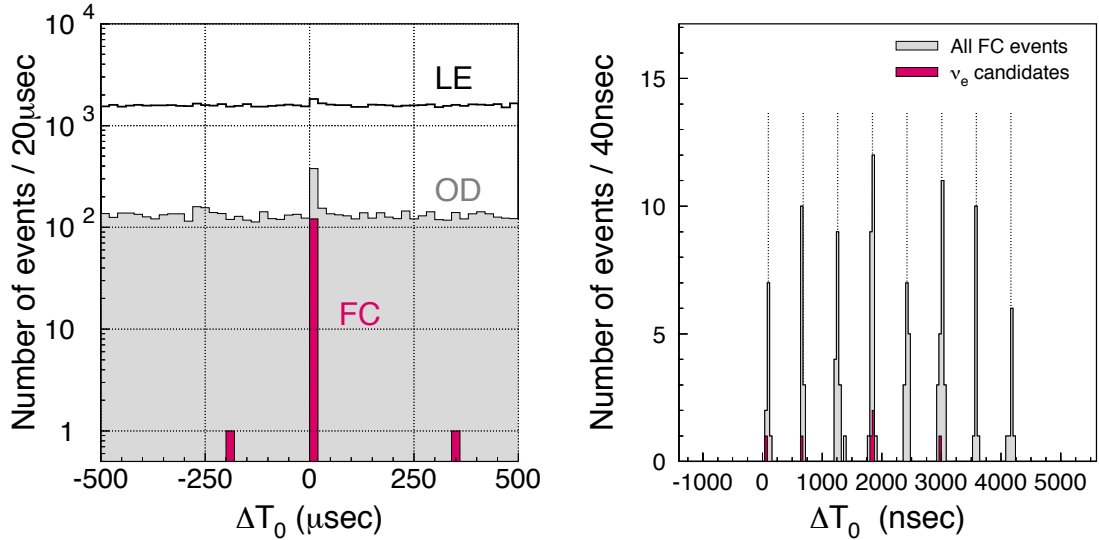


FIGURE 8.16: The left figure shows the timing of all events recorded in the T2K trigger window relative to the arrival time of the start of the beam spill. Low energy and OD background events are shown, and the FC events are in magenta. The two off-timing FC events are within background expectations. The right figure shows the timing of T2K events relative to the beam trigger, with an absolute offset fitted. The six ν_e candidates are highlighted in magenta. See the caption of Figure 3.3 for more information.

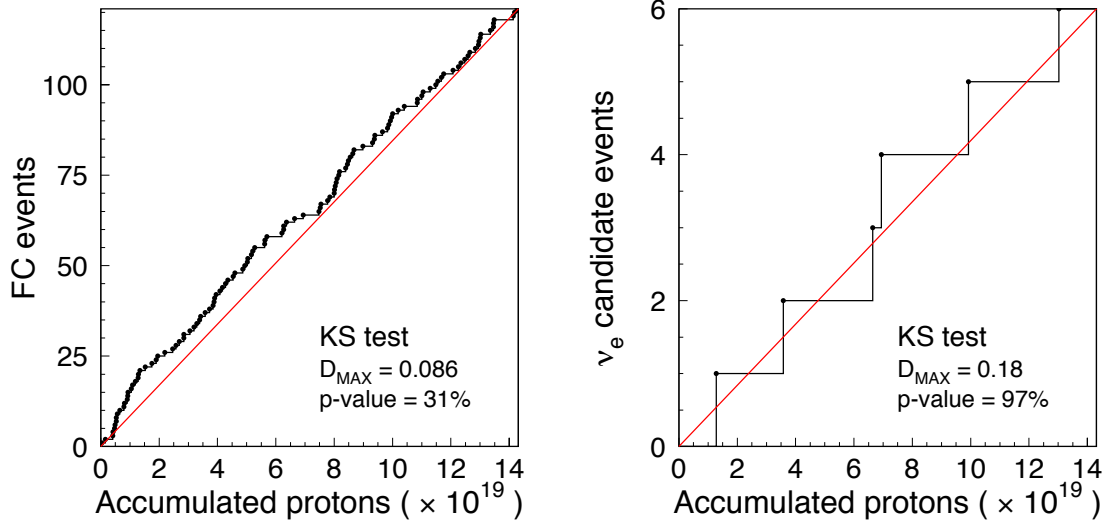


FIGURE 8.17: The cumulative FC (left) and ν_e signal candidate (right) events as a function of accumulated POT. The Kolmogorov-Smirnov (KS) test is applied to measure how well the observed cumulative distribution matches a uniform one. The matching goodness is presented as a p-value indicating how likely it is that a random draw of events would have a larger maximum deviation from expected than the observed one.

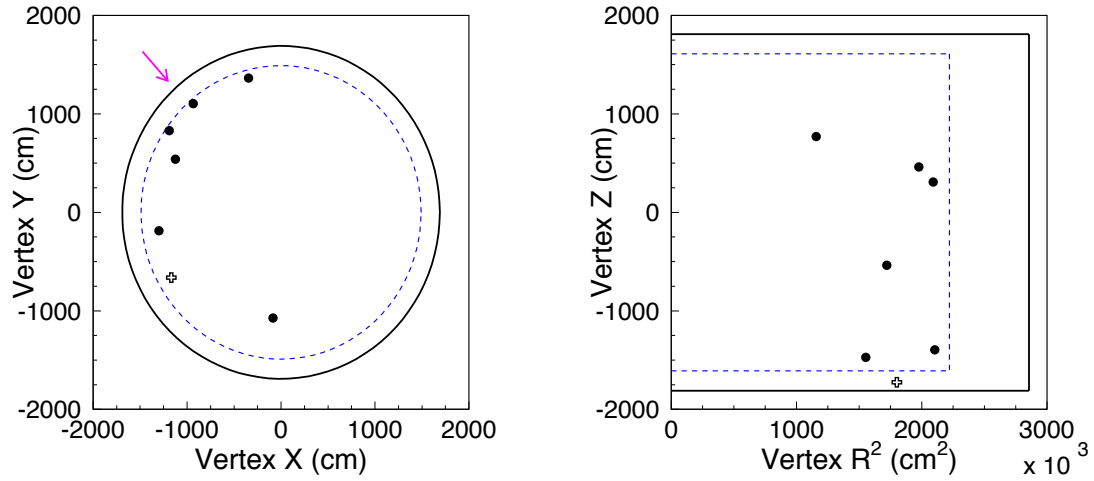


FIGURE 8.18: Reconstructed vertex distributions for events passing all the ν_e selection cuts. In addition to the six events passing all the cuts, a seventh event passes all cuts except the fiducial volume (FV) cut, and this event is shown as a cross, rather than a dot. The left plot shows the x - y plane, as viewed from above. The right plot shows the r^2 - z plane. We use r^2 so that equal area on these plots represents equal volume. The solid line indicates the inner detector wall, the outer detector is not illustrated here. The dashed blue line is the fiducial volume boundary, 200 cm away from the wall. The arrow on the left plot indicates the neutrino beam direction. The feature of concern is the clustering of events near the FV boundary, especially near the side where the beam enters the tank.

9

Conclusions

This dissertation describes indications of $\nu_\mu \rightarrow \nu_e$ appearance observed at T2K [153]. This provided the first evidence to better than 90% CL for non-zero θ_{13} . The contours for the 90% CL allowed region are shown in Figures 8.13 and 8.14. The 90% CL allowed region from this measurement is $0.03(0.04) < \sin^2 2\theta_{13} < 0.28(0.34)$ for $\delta_{\text{CP}} = 0$ and $|\Delta m_{32}^2| = 2.4 \times 10^{-3} \text{ eV}^2$ in the normal (inverted) hierarchy. The best fit is $\sin^2 2\theta_{13} = 0.11(0.14)$ in the normal (inverted) hierarchy.

The final data had six ν_e candidate events, with an expected background of 1.5 ± 0.3 . Under the $\sin^2 2\theta_{13} = 0$ hypothesis, there is only a 0.7% probability to observe six or more events. Thus, this is a strong indication, at 2.5σ , that θ_{13} is non-zero. Since this result was made public, the MINOS [58], Double Chooz [155], Daya Bay [156], and RENO [157] experiments have released results which appear to further support this conclusion, and which are consistent with the T2K measurement of $\sin^2 2\theta_{13}$.

If $\sin^2 2\theta_{13}$ is relatively large, as suggested by the T2K result, it should be possible to measure the neutrino oscillation CP-violating phase, δ_{CP} , using future beam oscillation experiments (such as the Hyper-Kamiokande long baseline experiment [65]

or LBNE [158]). Also, a large value for θ_{13} makes it easier to resolve the neutrino mass hierarchy by observing oscillation with matter effects on a very long baseline (as is proposed with NO ν A [159]). As the T2K experiment resumes operation, this result will quickly be improved upon, as the experiment is still in the statistically limited regime, and more beam time will quickly improve the experimental discovery potential.

Appendix A

Decay Electron Studies

This appendix describes some of the work done by the author using decay electrons for calibration and systematic error study purposes at SK.

A.1 Decay Electron Calibration Details

As described in Section 4.8, decay electrons from cosmic ray muons are used as a calibration point for the SK energy scale. Data were compared to MC to check the absolute energy scale, and data were compared over time for relative energy scale. Plots of these measurements can be found in Figures 4.14 and 4.16. Some of the details of the analysis are described here.

The cosmic ray stopping muon data come from the events passing the first step of partially contained (PC) reduction (see [46] for more about PC reduction). Events passing some basic stopping muon cuts are selected and are written to file in near real-time. These files contain good stopping muon candidates, as well as some which will be rejected by further selection cuts. The selection cuts for stopping muon candidates (for the momentum/range calibration) and decay electron candidates are

quite different; only the latter will be described here.

Decay electron candidates must pass the following cuts:

- **Single decay electron:** The cosmic ray muon has only one associated decay electron.
- **Reconstructable decay-electron:** The decay electron reconstruction algorithms only work if the time between the stopping muon and decay electron is at least 600 ns.
- **Good reconstruction:** The stopping muon did not fail, and the goodness of the decay electron fit is at least 0.5.
- **Decay time cut:** The time between the stopping muon and decay electron must be at least $1.2 \mu\text{s}$. This requirement is because the reconstruction for events right after the stopping muon is not as good as for later events, partially due to individual PMT trigger dead-times (see Section 4.3).
- **Total muon charge minimum:** This cut is applied in the first PC reduction step for data, but is repeated during analysis so that it is applied to MC as well. The total charge from the stopping muon must be at least 1000 p.e., corresponding to a muon momentum of around $300 \text{ MeV}/c$.
- **Low energy rejection:** Decay electron events with fewer than 60 hits in the sliding 50 ns time window are rejected. This removes very low energy decay electrons, and gammas from nuclear de-excitation following μ^- absorption in an oxygen nucleus. When the author first began the decay electron studies, the simulation of these nuclear gammas did not match data very well, so this cut was implemented to side-step the problem. Later on, the simulation was improved, though this cut is kept for consistency.

- **Fiducial volume:** The reconstructed decay electron vertex must be inside the FV (2 m from the ID wall).

The absolute scale calibration is done by applying these selection cuts to both decay electron data and MC. The MC comes from the stopping muon MC, which uses the reconstructed kinematics of data stopping muon events as an input for generation. The MC decay electron kinematics are not based on data, just physics. The mean values of the data and MC spectra are compared for the calibration, as described in Section 4.8. The data for the absolute scale calibration comes from April 2009, and the MC user water parameters tuned to those measured in that month.

This same procedure is applied for the time variation check, though in this case an additional cut is used on the date of the decay electron. The data are divided by date into the 1st-10th, 11th-20th, and 21st-end of the month, and this is what is plotted in Figure 4.16. The time variation plots are produced automatically, processing the new data once per day.

A.2 Muon Polarization

Decay electrons can also be used for position dependence studies in SK. A significant impediment to this study, however, was the variation in the Michel spectrum due to muon polarization. This is a relatively small effect in energy, but it is enough to affect analysis at the 1% level. Because the position dependence effects in SK are also at the 1% level, it would be necessary to account for this polarization. As most cosmic ray muons are downgoing (and none are upgoing), the muon polarization effects can appear as a position or direction dependence in SK, if not properly accounted for.

Atmospheric muons produced from cosmic ray interactions in the upper atmo-

sphere tend to have a preferred helicity due to the chirality of the weak interaction.

$$p + p \rightarrow \pi^+ + X \Rightarrow \pi^+ \rightarrow \mu^+ + \nu_\mu \quad (\text{A.1})$$

$$p + p \rightarrow \pi^- + X \Rightarrow \pi^- \rightarrow \mu^- + \bar{\nu}_\mu \quad (\text{A.2})$$

We use X to represent other daughter particles which are not of interest. The helicity is not entirely fixed because, in the center of mass frame, the muon energy and muon mass are of the same order, allowing boosts to affect the muon helicity. We expect that μ^+ should prefer negative helicity (left-handed), while μ^- should prefer positive helicity (right-handed). This preferred helicity is equivalent to a polarization of the muon. Assuming the muon's polarization is not affected by the muon's passage through air, rock, and water, a stopped muon in SK will show a bias in decays relative to the muon's initial direction. Considering the kinematic phase space and conservation of angular momentum, we expect more decays with e and μ momenta anti-aligned than aligned. Additionally, we expect higher energy decay electrons when the momenta are anti-aligned. These expectations do not depend on the ratio of μ^+/μ^- .

There is a key flaw with this very simple case: the muons at rest will tend to depolarize in the water. The mechanisms for depolarization, however are different between μ^+ and μ^- . Thus, μ^+ tend to stay mostly polarized in water, while μ^- , which can be captured by nuclei, are largely depolarized ($\sim 95\%$ depolarized) [89]. The depolarization in air and rock for muons is small. It is therefore only necessary to consider polarization for μ^+ .

In SKdetsim (see Section 6.1.4), muon decay is handled by a pair of custom routines. The μ^- decay routine computes decays isotropically, and computes the momentum spectra with consideration for nuclear capture, based on [160]. The μ^+ routine uses a simple momentum formula with isotropic decays.

To account for polarization effects, I (the author, working with J. Kameda (ICRR))

set up a special case in the μ^+ routine, to be used only for cosmic ray muons. The idea is to assume a certain polarization of atmospheric μ^+ , and compute the decays based on that. The polarization (and charge fraction) of atmospheric muons was measured by Kamiokande-II, which was located near where SK is located currently (in the same mountain). The similar overburden of rock means that the spectrum of muons stopping in SK is almost the same as the spectrum of those stopping in Kamiokande-II, at around 1.2 TeV. The polarization measurement from Kamiokande-II was [89]

$$P_0 = \frac{N_- - N_+}{N_- + N_+} = 0.26 \pm 0.04 \text{ (stat)} \pm 0.05 \text{ (syst)}. \quad (\text{A.3})$$

This is a measurement for the polarization at muon production, so we expect the observed value to be affected by the μ^+/μ^- ratio, water depolarization, and other such effects, but this is a starting point.

For each cosmic ray muon simulated, a polarization is selected randomly based on an input polarization level. A decay direction and energy is then selected randomly such that the rate is of the form [161][162]

$$R(\theta, E_e) \propto E_e^2 \left[\left(\frac{3}{4} m_\mu - E_e \right) - \cos \theta \left(\frac{1}{4} m_\mu - E_e \right) \right] \quad (\text{A.4})$$

where E_e is the electron energy and $\cos \theta$ is the cosine of the angle between the muon spin polarization and the decay electron momentum. Terms of order $(m_e/m_\mu)^2$ are neglected. The main tuning parameter for this is the polarization level, which was adjusted until an acceptable fit was found (with data matching MC) at 25% polarization. Histograms of the decay electron count as a function of $\cos \theta_{\mu-e}$ (cosine of the angle between the muon direction and electron direction) are in Figures A.1 and A.2, for no polarization and 25% polarization, respectively.

This addition to SKdetsim is important for position dependence studies, but should have no measurable effect on the absolute energies of decay electrons in the

simulation (if direction is ignored). Additionally, muon polarization can only be used for cosmic-ray stopping muons, as neutrino-produced muons will not follow the cosmic ray polarization rates.

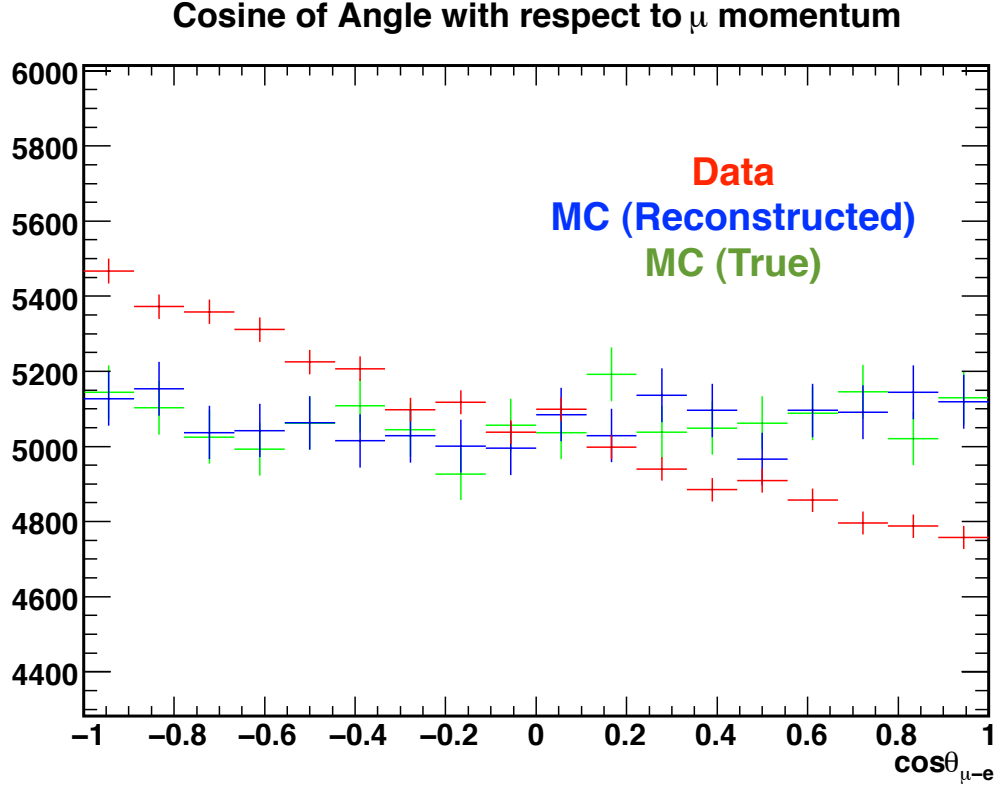


FIGURE A.1: Histograms of decay electron events by the angle between muon direction and electron direction (thus, $\cos\theta_{\mu-e} = 1$ for anti-aligned decays). The red crosses are data, blue crosses are MC, and green crosses are MC truth information (not reconstructed). The data and MC are normalized together. This is with MC which does not account for muon polarization. Error bars are statistical.

The data and MC mean energy variation for different $\theta_{\mu-e}$ also shows improvement with the polarized MC. This is shown in Table A.1. The energy variation between data and MC in decay-direction dependence is brought below 1%, and so decay electrons can be used for position and direction dependence studies.

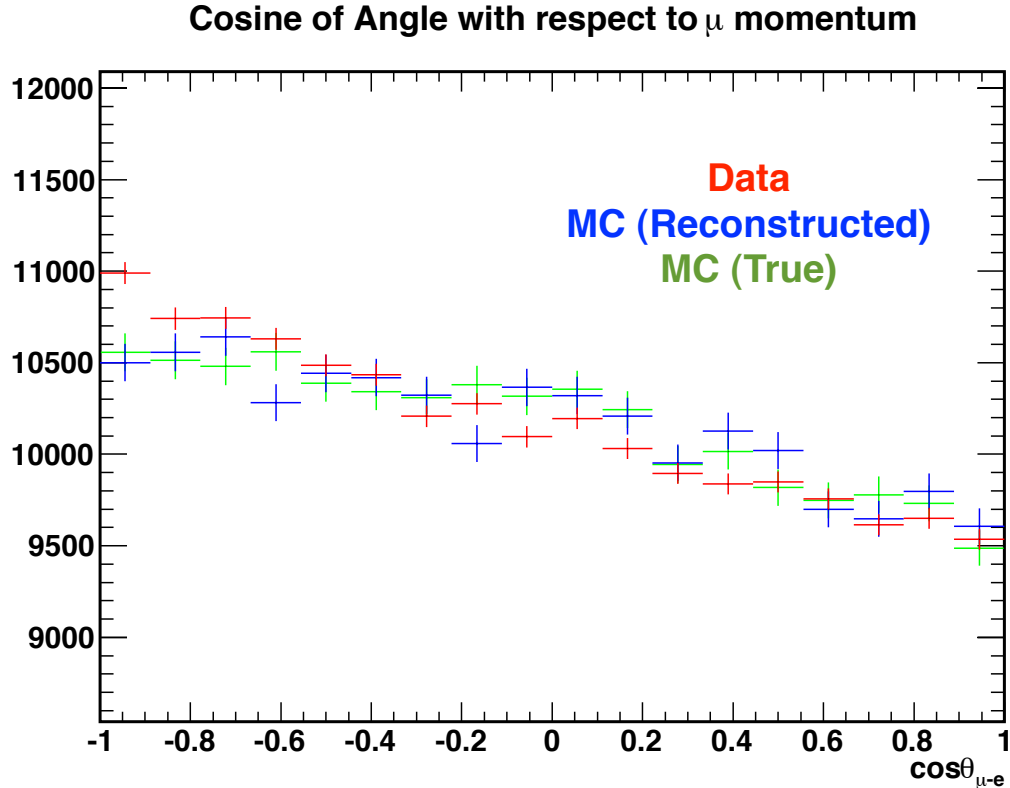


FIGURE A.2: Histograms of decay electron events by the angle between muon direction and electron direction (thus, $\cos \theta_{\mu-e} = 1$ for anti-aligned decays). The red crosses are data, blue crosses are MC, and green crosses are MC truth information (not reconstructed). The data and MC are normalized together. This is with MC assuming 25% polarization for μ^+ . More decay electron data are used in this plot than in Figure A.1. Error bars are statistical.

A.3 Position and Direction Dependence

There are two main things to check for with position and direction dependence. First, is matching between data and MC. Next, is variation over time. These checks can help determine whether water quality variation in the tank is appropriately modeled in SKdetsim, and may eventually lead to improved momentum reconstruction for SK.

As of 2009, a simple model for position-dependent water transparency has been implemented in SKdetsim. This helped improve the agreement of some energy-scale

Table A.1: Table of mean energy for decay electrons at different decay-angles. Events are divided into aligned ($\cos \theta_{\mu-e} > 0.3$), perpendicular ($|\cos \theta_{\mu-e}| < 0.3$), and anti-aligned ($\cos \theta_{\mu-e} < -0.3$) bins. The data and MC means are given, for both old (unpolarized) and new (polarized) MC. Other changes were made to the MC as well, so the absolute energy scale changed somewhat. Errors are statistical. Maximum MC/data variation between angle bins for old MC is $1.3\% \pm 0.2\%$, while for new MC it is $0.2\% \pm 0.2\%$. Thus, the MC/data ratios are much more consistent (between angle bins) with the polarized MC than with the unpolarized version.

Angle Bin	Sample	Old MC (Unpolarized)	New MC (Polarized)
Aligned ($\cos \theta_{\mu-e} > 0.3$)	+ Data	37.16 ± 0.03 MeV	37.16 ± 0.03 MeV
	+ MC	37.63 ± 0.07 MeV	36.85 ± 0.05 MeV
	MC/Data	1.013 ± 0.002	0.992 ± 0.002
Perpendicular ($ \cos \theta_{\mu-e} < 0.3$)	\perp Data	37.36 ± 0.03 MeV	37.36 ± 0.03 MeV
	\perp MC	37.42 ± 0.07 MeV	36.98 ± 0.05 MeV
	MC/Data	1.002 ± 0.002	0.990 ± 0.002
Anti-Aligned ($\cos \theta_{\mu-e} < -0.3$)	- Data	37.67 ± 0.03 MeV	37.67 ± 0.03 MeV
	- MC	37.67 ± 0.07 MeV	37.32 ± 0.05 MeV
	MC/Data	1.000 ± 0.002	0.991 ± 0.001

checks, but not others. This is a motivating factor in these studies. The general trend for water transparency is that the transparency is worse near the top of the tank. The bottom of the tank is where water is injected after purification, so it is not surprising that the water quality worsens closer to the top.

The first check for position dependence in the tank uses decay electrons from four z -direction quadrants. The usual decay electron selections (Section A.1) are applied, along with the following selections:

- Data are from April 2009
- MC is tuned to water parameters from April 2009
- Quadrants are as follows, in the z direction:

Top: $z > 800$ cm

Upper-Mid: $0 \text{ cm} < z < 800$ cm

Lower-Mid: $-800 \text{ cm} < z < 0 \text{ cm}$

Bottom: $z < -800 \text{ cm}$

- $|\cos \theta_z| < 0.4$ (use only roughly horizontal decay electrons)

This check is done with MC with and without the z -dependent water transparency activated in the detector simulation. The results are summarized in Figure A.3. It shows that the position dependence in the simulation improves data/MC matching, but that there are still effects which are not yet captured in the simulation; in particular, the anomalously high reconstructed momenta in the top of the tank is not understood. Studies on this are still ongoing at the time of this writing.

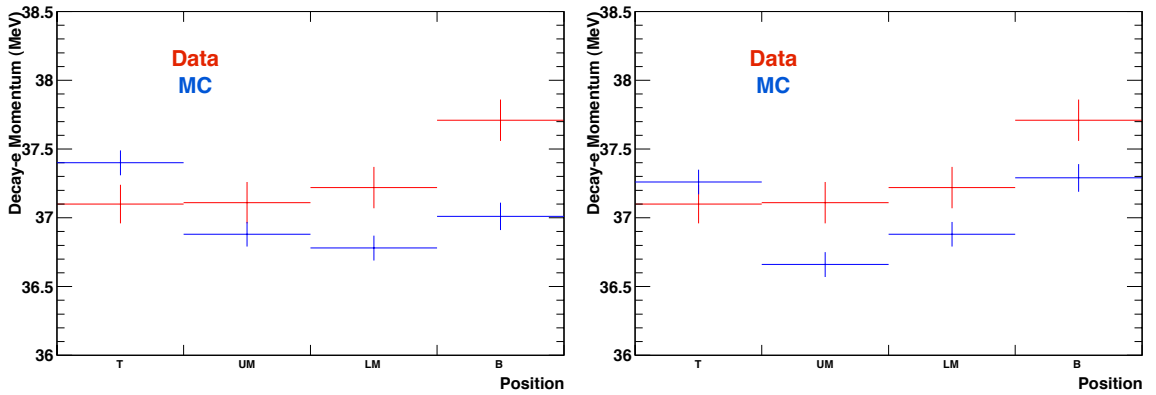


FIGURE A.3: Mean decay electron energy for each of the quadrants is plotted in these figures. Red is data, blue is MC. The quadrants are (left-to right in the plots) Top, Upper-Middle, Lower-Middle, and Bottom. The left plot uses MC without z -dependent water transparency in the detector simulation, the right plot is with z -dependent MC. Note the better agreement overall when the z -dependence is enabled in the detector simulation (especially near the bottom).

The next thing to check is directional dependence. We divide decay electron data and MC into up-going ($p_z > 0$) and down-going ($p_z < 0$) samples. There is a roughly 0.5% difference in energy between these samples in data, with the up-going and down-going mean momenta measured as $37.47 \pm 0.06 \text{ MeV}/c$ and $37.26 \pm 0.07 \text{ MeV}/c$, respectively. The cause of this asymmetry is unknown (it runs counter to what might

be expected based on the water quality), and still under investigation at the time of this writing. Figure A.4 shows the MC/data values for up-going and down-going electrons, with and without position dependent MC. Also shown are the stopping muon momentum/range MC/data values, for comparison. The stopping muons are all down-going. This study shows that non-isotropic calibration samples (such as stopping muons) will be affected differently than isotropic samples by z -dependent transparency in SKdetsim.

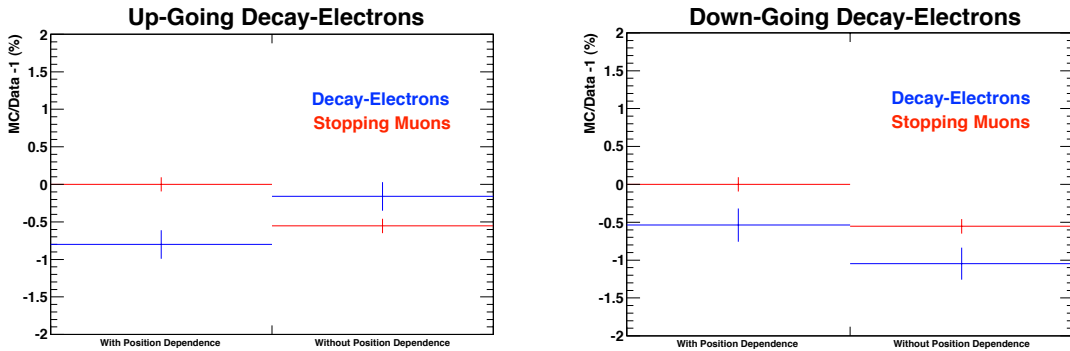


FIGURE A.4: $(MC-Data)/Data$ is plotted for decay electron (blue) and multi-GeV stopping muon calibration samples. The left plot shows only up-going decay electrons, the right plot shows only down-going ones. The bins are for with position dependent water quality in SKdetsim, and without (left and right bins respectively). This shows that the simulated dependence affects particles (e or μ) largely based on their direction of travel. This explains why the addition of water quality z -dependence in SKdetsim changed the decay electron and stopping muon samples in different ways.

Finally, the time variation of position dependence can be tracked through SK-IV. This can be tracked via xenon and nickel calibration in SK (see Section 4.7), but the use of decay electrons provides a calibration using data events, rather than calibration sources. The results are shown in Figure A.5. These results agree with those from the xenon and nickel calibration¹. This position-dependent calibration

¹ Credit to Luis Labarga and the SK Low Energy Calibration Group for their xenon and nickel calibration comparisons.

check can now be used to improve water quality position dependence beyond what is possible with just the low energy calibration sources.

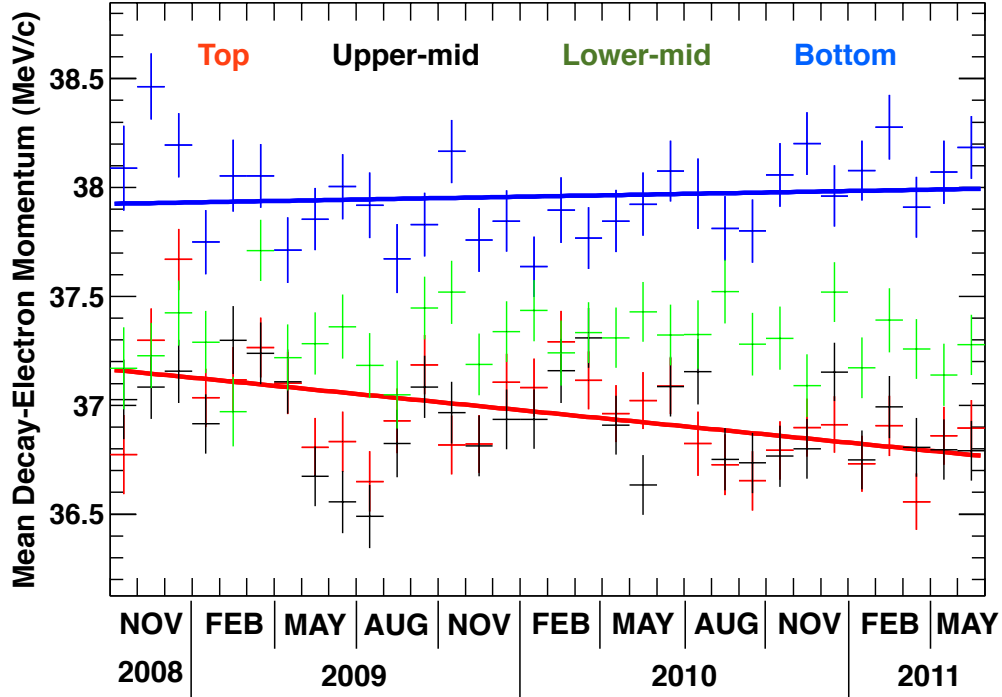


FIGURE A.5: As before with the position dependence check, the detector is divided into four z quadrants. The mean value for decay electron momentum for each of these quadrants is plotted for each month. The top and bottom quadrants have linear fits overlaid. The primary statistically significant variation over time is in the top quadrant, where the reconstructed momentum is decreasing at $(0.40 \pm 0.09)\%/year$.

The author's work on decay electrons for absolute energy scale calibration and time variation measurement was a significant part of the T2K energy-scale uncertainty for the far detector. The use of decay electrons as a tool for evaluating position and direction dependence in SK is a new development by the author. This has already shown some promise, especially as a cross-check for the calibration sources on time variation of position dependence. In the future, this work may lead to improvements in momentum reconstruction, and in the absolute energy scale determination.

Appendix B

ND280 Analysis Details

This appendix summarizes the ND280 tracker CC inclusive analysis, used in the T2K ν_e appearance analysis. The author of this dissertation was not involved with developing or executing the ND280 analysis. This particular analysis was developed primarily by a group of T2K collaborators from CEA Saclay in the ND280 working group. Information in this appendix comes from a thesis [137], T2K internal presentations, and internal technical notes [142]. It is included here to help provide a complete description of the analysis in one public document. This ND280 analysis was used for normalization of the SK event expectation in the ν_e appearance analysis.

B.1 Event Selections Overview

A diagram of the ND280 tracker with a good CC ν_μ event in it is shown in Figure B.1. The target mass for this analysis is the two FGD regions, and the second and third TPCs provide good measurements of particle tracks. The first TPC (the most upstream) operates as a veto for this analysis, rejecting neutrino events produced further upstream. The full set of CC-inclusive ν_μ selections is as follows:

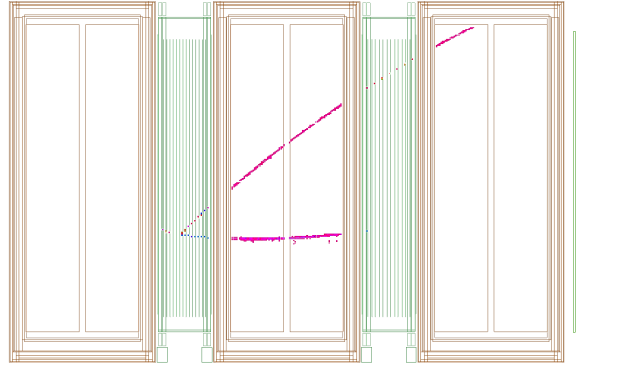


FIGURE B.1: Charged current ν_μ event detected in the ND280 tracker. The neutrino beam direction is left to right, and the segments of the tracker are, left to right: TPC1, FGD1, TPC2, FGD2, TPC3. The interaction occurs in FGD1. A proton track (lower, curving upwards in the magnetic field) and a muon track (upper, curving downwards) are produced.

1. No tracks in TPC1 (most upstream TPC).
2. At least one track in TPC2 with a starting point in the fiducial volume (FV) of FGD1, and momentum larger than 50 MeV/c.
3. Select the track with the highest momentum among negative (determined by curvature in the magnetic field) tracks in TPC2 with a starting point in the FV of FGD1.
4. Apply PID selection to the selected track (require μ -like). PID is based on the ionization rate in the TPC.
5. If no tracks in TPC satisfy these requirements, repeat the same procedure for TPC3 and FGD2 by repeating steps 2-4.

B.2 Track Matching/Vertex Finding

After the track is reconstructed in TPC2 (TPC3), the track can be extrapolated back to FGD1 (FGD2). The extrapolation is linear in the x - z plane, and circular in the y - z plane, due to the effect of the magnetic field. A hit in the FGD is considered associated with a track if it is within 3 cm of the extrapolated track. The most upstream hit is considered the vertex location. A FV cut is then applied based on this vertex.

B.2.1 Momentum Reconstruction

The momentum of particles is reconstructed from the TPC track. The magnetic field causes a curvature in the track, with a radius of curvature proportional to the transverse momentum (the momentum component perpendicular to the magnetic field) and inversely proportional to the magnetic field.

$$R = \frac{p_t}{eB} \tag{B.1}$$

The total momentum can be determined based on the transverse momentum and direction. The energy lost in the FGD is estimated based on the track length in the FGD, and this energy is added back to the total energy reconstructed for a particle.

B.3 Particle ID

The energy lost by a particle due to ionization is a function of that particle's velocity relative to the speed of light, β , and does not depend on the particle's mass. By comparing the ionization charge per track length in the TPCs to the momentum measured from the track curvature, it is possible to distinguish particles of different mass. Figure B.2 shows how the μ PID cut is applied to data.

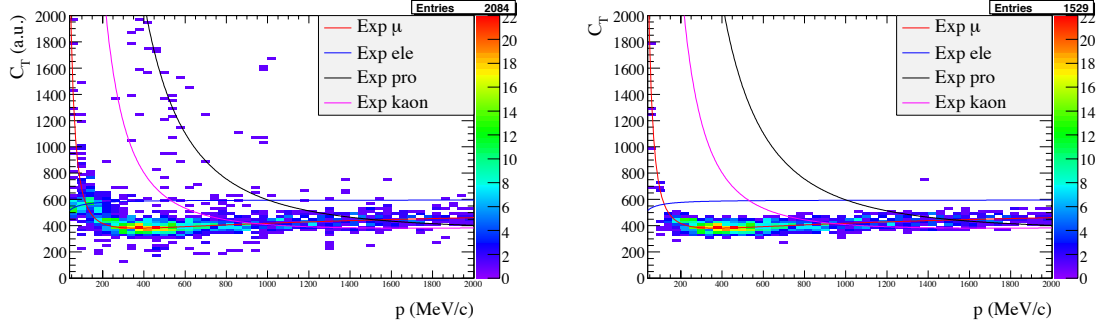


FIGURE B.2: The left figure shows the ionization charge per track length vs. momentum (reconstructed from curvature) for ν_μ candidates in the ND280 tracker, before the PID cut is applied. The right figure shows the same after the PID cut is applied.

B.4 Additional Considerations

Additional cuts are made to reject events which are reconstructed inside the FGD FV, but which originated outside of it. If the TPC track is extrapolated to within 15 cm of FGD hits outside the FGD FV, it is flagged as entering. If this flagged track has $\cos\theta < 0.9$ (θ with respect to beam direction) and $p < 500$ MeV/c, it is rejected for entering outside the FV.

One of the MicroMegas detectors in TPC3 had a low gain for the first physics run, necessitating a correction to the PID selection efficiency, modifying the final event rate by a factor of 1.025 ± 0.0004 .

The analysis produces only a single event per beam spill, regardless of how many neutrinos interact in the tracker during the spill. Multiple interactions per spill is called pile-up. Pile-up can either lead to a good neutrino event being vetoed by another track in TPC1, or to one neutrino being ignored if two neutrinos interact in the FGDs. The pile-up is simulated in the MC; however, the beam power (and therefore pile-up rate) in MC does not match the beam power in data. Therefore, a pile-up correction factor is needed to bring the MC pile-up in line with that expected in data. This factor is a correction to data/MC of 0.982 ± 0.009 .

A certain number of events are expected to be reconstructed inside the FGD

FV, which originate from another interaction outside the FGD, which produces a neutral particle (such as a γ) which enters the FGD and interacts. This fraction was estimated with MC, and with a search for positive particle tracks (which will have an enhanced fraction of events originating outside the FGD). The out of FGD contribution was then subtracted from the total events in data and MC.

Appendix C

Systematic Error Details

This appendix details the methods for estimating systematic uncertainties. With the exception of the energy scale systematic error from decay electrons, this work was done by T2K collaborators other than the author of this dissertation. The information is reproduced here from internal T2K documents to help provide a complete understanding of the T2K analysis for non-T2K collaborators.

C.1 ND280 Systematic Errors

Systematic errors for the ND280 contributions to the analysis were estimated by the ND280 working group. Details are reproduced here from internal T2K notes [142][163].

C.1.1 ND280 Statistical Uncertainty

The statistical uncertainty is the simple Poisson (\sqrt{N}) uncertainty on the number of expected events. Thus, with 1405 events predicted by MC (after correction for out of FGD events), the uncertainty becomes $\pm 2.7\%$. In the analysis, this uncertainty is incorporated into the toy MC as a Poisson PDF, rather than the usual Gaussian,

although this results in a negligible difference in the final result.

C.1.2 ND280 Physical Model Uncertainty

The physical model systematics include neutrino interaction uncertainties that are not included in the neutrino interactions uncertainties from Section 7.1. Those uncertainties are applied to both SK and ND280 in a correlated way (with the exceptions of the CCQE shape error and FSI errors) in toy MC fluctuations during analysis. These uncertainties are considered part of the neutrino interactions systematics, and are not discussed here.

The remaining physical model systematics come from FSI, nuclear ejection, and kinematical variations. The FSI and nuclear ejection systematic effects were studied by reweighting the MC with variations on pion FSI and nuclear ejection parameters. The pion FSI parameter tuning had minimal effect on the number of events, as the CC-inclusive analysis includes events whether or not there is an extra pion track, as long as the muon track is the most energetic. The nuclear ejection parameter tuning (for when nucleons can be ejected following the absorption of a pion or delta) had slightly more of an effect, likely because the ejected protons could trigger the TPC1 veto. Finally, the interaction kinematics were varied by modifying the axial mass and vector mass (as implemented in NEUT) to see how the detector efficiency changes. The result of these studies gave the following systematics on event rate:

- Nucleon Ejection: -2.7%
- FSI Tuning: $\pm 0.7\%$
- Kinematical Variation $M_A + M_V$: $\pm 2.4\%$

These uncertainties were added in quadrature (assuming symmetric variation for all of them), yielding a physical model uncertainty of 3.7%. This uncertainty is applied to the number of ND280 events, without any correlation to SK uncertainties.

C.1.3 ND280 Detector Efficiency Uncertainties

Detector efficiency systematics were estimated for many sources on ND280. Here, only the uncertainties greater than 1% will be discussed. The remaining uncertainty sources (FV and FGD mass, event time determination, highest momentum track identification, the low gain MicroMegas module, pile-up, cosmic ray muons, and out of FGD events) are not discussed here, but their effect will be included in the summary table.

The TPC1 veto uncertainty is primarily due to differences in the number of pile-up neutrinos triggering the TPC1 veto. This was studied using statistical checks on the number of such pile-up events expected, and by visually scanning events passing the selection cuts if the TPC1 veto is removed. The result of this study was a $\pm 1.2\%$ systematic uncertainty.

The TPC efficiency was checked using events which had a good track in TPC1 and TPC3, and examining the efficiency for the track to be found in TPC2. The efficiency in both data and MC from this TPC1+2+3 sample was reweighted to match the number of TPC hits in events selected for the CC inclusive analysis. This resulted in an estimate of 35.2 ± 3.4 events missed due to TPC inefficiency in data, and 58.7 ± 4.2 missed in MC. This was conservatively converted to a -2.0% systematic uncertainty on TPC efficiency.

The TPC charge mis-identification uncertainty was estimated by taking tracks which cross more than one TPC, and counting the number of times where the charge ID differed between the TPCs. This was done for both data and MC. The result was an expectation a charge mis-ID rate of $(1.6 \pm 0.4)\%$ for data, and $(1.9 \pm 0.1)\%$ for MC. The maximum possible data/MC difference due to this is estimated at $\pm 1.0\%$.

The TPC-FGD matching was studied using two samples: ν_μ events, where the charge in each plane of the FGD was studied independently, and through-going μ

events where TPC1 and TPC3 have clean tracks, in data and MC. The effects of efficiency differences along the z -direction of the FGD planes, the transverse direction, and general alignment effects are considered. The result of this study is a $\pm 2.1\%$ uncertainty.

The PID physics are described in Section B.3, though the details of how the events are selected are somewhat more complicated and the analysis uses a parameter called the pull which parameterizes the difference in expected and measured charge, for a particle hypothesis. The distributions of the pulls are different for data and MC, and this is corrected for through a calibration procedure. A systematic error is developed for uncertainty in the pull distributions by comparing them in the different TPCs using through-going muon events. The result was a $+3.0\%$ asymmetric uncertainty on data/MC due to PID.

The effect of all the ND280 detector systematic uncertainties on the expected number of events is shown in Table C.1. The uncertainties are added in quadrature, to yield a ${}^{+4.2}_{-3.6}\%$ uncertainty. For the oscillation analysis, a conservative symmetric approximation of $\pm 4.2\%$ was used, though this difference has a negligible effect on the final analysis.

C.2 Beam Systematic Errors

This section details the computation of beam systematic errors. This work was done by the T2K beam group. Information from T2K internal presentations and technical notes [143][106][107] is summarized here.

The beam errors come from two major categories of sources: hadron production multiplicity uncertainties (binned, from external data measurements), and from beam simulation systematic parameter variation (such as horn current uncertainty). These are treated in slightly different ways, and the simpler of the two, the simulation

Table C.1: Table of ND280 detector systematics. Some of the systematic studies found no measurable systematic uncertainty, and thus had none set. Errors are given as a fractional change in the Data/MC ratio.

Source	sys. err. +	sys. err. -
TPC1 veto	0.012	0.012
TPC efficiency	-	0.020
TPC charge mis-ID	0.010	0.010
TPC-FGD track matching	0.021	0.021
FV	-	-
FGD mass	0.005	0.005
T_0 (timing)	0.001	-
Highest momentum track	-	-
PID pull width	0.030	-
Low gain MicroMegas	0.004	0.004
Pile-up	0.009	0.009
Cosmics	-	0.004
Out of FGD	0.009	0.009
Total	0.042	0.036

systematic parameters, will be discussed first.

The simulation parameter adjustment is based on 1σ variations in physical parameters, mostly determined from measurements on the neutrino beam production setup. The parameters that are varied include:

- hadron production cross-section (from external data)
- off-axis angle (constrained by INGRID data)
- proton beam position/angle (constrained by beam monitor data)
- absolute horn current (constrained by horn current monitors and magnetic field measurements)
- horn alignment (from beamline survey)
- target alignment (from beamline survey)

The beam simulation is re-run to determine the effect on the beam flux from a $\pm 1 \sigma$ variation in these parameters. The flux difference for each bin i in energy is computed for the variation of a flux systematic parameter f_j^ϕ from the default set of parameters \vec{f}_0^ϕ .

$$\delta_j \Phi_{\text{SK},i}^{\text{MC},x} = \Phi_{\text{SK},i}^{\text{MC},x} \left(\vec{f}_0^\phi + \delta f_j^\phi \right) - \Phi_{\text{SK},i}^{\text{MC},x} \left(\vec{f}_0^\phi \right) \quad (\text{C.1})$$

$$\delta_j \Phi_{\text{ND},i}^{\text{MC},x} = \Phi_{\text{ND},i}^{\text{MC},x} \left(\vec{f}_0^\phi + \delta f_j^\phi \right) - \Phi_{\text{ND},i}^{\text{MC},x} \left(\vec{f}_0^\phi \right) \quad (\text{C.2})$$

Here, the fluxes Φ are labeled as MC and by neutrino species ($x = \nu_\mu, \nu_e, \bar{\nu}_\mu$) in the superscript, and detector (ND or SK) and energy bin i in the subscript.

The revised number of events expected at the near and far detector is then computed by integrating (bin-by-bin) the flux difference with the expected spectrum at ND or SK for a given oscillation point $\Theta = (\sin^2 2\theta_{13}, \Delta m^2, \text{etc.})$. No oscillations need to be considered at the near detector.

$$N_{\text{SK}}^{\text{MC}} \left(\Theta; \vec{f}_0^\phi + \delta f_j^\phi \right) = \sum_{x=\nu_\mu, \nu_e, \bar{\nu}_\mu} \sum_i N_{\text{SK},i}^{\text{MC},x} \left(\Theta; \vec{f}_0^\phi \right) \frac{\Phi_{\text{SK},i}^{\text{MC},x} \left(\vec{f}_0^\phi + \delta f_j^\phi \right)}{\Phi_{\text{SK},i}^{\text{MC},x} \left(\vec{f}_0^\phi \right)} \quad (\text{C.3})$$

$$N_{\text{ND}}^{\text{MC}} \left(\vec{f}_0^\phi + \delta f_j^\phi \right) = \sum_{x=\nu_\mu, \nu_e, \bar{\nu}_\mu} \sum_i N_{\text{ND},i}^{\text{MC},x} \left(\vec{f}_0^\phi \right) \frac{\Phi_{\text{ND},i}^{\text{MC},x} \left(\vec{f}_0^\phi + \delta f_j^\phi \right)}{\Phi_{\text{ND},i}^{\text{MC},x} \left(\vec{f}_0^\phi \right)} \quad (\text{C.4})$$

Here, the N are the number of events passing all selection cuts.

Finally, the change in the Far/Near ratio is computed.

$$\delta R_{F/N,j}(\Theta) = \frac{N_{\text{SK}}^{\text{MC}} \left(\Theta; \vec{f}_0^\phi + \delta f_j^\phi \right) / N_{\text{ND}}^{\text{MC}} \left(\vec{f}_0^\phi + \delta f_j^\phi \right)}{N_{\text{SK}}^{\text{MC}} \left(\Theta; \vec{f}_0^\phi \right) / N_{\text{ND}}^{\text{MC}} \left(\vec{f}_0^\phi \right)} - 1 \quad (\text{C.5})$$

This is the uncertainty in Far/Near ratio for the systematic variation j at some oscillation point Θ . This method is used for all the above listed systematic uncertainties.

The hadron production multiplicity uncertainties are computed on a bin-by-bin basis for the hadron production data. This uses bins of (p, θ) for pion production, and bins of (x_F, p_t) for kaon production (Feynman scaling parameter and transverse momentum). Uncertainties on the pion multiplicity in each bin from the NA61 data [108] typically range from 5-10%. For bins in (p, θ) not covered by NA61, a 50% error is assigned.

The far/near ratio uncertainty for pion multiplicity is computed in much the same way as the other errors (Equation C.5, although we now sum over the 707 bins j in (p, θ) , and over the different pion types (π^+ and π^-)). There was some question as to how to properly deal with correlations between bins, and so it was decided to be conservative, and to maximize the correlation effects by always taking the absolute value of the change in $R_{F/N}$.

$$\delta R_{F/N,\pi}(\Theta) = \sum_{c=+,-} \sum_{j=1}^{707} \left| \frac{N_{\text{SK}}^{\text{MC}}(\Theta; \vec{f}_0 + \delta f_j^{\pi^c}) / N_{\text{ND}}^{\text{MC}}(\vec{f}_0 + \delta f_j^{\pi^c})}{N_{\text{SK}}^{\text{MC}}(\Theta; \vec{f}_0) / N_{\text{ND}}^{\text{MC}}(\vec{f}_0)} - 1 \right| \quad (\text{C.6})$$

An analogous computation is made summing over the 675 bins in (x_F, p_t) space and (K^+, K^-, K^0) for the kaon multiplicity error. The kaon multiplicity uncertainty comes from comparisons between FLUKA and results from Eichten *et al.* [164]. The multiplicity uncertainty is typically between 20% and 50% inside the data region, and a 50% error is assigned outside of it, as in the pion multiplicity case.

Uncertainties on the production of tertiary pions (pions from secondary proton interactions in the target) are due to uncertainties with the Feynman scaling used. The scaling error is estimated by using an alternative scaling scheme and seeing how the data changes. This error was found to be $\sim 1\%$.

Secondary nucleon production uncertainties are estimated by comparing FLUKA data to external data [164] and checking differences. The secondary proton and neu-

tron production differences are used to compute flux shifts, from which a systematic uncertainty is derived.

The expected percent errors on the number of events selected at ND280, the number selected at SK, and the far/near ratio are shown in Table C.2. Of course, this is only for one point in oscillation space, with $\sin^2 2\theta_{13} = 0.1$. Note the dramatic cancellation of errors in the ratio. Each source of error is listed separately, and the total uncertainty comes from adding each error source in quadrature.

Table C.2: Table of beam systematic errors. Each source is listed separately. The uncertainty on the number of CC inclusive μ events at the near detector, the number of ν_e candidates at SK, and the far/near ratio are listed. The SK errors are computed for $\Delta m^2 = 2.4 \times 10^{-3} \text{ eV}^2$, $\delta_{\text{CP}} = 0$ and $\sin^2 2\theta_{13} = 0.1$. All errors are in %, and are added in quadrature to find the total error.

Source	δN_{ND}	δN_{SK}	$\delta (N_{\text{SK}}/N_{\text{ND}})$
Pion Multiplicity	5.53	6.06	3.04
Tertiary Pion Scaling	1.39	1.27	0.13
Kaon Multiplicity	10.01	4.21	7.30
Production Cross Sections	7.65	10.39	2.54
Sec. Nucleon Multiplicity	5.87	6.69	0.87
Proton Beam	2.22	0.80	1.39
Off-axis Angle	2.65	2.08	0.56
Target Alignment	0.26	0.05	0.31
Horn Alignment	0.57	0.42	0.15
Absolute Horn Current	0.47	1.11	0.63
Total	15.43	14.92	8.52

C.3 SK Systematic Errors

The SK systematic errors were computed by the T2K-SK group. The author was involved with the energy scale error estimation, specifically using decay electrons. The systematic error estimation by other T2K-SK members is described in T2K internal talks and technical notes [165][166][167][168] and is reproduced here for completeness.

C.3.1 Reduction/OD Cut Uncertainty

The reduction process to select events as FC candidates is similar to, but simpler than that used by SK for atmospheric neutrinos. Fewer reduction cuts are needed because the beam timing is able to reject nearly all cosmic ray backgrounds. The dominant source of error for this process is from the flasher cut (see Section 4.5). The uncertainty for the flasher cut was estimated by comparing the flasher cut parameter distributions (measures of event correlation) between data and MC. The differences in the distributions were measured, and the MC parameters were shifted by this difference. The result was a change in the number of FCFV events of less than 1%, so a systematic error of 1% was applied.

The OD cut (largest hit cluster in the OD has fewer than 16 hits) was checked using partially contained atmospheric neutrino data and MC from SK-IV. The difference in OD hit distributions was small, leading to a negligible effect on the final event rate.

C.3.2 Fiducial Volume Cut Uncertainty

The uncertainty on the vertex resolution was estimated using cosmic-ray muons. Muons entering the tank begin emitting Cherenkov light in the ID when they pass the ID wall, so their vertex along the track can be known exactly (the resolution perpendicular to the track direction is already very well reconstructed based on timing). The fine vertex fitter, MS-fit, is adjusted to allow vertex reconstruction anywhere, including outside of the ID volume. Then, it is run on these cosmic ray muons. The variation in reconstructed vertex from the ID wall is compared between data and MC, and the difference in mean reconstructed position is found to be ± 5 cm. Applying this variation to the FV boundary gives a 1% error on the FV cut. As only single-ring events are selected for the ν_e appearance analysis, it is not necessary to apply a systematic error for multi-ring events, which are not fitted with MS-fit.

C.3.3 Energy Scale Uncertainty

The absolute uncertainty on the energy scale comes from the maximum MC/data deviation from all the energy scale calibration samples, seen in Figure 4.15. The largest deviation comes from a sub-GeV stopping muon sample, at +2.19%. The RMS of both time variation checks (Figure 4.16) is 0.4%, with data binned in 10-day periods. These two errors are added in quadrature, to yield a final energy scale uncertainty of $\pm 2.3\%$ on the energy of events. This shift in reconstructed energy was applied to the T2K MC to find the change in selected number of events. This yielded a $\pm 0.4\%$ shift in signal events, and a $\pm 1.1\%$ shift in background events.

C.3.4 Ring Counting, Electron PID, and POLfit Mass

The ring counting, electron PID, and POLfit mass uncertainties were partially constrained by atmospheric neutrino data and MC, and partially dealt with by a conservative error estimate. The events that go in to the final T2K MC sample passing all selection cuts are divided into categories based on the MC final state of the events. These categories are assigned a systematic error on reconstruction efficiency, either via a control sample (described later), or via a conservative 100% uncertainty. The samples, their uncertainties, and their control samples are shown in Table C.3. Note that the “Hybrid π^0 ” control sample error is not included in the ring counting, PID, or POLfit mass uncertainties, but in a separate uncertainty used to describe π^0 reconstruction efficiency uncertainty (Section C.3.8).

The atmospheric neutrino sample is quite effective at setting tight limits on the systematic error, so the uncertainties here are largely driven by the 100% errors. In future analyses, control samples will be developed to reduce these uncertainties.

Table C.3: Table of final states used for estimating systematic errors for ring counting, PID, and POLfit mass. The final states count the number of charged particles (for example, NC1 π^\pm) based on the number of particles above Cherenkov threshold, according to the MC truth information. The Hybrid π^0 control sample uncertainties are not added here, but in the separate Hybrid π^0 error. The uncertainty for each separate final state component is added together in an uncorrelated way. The uncertainty for the two background components is also added together in an uncorrelated way, with the total background made up of 54% ν_e and 46% $\nu_\mu + \bar{\nu}_\mu$. The PID uncertainties described here are for electron identification efficiency uncertainty. The muon PID is calculated using a different method.

Final State	Fraction	Control Sample	RC Unc.	PID Unc.	POLfit Unc.
Beam $\nu_\mu + \bar{\nu}_\mu$					
NC 1 π^0	70.9%	Hybrid π^0	n/a	n/a	n/a
NC 1 π^\pm	8.5%	None	100%	100%	100%
NC 1 γ	5.7%	None	100%	100%	100%
NC other	10.3%	None	100%	100%	100%
CC	4.6%	None	100%	100%	100%
Total	100%		15.2%	14.5%	15.2%
Beam ν_e					
CC 1 e	90.0%	Atm. Neutrino	1.9%	1.1%	6.1%
CC other	8.0%	None	100%	100%	100%
NC	2.0%	None	100%	100%	100%
Total	100%		8.4%	8.3%	9.6%
Bkg. Total			8.4%	8.1%	8.7%
Signal ν_e					
CC 1 e	96.4%	Atm. Neutrino	1.6%	1.4%	4.1%
CC other	3.6%	None	100%	100%	100%
Total	100%		3.9%	3.8%	5.1%

C.3.5 Atmospheric Neutrino Control Sample

The idea of the atmospheric neutrino control sample is to test how well data and MC match, and what room for an uncertainty in the signal selection efficiency exists. This section will describe primarily the procedure for finding the ring counting uncertainty, but it is very similar for the electron PID and POLfit mass uncertainties.

The following procedure is done twice for each systematic error (RC, PID, POLfit): once for the beam ν_e background, and once for the signal ν_e . The following will de-

scribe the procedure for ν_e background, but it is simple to modify to work for signal.

We begin with the T2K beam ν_e background MC. We will apply the normal T2K ν_e cuts to this, with the exception that we will only use visible energy for the cuts, as reconstructed neutrino energy is not a meaningful parameter for atmospheric neutrino data. Thus, the cuts are:

- FC FV
- PID is e -like
- POLfit $m_{\pi^0} < 105 \text{ MeV}/c^2$
- No decay electrons ($N_{\text{decy}} = 0$)
- $100 \text{ MeV} < E_{\text{vis}} < 1200 \text{ MeV}$

Note that the single-ring (1R) cut is not yet applied, as we are testing ring counting. The events passing these cuts are categorized into the “core” sample if they pass the $N_{\text{ring}} = 1$ cut, and into the “tail” sample if they fail it. Now, using these cuts, a corresponding sample of events can be made in the atmospheric neutrino data and MC. To make it correspond to the T2K beam ν_e MC, the events are weighted by visible energy to make the E_{vis} spectra of the atmospheric data and MC match the T2K MC. For the atmospheric MC samples, the tail and core samples can be broken down in MC based on the type of interaction producing events. This breakdown is shown in Table C.4.

Beyond this, three background-enhanced samples are set up, designed to have a high concentration of a certain background. These samples are also made of atmospheric neutrino data and MC, reweighted to match visible energy distributions with the T2K MC. All five samples, their cuts, and purities are described in Table C.5.

Table C.4: Breakdown of interaction modes in the ring-counting control sample. Note that the categories here are based on MC truth information from the atmospheric MC.

	Core Events	Tail Events
ν_e CC 1- e	94%	68%
ν_e CC other	3.2%	12%
ν_μ CC	0.8%	6.6%
NC	2.0%	13%

Table C.5: Description of the atmospheric neutrino samples used to study the ring counting systematic uncertainty. All of them share the following cuts: FCFV, $E_{\text{vis}} \in (100, 1200)$ MeV.

Sample	Cuts	Purity
1 CC 1- e ν_e Tail	$m_{\pi^0} < 105 \text{ MeV}/c^2$, $N_{\text{dcy}} = 0$, e -like, $N_{\text{ring}} > 1$	94%
2 CC 1- e ν_e Core	$m_{\pi^0} < 105 \text{ MeV}/c^2$, $N_{\text{dcy}} = 0$, e -like, $N_{\text{ring}} = 1$	68%
3 ν_μ Enriched	μ -like	91%
4 NC Enriched	e -like, $105 \text{ MeV}/c^2 < m_{\pi^0} < 170 \text{ MeV}/c^2$	47%
5 ν_e CC Other Enriched	e -like, $m_{\pi^0} < 105 \text{ MeV}/c^2$, $N_{\text{dcy}} = 1$	54%

The idea, now, is to reweight the atmospheric MC consistently across these five samples to best make the number of data and MC events in each of these samples match. The MC is reweighted according to the four interaction modes (listed in Table C.4). The total fitting χ^2 function is given by

$$\chi^2 = \sum_{i=1}^5 \left[2 (N_i^{\text{MC}} - N_i^{\text{data}}) + 2N_i^{\text{data}} \ln \left(\frac{N_i^{\text{data}}}{N_i^{\text{MC}}} \right) \right] + \left(\frac{\alpha}{\sigma_\alpha} \right)^2 + \left(\frac{\beta}{\sigma_\beta} \right)^2 + \left(\frac{\gamma}{\sigma_\gamma} \right)^2 + \left(\frac{\delta}{\sigma_\delta} \right)^2 \quad (\text{C.7})$$

where

N_i^{data} = Number of observed events in i th sample,

N_i^{MC} = Number of MC events in i th sample (after reweighting),

α, σ_α = fitting parameter for overall normalization and its uncertainty (25%),
 β, σ_β = fitting parameter for CC non QE scaling and its uncertainty (20%),
 γ, σ_γ = fitting parameter for ν_e/ν_μ ratio and its uncertainty (5%),
 δ, σ_δ = fitting parameter for NC event scaling and its uncertainty (20%).

The uncertainties on the scaling parameters come from a recent SK atmospheric neutrino analysis [61]. Note that the χ^2 function is just a log likelihood (using the Poisson distribution as that likelihood) with pull terms for the uncertainties.

The formulas for the number of MC events in each sample, after reweighting, are:
 For $i = 1$ (the tail sample):

$$N_1^{\text{MC}} = (1 + \alpha) [(1 + \epsilon)N_1^{\text{CC1e}} + (1 + \beta)N_1^{\text{CCoth}} + (1 + \gamma)N_1^\mu + (1 + \delta)N_1^{\text{NC}}] \quad (\text{C.8})$$

For the other samples:

$$N_i^{\text{MC}} = (1 + \alpha) [N_i^{\text{CC1e}} + (1 + \beta)N_i^{\text{CCoth}} + (1 + \gamma)N_i^\mu + (1 + \delta)N_i^{\text{NC}}] \quad (\text{C.9})$$

where

ϵ = Uncertainty parameter for ν_e CCQE efficiency between core and tail,

N_i^{CC1e} = Number of ν_e CC 1e events in i th sample,

N_i^{CCoth} = Number of ν_e CC other events in i th sample,

N_i^μ = Number of ν_μ CC events in i th sample,

N_i^{NC} = Number of NC events in i th sample.

In this way, the MC is reweighted to cause the best possible fit between data and MC in a diverse set of five samples. The lone parameter which we are concerned about is ϵ , which only appears once in this, parameterizing the ring counting selection efficiency for ν_e events. The final selection efficiency for ν_e CC 1e events will be estimated as:

$$\frac{N_2^{\text{CC1e}}}{N_2^{\text{CC1e}} + (1 + \epsilon)N_1^{\text{CC1e}}}. \quad (\text{C.10})$$

The fit is done in three ways: first, ϵ is constrained to be zero, and the other parameters are fitted. This is the default efficiency. Next, the absolute best fit is found, where ϵ is fitted with the other parameters. This is the best-fit efficiency. Finally, the value of ϵ is increased and decreased from the best-fit value (with other parameters always re-fit to optimize) until the $\Delta\chi^2$ between the best-fit and the ϵ -shifted value is equal to 1, a single standard deviation. Now, the efficiency at the default position and the efficiency at the $\Delta\chi^2 = 1$ position are compared, and the difference becomes the ring counting uncertainty on beam ν_e . During the fitting process, ϵ is not allowed to become less than 1, as that would lead to an efficiency of greater than 100%.

This process is repeated with signal ν_e ; the only difference is the re-scaling using visible energy. Similar procedures are done for the POLfit π^0 mass and the e -like PID cut. The final efficiencies with their systematic uncertainties are shown in Table C.6.

Table C.6: Table of default efficiencies found, along with the 1σ uncertainty, using the atmospheric neutrino control samples.

Selection	T2K Beam ν_e Efficiency (%)	T2K Signal ν_e Efficiency (%)
Ring counting	96.8 ± 1.9	96.6 ± 1.6
Electron PID	98.9 ± 1.1	98.8 ± 1.4
POLfit cut	90.1 ± 6.1	90.7 ± 4.1

Note that these uncertainties estimated here are for a particular group of events (signal ν_e or background ν_e) to be rejected by the cut. The cut uncertainty for other backgrounds to pass the cut must either be treated with a conservative 100% uncertainty or some other type of control sample.

C.3.6 Muon PID

The uncertainty on the number of muon events which would be identified as electron-like was estimated using cosmic ray muons, as well as a method similar to that

described in Section C.3.5. A 0.3% mis-PID rate was estimated, with a 1.0% uncertainty on the final number of events.

C.3.7 Decay Electron Efficiency

The decay electron tagging efficiency is estimated in two ways. First, there is the difference in tagging efficiency in cosmic ray stopping muon data and MC. This difference came out to 0.8%. The difference is applied to the various components of the MC to get the decay electron efficiency errors of 0.2% for beam ν_e , 0.4% for $\nu_\mu + \bar{\nu}_\mu$, and 0.1% for signal ν_e .

C.3.8 Hybrid π^0

The final uncertainty estimation comes from the “hybrid π^0 ” sample. This sample is used to estimate the overall rejection rate uncertainty for NC $1\pi^0$ events. This important error is difficult to constrain, as there is no good high-statistics source of π^0 events. The main uncertainty comes from the reconstruction efficiency for highly asymmetric decays (that is, $\pi^0 \rightarrow \gamma_1 + \gamma_2$ with $E_{\gamma_1} \gg E_{\gamma_2}$). To study this, it was decided to make “hybrid” π^0 events, using one ring from data, and one from MC.

There is a plentiful source of low-energy e -like rings: decay electrons from cosmic-ray muons. Higher energy e -like rings can come from atmospheric neutrino events, though the statistics for these are lower. Electrons and gammas both appear like showering (e -like) rings in SK, so they are mostly interchangeable. One difference is that a gamma will travel some distance in the water before pair producing ($\gamma \rightarrow e^+ + e^-$) and showering. This is accounted for by randomly selecting an offset for electron vertices relative to where the true gamma vertex would be.

There are four hybrid π^0 samples:

1. **Primary Data** hybrid π^0 : Single electron ring from atmospheric neutrino data for the high energy gamma (γ_1), and a MC produced gamma for the

lower energy gamma (γ_2).

2. **Primary MC** hybrid π^0 : Single electron ring from atmospheric neutrino MC for γ_1 , and a MC produced gamma for γ_2 .
3. **Secondary Data** hybrid π^0 : MC produced gamma for γ_1 , and a decay electron from the cosmic ray data for γ_2 .
4. **Secondary MC** hybrid π^0 : MC produced gamma for γ_1 , and a decay electron from the cosmic ray MC for γ_2 .

If the energy of γ_2 is greater than 60 MeV, a decay electron will not be a viable replacement, so an atmospheric neutrino single electron ring event may be used for the Secondary Data sample.

The hybrid π^0 sample is produced based on NC π^0 events in the T2K MC. The true direction and energy of the decay gammas is recorded, and suitable electron candidates from the atmospheric or cosmic ray data or MC are selected to represent one of the gammas. The electron candidates are selected to have energy as close as possible to the gamma they are replacing. The direction of the electron is selected to maintain the same kinematics in SK as the original π^0 , allowing for rotation about the detector z axis and the neutrino beam axis. The remaining gamma is then generated based on MC truth information.

The electron ring and MC gamma ring are composited by directly adding the charge measured in each event by each PMT. The MC gamma is generated with detector dark noise turned off in simulation, so as to avoid double-counting this source of background hits.

The T2K event selection cuts are applied to all four of the hybrid samples. The distributions for each of the cuts are checked, to be sure there are not any discrepancies. The final efficiencies for these events to pass the T2K cuts are shown

in Table C.7. The differences in efficiencies between the data and MC hybrid π^0 samples is used to estimate the T2K π^0 efficiency uncertainty.

Table C.7: Efficiencies for each hybrid π^0 sample to pass the T2K ν_e event selection cuts. The efficiency differences are used to estimate the final error. Uncertainties on the efficiencies come from statistical error.

Sample	Efficiency (%)
Primary data hybrid π^0	6.27 ± 0.31
Primary MC hybrid π^0	5.78 ± 0.31
(MC - data)/data	-7.8 ± 6.7
Secondary data hybrid π^0	6.42 ± 0.17
Secondary MC hybrid π^0	6.14 ± 0.14
(MC - data)/data	-4.3 ± 3.3
Quadratic sum of primary and secondary	8.9 ± 6.1

The quadratic sum of the fractional efficiency difference from the primary and secondary samples yields $8.9 \pm 6.1\%$. The final error is then taken to be the quadratic sum of the efficiency difference error and the statistical error on that, giving a final 10.8% hybrid π^0 error. This error is applied only to background π^0 events. This makes up 70.9% of the $\nu_\mu + \bar{\nu}_\mu$ background, which is approximately 48% of the $\nu_\mu + \bar{\nu}_\mu + \nu_e$ background (depending on the oscillation point). This results in a hybrid π^0 error of 3.6% applied to all background events.

Bibliography

- [1] J. Chadwick. The intensity distribution in the magnetic spectrum of β particles from radium (B + C). *Verh. Phys. Gesell.*, 16:383–391, 1914.
- [2] C. D. Ellis and W. A. Wooster. The average energy of disintegration of radium E. *Proceedings of the Royal Society of London. Series A, Containing Papers of a Mathematical and Physical Character*, 117(776):pp. 109–123, 1927.
- [3] E. Fermi. An attempt of a theory of beta radiation. 1. *Z. Phys.*, 88:161–177, 1934.
- [4] J. Chadwick. Possible existence of a neutron. *Nature*, 129:312, 1932.
- [5] F. Reines and C. L. Cowan. Detection of the free neutrino. *Phys. Rev.*, 92:830–831, 1953.
- [6] C. L. Cowan, F. Reines, F. B. Harrison, H. W. Kruse, and A. D. McGuire. Detection of the free neutrino: a confirmation. *Science*, 124:103–104, 1956.
- [7] R. Davis and D. Harmer. Attempt to observe the $^{37}\text{Cl}(\nu, e^-)^{37}\text{Ar}$ reaction induced by reactor antineutrinos. *Bull. Am. Phys. Soc.*, 4:217, 1959.
- [8] Bruno Pontecorvo. *Chalk river Report PD-205*, 1946.
- [9] G. Danby et al. Observation of high-energy neutrino reactions and the existence of two kinds of neutrinos. *Phys. Rev. Lett.*, 9:36–44, 1962.
- [10] K. Kodama et al. Observation of tau-neutrino interactions. *Phys. Lett.*, B504:218–224, 2001, hep-ex/0012035.
- [11] Y. Fukuda et al. Evidence for oscillation of atmospheric neutrinos. *Phys. Rev. Lett.*, 81:1562–1567, 1998, hep-ex/9807003.
- [12] T. D. Lee and Chen-Ning Yang. Question of Parity Conservation in Weak Interactions. *Phys. Rev.*, 104:254–258, 1956.
- [13] C. S. Wu, E. Ambler, R. W. Hayward, D. D. Hoppes, and R. P. Hudson. Experimental test of parity conservation in beta decay. *Phys. Rev.*, 105:1413–1414, 1957.

- [14] T. D. Lee and Chen-Ning Yang. Parity Nonconservation and a Two Component Theory of the Neutrino. *Phys. Rev.*, 105:1671–1675, 1957.
- [15] M. Goldhaber, L. Grodzins, and A. W. Sunyar. Helicity of neutrinos. *Phys. Rev.*, 109:1015–1017, 1958.
- [16] Raymond Davis, Jr., Don S. Harmer, and Kenneth C. Hoffman. Search for neutrinos from the sun. *Phys. Rev. Lett.*, 20:1205–1209, 1968.
- [17] B. T. Cleveland et al. Measurement of the solar electron neutrino flux with the Homestake chlorine detector. *Astrophys. J.*, 496:505–526, 1998.
- [18] John N. Bahcall. Solar neutrinos. I: Theoretical. *Phys. Rev. Lett.*, 12:300–302, 1964.
- [19] Gian Luigi Fogli, E. Lisi, and D. Montanino. A comprehensive analysis of solar, atmospheric, accelerator and reactor neutrino experiments in a hierarchical three generation scheme. *Phys. Rev.*, D49:3626–3642, 1994.
- [20] V. N. Gribov and B. Pontecorvo. Neutrino astronomy and lepton charge. *Phys. Lett.*, B28:493, 1969.
- [21] R. M. Bionta et al. Observation of a neutrino burst in coincidence with supernova SN 1987a in the Large Magellanic Cloud. *Phys. Rev. Lett.*, 58:1494, 1987.
- [22] K. Hirata et al. Observation of a neutrino burst from the supernova SN 1987a. *Phys. Rev. Lett.*, 58:1490–1493, 1987.
- [23] K. S. Hirata et al. Constraints on neutrino oscillation parameters from the Kamiokande-II solar neutrino data. *Phys. Rev. Lett.*, 65:1301–1304, 1990.
- [24] K. S. Hirata et al. Experimental study of the atmospheric neutrino flux. *Phys. Lett.*, B205:416, 1988.
- [25] Y. Fukuda et al. Atmospheric muon-neutrino / electron-neutrino ratio in the multi-GeV energy range. *Phys. Lett.*, B335:237–245, 1994.
- [26] Q. R. Ahmad et al. Measurement of the charged current interactions produced by B-8 solar neutrinos at the Sudbury Neutrino Observatory. *Phys. Rev. Lett.*, 87:071301, 2001, nucl-ex/0106015.
- [27] Q.R. Ahmad et al. Direct evidence for neutrino flavor transformation from neutral current interactions in the Sudbury Neutrino Observatory. *Phys.Rev.Lett.*, 89:011301, 2002, nucl-ex/0204008.
- [28] D.J. Griffiths. *Introduction to Elementary Particles*. Wiley-VCH, 2008.

- [29] Robert B. Mann. *An Introduction to Particle Physics and the Standard Model*. CRC Press, 2010.
- [30] Makoto Kobayashi and Toshihide Maskawa. CP violation in the renormalizable theory of weak interaction. *Prog. Theor. Phys.*, 49:652–657, 1973.
- [31] Nicola Cabibbo. Unitary symmetry and leptonic decays. *Phys. Rev. Lett.*, 10:531–533, 1963.
- [32] Ch. Kraus et al. Final results from phase II of the Mainz neutrino mass search in tritium β decay. *Eur. Phys. J.*, C40:447–468, 2005, hep-ex/0412056.
- [33] D. N. Spergel et al. First year wilkinson microwave anisotropy probe (WMAP) observations: determination of cosmological parameters. *Astrophys. J. Suppl.*, 148:175–194, 2003, astro-ph/0302209.
- [34] Ziro Maki, Masami Nakagawa, and Shoichi Sakata. Remarks on the unified model of elementary particles. *Prog. Theor. Phys.*, 28:870–880, 1962.
- [35] W. M. Yao et al. Review of particle physics. *J. Phys.*, G33:1–1232, 2006.
- [36] C. Amsler et al. Review of particle physics. *Phys. Lett.*, B667, 2008.
- [37] Andrew G. Cohen, Sheldon L. Glashow, and Zoltan Ligeti. Disentangling neutrino oscillations. *Phys. Lett.*, B678:191–196, 2009, 0810.4602.
- [38] M. Bargiotti et al. Present knowledge of the Cabibbo-Kobayashi-Maskawa matrix. *Riv. Nuovo Cim.*, 23N3:1, 2000, hep-ph/0001293.
- [39] Boris Kayser. CP effects when neutrinos are their own anti-particles. *Adv. Ser. Direct. High Energy Phys.*, 3:334–361, 1989.
- [40] F. J. P. Soler, Colin D. Froggatt, and Franz Muheim. Neutrinos in particle physics, astrophysics and cosmology. Proceedings, 61st Scottish Universities Summer School in Physics, SUSSP61, St. Andrews, UK, August 8-23, 2006.
- [41] Lincoln Wolfenstein. Neutrino oscillations in matter. *Phys. Rev.*, D17:2369–2374, 1978.
- [42] A. Yu. Smirnov. The MSW effect and matter effects in neutrino oscillations. *Phys. Scripta*, T121:57–64, 2005, hep-ph/0412391.
- [43] S. P. Mikheev and A. Yu. Smirnov. Resonance enhancement of oscillations in matter and solar neutrino spectroscopy. *Sov. J. Nucl. Phys.*, 42:913–917, 1985.
- [44] Vernon D. Barger, K. Whisnant, S. Pakvasa, and R. J. N. Phillips. Matter effects on three-neutrino oscillations. *Phys. Rev.*, D22:2718, 1980.

- [45] R. Wendell. Prob3++. <http://www.phy.duke.edu/~raw22/public/Prob3++/>.
- [46] Roger Alexandre Wendell. *Three flavor oscillation analysis of atmospheric neutrinos in Super-Kamiokande*. PhD thesis, Duke University, 2008. AAT-3304410.
- [47] J. H. Christenson, J. W. Cronin, V. L. Fitch, and R. Turlay. Evidence for the 2π decay of the K^0 meson. *Phys. Rev. Lett.*, 13:138–140, 1964.
- [48] K. Nakamura et al. Review of particle physics. *J. Phys.*, G37:075021, 2010.
- [49] C. Athanassopoulos et al. Evidence for $\nu_\mu \rightarrow \nu_e$ neutrino oscillations from LSND. *Phys. Rev. Lett.*, 81:1774–1777, 1998, nucl-ex/9709006.
- [50] A. A. Aguilar-Arevalo et al. A Search for electron neutrino appearance at the $\Delta m^2 \sim 1 \text{ eV}^2$ scale. *Phys. Rev. Lett.*, 98:231801, 2007, 0704.1500.
- [51] Hitoshi Murayama. Theory of neutrino masses and mixings. *Int. J. Mod. Phys. A*, 17:3403–3420, 2002.
- [52] A. D. Sakharov. Violation of CP invariance, c asymmetry, and baryon asymmetry of the universe. *Pisma Zh. Eksp. Teor. Fiz.*, 5:32–35, 1967.
- [53] M. Fukugita and T. Yanagida. Baryogenesis without grand unification. *Phys. Lett.*, B174:45, 1986.
- [54] Boris Kayser. Two questions about neutrinos. 2010, 1012.4469.
- [55] M. H. Ahn et al. Measurement of neutrino oscillation by the K2K experiment. *Phys. Rev.*, D74:072003, 2006, hep-ex/0606032.
- [56] S. Yamamoto et al. An improved search for $\nu(\mu)$ to $\nu(e)$ oscillation in a long-baseline accelerator experiment. *Phys.Rev.Lett.*, 96:181801, 2006, hep-ex/0603004.
- [57] P. Adamson et al. A study of muon neutrino disappearance using the Fermilab main injector neutrino beam. *Phys.Rev.*, D77:072002, 2008, 0711.0769.
- [58] P. Adamson et al. Improved search for muon-neutrino to electron-neutrino oscillations in MINOS. *Phys. Rev. Lett.*, 107:181802, 2011, 1108.0015.
- [59] P. Adamson et al. First direct observation of muon antineutrino disappearance. *Phys.Rev.Lett.*, 107:021801, 2011, 1104.0344.
- [60] P. Adamson et al. Measurement of neutrino oscillations with the MINOS detectors in the NuMI beam. *Phys. Rev. Lett.*, 101:131802, 2008, 0806.2237.

- [61] R. Wendell et al. Atmospheric neutrino oscillation analysis with sub-leading effects in Super-Kamiokande I, II, and III. *Phys.Rev.*, D81:092004, 2010, 1002.3471.
- [62] M. Apollonio et al. Search for neutrino oscillations on a long base-line at the CHOOZ nuclear power station. *Eur. Phys. J.*, C27:331–374, 2003, hep-ex/0301017.
- [63] Y. Itow et al. The JHF-Kamioka neutrino project. 2001, hep-ex/0106019.
- [64] K. Nakamura. Hyper-Kamiokande: A next generation water Cherenkov detector. *Int. J. Mod. Phys.*, A18:4053–4063, 2003.
- [65] K. Abe, T. Abe, H. Aihara, Y. Fukuda, Y. Hayato, et al. Letter of intent: the Hyper-Kamiokande experiment — detector design and physics potential —. 2011, 1109.3262.
- [66] D. Beavis, A. Carroll, I. Chiang, et al. Long baseline neutrino oscillation experiment at the AGS (proposal E889). Physics Design Report, BNL 52459, 1995.
- [67] Y. Yamazaki, K. Hasegawa, M. Ikegami, Y. Irie, T. Kato, et al. Accelerator technical design report for J-PARC. 2003. Hardcopy at DESY, <http://hadron.kek.jp/~accelerator/TDA/tdr2003/index2.html>.
- [68] S. Sato. J-PARC facilities and physics. *Nucl.Phys.*, A862-863:238–243, 2011.
- [69] K. Abe et al. The T2K experiment. *Nucl.Instrum.Meth.*, A659:106–135, 2011, 1106.1238.
- [70] Sacha E. Kopp. Accelerator neutrino beams. *Phys. Rept.*, 439:101–159, 2007, physics/0609129.
- [71] E. Zimmerman. Physics design of horn systems, August 2010. Presentation at the 2010 International Neutrino Summer School, Tokai, Japan.
- [72] M. Yokoyama et al. Application of Hamamatsu MPPC to T2K neutrino detectors. *Nucl. Instrum. Meth.*, A610:128–130, 2009, 0807.3145.
- [73] M. Yokoyama et al. Performance of Multi-Pixel Photon Counters for the T2K near detectors. *Nucl. Instrum. Meth.*, A622:567–573, 2010, 1007.2712.
- [74] I. Giomataris et al. Micromegas in a bulk. *Nucl. Instrum. Meth.*, A560:405–408, 2006, physics/0501003.
- [75] N. Abgrall et al. Time projection chambers for the T2K near detectors. *Nucl. Instrum. Meth.*, A637:25–46, 2011, 1012.0865.

- [76] M. Ziembicki, R. Sulej, S. Aoki, J. Blocki, J. Brinson, et al. The SMRD subdetector at the T2K near detector station. *Acta Phys.Polon.*, B41:1579–1584, 2010.
- [77] Y. Fukuda et al. The Super-Kamiokande detector. *Nucl. Instrum. Meth.*, A501:418–462, 2003.
- [78] S. Yamada et al. Commissioning of the new electronics and online system for the Super-Kamiokande experiment. *IEEE Trans. Nucl. Sci.*, 57:428–432, 2010.
- [79] H. Nishino et al. High-speed charge-to-time converter ASIC for the Super-Kamiokande detector. *Nucl. Instrum. Meth.*, A610:710–717, 2009, 0911.0986.
- [80] W. R. Leo. Techniques for nuclear and particle physics experiments: A how to approach. Berlin, Germany: Springer (1987) 368 p.
- [81] John David Jackson. Classical Electrodynamics, 1998.
- [82] H. G. Berns. *Radon Hut User Manual*. Super-Kamiokande, 2005. Internal SK Documentation.
- [83] Y. Takeuchi et al. Measurement of radon concentrations at Super-Kamiokande. *Phys. Lett.*, B452:418–424, 1999, hep-ex/9903006.
- [84] *WHO handbook on indoor radon: a public health perspective*. World Health Organization, 2009.
- [85] Y. Ashie et al. A Measurement of atmospheric neutrino oscillation parameters by Super-Kamiokande I. *Phys.Rev.*, D71:112005, 2005, hep-ex/0501064.
- [86] Christopher Regis. *A search for proton decay via p going to $\mu^+ \text{kaon}(0)$ in Super Kamiokande I*. PhD thesis, University of California, Irvine, 2011.
- [87] M. Shiozawa. Reconstruction algorithms in the Super-Kamiokande large water Cherenkov detector. *Nucl. Instrum. Meth.*, A433:240–246, 1999.
- [88] E. R. Davies. *Machine Vision: Theory, Algorithms, Practicalities*. Morgan Kaufmann Publishers Inc., San Francisco, CA, USA, 2004.
- [89] M. Yamada et al. Measurements of the charge ratio and polarization of 1.2-TeV/c cosmic ray muons with the KAMIOKANDE-II detector. *Phys. Rev.*, D44:617–621, 1991.
- [90] Tomasz Barszczak. *The efficient discrimination of electron and pi-zero events in a water Cherenkov detector and the application to neutrino oscillation experiments*. PhD thesis, University of California, Irvine, 2005. UMI-31-71221.

- [91] F. James and M. Roos. Minuit: A system for function minimization and analysis of the parameter errors and correlations. *Comput. Phys. Commun.*, 10:343–367, 1975.
- [92] T. Tanaka. SK4 1p.e. analysis and global pC2p.e., November 2008. Presentation at SK Collaboration Meeting (internal).
- [93] L. Michel. Interaction between four half spin particles and the decay of the mu meson. *Proc. Phys. Soc.*, A63:514–531, 1950.
- [94] K. Iyogi, S. Nakayama, and Y. Obayashi. T2K data acquisition and FC event selection at Super-Kamiokande, 2011. T2K-TN-027 (T2K internal technical note).
- [95] S. Nakayama. T2K ν_e event selection at Super-Kamiokande using the RUN1+RUN2 data, 2011. T2K-TN-055 (T2K internal technical note).
- [96] M. Maltoni, T. Schwetz, M. A. Tortola, and J. W. F. Valle. Status of global fits to neutrino oscillations. *New J. Phys.*, 6:122, 2004, hep-ph/0405172.
- [97] A. M. Dziewonski and D. L. Anderson. Preliminary reference earth model. *Phys. Earth Planet. Interiors*, 25:297–356, 1981.
- [98] K. Abe et al. Solar neutrino results in Super-Kamiokande-III. *Phys. Rev.*, D83:052010, 2011, 1010.0118.
- [99] Gary J. Feldman and Robert D. Cousins. A Unified approach to the classical statistical analysis of small signals. *Phys.Rev.*, D57:3873–3889, 1998, physics/9711021.
- [100] J. B. Albert. Sensitivity and discovery potential vs. beam exposure, 2012. T2K-TN-102 (T2K internal technical note).
- [101] Ryan Vincent Terri. *Measurement of ν_e/ν_μ disappearance in the K2K experiment with an expanded fiducial volume at Super-Kamiokande*. PhD thesis, Stony Brook University, 2007. AAT-3337618.
- [102] Maximilien Fechner. *Study of the expected performance of the T2K experiment on ν_{μ} to ν_e oscillation using data from the K2K experiment*. PhD thesis, Université Paris VI, 2006. DAPNIA-06-01-T (In French).
- [103] A. A. Aguilar-Arevalo et al. Unexplained excess of electron-like events from a 1-GeV neutrino beam. *Phys. Rev. Lett.*, 102:101802, 2009, 0812.2243.
- [104] Wolfgang A. Rolke, Angel M. Lopez, and Jan Conrad. Limits and confidence intervals in the presence of nuisance parameters. *Nucl.Instrum.Meth.*, A551:493–503, 2005, physics/0403059.

- [105] N. Abgrall et al. Neutrino flux prediction, 2011. T2K-TN-038 (T2K internal technical note).
- [106] V. Galymov et al. Beam inputs to the 2010a oscillation analysis, 2011. T2K-TN-040 (T2K internal technical note).
- [107] N. Abgrall et al. Beam update for 2010a nue analysis using Run I+II data, 2011. T2K-TN-054 (T2K internal technical note).
- [108] N Abgrall et al. Measurements of cross sections and charged pion spectra in proton-carbon interactions at 31 GeV/c. *Phys.Rev.*, C84:034604, 2011, 1102.0983.
- [109] Rene Brun, Federico Carminati, and Simone Giani. GEANT Detector Description and Simulation Tool. 1994. CERN Program Library Long Writeup.
- [110] Giuseppe Battistoni, S. Muraro, Paola R. Sala, Fabio Cerutti, A. Ferrari, et al. The FLUKA code: Description and benchmarking. *AIP Conf.Proc.*, 896:31–49, 2007.
- [111] A. Ferrari, P.R. Sala, A. Fasso, and J. Ranft. FLUKA: A multi-particle transport code (Program version 2005). 2005.
- [112] C. Zeitnitz and T. A. Gabriel. The GEANT-CALOR interface. In Proc. of International Conference on Calorimetry in High Energy Physics, Tallahassee, FL, USA, February 1993.
- [113] Richard P. Feynman. Very high-energy collisions of hadrons. *Phys. Rev. Lett.*, 23:1415–1417, 1969.
- [114] U. Amaldi, R. Biancastelli, C. Bosio, G. Matthiae, J.V. Allaby, A.N. Diddens, R.W. Dobinson, A. Klovning, J. Litt, L.S. Rochester, K. Schlüpmann, and A.M. Wetherell. Momentum spectra of secondary particles produced in proton-proton collisions at 14.2, 19.2 and 24.0 GeV/c. *Nuclear Physics B*, 86(3):403 – 440, 1975.
- [115] C. Andreopoulos et al. The GENIE neutrino monte carlo generator. *Nucl. Instrum. Meth.*, A614:87–104, 2010, 0905.2517.
- [116] Y. Hayato. NEUT. *Nucl.Phys.Proc.Suppl.*, 112:171–176, 2002.
- [117] Yoshinari Hayato. A neutrino interaction simulation program library NEUT. *Acta Phys. Polon.*, B40:2477–2489, 2009.
- [118] S. Agostinelli et al. GEANT4: A Simulation toolkit. *Nucl.Instrum.Meth.*, A506:250–303, 2003.

- [119] Masayuki Nakahata et al. Atmospheric neutrino background and pion nuclear effect for Kamioka Nucleon Decay Experiment. *J. Phys. Soc. Jap.*, 55:3786, 1986.
- [120] C. H. Llewellyn Smith. Neutrino reactions at accelerator energies. *Phys. Rept.*, 3:261–379, 1972.
- [121] R. A. Smith and E. J. Moniz. Neutrino reactions on nuclear targets. *Nucl. Phys.*, B43:605, 1972.
- [122] L. A. Ahrens et al. Precise determination of $\sin^2\theta_w$ from measurements of the differential cross-sections for muon-neutrino $p \rightarrow$ muon-neutrino p and anti-muon-neutrino $p \rightarrow$ anti-muon-neutrino p . *Phys. Rev. Lett.*, 56:1107, 1986.
- [123] Carl H. Albright, C. Quigg, R. E. Shrock, and J. Smith. Neutrino - proton elastic scattering: Implications for weak interaction models. *Phys. Rev.*, D14:1780, 1976.
- [124] Dieter Rein and Lalit M. Sehgal. Neutrino excitation of baryon resonances and single pion production. *Annals Phys.*, 133:79–153, 1981.
- [125] D. Rein. Angular distribution in neutrino induced single pion production processes. *Z. Phys.*, C35:43–64, 1987.
- [126] Dieter Rein and Lalit M. Sehgal. Coherent π^0 production in neutrino reactions. *Nucl. Phys.*, B223:29, 1983.
- [127] M. Gluck, E. Reya, and A. Vogt. Dynamical parton distributions revisited. *Eur. Phys. J.*, C5:461–470, 1998, hep-ph/9806404.
- [128] A. Bodek and U.K. Yang. Modeling neutrino and electron scattering inelastic cross-sections in the few GeV region with effective LO PDFs TV Leading Order. *Nucl.Phys.Proc.Suppl.*, 2003, hep-ex/0308007.
- [129] L. L. Salcedo, E. Oset, M. J. Vicente-Vacas, and C. Garcia-Recio. Computer simulation of inclusive pion nuclear reactions. *Nucl. Phys.*, A484:557, 1988.
- [130] Patrick de Perio. NEUT pion FSI. *AIP Conf. Proc.*, 1405:223–228, 2011.
- [131] Y. Nakajima et al. Measurement of inclusive charged current interactions on carbon in a few-GeV neutrino beam. *Phys. Rev.*, D83:012005, 2011, 1011.2131.
- [132] Y. Kurimoto et al. Measurement of inclusive neutral current neutral pion production on carbon in a few-GeV neutrino beam. *Phys. Rev.*, D81:033004, 2010, 0910.5768.

- [133] A. A. Aguilar-Arevalo et al. First measurement of the muon neutrino charged current quasielastic double differential cross section. *Phys. Rev.*, D81:092005, 2010, 1002.2680.
- [134] M. Hasegawa et al. Search for coherent charged pion production in neutrino carbon interactions. *Phys. Rev. Lett.*, 95:252301, 2005, hep-ex/0506008.
- [135] J. Formaggio and G. P. Zeller. From eV to EeV: Neutrino cross sections across energy scales. *to be published in Rev. Mod. Phys.*, 2012. Pending publication.
- [136] C. Zeitnitz and T. A. Gabriel. The GEANT - CALOR interface and benchmark calculations of ZEUS test calorimeters. *Nucl. Instrum. Meth.*, A349:106–111, 1994.
- [137] Claudio Giganti. *Particle Identification in the T2K TPCs and study of the electron neutrino component in the T2K neutrino beam*. PhD thesis, Université Paris Sud-XI, 2010. IRFU-SPP/Saclay09-2010.
- [138] P. de Perio et al. 2010a neutrino interaction systematic uncertainty choices for the NEUT generator, 2011. T2K-TN-030 (T2K internal technical note).
- [139] P. de Perio, Y. Hayato, K. McFarland, R. Terri, and M. O. Wascko. Neut systematic studies for 2010a analysis, 2011. T2K-TN-032 (T2K internal technical note).
- [140] P. de Perio, Y. Hayato, and R. Tacik. NEUT nuclear effects (FSI), 2011. T2K-TN-033 (T2K internal technical note).
- [141] Cezary Juszczak. Running Nuwro. *Acta Phys. Polon.*, B40:2507–2512, 2009, 0909.1492.
- [142] C. Giganti, F. Blaszczyk, A. Longhin, and M. Zito. Study of neutrino charged current interactions in the ND280 tracker, 2011. T2K-TN-015 (T2K internal technical note).
- [143] V. Galymov et al. Neutrino flux uncertainty for 10a data analysis, 2011. T2K-TN-039 (T2K internal technical note).
- [144] Maurice G. Kendall and Alan Stuart. *The Advanced Theory of Statistics*. C. Griffin, London, 4th edition, 1977.
- [145] J. Neyman. Outline of a theory of statistical estimation based on the classical theory of probability. *Philosophical Transactions of the Royal Society of London. Series A, Mathematical and Physical Sciences*, 236(767):pp. 333–380, 1937.

- [146] Jan Conrad, O. Botner, A. Hallgren, and Carlos Perez de los Heros. Including systematic uncertainties in confidence interval construction for Poisson statistics. *Phys.Rev.*, D67:012002, 2003, hep-ex/0202013.
- [147] Robert D. Cousins and Virgil L. Highland. Incorporating systematic uncertainties into an upper limit. *Nucl.Instrum.Meth.*, A320:331–335, 1992. Revised version.
- [148] Juan Pedro Ochoa Ricoux. A search for muon neutrino to electron neutrino oscillations in the MINOS Experiment. FERMILAB-THESIS-2009-44.
- [149] P. Adamson et al. Search for muon-neutrino to electron-neutrino transitions in MINOS. *Phys. Rev. Lett.*, 103:261802, 2009, 0909.4996.
- [150] J. Lundberg, J. Conrad, W. Rolke, and A. Lopez. Limits, discovery and cut optimization for a Poisson process with uncertainty in background and signal efficiency: TRolke 2.0. *Comput.Phys.Commun.*, 181:683–686, 2010, 0907.3450.
- [151] K. Abe et al. First muon-neutrino disappearance study with an off-axis beam. *Phys.Rev.*, D85:031103, 2012, 1201.1386. 7 pages, 4 figures.
- [152] R. Brun and F. Rademakers. ROOT: An object oriented data analysis framework. *Nucl.Instrum.Meth.*, A389:81–86, 1997.
- [153] K. Abe et al. Indication of electron neutrino appearance from an accelerator-produced off-axis muon neutrino beam. *Phys. Rev. Lett.*, 107:041801, 2011, 1106.2822.
- [154] J. Hignight, K. Iyogi, H. Kaji, S. Nakayama, Y. Nishimura, R. Wendell, and T. Wongjirad. Vertex, entering background, and reconstruction studies at Super-Kamiokande for T2K run 1+2, 2011. T2K-TN-085 (T2K internal technical note).
- [155] Y. Abe et al. Indication for the disappearance of reactor electron antineutrinos in the Double Chooz experiment. *Phys.Rev.Lett.*, 108:131801, 2012, 1112.6353. 7 pages, 4 figures, (new version after PRL referee’s comments).
- [156] F.P. An et al. Observation of electron-antineutrino disappearance at Daya Bay. 2012, 1203.1669. 5 figures. Version to appear in *Phys. Rev. Lett.*
- [157] J.K. Ahn et al. Observation of reactor electron antineutrino disappearance in the RENO experiment. 2012, 1204.0626.
- [158] C. Mariani. DUSEL (Deep Underground Science and Engineering Laboratory) and LBNE (Long Baseline Neutrino Experiment). *Nucl. Phys. Proc. Suppl.*, 217:344–346, 2011.

- [159] D. S. Ayres et al. NOvA proposal to build a 30-kiloton off-axis detector to study neutrino oscillations in the Fermilab NuMI beamline. 2004, hep-ex/0503053.
- [160] P. Haenggi, R. D. Viollier, U. Raff, and K. Alder. Muon decay in orbit. *Phys. Lett.*, B51:119–122, 1974.
- [161] W. N. Cottingham and D. A. Greenwood. An Introduction to the Standard Model of Particle Physics. Cambridge, UK: Univ. Pr. (2007) 272 p.
- [162] J. F. Donoghue, E. Golowich, and Barry R. Holstein. Dynamics of the standard model. *Camb. Monogr. Part. Phys. Nucl. Phys. Cosmol.*, 2:1–540, 1992.
- [163] J. B. Albert and K. Okumura. Updated ν_e oscillation analysis with RUN1+2 data, 2011. T2K-TN-052 (T2K internal technical note).
- [164] T. Eichten et al. Particle production in proton interactions in nuclei at 24-GeV/c. *Nucl. Phys.*, B44:333–343, 1972.
- [165] S. Mine. SK detector stability, 2010. T2K-TN-019 (T2K internal technical note).
- [166] J. B. Albert, H. Kaji, S. Nakayama, S. Mine, and K. Okumura. Study on SK ν_e candidates and systematic errors with T2K 3.23×10^{19} POT data, 2011. T2K-TN-028 (T2K internal technical note).
- [167] K. Okumura. π^0 background study using hybrid π^0 sample at Super-K, 2011. T2K-TN-029 (T2K internal technical note).
- [168] J. P. A. M. de Andre and S. Mine. Updates of π^0 background systematic error at SK for ν_e search, 2011. T2K-TN-057 (T2K internal technical note).

Biography

Joshua Benjamin Albert was born April 8, 1984, in Upper Darby, Pennsylvania. His parents are Laurie and David Albert, and he has two siblings, Elizabeth and Daniel. He grew up in Broomall, and then Newtown Square, Pennsylvania.

After graduating from Marple Newtown High School in 2002, he enrolled at Penn State University, in the Schreyer Honors College. Initially an engineering science major, he switched to physics before his junior year. He graduated in August 2006, with honors in physics. His honors thesis title was “A System To Produce A Feshbach Resonance In Ultra-Cold Rubidium-87”, based on undergraduate research with Professor David Weiss.

In 2006, Josh started graduate studies in physics at Duke University, as a James B. Duke fellow. Under advisor Chris Walter, Josh was an active member of the Super-Kamiokande and T2K collaborations. The primary research result was the ν_e appearance analysis at T2K, the subject of this dissertation, as well as [153]. Upon successful defense, Josh will graduate with a Ph.D. in physics from Duke University.